Clustering and Impact Analysis of Compound Hydro-Meteorological Hazards in Germany Based on Insurance Loss Data

Zur Erlangung des akademischen Grades einer
DOKTORIN DER NATURWISSENSCHAFTEN (Dr. rer. nat.)
von der KIT-Fakultät für
Bauingenieur-, Geo- und Umweltwissenschaften des
Karlsruher Instituts für Technologie (KIT)

genehmigte

DISSERTATION

von

M. Sc. Katharina Küpfer

Tag der mündlichen Prüfung:	27.06.2025
Referent:	Prof. Dr.-Ing. Stefan Hinz
Korreferent:	Prof. Dr. Michael Kunz

Karlsruhe (2025)

Abstract

Multi-hazard or compound weather and climate events occur frequently across Europe and in Germany. However, research and risk management practices often remain focused on single hazards. To effectively anticipate and adapt to an increasingly complex and dynamic risk landscape, assessments of dynamics between different hazards are crucial, including their temporal dependence. While previous studies have examined the temporal clustering in specific hazards such as precipitation or windstorms, temporal dependencies across multiple hazard types remain underexplored. In addition, most research relies on observational or model data, with limited use of impact-based data to assess such dependencies.

This thesis presents a detailed analysis of losses from various hydrometeorological hazards in two study areas – Baden-Württemberg (southwestern Germany, 1986–2023) and Germany as a whole (1997–2022) – with a focus on their temporal clustering and potential atmospheric drivers. The analyses are based on daily building insurance loss data with a high insurance density, particularly in Baden-Württemberg. Major damaging events were identified using a 90th percentile threshold applied to inflation-adjusted losses and claims. Meteorological observation data were used to classify these events into hazard types, including pluvially dominated, fluvially dominated, and mixed floods, hail, convective gusts, and windstorms.

Analyses of the loss distribution reveal an extreme skewness in the data, with a small number of events accounting for the majority of the losses. A clear seasonality is evident, causing events to mainly occur between May and August (MJJA) or between December and February (DJF). Regional differences exist depending on the hazard, where the northwest is most affected by windstorm events, eastern Germany is most prone to flooding, and the south is most affected by hail and convective gust events.

Sub-seasonal clusters (within 2–3 weeks) of single and multiple hazards occurred most frequently in the early 2000s, with convective clusters concentrated in MJJA. For many combinations, events occurring within clusters are associated with higher losses than isolated events. While the temporal distribution of some single hazard types deviates little from a homogeneous Poisson process, that is, a random occurrence, convective multi-hazard events cluster significantly during MJJA. Large-scale atmospheric patterns provide insights into these clusters: Windstorm clusters and combined windstorm and fluvial flood clusters in DJF are linked to strong westerlies and a positive phase of the North Atlantic Oscillation. In contrast, convective clusters during MJJA are associated with pronounced atmospheric blocking, typically positioning Germany on the western flank of the block. Minimal differences between convective hazards suggest that similar synoptic conditions favor hail, convective gusts, and pluvial floods.

The investigation of temporal clustering of multiple hydro-meteorological hazards in Germany shows that there are temporal dependencies between these hazards, which can amplify their impacts and which are modulated by large-scale atmospheric circulation patterns. This thesis highlights the need for integrated, impact-based assessments of compound hydro-meteorological hazards and their associated risks.

Zusammenfassung

Immer wieder treten in Europa und auch in Deutschland Häufungen verschiedener Extremwetterereignisse auf. Forschung und Risikomanagement konzentrieren sich jedoch häufig auf einzelne Gefahren. Für eine wirksame Vorhersage und effektive Anpassung an eine zunehmend komplexe und dynamische Risikolandschaft ist die Bewertung der Dynamik zwischen verschiedenen Gefahren, einschließlich ihrer zeitlichen Abhängigkeit, von entscheidender Bedeutung. Während frühere Arbeiten die zeitliche Häufung bei bestimmten Gefahren wie niederschlagsinduzierte Überschwemmungen oder Stürmen untersucht haben, sind zeitliche Abhängigkeiten zwischen verschiedenen Gefahrentypen noch nicht ausreichend erforscht. Darüber hinaus stützen sich die meisten Forschungsarbeiten auf Beobachtungs- oder Modelldaten und verwenden nur in begrenztem Umfang Schadendaten, um solche Abhängigkeiten zu bewerten.

In dieser Arbeit wird eine detaillierte Analyse der Schäden durch verschiedene hydrometeorologischen Gefahren in zwei Untersuchungsgebieten - Baden-Württemberg (1986-2023) und Deutschland insgesamt (1997-2022) - vorgestellt, wobei der Schwerpunkt auf ihrer zeitlichen Häufung und möglichen atmosphärischen Einflussfaktoren liegt. Die Analysen basieren auf täglichen Schadendaten einer Gebäudeversicherung, mit einer hohen Versicherungsdichte insbesondere in Baden-Württemberg. Großschadenereignisse wurden anhand einer 90-Perzentil-Schwelle identifiziert, die auf inflationsbereinigte Schäden und Schadenmeldungen angewendet wurde. Meteorologische Beobachtungsdaten wurden verwendet, um diese Ereignisse in verschiedene Gefahrentypen zu klassifizieren: pluvial und fluvial dominierte Überschwemmungen sowie deren Mischform, Hagel, konvektiver Böen und Windstürme. Die Analyse der Schadenverteilung zeigt eine extreme Rechtsschiefe der Daten, wobei eine kleine Anzahl von Ereignissen den Großteil der Schäden ausmacht. Es ist eine deutliche Saisonalität zu erkennen, die dazu führt, dass die Ereignisse hauptsächlich zwischen Mai und August (MJJA) oder zwischen Dezember und Februar (DJF) auftreten. Je nach Naturgefahr bestehen regionale Unterschiede: So ist der Nordwesten am stärksten von Sturmereignissen betroffen, Ostdeutschland am stärksten von Überschwemmungen und im Süden werden die höchsten Schäden durch Hagel und konvektive Böen verursacht.

Sub-saisonale Häufungen (innerhalb von 2-3 Wochen) von Ereignissen einzelnen oder kombinierten (*multi-hazard*) Typs traten am häufigsten in den frühen 2000er Jahren auf, wobei sich Häufungen konvektiven Typs auf MJJA konzentrierten. Bei vielen Kombinationen sind Ereignisse, die innerhalb von Clustern auftreten, mit höheren Schäden verbunden als Einzelereignisse. Während die zeitliche Verteilung einiger Einzelgefahrenarten kaum von einem homogenen Poisson-Prozess, also einem zufälli-

gen Auftreten, abweicht, häufen sich konvektive Multi-Hazard-Ereignisse während des MJJA deutlich. Großräumige atmosphärische Muster geben Aufschluss über diese Häufungen: Cluster aus Winterstürmen, auch in Kombination mit Flusshochwassern, sind im Winter mit starken Westwinden und einer positiven Phase der Nordatlantischen Oszillation verbunden. Im Gegensatz dazu sind konvektive Cluster während MJJA mit einem ausgeprägten atmosphärischen Blocking assoziiert, welches Deutschland typischerweise an der Westflanke des Blocks positioniert. Minimale Unterschiede zwischen den konvektiven Ereignistypen deuten darauf hin, dass ähnliche synoptische Bedingungen Hagel, konvektive Böen und pluvial dominierte Überschwemmungen begünstigen.

Die Untersuchung der zeitlichen Häufung mehrerer hydrometeorologischer Naturgefahren in Deutschland zeigt, dass zeitliche Abhängigkeiten zwischen den einzelnen Gefahren bestehen, die deren Auswirkungen verstärken können, und durch die großräumige atmosphärische Zirkulation moduliert werden. Diese Arbeit unterstreicht die Notwendigkeit integrierter, auswirkungsbasierter Analysen komplexer hydrometeorologischer Naturgefahren und den damit verbundenen Risiken.

Preface

The PhD candidate confirms that the research presented in this thesis contains significant scientific contributions by herself. Parts of chapters 3, 4, and 6 reuse material from the following publication, where direct citations are marked with a vertical line next to the text:

Küpfer, K., A. Tuel, and M. Kunz, 2024 [*Preprint*, submitted to *Natural Hazards and Earth System Sciences*]: Impact-based temporal clustering of multiple meteorological hazard types in southwestern Germany. EGUsphere, 2024, 1–30, URL https://egusphere.copernicus.org/preprints/2024/egusphere-2024-2803/.

Chapters 1, 5, 7, and 8 in part also contain ideas from Küpfer et al. (2024), which have been fully rephrased and integrated in the text. The concept of the study presented in Küpfer et al. (2024) was developed by Katharina Küpfer and Michael Kunz. Data analysis and Figures were done by Katharina Küpfer. A part of the code used was developed by Alexandre Tuel. Katharina Küpfer wrote the original draft. All authors have contributed with methods, the discussion and revision of the original draft. © The Authors.

During the candidate's doctoral studies, the candidate also contributed to the following publications, which are not included in this thesis:

- Mohr, S., U. Ehret, M. Kunz, P. Ludwig, A. Caldas-Alvarez, J. E. Daniell, F. Ehmele, H. Feldmann, M. J. Franca, C. Gattke, M. Hundhausen, P. Knippertz, K. Küpfer, B. Mühr, J. G. Pinto, J. Quinting, A. M. Schäfer, M. Scheibel, F. Seidel, and C. Wisotzky, 2023: A multi-disciplinary analysis of the exceptional flood event of July 2021 in central Europe – Part 1: Event description and analysis. Nat. Hazards Earth Syst. Sci., 23, 525–551, DOI: https://doi.org/10.5194/nhess-23-525-2023.
- Ludwig, P., F. Ehmele, M. J. Franca, S. Mohr, A. Caldas-Alvarez, J. E. Daniell, U. Ehret, H. Feldmann, M. Hundhausen, P. Knippertz, et al., 2023: A multi-disciplinary analysis of the exceptional flood event of July 2021 in central Europe – Part 2: Historical context and relation to climate change. Nat. Hazards Earth Syst. Sci., 23, 1287–1311, DOI: https://doi.org/10.5194/nhess-23-1287-2023.
- Brett, L., H. C. Bloomfield, A. Bradley, T. Calvet, A. Champion, S. De Angeli, M. C. de Ruiter, S. B. Guerreiro, J. Hillier, D. Jaroszweski, B. Kamranzad, M. M. Keinänen-Toivola, K. Kornhuber, K. Küpfer, C. Manning, K. Mattu, E. Murtagh, V. Murray, Á. Ní Bhreasail, F. O'Loughlin, C.

Parker, M. Pregnolato, A. M. Ramos, J. Schlumberger, D. Theochari, P. Ward, A. Wessels, and C. J. White, 2025: Science–policy–practice insights for compound and multi-hazard risks. Meteorol. Appl., 32(2), e70043, DOI: https://doi.org/10.1002/met.70043.

The candidate wrote the text of this manuscript having considered feedback from Michael Kunz. Analyses were performed solely by the candidate based in part on discussions with Michael Kunz. The research presented in this thesis has been accomplished using Python (available at: https://www.python.org/, last visited 11 March 2025) and RStudio (available at: https://posit.co/download/rstudio-desktop/, last visited 11 March 2025). The code developed by the PhD candidate for parts of the results in Küpfer et al. (2024) and in Chapters 5, 6 and 7 is available at: https://radar.kit.edu/radar/de/dataset/bkbwu1c6cbrqjsq6. The artificial intelligence tools DeepL, ChatGPT, Elicit, and Perplexity have been used for the improvement of data analysis scripts, plotting scripts, and stylistic improvements in the thesis.

The research of the PhD candidate has been supported by the "Foundation for Protection Against Natural Hazards"(Stiftung Umwelt und Schadenvorsorge) and was embedded in the work of the Center for Disaster Management and Risk Reduction (CEDIM, www.cedim.de). Two research stays, one at the *University of Bern* and one at the *Vrije Universiteit Amsterdam*, and a winter school were supported by the GRACE Graduate School. Other travel activities including conferences, a workshop, and a summer school were supported by the EU COST Action Understanding and modeling compound climate and weather events (DAMOCLES).

Contents

1. Introduction and research questions

Weather- and climate-related hazards frequently cause considerable loss and damage in Germany. Recent examples include the extreme flood caused by the low pressure system *Bernd* in western Germany and Belgium in July 2021 (Mohr et al., 2023) or the storm series *Dudley, Eunice*, and *Franklin* in February 2022 (Mühr et al., 2022). In 2024, Germany was again affected by widespread and compound flooding from cyclone *Boris* (Zscheischler et al., 2025). Each of these events was driven by the large-scale atmospheric circulation, which significantly influenced their occurrence and severity: *Bernd* developed under a blocking pattern, resulting in a low propagation of the rain field and thus heavy rainfall; the 2022 storms were steered by a strong North Atlantic jet stream; and *Boris* followed a typical northward track from the western Mediterranean, directing moist air into central Europe. All three cases led to fatalities and severe societal impacts. The floods and storms resulted in extensive damage to critical infrastructure with potential long-term consequences (Mohr et al., 2023), and were associated with considerable economic losses. The financial impacts of such hazards have increased globally (Swiss Re, 2024) and in Europe (Kron et al., 2019), which can partly be attributed to climate change.

Between 1980 and 2023, total losses caused by natural hazards are estimated at €738 billion in the European Union (EEA, 2023). In Germany, the most frequent damaging natural hazards were related to wind extremes and flood events both historically (1950–2013, Kreibich et al., 2014) as well as in recent years (1990–2024, Thieken and Keyserlingk, 2025). Germany, and the southwest in particular, has been a hotspot for damaging meteorological hazards in recent decades, resulting in high losses compared to other regions in Europe (Kron et al., 2019; Púčik et al., 2019). Between 2001 and 2021, extreme events have amounted to annual losses of about €6.6 billion in Germany, including indirect effects (Trenczek et al., 2022). For example, the winter storm *Lothar* in 1999 caused total economic losses of more than €15 billion (Swiss Re, 2019), the hail event *Andreas* in 2013 led to an economic loss of more than €1 billion (Kunz et al., 2018), and most recently, flood event *Boris* in June 2024 caused expected economic losses of more than €2 billion (GDV, 2024c).

Weather extremes frequently occur not in isolation, but as part of a sequence or in combination with other events. For example, there was a sequence of multiple events in 2013 in southwestern Germany: an exceptional flood occurred during the end of May and the beginning of June, which was followed by extreme heat and a severe hailstorm in July, as well as extreme heat in the beginning of August (DWD, 2013). All of these events caused severe impacts, with inundated towns and villages after the flooding, damaged roofs and facades of buildings due to large hail (Kunz et al., 2018), and blocked water routes

due to drought hindering the transportation of goods (Thieken et al., 2016). Impacts of cascading events can lead to an amplification of the damage or additional emerging impacts. As an example, compound extremes in winter have been shown to increase mortality (Plavcova and Urban, 2020). Buildings can suffer additional damage, for example, due to damaged roofs offering insufficient protection against rain (Martius et al., 2016). Additionally, indirect effects include blocked traffic routes after a previous event (Mohr et al., 2023), disturbed emergency responses (Raymond et al., 2020), and an increased recovery time (Ruiter et al., 2020). Other examples of cascading impacts include an increased runoff in case of a heavy rain event after a heatwave, or an increased debris flow with damage potential in case of flooding after a storm event (see, e. g., Kreibich et al., 2014). Cascading events can also cause societal impacts, for example, while recovery is still ongoing: Authorities and technical organizations can become overburdened in a series of events due to limited capacity for repeated action (Raymond et al., 2020). The issue of overload is particularly relevant in Germany, as a significant proportion of relief organizations rely heavily on volunteer engagement (Bartel and Schubert, 2025). In longer periods of action, a lack of food supply or rest for rescuers can harm recovery. With respect to economic impacts, the allocation of financial resources is challenged in the case of high-impact events (Hurk et al., 2023), challenging an effective response to complex events with temporal overlaps (Raymond et al., 2020). Major damaging hazards happening in close succession can therefore cause capacity problems for civil protection, local authorities, insurance companies, and NGOs, while an understanding of their complex interactions could still be improved (Brett et al., 2025). In the coming decades, changes in the frequency and/or intensity of compound extremes are expected, caused by human-induced climate change (Masson-Delmotte et al., 2021).

When a combination of multiple drivers and/or hazards contributes to societal or environmental risk, they are referred to as compound weather or climate events (Zscheischler et al., 2018). Similarly, the United Nations Office for Disaster Risk Reduction (UNDRR) defines multi-hazards as 'the specific contexts where hazardous events may occur simultaneously, cascadingly or cumulatively over time, and taking into account the potential interrelated effects' (UNDRR, 2016, p. 19). The Intergovernmental Panel on Climate Change (IPCC) Special Report on Managing the Risks of Extreme Events and Disasters to Advance Climate Change Adaptation (SREX) highlights the relevance of compound weather and climate events to address modeling and risk estimation of extreme weather impacts (Masson-Delmotte et al., 2021). Compound or multi-hazard events are frequent; for example, it has recently been shown that 19 % of events in the Emergency Events Database (EM-DAT) can be classified as multi-hazard events, leading to an over-proportionally high share of 59 % of global economic losses, with the primary meteorological hazard types being floods and storms (Lee et al., 2024). Despite this large proportion, risk models such as those used by the insurance industry generally consider the different hazard types independently (Hillier et al., 2015; Mitchell-Wallace et al., 2017; Priestley et al., 2018). Risk analyses and risk management often lack this multi-hazard perspective as well (Kreibich et al., 2014). While being hard to quantify (e. g., Hillier et al., 2025), the risk of compound weather and climate extremes may be

underestimated when interactions between extreme events are neglected (e. g., Hillier and Dixon, 2020; Hillier et al., 2025).

To date, many studies have investigated compound weather and climate events. In the beginning, most of them focused on single hazard types such as compound flooding, or multiple dry hazard types, such as heatwaves and droughts (Ruiter and Loon, 2022). In recent years, the compound occurrence of seemingly independent hazard types has gained increasing attention in the literature. For example, Ruiter et al. (2020) evaluated consecutive disasters of different types, and recent work focuses on the classification of multiple hazards, including a range of hazard types (Claassen et al., 2023). Specifically, the interrelationship between flood and wind occurrence has received quite some attention (e. g., Hillier et al., 2015; Martius et al., 2016; Bloomfield et al., 2023, 2024; Hillier et al., 2025).

The occurrence of weather extremes is fundamentally driven by physical processes in the atmosphere. The variability in the large-scale atmospheric circulation can be described by a defined number of states by so-called modes of variability, also known as teleconnections. Teleconnections govern surface weather, and are closely linked to many local atmospheric hazards, which can include simultaneous regional hazards (e. g., Steptoe et al., 2018). Another way to describe the atmospheric circulation with a set of defined states are weather regimes, which determine regional weather conditions (e. g., wind speed) on time scales of several days to weeks (Grams et al., 2017). While the physical background of these modes of variability is not fully understood yet, many studies have focused on the relationship of surface extremes with these modes of variability. In central Europe, an influence of variability modes on weather extremes has been found in winter for windstorms (e. g., Donat et al., 2010), and in summer for convective hazards (e. g., Piper et al., 2019). The connection of temporally related hazards of different types and their underlying meteorological conditions remains underexplored, particularly when examined from an impact-focused perspective (Hillier and Dixon, 2020).

The temporal dependence of multiple hazards can be quantified using different clustering techniques. Temporal clustering, also referred to as serial clustering (Mailier et al., 2006), has been widely investigated for single hazard types, mainly for extratropical cyclones in Europe (e. g., Mailier et al., 2006; Vitolo et al., 2009; Pinto et al., 2013; Karremann et al., 2014; Pinto et al., 2016; Dacre and Pinto, 2020), and heavy precipitation at various spatial scales (Barton et al., 2016; Kopp et al., 2021; Tuel and Martius, 2021a; Banfi and De Michele, 2024). There are also some studies on the serial clustering of hail (Barras et al., 2021) as well as droughts (Brunner and Stahl, 2023). The basic idea of serial clustering is to quantify the deviation of a binary time series from a homogeneous Poisson process, which is characterized by a constant rate of occurrence. Two approaches are commonly used for this assessment. First, the dispersion index can identify overdispersion, that is, the overall tendency of a time series to cluster (e. g., Mailier et al., 2006; Vitolo et al., 2009; Karremann et al., 2014). Second, the Ripley's K function (e. g., Barton et al., 2016; Tuel and Martius, 2021b,a) is a statistical metric that quantifies the average number of events within a given temporal window around a randomly chosen event in the time series.

Compound and multi-hazard events have been assessed with hydro-meteorological observation and model data in many studies (e. g., Bevacqua et al., 2021), with a research body rapidly increasing over the past decades (Brett et al., 2024). However, to adequately assess the risk, accurate impact information is essential. Impact-based mapping of hazards has also been shown to be practical, stakeholder-relevant, and broadly applicable (Hillier and Dixon, 2020). The main challenge with impact data is their scarcity (e. g., Brito et al., 2024). Impact databases covering large temporal and spatial scales are rare, and if they exist, often contain incomplete information. Consequently, there is a gap in understanding how the impacts of different hazards interact across time and space (Brito et al., 2024). In databases like EM-DAT, which is among the few public databases including impacts across hazards, reporting differences exist, which lead to incomplete and inconsistent information on the temporal and spatial characteristics of events (Jäger et al., 2024). Towards this end, insurance loss data allow to address some of these issues, since they rely on daily claims and losses and allow to compare the damage of different hazard types (e. g., Hillier et al., 2015), although they also come with shortcomings (e. g., Gall et al., 2009). Furthermore, Europe's multi-hazard profile is characterized more by economic damage than by population impact, compared to regions such as Southeast Asia, where the number of people affected by multi-hazard events is substantially higher (Steptoe et al., 2018). In particular, (southern) Germany exhibits disproportionately high economic losses (Kron et al., 2019; Púčik et al., 2019; EEA, 2023).

According to the research gaps outlined above, the overarching aim of this work is to assess the temporal (serial) clustering of losses from multiple hydro-meteorological hazard types in Baden-Württemberg (BW) and Germany (GER), also with regard to potential triggers. This is approached by investigating the loss distribution of major loss events in GER and BW, regarding their severity, regional differences over GER and trends in the losses. Furthermore, the temporal variability of multiple hazards at annual and sub-seasonal scales is investigated by identifying and quantifying their temporal clustering on the sub-seasonal timescale. In addition, the serial clusters are set in context with the large-scale atmospheric circulation present during their occurrence. Distinct and persistent patterns in the large-scale flow caused the occurrence of the windstorm series in 2020, the sequence of events in 2013, and 2021 western Germany flood triggered by low *Bernd*, for example.

As seen above, the temporal clustering of hydro-meteorological hazards has so far been mainly investigated for single hazard types. To the author's knowledge, the serial clustering of multiple (meteorological) hazard types has not been researched so far, and studies assessing the temporal dependence of multiple hazard types with respect to impact are scarce. Furthermore, impact data is rarely put in context with potential large-scale meteorological triggers.

To help close these research gaps, an event catalog of major extreme events is produced using insurance loss data (i) from the SV SparkassenVersicherung (SV) insurance company (1986–2023) operating mainly in southwestern Germany and (ii) from the German Insurance Association (*Gesamtverband der deutschen Versicherungswirtschaft*, GDV; 1997–2022). After identifying extreme events from the daily

loss data, the events in this catalog are categorized according to their meteorological drivers: pluvial, mixed, and fluvial floods, hail, convective gusts, and windstorms. With this set of six distinct hydro-meteorological hazard types, at first, the loss distribution across Germany is evaluated with respect to severity, spatial and temporal scales. Second, clustering periods are identified using a count-based algorithm, and the statistical tool Ripley's K is used to assess the degree of clustering. Ripley's K, primarily used in hydrologic data analysis, is here being newly applied to impact data. Furthermore, two methods are used to identify extreme events: a flexible event definition with a varying event duration, and a fixed definition and corresponding event duration. The flexible event definition is common in meteorological and hydrological research, whereas the fixed definition is common for insurance applications. Both methods lead to a different number of events. This is relevant, as the impact of a set of loss events on an insurance is often not only dependent on the overall loss, but also on the number of individual loss events. Reasons for this are the Solvency II European Directive as well as the structure of reinsurance contracts (Vitolo et al., 2009), which take into account the frequency of losses and therefore also the number of events. In addition, the relationship of identified clustered and isolated periods with the large-scale atmospheric circulation (geopotential height anomalies) and modes of variability (teleconnections and weather regimes) is investigated. This analysis is performed separately for wintertime and summertime extremes and illustrated by case studies.

Thus, the following research questions are addressed in this thesis:

1. How are insured losses from fluvial, pluvial, and mixed floods, hail, convective gusts, and windstorms distributed in BW and GER with regard to their spatio-temporal variability?
2. When do sub-seasonal clusters of individual damaging hazard types as well as clusters of their serial combination occur, and is this clustering significant compared to a random process?
3. How do the degree and significance of clustering depend on the chosen duration of the event?
4. Does clustering exacerbate the impact of hydro-meteorological hazards, as measured by insured losses?
5. Which large-scale circulation patterns are associated with the occurrence of clustered and isolated hydro-meteorological extremes?

This thesis is structured as follows: First, an overview of the theoretical background of the meteorological drivers behind the hazards, their interactions, and the large-scale circulation is given (Chapter 2). This also includes an overview of the main statistical background. Chapter 3 presents the variety of data sets used within this thesis, including the loss data, which provide the basis for subsequent analyses. Subsequently, Chapter 4 covers the methodological approaches applied within this thesis. This work consists of three results chapters (Fig. 1.1): An analysis of the loss distribution regarding time and space is provided in Chapter 5. Chapter 6 addresses clustering of multiple hydro-meteorological hazards in Germany on the time scale of calendar years as well as sub-seasonal clustering, including a count-based

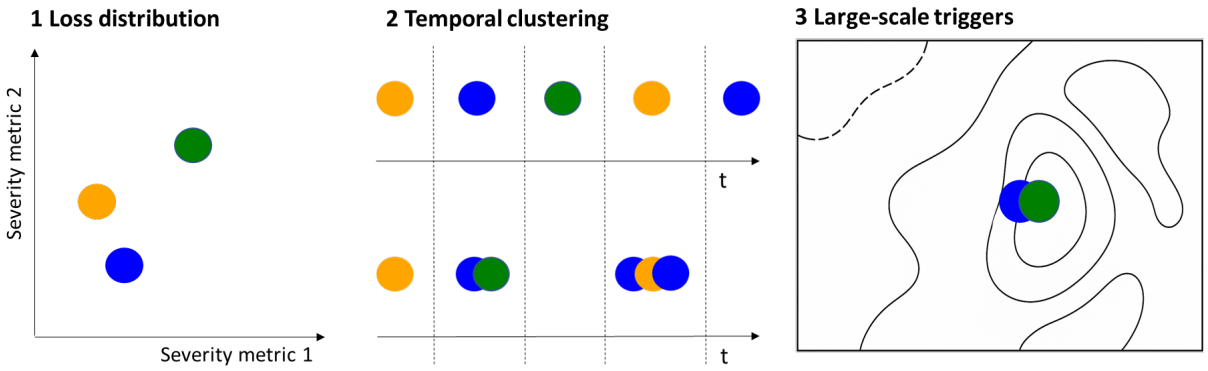

Figure 1.1.: Schematic overview of the results chapters in this thesis, with the rightmost panel created with the help of ChatGPT.

algorithm, the statistical metric Ripley's K, and impact metrics. The third results chapter deals with the large-scale atmospheric circulation present during the occurrence of clustered and isolated extremes, potentially functioning as triggers of events (Chapter 7). Finally, Chapter 8 concludes with a summary and discussion of the most important results.

2. Theoretical background

In this chapter, at first, the meteorological drivers behind the hazards of windstorms, convective gusts and hail, and fluvial and pluvial flooding are introduced (Sect. 2.1). The chapter starts with a section describing wind (Sect. 2.1.1), followed by an outline of convection (Sect. 2.1.2) and precipitation (Sect. 2.1.3). Each of these sections follows the same structure, starting with formation, followed by extreme events and/or associated weather phenomena, and ending with the damage potential. This is followed by a description of the interactions between meteorological extreme events (Sect. 2.2). After introducing relevant concepts regarding large-scale atmospheric circulation patterns (Sect. 2.3), the chapter is closed with an overview on the basic statistical methods applied in this work (Sect. 2.4).

2.1 Meteorological drivers behind the hazards

Atmospheric phenomena can occur on short temporal scales of less than a second, such as turbulence on small spatial scales, or can last for more than a month, such as Rossby waves affecting the planetary scale (see blue rectangles in Figure 2.1). The scales of these phenomena differ largely, but timescale and spatial scale are closely related to each other; the ratio of time to spatial scales is approximately $10\,\mathrm{m\,s^{-1}}$ and the same order of magnitude for most phenomena. According to the definitions of the IPCC and the Deutscher Wetterdienst (DWD), extreme weather events are events related to meteorological phenomena that are rare at a particular place and time of year (Masson-Delmotte et al., 2021; DWD, 2025c). They are often defined by values above the 90th percentile (also in this work, see Sect. 4.2) or below the 10th percentile of a probability distribution. Therefore, the characteristics of extreme weather events differ depending on the season and geographic area considered. When these extremes have adverse or even devastating impacts, they are also referred to as meteorological hazards. A hazard is defined as a process, phenomenon or human activity potentially causing loss of life, injury or other health impacts, social and economic disruption, environmental degradation and property damage (UNDRR, 2007). Meteorological hazards in Germany include severe wind gusts, thunderstorms, heavy precipitation, persistent precipitation, snowfall, snow drift, black/ice, frost, fog, thaw, heat, and high UV radiation – as for these hazard types, weather warnings are issued (DWD, 2025b). The term peril is often used interchangeably with the term *hazard*, particularly in an insurance context, where it can be defined as a potential cause of loss or damage (e. g., Mitchell-Wallace et al., 2017). This work focuses on wind gusts, thunderstorms, heavy rain and persistent rain (see circles in Fig. 2.1), which are referred to meteorological hazards in this work, since this is the prevalent term in the literature.

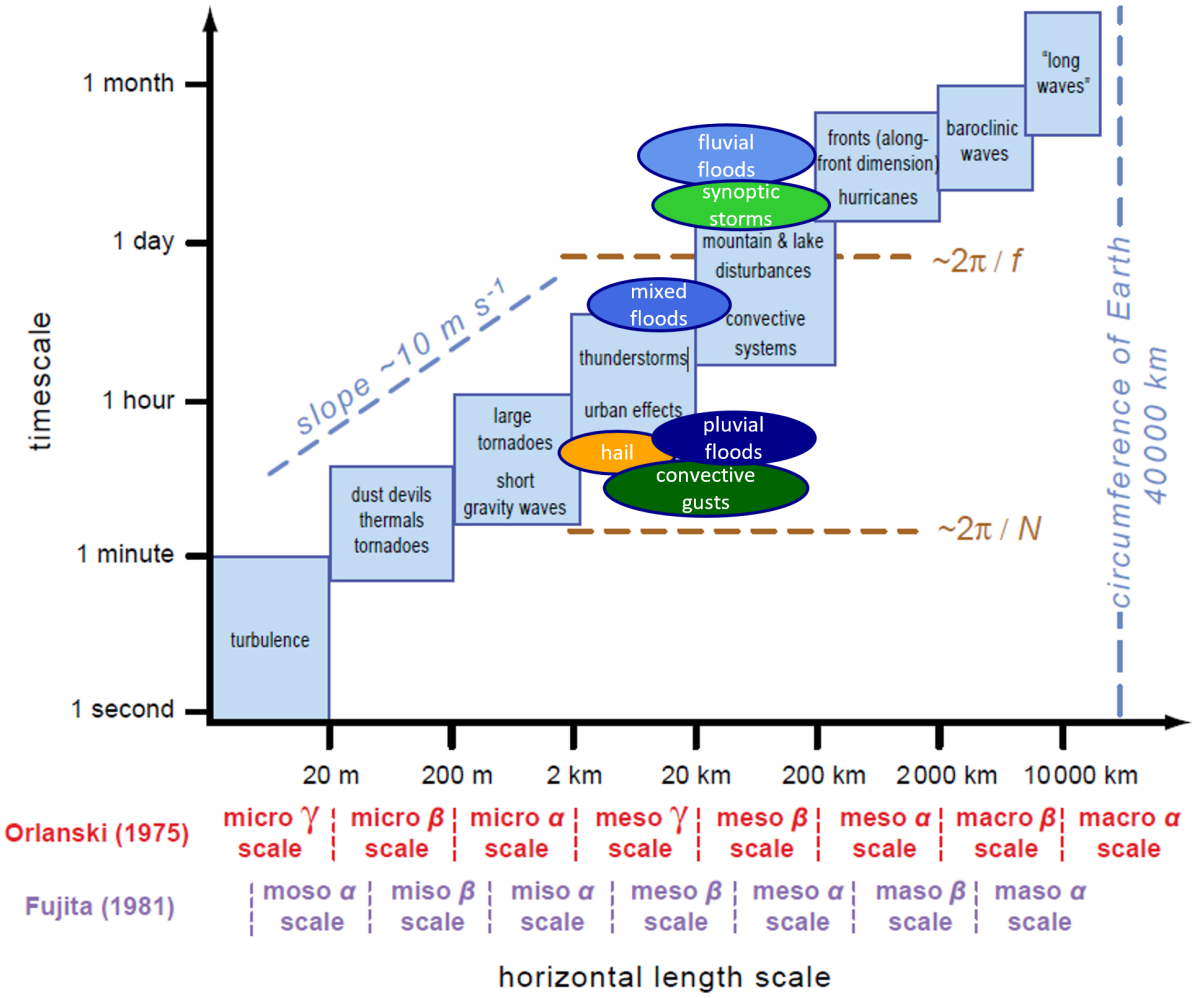

Figure 2.1.: Weather systems and atmospheric phenomena across various spatial and temporal scales (adapted from Markowski and Richardson (2010), their Fig. 1.1), including the major hazards (in circles) discussed in this work. Used with permission of John Wiley & Sons - Books, from *Mesoscale Meteorology in Midlatitudes* by Paul Markowski and Yvette Richardson, ©2010; permission conveyed through Copyright Clearance Center, Inc.

2.1.1 Wind and windstorms

Wind is generated by pressure gradient accelerations acting upon the air (e. g., Stull, 2017). Wind speed is the speed of motion of air parcels, defined as a vector $\vec{v}$ with common units $\mathrm{m\,s^{-1}}$ or $\mathrm{km\,h^{-1}}$ and the dimension of length divided by time. Wind speed is commonly decomposed into a vertical component w and horizontal components u and v, with i, j and k as unit vectors:

$$\vec{v} = ui + vj + wk. \tag{2.1}$$

Under average conditions, the horizontal wind components exceed the vertical velocity by a factor of 10^3 to 10^4 ($u, v \ll w$). During the development of windstorms (Sect. 2.1.1) or thunderstorms (Sect. 2.1.2), this component, however, can become very large and highly relevant for severe weather events.

Nevertheless, due to the differences in scale and the difficulty of estimation, the vertical component is often neglected (Kraus, 2004).

To describe wind speed accurately, it is important to distinguish between mean wind and wind gusts. Mean wind typically refers to the 10-minute average, whereas gusts are determined over just a few seconds or even less. To classify wind speed, different scales are used, depending on the hazard type: Tropical cyclones are classified according to the Saffir-Simpson scale, tornadoes are classified using the Fujita or Enhanced Fujita scales, respectively (see Sect. 2.1.2), and Extratropical Cyclone (ETC)s are classified according to the Beaufort scale (e. g., Stull, 2017). The Beaufort scale defines a storm at a wind speed of $> 75\,\mathrm{km\,h^{-1}}$.

Formation of extratropical cyclones

ETCs are mid-latitude (30°–70° N) cyclonic weather systems. Often forming over the North Atlantic ocean, they are typical weather patterns in Europe and occur at the synoptic scale (meso-α-scale, Fig. 2.1). By definition, ETCs occur on the meso-α-scale (synoptic scale), extending from 200 to 2,000 km (see Fig. 2.1). Characteristic horizontal extents are about 1,000 km, with durations of one day to two weeks, and typical durations of three days (Stull, 2017). When ETCs generate strong surface winds, they are referred to as windstorms, although no uniform definition exists (Mitchell-Wallace et al., 2017). As they mainly occur during the northern hemispheric winter months, they are also called winter storms.

Dynamic fundamentals

To understand how weather and specifically wind extremes form, it is fundamental to understand when, how and why air moves. The equation of motion, based on the principle of momentum conservation, describes how accelerations act on an air parcel and influence its motion in the atmosphere. It consists of the Pressure Gradient Acceleration (PGA), the Coriolis Acceleration (CA), the Gravitational Acceleration (GA) and friction. It can be formulated as a vector equation

$$\frac{d\vec{v}}{dt} = -\frac{1}{\rho}\vec{\nabla}p - f\vec{k}\times\vec{v} - g\vec{k} + \vec{a}_R. \tag{2.2}$$

The first term refers to the PGA, which is a result of horizontal and vertical pressure differences, where p is atmospheric pressure, and ρ is the atmospheric density. The PGA is directed perpendicular to the isobars (lines of equal pressure) and causes air parcels to move from areas of high pressure towards areas of low pressure. The second term is the CA, which considers the effect of the Earth's rotation, with f as the Coriolis parameter and $\vec{k}$ as the unit vector in vertical direction. The Coriolis acceleration increases with increasing latitude, and has its maximum at the poles, whereas at the Equator, it is zero. The third term is the gravitational acceleration directed to the Earth's center, with a value of $9.8\,\mathrm{m\,s^{-1}}$ in

mid-latitudes (45° latitude). The last term $\vec{a}_R$ refers to friction, which is usually neglected for large-scale atmospheric motion.

For large-scale atmospheric motion, scale analysis and the quasi-geostrophic approximation assumes a hydrostatic balance (balance of PGA and GA) in the vertical dimension and a geostrophic balance (balance of PGA and CA) in the horizontal dimension. The geostrophic wind, approximating the actual horizontal (h) wind in the free atmosphere, occurs perpendicular to the geostrophic balance, and parallel to the isobars:

$$\vec{v}_g = \frac{1}{\rho f}\vec{k} \times \nabla_h p. \tag{2.3}$$

Therefore, the geostrophic wind does not allow for pressure gradients to evolve or balance. In the planetary boundary layer, however, friction reduces wind speed (and the CA). With PGA unchanged, this leads to an additional ageostrophic wind component towards the low pressure. Friction at the surface, especially on land, therefore leads to an inflow of air towards the low-pressure system (convergence) and away from a high-pressure system (divergence).

In addition to the geostrophic winds $\vec{v}_g$, there is an ageostrophic wind component $\vec{v}_a$:

$$\vec{v}_h = \vec{v}_g + \vec{v}_a. \tag{2.4}$$

Since this ageostrophic component controls the temporal development of wind and atmospheric pressure, it also controls the development of large-scale weather systems.

When isobars are strongly tilted, the centrifugal acceleration can no longer be ignored. A balance between PGA, CA and centrifugal acceleration forms, called gradient wind balance. This gradient wind balance leads to winds higher than the geostrophic wind (supergeostrophic) for anticyclonic rotation, because PGA and CA point in the same direction. Thus, CA is in balance with the sum of GA and centrifugal force. Because CA is proportional to wind speed (for constant latitude), this leads to supergeostrophic flow. The opposite is the case for cyclonic rotation, where subgeostrophic winds occur.

A low-pressure system can be described by a deficit of mass in the atmosphere, since pressure at height z is the weight per unit area above z. Neglecting vertical wind speed, the pressure tendency equation in the pressure coordinate system (p-system), which uses pressure p instead of height z as the vertical coordinate, is given by

$$\frac{\partial p}{\partial t} = -g \int_{p_0}^{0} \nabla_p \cdot \vec{v}_h \, \mathrm{d}p, \tag{2.5}$$

showing that the pressure decreases with net divergence, that is, the decrease of mass with time, of (ageostrophic) horizontal winds. Horizontal net divergence leads to lifting, assuming an incompressible air mass ($\nabla \cdot \vec{v} = 0$). Thus, divergence above p_0 (upper-level high) leads to the decrease of surface pressure, whereas convergence above p_0 (upper-level low) leads to an increase of surface pressure.

The curvature of the flow is described by the rotation of a volumetric element by the vorticity vector $\vec{\nabla} \times \vec{v}$, which has three components (ξ, η, and ζ): The most important vertical vorticity component ζ is positive for cyclonic rotation, and negative for anticyclonic rotation. Therefore, low-pressure centers are a maximum of positive vorticity, and an increase in vorticity is related to a decrease in atmospheric pressure (and vice versa). The quasi-geostrophic vorticity equation for the large-scale flow in the p-system is:

$$\frac{\partial \zeta_g}{\partial t} = -\vec{v}_g \cdot \nabla(\zeta_g + f) - f_0(\nabla_h \cdot \vec{v}_h), \tag{2.6}$$

with f as the Coriolis parameter. This equation shows that the local temporal change in relative vorticity ζ_g at a location is influenced by the advection of absolute vorticity (relative vorticity and planetary vorticity due to the Earth's rotation) with the geostrophic wind $\vec{v}_g$ and the divergence of the horizontal wind. If the vorticity is approximately stationary, positive vorticity advection (Eq. 2.6) in front of a trough leads to divergence of the flow, which in turn leads to pressure decrease (Eq. 2.5) and lifting. The area downstream of a trough is an area of maximum vorticity advection and therefore highly relevant for cyclogenesis and the intensification of windstorms.

According to the continuity equation (not shown), divergence is associated with lifting. The Omega equation describes the vertical speed ω in the p-system:

$$\left(\sigma\nabla^2 + f_0^2 \frac{\partial^2}{\partial p^2}\right)\omega = -f_0 \frac{\partial}{\partial p}\left[-\vec{v}_g \cdot \nabla_p(\zeta_g + f)\right] - \frac{R_l}{p}\nabla^2\left[-\vec{v}_g \cdot \nabla_p T\right] - \frac{R_l}{c_p p}\nabla^2 H, \tag{2.7}$$

where f_0 is the (constant) Coriolis parameter, R_l is the specific gas constant for dry air, T is the temperature, c_p describes the specific heat capacity of dry air at constant pressure, and H describes to diabatic heat exchange. Since σ is a stability parameter, the left term is proportional to ω. Lifting ($\omega < 0$) occurs in areas with positive vorticity advection, increasing with height (first term on the right). It is further expected within the strongest warm air advection (second term) and the strongest diabatic phase changes due to condensation (third term).

The jet stream and cyclogenesis

Since the Earth has a spherical shape, there is a strong temperature gradient between the poles and the Equator due to differences in radiative forcing (Lambert's law). This gradient is enhanced during the Northern Hemispheric winter months, when less or even no radiation reaches the polar region. The horizontal temperature gradient implies a horizontal pressure gradient increasing with height, since the density of warm air is lower than that of cold air.

The stronger the temperature gradient, the stronger is the pressure gradient and thus the wind speed. In the transition area of the polar and subtropical air masses, a frontal zone exists, where a jet stream, that is, a strong wind band, evolves. Because of the CA, the jet stream is usually zonally oriented with a flow direction from west to east. For the midlatitudes, the polar jet stream is particularly relevant,

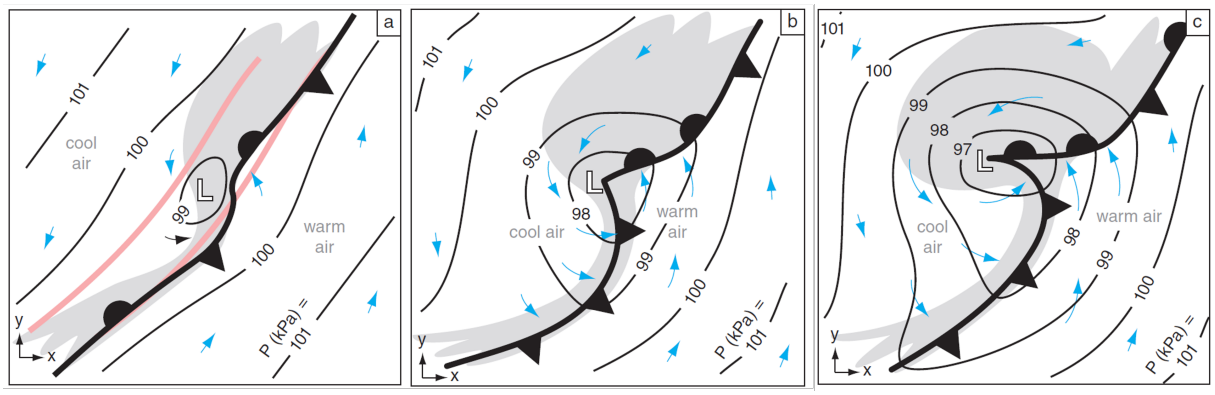

Figure 2.2.: Schematic cyclogenesis in the Northern Hemisphere. Grey shading indicates clouds, solid black lines are isobars (kPa), thin cyan arrows are near-surface winds, L is at the low center, and pink lines in (a) bound the original frontal zone. Adopted from Stull (2017), their Fig. 13.32: Copyright ©2017 by Roland Stull, licensed under a CC-BY-NC-SA 4.0 License (`http://creativecommons.org/licenses/by-nc-sa/4.0/`), image layout adjusted.

encircling the globe at around 200 hPa to 300 hPa (at geostrophic balance, see Eq. 2.3). The jet stream, however, is not a straight line from west to east, but meanders in waves, so-called planetary waves or Rossby waves. These waves create ridges and troughs, which are the only way for subpolar, cold air masses to be advected southward and for subtropical air masses to flow northwards. Within these ridges and troughs, dynamical high- and low-pressure systems may evolve because of vorticity advection and flow divergence. In this work, the relationship between the jet stream, or more generally, the large-scale atmospheric circulation, and windstorm impacts will be explored (Chapter 7).

As seen above, low pressure systems can form in regions with high horizontal temperature gradients and consequently strong jet streams. Since temperature gradient and pressure gradient are then misaligned, baroclinicity exists. Baroclinicity evolves through differential solar radiation or changes in the surface (land vs. sea). Gradient wind balance (see above) occurs when the wave disturbance becomes larger and the rotation is strengthened. This stage is also called spin-up stage, since vorticity increases with an intensifying cyclone. If the surface low is positioned downstream of a trough, a divergent upper air flow supports a further decrease in pressure according to the pressure tendency equation (Eq. 2.5). Due to the cyclonic rotation, two fronts evolve from the frontal zone: the warm front at the front of the system, transporting warm air northwards, and the cold front, causing cold air to be transported southwards. This leads to a curved front, also called frontal wave (see Fig. 2.2b, Stull (2017)). When the cyclone deepens, winds and clouds (and potentially precipitation) intensify and spiral around the low center as a vortex. At the cold front, cold air masses are pushed below the air in the warm sector (located between the warm and cold front) and cause lifting. If cold air gets above warm air masses (caused by a higher friction at the surface and leading to a backward tilted cold front), an unstable environment exists and deep moist convection can occur (see Sect. 2.1.2). In the warm sector, large-scale lifting with moderate vertical velocities occurs, as described by the Omega equation (positive vorticity advection, warm air advection,

and/or diabatic heating, see Eq. 2.7), usually leading to stratiform precipitation with low to moderate intensities (see Sect. 2.1.3). At the peak intensity of the cyclone, the cold front has reached the warm front, which is moving slower due to friction (see Fig. 2.2c). This is associated with the lowest central pressure and strongest winds. As the cold front approaches the warm front, the warm sector becomes smaller and smaller, until the warm air is completely lifted (occluded front), and the cyclone starts to weaken and finally to dissolve (beginning of cyclolysis).

From low-pressure systems to windstorms

Because a horizontal temperature gradient implies a change of the horizontal pressure gradient with height, the geostrophic wind (see Eq. 2.3) also changes with height z. The difference vector of the geostrophic wind is referred to as the thermal wind $\vec{v}_t$:

$$\vec{v}_t = \Delta\vec{v}_g = \frac{\partial \vec{v}_g}{\partial z}\Delta z, \tag{2.8}$$

where the Δz is the height interval. The thermal wind balance therefore explains the vertical shear of the wind, caused by horizontal temperature and thus pressure gradients. Ideal conditions for an increase of the horizontal pressure gradient with height and, thus, strong winds, are cold air masses within a low-pressure system and warm air masses within a high-pressure system.

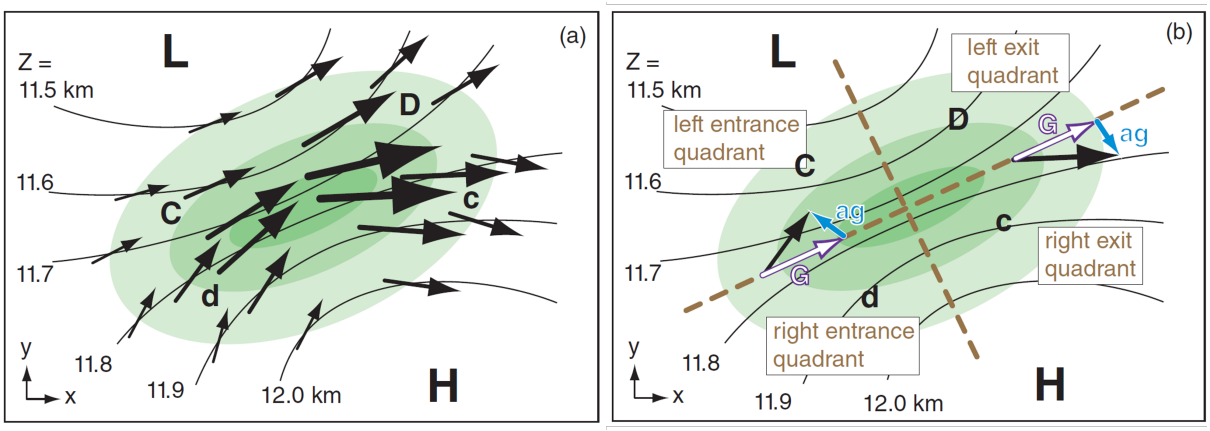

Figure 2.3.: Horizontal divergence (D = strong, d = weak) and convergence (C = strong, c = weak) near a jet streak. Back arrows represent winds, green shading indicates isotachs (=lines of equal wind speed, darkest green relating to the highest speeds), thin curved black lines are height contours of the 200 hPa isobaric surface, L & H indicate low & high height centers. Geostrophic (G) winds are parallel to the isobars (white arrow), while (ag) indicates the ageostrophic wind component (blue arrow). Brown dashed lines parallel and perpendicular to the jet axis divide the jet streak into four quadrants. Adopted from Stull (2017), their Fig. 13.3: Copyright ©2017 by Roland Stull, licensed under a CC-BY-NC-SA 4.0 License (`http://creativecommons.org/licenses/by-nc-sa/4.0/`, cropped and image layout adjusted.

Extreme ETCs can form through the interplay of vorticity advection, divergence and the ageostrophic wind component v_a (see Eq. 2.4). This ageostrophic component (v_a and u_a) is the difference vector be-

tween the horizontal and geostrophic wind. The equation of motion in the p-system for quasi-geostrophic conditions can be expressed for the horizontal components u and v as:

$$\frac{du}{dt} = -fv_a \quad \text{and} \quad \frac{dv}{dt} = -fu_a, \tag{2.9}$$

showing that an ageostrophic wind component results from acceleration and deceleration (geostrophic imbalance).

Since the speed of the jet stream is not constant even in the jet core (center region), an air parcel accelerates (in direction x) when entering the region of the jet streak (Stull (2017), see Fig. 2.3a). Assuming a constant PGA, this leads to an ageostrophic wind in direction y ($fv_a > 0$ and $v_a > 0$). This is associated with strong convergence in the left entrance quadrant ('C'), and with divergence in the right entrance quadrant ('d', see Fig. 2.3b). In the exit region of the jet, the air parcel is decelerated ($fv_a < 0$), leading to an ageostrophic wind component in negative y direction. This is associated with strong divergence in the left exit quadrant ('D') and a convergence in the right exit quadrant ('c'). Divergence aloft can lead to cyclogenesis at the surface, as seen in Eq. 2.5. In addition, vorticity advection increasing with height is associated with lifting and divergence or convergence according to Eq. 2.7. The strongest vorticity advection occurs in the left exit quadrant ('D'), as the vorticity maximum is strongest upstream. The surface low below the left exit quadrant can evolve to a major windstorm due to the combination of both effects of gradient wind balance and acceleration. In contrast, surface lows in area 'C' or 'c' favor cyclolysis.

If divergent zones of multiple jet streaks overlap, their driving mechanisms amplify and cyclogenesis is enhanced. In this case, the left exit quadrant of the western jet stream overlaps with the right entrance quadrant of the eastern jet stream. Positive advection of vorticity and divergence can lead to a rapid decrease in pressure (explosive cyclones, see below). Multiple jets and overlapping divergence zones occurred, for example, in the case of windstorm *Lothar* in 1999 (see also below).

Wind extremes

In Europe, characteristic windstorms develop over the North Atlantic, as large horizontal temperature gradients can form there easily (high latitudes, land vs. sea gradients). Furthermore, friction is much lower over the ocean, whereas over land, ETCs dissolve quickly. With the jet stream, ETCs usually move towards Europe, often affecting the United Kingdom or Scandinavia (see Fig. 2.4) before weakening further inland. Storm tracks of severe ETCs, related to their pressure minimum, typically show a tendency to move from the southwest to the northeast, but also with a large variety in their paths. Cyclone Xynthia (February 2010) differed strongly from other storm tracks, mainly driven by positive vorticity advection, and affected Portugal and Galicia in particular. Although ETCs occur most frequently close to the Icelandic low (Pinto et al., 2007), central Europe was regularly affected by them during past decades

(see also below), although the last severe storm occurred in 2007, with no comparably intense events since then (see also Sect. 2.1.1). This naturally includes Germany, which is why this thesis investigates windstorms in depth.

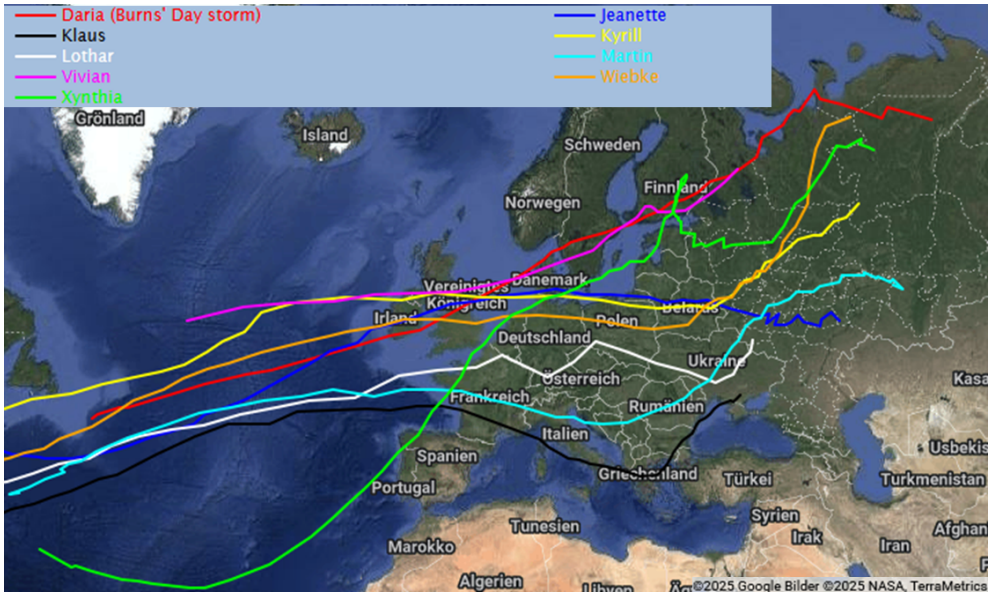

Figure 2.4.: Storm tracks of selected storms over central Europe. Created with the Extreme Wind Storms Catalogue (`https://www.europeanwindstorms.org/`). ©Copyright Met Office, University of Reading and University of Exeter; licensed under Creative Commons CC BY 4.0 International License (`http://creativecommons.org/licenses/by/4.0/`).

ETCs can be of various forms, types and structures: Apart from divergence and baroclinicity, cyclones can also develop as secondary systems from pre-existing cyclones, evolving further downstream and primarily influenced by lower-level processes, such as latent heat release (Gliksman et al., 2023). Large mountain ranges can also be a trigger for the development of ETCs due to the interaction of atmospheric waves, mainly in the Mediterranean basin (Trigo et al., 1999). Strong winds can occur in three zones, namely at the warm conveyor belt (warm jet), the cold conveyor belt (cold jet) and at the sting jet, which is a small-scale embedded feature with the highest wind speeds (Gliksman et al., 2023). The warm conveyor belt refers to the flow of warm and moist air ahead of the cyclone, whereas the cold conveyor belt relates to the flow of cold, dry air into and around the back of the central low pressure (Browning, 1990).

The potentially most damaging ETC types include slow movers, rapid developers and serial storms. Slow movers can trigger severe flooding due to large accumulations of precipitation within the same area (Grams et al., 2014). Rapid developers deepen fast and are often secondary cyclones, fulfilling the conditions for a so-called *bomb* cyclone (Gyakum and Danielson, 2000), which refers to a rapid or explosive cyclogenesis with central pressures dropping about 24 hPa or more within 24 h (Stull, 2017). An extreme example for such a phenomenon in Germany is windstorm *Lothar*, which occurred on 26 December 1999, with a pressure decrease of more than 28 hPa within a 3-hour-period.

Serial storms (cyclone families) are series of cyclones triggered by a central low pressure and affecting the same area within a short period of time (Mailier et al., 2006). Series of severe storms occurred in December 1999 with *Anatol* (3 December), *Lothar* (26 December), *Martin* (27 and 28 December) and, more recently, in February 2022 (e. g., Mühr et al., 2022) with *Ylenia* (int. Dudley, 17 February), *Zeynep* (int. *Eunice*, 18 and 19 February), and *Antonia* (int. *Franklin*, 21 February). Serial clustering with respect to ETCs will be discussed in detail in Chapter 6, and its potential large-scale triggers are discussed in Chapter 7.

Damage potential of windstorms

ETCs can cause injuries and loss of life, and damage to forestry by tree breaking and subsequent damage to houses or vehicles, crop damage, damage to critical infrastructure including roads and bridges, and to buildings by loss of tiles on roofs or roof lifting (Mitchell-Wallace et al., 2017; Gliksman et al., 2023; Barredo, 2010). Damage can be caused either directly by wind pressure or by the impact of objects, transported by the wind at high speed (Tamura, 2009).

Average annual insured losses of winter storms in Europe are estimated between $ 2 billion (Schwierz et al., 2010) and $ 3.6 billion (1978–2008, Barredo (2010)), with individual events exceeding € 10 billion (Mitchell-Wallace et al., 2017). As of 2010, this made them the major hazard for insurance companies in Europe (Barredo, 2010). In recent years, winter storms have occurred less frequently. Germany is among the most affected countries in Europe, together with other western European countries like the United Kingdom, Ireland, France, Denmark and the Netherlands. Between 1981 and 2013, Germany was most affected by windstorm losses compared to other European countries, with major losses at the coast and in southern Germany (Koks and Haer, 2020). This rank is however heavily influenced by two major windstorms (*Lothar* in 1999 and *Vivian/Wiebke* in 1990). Forming over the Atlantic, ETCs are often able to maintain their strength over land and can affect areas with a high population density (e. g., northwestern Europe), often with many small claims per insured property (Mitchell-Wallace et al., 2017).

Drivers for wind damage are maximum wind gusts (e. g., Gliksman et al., 2023), the horizontal extent of the wind field (Kreibich et al., 2014), topography, and non hazard-related factors (Kreibich et al., 2014; Mitchell-Wallace et al., 2017). The contribution of the duration is debated (Mitchell-Wallace et al., 2017; Kreibich et al., 2014).

Wind damage is mainly driven by short-lived wind gusts (see Sect. 2.1.1) lasting for less than 20 s (Gliksman et al., 2023). Gust factors usually range between 1.5 and 2 during winter storms (Hofherr and Kunz, 2010; Brasseur, 2001). Mean winds are less important for wind damage. Gust factors relate hourly maximum gusts to the hourly mean wind (e. g., Kreibich et al., 2014; Mohr et al., 2017). Because of turbulence, high wind speeds are transported vertically from the free atmosphere to the Earth's surface through horizontal vortices. With higher instability and lower friction, vertical transport of horizontal

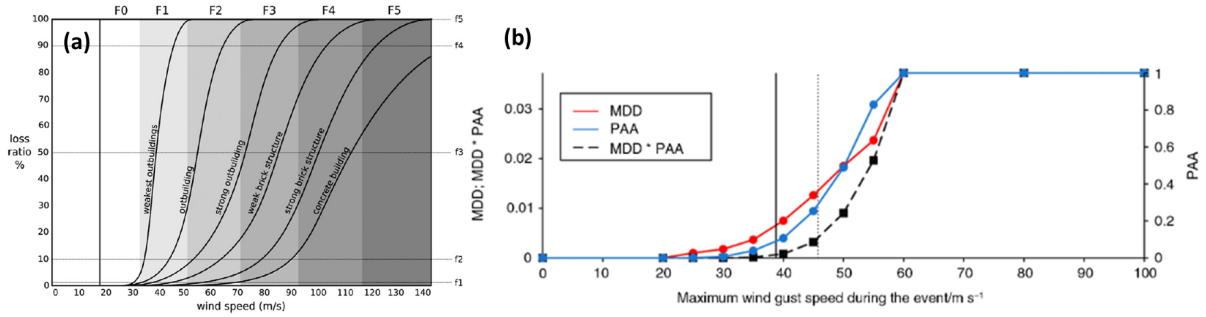

Figure 2.5.: (a) Loss ratio curves for buildings as function of the wind speed adapted for central Europe, from Feuerstein et al. (2011), their Fig. 2: Towards an improved wind speed scale and damage description adapted for central Europe, B. Feuerstein et al., Copyright ©2011 Elsevier B. v., Reproduced with permission of The Licensor through PLSclear; (b) Mean damage degree (red; left y-axis), percentage of assets affected (blue; right y-axis), and product of mean damage degree and percentage of assets affected (black; left y-axis) as a function of maximum wind gust speed during the windstorm event, all consecutive points are linearly interpolated. A linear interpolation was applied between two consecutive points (denoted with a straight line segment). From Welker et al. (2016), their Fig. 3: ©2016 C. Welker et al., licensed under Creative Commons Attribution 4.0 International License (`http://creativecommons.org/licenses/by/4.0/`), no changes made.

momentum increases and therefore gust speed near the surface. Gust factors therefore depend primarily on atmospheric stability and terrain's roughness (Hofherr and Kunz, 2010; Brasseur, 2001). The German Insurance Association (GDV) defines a storm by reaching wind speeds of at least category 8 of the Beaufort Scale (GDV, 2023), which relates to a wind speed of at least $17\,\mathrm{m\,s^{-1}}$ (e. g., Stull, 2017). Damage from daily maximum wind gusts increases non-linearly above $20\,\mathrm{m\,s^{-1}}$, approximately with the third power of the maximum wind speed. This is because the cube of wind speed is proportional to the horizontal transport of kinetic energy (e. g., Klawa and Ulbrich, 2003; Nordhaus, 2010; Mitchell-Wallace et al., 2017). Although this cubic function is only applicable to extreme losses (Prahl et al., 2015), it is most commonly used (Gliksman et al., 2023). Other power-law functions are common as well, and exponents ranging from 2 to 12 can be found in the literature (Gliksman et al., 2023).

Other hazards than wind gusts occurring with ETCs can likewise amplify the damage. Damage is driven up with storm surges, where low pressure and the wind force combined can push the water towards the shore (Lowe and Gregory, 2005). This can lead to coastal flooding, especially with a high previous water tide. ETCs may also come with heavy precipitation, leading to flash flooding or river flooding (see Sect. 2.1.3), especially in catchments with short response timescales, where water levels rise rapidly after rainfall. Multiple ETCs throughout a season can amplify flooding in larger river catchments due to saturated catchments and high water levels (Hillier et al., 2015; Mitchell-Wallace et al., 2017). The relationship between impacts of wind and flood extremes is investigated in Chapter 6. Non hazard-related factors driving the damage include, for example, the shape of buildings and the behavior of the population (e. g., closing doors and windows)[1].

[1]Note however, that in Germany, windows and doors are not insured according the general insurance conditions (GDV (2023), Sect. 5.5.2)

The accumulated impact of ETCs over a given time period can be measured (and applied in a storm loss model), for example, by the Storm Severity Index (SSI; Klawa and Ulbrich, 2003). This index follows the assumption that (building) losses become relevant when a critical wind speed is exceeded. A common threshold is the 98th percentile of the daily maximum gust wind speed ($V_{i,j}^{98}$). This is applied locally in a given region with longitude i and latitude j and is compared to the climatology (e. g., Dacre and Pinto, 2020):

$$SSI = \sum_{i=1}^{N_j} \sum_{j=1}^{N_j} \left(\frac{V_{i,j}}{V_{i,j}^{98}} - 1 \right)^3 . \tag{2.10}$$

The threshold of the 98th percentile of the wind speed climatology is established because it corresponds quite well to the threshold of $20\,\mathrm{m\,s^{-1}}$, above which insurance companies in Germany regularly register payouts (Klawa and Ulbrich, 2003). The SSI can be applied over land and is often normalized with the population density in a given location (Bloomfield et al., 2023). The SSI in this or slightly different forms (Gliksman et al., 2023) is widely used, but has difficulties distinguishing high-impact events at the tail of the wind gust distribution (Moemken et al., 2024). The SSI can also be used to assess annual loss clustering (see Sect. 4.5.3), which is investigated in this work as well (Sect. 6.3.2).

Losses to individual buildings are typically assessed with vulnerability functions or fragility functions, which are a function of storm intensity vs. the impact to the building (Koks and Haer, 2020; Feuerstein et al., 2011; Li et al., 2024; Khanduri and Morrow, 2003). Originally developed by Fujita (1992) for the United States and for convective gusts, these functions depend on the (maximum) wind speed and can be distinguished by the building type (number of storeys) and construction type (see Fig. 2.5a, Feuerstein et al., 2011). Note that the most common types in Europe are weak brick structures and concrete buildings (Koks and Haer, 2020), which are assumed to be less susceptible to gusts than outbuildings but show the strongest increases in the loss ratio (here: monetary damage divided by reinstatement value) from about 80 to $100\,\mathrm{m\,s^{-1}}$. From an insurance perspective, vulnerability can be assessed by the product of the overall mean damage degree and percentage of assets affected (Welker et al., 2016). This vulnerability function is also a function of the wind gust speed, with strongest increases from about 45 to $55\,\mathrm{m\,s^{-1}}$ (see Fig. 2.5b, Welker et al., 2016). In loss models, vulnerability curves can also be differentiated by the type of use (for example, residential vs. commercial, Schwierz et al. (2010)) instead of the building construction type. Building components affected by strong winds include roof tiles, or in very severe cases, roof lift-off and the collapse of walls (Gliksman et al., 2023). The damage also depends on the exposure as well as the structural vulnerability of individual buildings to severe wind gusts (Gliksman et al., 2023). It should be noted here that damage functions and vulnerability curves are difficult to estimate and kept secret by insurance companies.

The European wind loading standard, DIN EN 1991-1-4, regulates how the structural design of buildings needs to be adapted to expected wind loads (DIN, 2010). Basic reference wind velocities are defined, based on the 50-year return level of 10 min wind speed at 10 m height from weather station data (Gliks-

man et al., 2023). In Germany, basic velocities range from 22.5 $\mathrm{m\,s^{-1}}$ (wind load zone 1) to 30 $\mathrm{m\,s^{-1}}$ (wind load zone 4, DIN, 2010). Based on terrain roughness and terrain above ground, these basic velocities are further adjusted.

Spatial distribution and trends of windstorms

In Germany, a distinct north-to-south (and west-to-east) gradient is shown by return values of turbulent gusts over Germany (see Fig. 2.10a,b), caused by the higher frequency of low-pressure systems coming from the Atlantic Ocean in the north (Klawa and Ulbrich, 2003; Hofherr and Kunz, 2010; Kreibich et al., 2014). On the local scale, the wind field is influenced by the roughness of the terrain and by orographic features, associated with small-scale variations in gust speed (see Fig. 2.6a, Hofherr and Kunz, 2010; Kreibich et al., 2014). Germany is divided into four geographic wind load zones by the European wind loading standard (see Fig. 2.6b, DIN, 2010). The highest wind loads are expected at the northwestern coast, followed by Brandenburg and Mecklenburg-Vorpommern as well as pre-alpine regions, whereas inland areas in southern Germany are less affected (however, local-scale variations in the wind field and orographic influences are not considered in the wind loading standard). The coast and northwestern Germany (see Fig. 2.6c, Koks and Haer, 2020) are also most affected by windstorm losses, with a second hot spot in Baden-Württemberg and southern Bavaria. When comparing Figure 2.6c and 2.6a with 2.6b, southern Germany seems to be over-proportionally affected by windstorm losses in comparison to the wind speeds. This is also influenced by the distribution of assets (Schröder et al., 2020); the spatial distribution of windstorm losses and its dependence on meteorological and socio-economic factors will be discussed in Chapter 5.

Between 1970 and 2008, an analysis found about one damaging ETC (above a certain threshold) occurring per year in central Europe (Barredo, 2010). This is, however, subject to a high annual and decadal variability, including temporal clustering (Vitolo et al., 2009). Trend analyses found an increase in the number of storms for the last four to six decades, but also a large decadal variability when analyzing longer time periods. The increase in storm activity applies mainly to the North Atlantic and northern European countries (Feser et al., 2015). Most studies on future trends indicate a further increase in storm intensity (not in storm numbers) over the North Atlantic and western Europe (Feser et al., 2015), for example, with the SSI doubling until the end of the 21st century (Little et al., 2023). Trends with respect to windstorm losses and clustering will be discussed in Sects. 5.4 and 6.4.

2.1.2 Convection and thunderstorms

Convection in meteorology refers to the vertical motion of particles. Deep Moist Convection (DMC) arises when air is lifted until it reaches saturation and becomes positively buoyant, allowing it to ascend to great heights (Markowski and Richardson, 2010). Convective storms evolve from DMC and are characterized by a strong thermal updraft, which can extend up to the tropopause and even into the

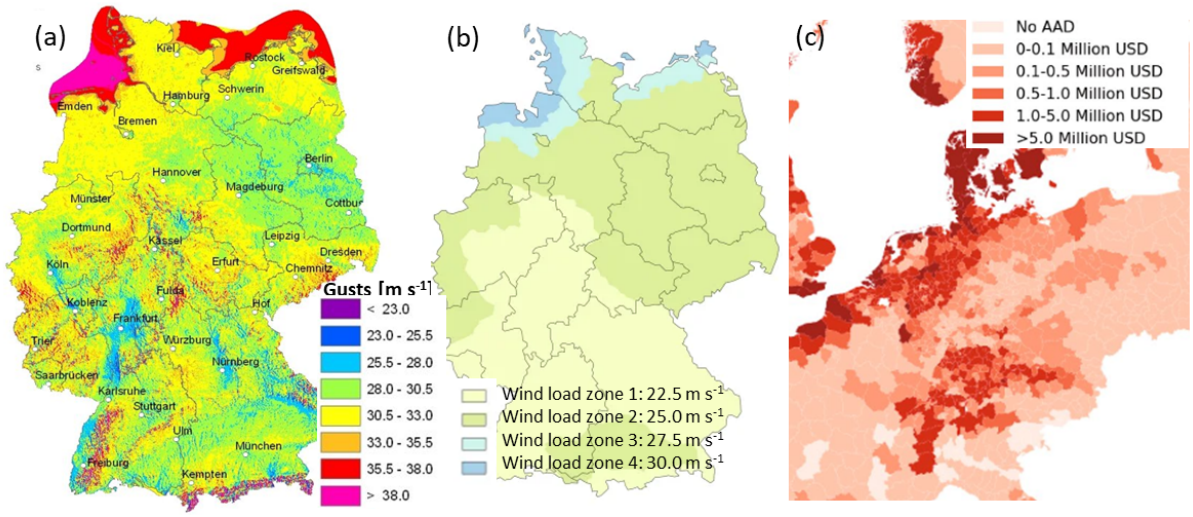

Figure 2.6.: (a) Maximum wind speeds in Germany on a 1 × 1 km grid, for an exceedance probability of p = 0.2 (return period of 5 years), from Hofherr and Kunz (2010), Copyright ©2010 T. Hofherr and M. Kunz, reproduction licensed by Inter-Research; (b) Wind zones in Germany derived from building codes (DIN EN 1991-1-4, Schmidt (2024)); (c) Total average annual damage (AAD) in Europe per NUTS3 (region classification) area, adapted from Koks and Haer (2020), their Fig. 3, Copyright ©2020 E. Koks and T. Haer, licensed under a Creative Commons Attribution 4.0 License (`http://creativecommons.org/licenses/by/4.0/`), cropped to Germany and with adjusted legend.

lower stratosphere, forming overshooting tops (Markowski and Richardson, 2010). As a result, convective storms can visibly be detected as towering cumulonimbus clouds with a significant vertical extent and characteristic cauliflower-like structures. A thunderstorm, by definition, is always produced by a cumulonimbus cloud and accompanied by lightning and thunder (AMS, 2025b). The spatial extent of convective systems ranges from the meso-γ-scale (a few kilometers, see Fig. 2.1) to the meso-α-scale ($\geq 100\,\mathrm{km}$).

Thermodynamic laws describe thermodynamic systems, such as the atmosphere, by state variables, such as pressure p, temperature T, or volume v. Enthalpy $h = u + pv$ represents the sum of mass-specific internal energy u and the product of p and mass-specific volume v. In the form of enthalpy, the first law of thermodynamics is expressed as

$$\mathrm{d}h = v\,\mathrm{d}p + \delta q, \tag{2.11}$$

with δq as the heat flux supplied to or removed from the system. When an air parcel rises adiabatically, it rises without an exchange of heat (or energy) with its surroundings ($\mathrm{d}h = v\,\mathrm{d}p$). Since p decreases when an air parcel rises, the air parcel expands and v rises, for which expansion labor done at the system is required (decrease in u and thus also in h). Since $\mathrm{d}h$ depends linearly on $\mathrm{d}T$ by

$$\mathrm{d}h = c_p \mathrm{d}T, \tag{2.12}$$

with c_p as the specific heat constant at constant pressure, the temperature of an air parcel decreases when it rises. This temperature decrease first takes place dry adiabatically until the dew point temperature[2] is reached and condensation (and therefore cloud formation, see Sect. 2.1.3) begins. When the air parcel is lifted further, heat of condensation is released, which reduces the cooling compared to the dry adiabatic process. Including the effects of condensation, the first law of thermodynamics is therefore described by

$$\mathrm{d}h = c_p \mathrm{d}T + l_v \mathrm{d}r_s = v\mathrm{d}p, \tag{2.13}$$

with l_v as specific heat of evaporation, and r_s as the saturation mixing ratio. The change in enthalpy (and the cooling) is therefore reduced by the amount of latent heat compared to a dry adiabatic process (where $\mathrm{d}h = c_p \mathrm{d}T$). Thermodynamic diagrams (see Fig. 2.7) describe this vertical ascent assuming adiabatic vertical motions, often measured by a radiosonde. Thereby, the potential of convection given a vertical temperature and moisture profile of an air mass can be analyzed, with an air parcel first lifted along a dry adiabat until it reaches saturation, and then continuing to rise along a pseudo adiabat.

Based on the first law of thermodynamics applied to an adiabatically risen air parcel, fundamental prerequisites for DMC can be derived: (1) High moisture content in the lower parts of the atmosphere, which is related to a change in enthalpy according to first law of thermodynamics (Eq. 2.13). Condensation thus releases a high share of latent energy, which is subsequently transformed into kinetic energy. With high moisture content, the condensation level and therefore the Level of Free Convection (LFC) is attained earlier (see Fig. 2.7). Another prerequisite for DMC is a (2) unstable stratification above the LFC or the Lifting Condensation Level (LCL), depending on the type of convection. Unstable stratification of the atmosphere leads to continuous positive buoyancy. This instability can be quantified by the Convective Available Potential Energy (CAPE), that is, the energy required for an air parcel to rise. CAPE can be calculated by multiplying the gravitational acceleration g with the difference between the virtual temperature[3] of a lifted air parcel and its surroundings, which equals integrating buoyancy B from the LFC to the Equilibrium Level (EL), where the pseudo adiabat intersects with the air parcel temperature curve (again):

$$CAPE = g \int_{LFC}^{EL} B \,\mathrm{d}z \approx g \frac{T_v^{'} - T_v}{T_v} \mathrm{d}z. \tag{2.14}$$

In this equation, $T_v^{'}$ represents the temperature of the lifted parcel, and T_v is the temperature of its surroundings. With CAPE, the maximum vertical speed in a convective cell can be calculated, using the equation of motion, the vertical wind speed and the time required for an air parcel to rise from the LFC to the EL.

[2] The dew point is the temperature the air needs to be cooled to (at constant pressure) in order to achieve a relative humidity of 100 %.

[3] The virtual temperature is the temperature of dry air that matches the density of moist air at the same pressure (e. g., Markowski and Richardson, 2010)

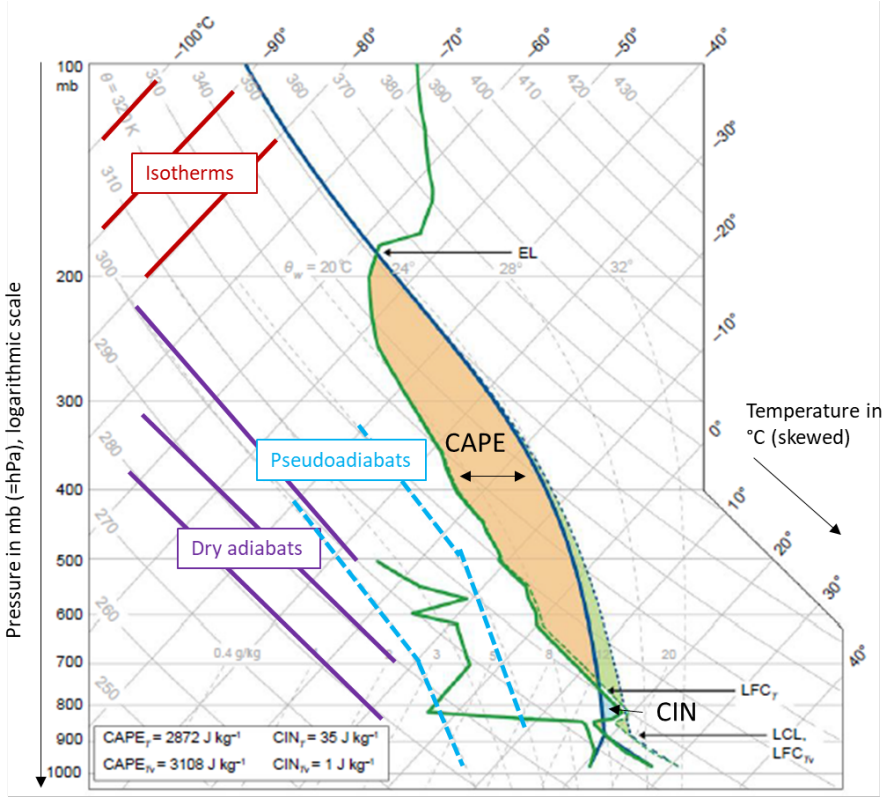

Figure 2.7.: Example skew$T$-log$p$ diagram. The temperature and dew point (until 500 hPa) curves are solid green, the virtual temperature profile is denoted by the dashed green line. The solid dark blue line indicates the trajectory of an ascending air parcel to its Lifting Condensation Level (LCL$_T$), Level of Free Convection (LFC$_T$) and Equilibrium Level (EL). The Convective Inhibition (CIN) area, excluding moisture effects, is shaded light blue and the Convective Available Potential Energy (CAPE) area is shaded light orange (see main text). The dashed blue line denotes the virtual temperature of the parcel (and corresponding LFC$_{Tv}$) and the resulting additional CAPE is shaded light green. Adapted from Markowski and Richardson (2010), their Fig. 2.9. Used with permission of John Wiley & Sons - Books, from *Mesoscale Meteorology in Midlatitudes* by Paul Markowski and Yvette Richardson, ©2010; permission conveyed through Copyright Clearance Center, Inc.

For the initiation of DMC, (3) a trigger is required so that air parcels can overcome the negative temperature difference near ground level (see Fig. 2.7). Convective Inhibition (CIN) describes the energy required for an air parcel to raise from the surface (h_0) to the LFC:

$$CIN = -g \int_{h_0}^{LFC} \frac{T_v' - T_v}{T_v} \mathrm{d}z. \tag{2.15}$$

Triggers can take various forms, including large-scale lifting after the divergent front of a trough (Omega equation, 2.7), or thermal convection (Doswell III, 1987). Lastly, a non-thermodynamic component determines the organization of the storms: the (4) wind shear, which refers to the vertical change of horizontal winds. This is decisive for the type of convection and therefore also for the damage, which is described below (see also Table 2.1).

Convective systems

Convective storms can be organized in various ways. Some convective systems occur as isolated cells, whereas others occur within larger complexes or lines (mesoscale convective systems). Vertical motion triggering DMC can result from dynamic processes (forced convection) or from thermal buoyancy (free convection), where rising warm air drives the updraft itself. Free convection evolves through buoyancy caused by a warming of air layers close to the ground (due to strong radiation) or by advection of cold air at higher altitudes. Forced convection evolves based on vertical pressure gradient accelerations, e. g., as a result of lifting at the cold front or by orography.

Isolated convection: Single cells, multicells and supercells

Isolated convective systems with only a single updraft and one downdraft without significant vertical tilt are referred to as single cells (Markowski and Richardson, 2010). The lifecycle of single cells can be distinguished into three stages (Byers and Braham, 1949; Markowski and Richardson, 2010): the towering cumulus, mature and dissipation stages. The cumulus stage starts when an air parcel reaches the LFC, where warm and moist air condenses and cloud particles (of cumulus clouds) form (see Sect. 4.3.1). Only one updraft exists, which (according to the definition of buoyancy) increases in intensity with height. Air from the surroundings and thus further moisture is drawn into the cloud and a cumulonimbus cloud is formed. In the mature stage, the production of precipitation particles (see Sect. 2.1.3) starts. When the precipitation particles are heavy enough, they fall through the updraft and reduce its buoyancy because of air resistance. Falling precipitation and subsequent evaporation and cooling finally induces a downdraft, which initiates a gust front when reaching the surface. The gust front is, compared to other convection types, relatively weak (see below). When the downdraft starts dominating the cell, it weakens the inflow into the updraft, ultimately causing the cell to dissipate (dissipation stage). The characteristic lifetime of a single cell is 30–60 minutes (see also Table 2.1). Weak vertical wind shear present in single-cell convection environments usually indicates a weak forcing on the synoptic scale. Therefore, single-cell convection is usually dominated by thermal processes. Therefore, it often occurs close to the maximum daytime heating at the surface (that is, highest CAPE and lowest CIN).

Compared to other types of convective systems, the damage potential of single cells is limited, as they only occasionally produce small hail or strong gusts. Severe weather associated with single cells is usually short-lived (*pulse* variety) and occurs during the transition from the mature to the dissipating stage. However, if a single cell moves very slowly or remains stationary, it can produce significant precipitation amounts at a given location (Piper et al., 2016).

Multicells are assumed to be the most common convective system in the midlatitudes (Markowski and Richardson, 2010). They consist of a cluster of several single cells, each undergoing the same development process, but interacting with each other. Convective cells are triggered repeatedly along the gust front of the preceding cell, depending on its vertical motion and the surrounding CIN. At the gust front,

warm air is forced to the LFC, which allows for the formation of new cells. This can be enhanced by a superpositioning of the horizontal vorticity vectors (Markowski and Richardson, 2010) of the environment and the gust front. Multi-cells are characterized by higher vertical wind shear in comparison to single cells (about $10-20$ m s^{-1} of the 0–6 km vector wind difference as opposed to $< 10\,\mathrm{m\,s^{-1}}$ for single cells, see Table 2.1). The regular initiation of new cells allows a larger-scale convective system, including several cells at different stages, to persist for over one hour, despite individual cells within the multicellular system typically having the shorter lifespan of a single cell (see above). In its most severe form, multicellular convection can last for hours and produce hail of about golf ball size as well as large swaths of straight-line winds (Markowski and Richardson, 2010).

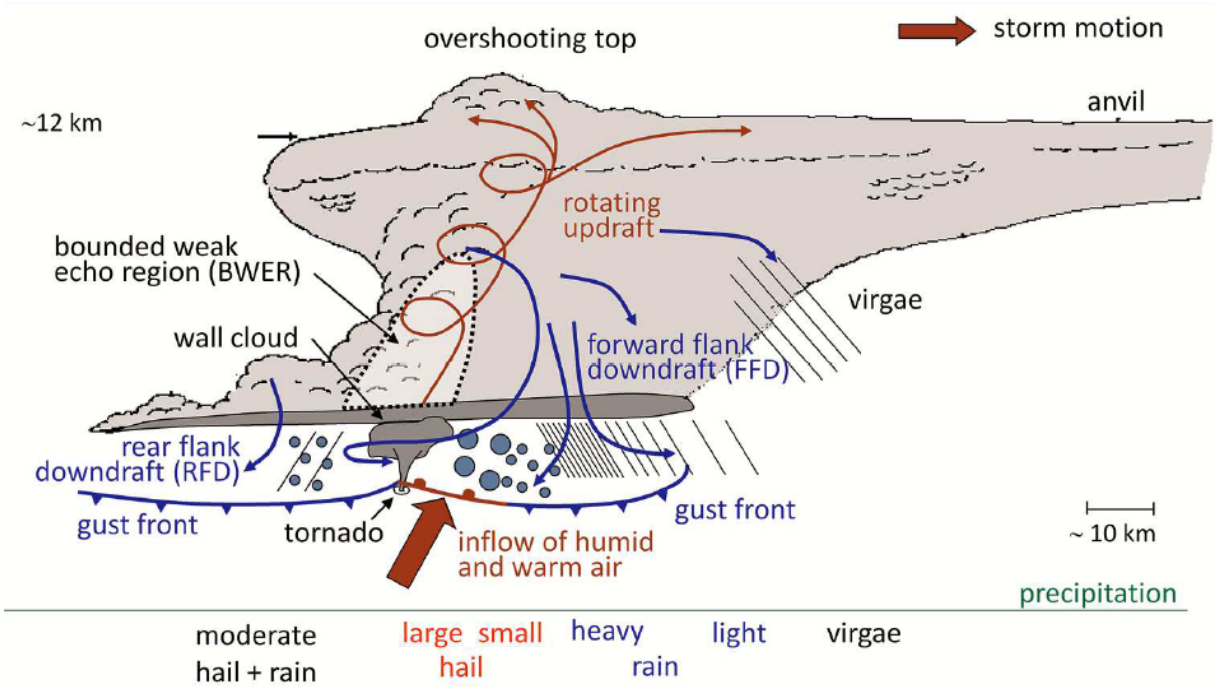

Figure 2.8.: Schematic of a supercell (vertical cross section), including wind and precipitation characteristics. A rotating updraft forms within humid and warm air, which is advected into the cloud by buoyancy (red). Hydrometeors remain small due to high ascent speeds in the bounded weak echo region (BWER), which is therefore shown as a low reflectivity region in radar images. BWERs cause a typical *hook echo* in radar images, which helps to identify supercells (black dotted line). The two downdrafts, RFD and FFD, procuce gust fronts near the surface with high wind speeds (blue and red lines). Diffent forms of precipitation evolve from different parts of the supercell (bottom). Adapted from Mitchell-Wallace et al. (2017), their Fig. 3.10: 9 Natural Catastrophe Risk Management and Modelling - A Practitioner's Guide, K. Mitchell-Wallace et al., Copyright ©2017 Wiley Blackwell, reproduced with permission of The Licensor through PLSclear.

Supercells are much less common compared to single and multicells, but have a particularly large damage potential (e. g., Kunz et al., 2018; Wilhelm et al., 2021). Hail of more than 5 cm is (almost) exclusively associated with supercells, as well as virtually all strong or violent tornadoes (Markowski and Richardson, 2010). Supercells consist – just like single cells – of only one updraft, but with supercells, the updraft is rotating and flanked by two downdrafts (see Fig. 2.8, Davies-Jones, 2015). Supercells are characterized by a persistently rotating updraft, referred to as mesocyclone, creating a central pressure minimum within

Table 2.1.: Overview of thunderstorm types, their typical environmental conditions and damage potential, adapted from Mitchell-Wallace et al. (2017)

Form	Temporal Scale	Spatial Scale	Wind shear	Hazards
Single-cell	30 min-1 h	1-10 km	$< 10\,\mathrm{m\,s^{-1}}$	low risk
Multi-cell	>1 h	<50 km	$10-20\,\mathrm{m\,s^{-1}}$	heavy rain, small hail
MCS	6–24 h	>100 km	$10-20\,\mathrm{m\,s^{-1}}$	flooding, med. hail, weak tornadoes
Supercell	1-8 h	50 km	$> 20\,\mathrm{m\,s^{-1}}$	heavy rain, large hail, tornadoes

the cell – a key characteristic that distinguishes it from other forms of organized convection (Lemon and Doswell, 1979). Mesocyclones typically have a width of about 3–8 km, extend over at least half of the updraft depth, and persist long enough so that air parcels can pass the entire updraft (Markowski and Richardson, 2010). They furthermore differ dynamically from multicells, as their propagation is not dominated by the triggering of new cells by the gust front. In contrast to the motion of single cells or multicells, supercell motion is characterized by cyclonically (anticyclonically) rotations propagating to the right (left) of the mean wind shear. Supercells occur in environments with large vertical wind shear in comparison to those of single cells and multicells (> 20 m s^{-1}, see also Table 2.1), a continuous inflow of warm and moist air masses, and (at least) moderate CAPE values ($> 1,000$ J kg^{-1}). Supercells can have a very long lifetime of about 1–8 h.

The mesocyclone develops at the mature stage of a convective cell and requires advection, tilting, and stretching. The large vertical wind shear compared to other convective systems (spanning a significant depth of the troposphere) is associated with a large horizontal vorticity, which is a source for the vertical vorticity in the midlevel cyclone (tilting) – and therefore the rotation. Vertical wind shear can interact with the updraft, resulting in dynamically-induced vertical pressure gradients. These gradients and dynamical effects related to the mesocyclone can lead to a further enhancement of the updraft.

Regarding the structure of the supercell, the two downdrafts are named according to their positions: Forward Flank Downdraft (FFD) andRear Flank Downdraft (RFD). The intensity of storm-relative winds has an influence on the position and strength of the FFD and RFD as well as on the intensity of precipitation. Supercells are therefore categorized into low-precipitating (high storm-relative winds of $> 28\,\mathrm{m\,s^{-1}}$), high-precipitating ($< 18\,\mathrm{m\,s^{-1}}$) and classic supercell archetypes (> 18 and $< 28\mathrm{m\,s^{-1}}$, Markowski and Richardson (2010)). In low-precipitation supercells, the updraft is tilted downstream, and the FFD is far from the updraft, which leads to a long transportation of cloud and precipitation particles and therefore to their evaporation. In contrast, in high-precipitation supercells, updraft and downdraft are less separated. Due to a shorter transportation of particles and less evaporation, larger precipitation particles can form. High-precipitation supercells are therefore associated with the highest precipitation intensities and the occurrence of large hail, and an increased probability of tornadoes in comparison to low-precipitation supercells. A classic supercell is a hybrid of the low-precipitation and high-precipitation archetypes.

Mesoscale convective systems

Convection embedded in a larger system of stratiform precipitation (see Sect. 2.1.3) occurs in a Mesoscale Convective System (MCS). An MCS is a cloud system occurring in connection with an ensemble of thunderstorms and producing a contiguous precipitation area on the order of at least 100 km in horizontal scale in at least one direction (AMS, 2024c). At this scale, the Coriolis acceleration plays a role, enabling the development of meso-α-scale circulation.

An MCS can form from pre-existing isolated convective systems (lifting at the front of the cold pool, type I) or externally through large-scale lifting (e. g., at a front) in the middle and upper troposphere (type II, Schumacher and Rasmussen, 2020). Therefore, MCSs are always dominated by synoptic-scale forcing, which allows for a relatively long lifetime of up to 24 h (see Table 2.1). In the early stages of its development, an MCS consists of a group of organized single cells, which merge (mature stage) and go through the life cycle of a single cell (see above). As other convective systems, they are driven by deep moist convective processes (lifting, moisture and instability) and vertical wind shear (about 10–20 $\mathrm{m\,s^{-1}}$ of the 0–6 km vector, Schumacher and Rasmussen (2020)).

Typically, MCSs occur in the area of the warm sector of a trough and the associated surface low. Although MCSs are most intense during the summer months because of the higher latent energy available, they can occur throughout the year. As MCSs are defined by the spatial extent of the precipitation field, they encompass various forms identifiable from radar images, such as squall lines (nearly unbroken lines of convective cells), bow echoes, or mesoscale convective complexes (MCCs). According to Maddox (1980), MCCs are particularly large MCSs characterized by an infrared cloud shield with temperatures $\leq 32\,^{\circ}\mathrm{C}$ (as measured by satellites) covering an area of at least $100,000\,\mathrm{km^2}$ and persisting for more than 6 h.

Convective activity decreases throughout the lifetime of an MCS, whereas stratiform precipitation increases with increasing lifetime of the system. Although the intensity of stratiform precipitation is much lower than that of convective precipitation, the former can contribute to about 35–50 % of the total precipitation of the MCS because of its large horizontal extent and the decreasing convective activity (Watson et al., 1988).

Weather phenomena associated with convective systems

Convective systems and especially Severe Convective Storms (SCSs) are associated with a number of weather phenomena, such as heavy precipitation, hail, convective gusts, and tornadoes. These severe weather phenomena become more likely as the product of CAPE and shear increases, with this product serving as a useful rule of thumb to estimate the likelihood of severe weather, assuming convection is able to develop (Markowski and Richardson, 2010). Tornadoes are rapidly rotating columns of air which extend vertically from the surface to the base of a cumuliform cloud, with horizontal extents of

$\leq 2\,\mathrm{km}$ (AMS, 2025c). Major hazards resulting from SCSs in Europe include hail, convective gusts, and flooding. Since these hazards are of major relevance for this work, hail and convective gusts are described in detail in this section and in Sect. 2.1.2 with a focus on their damage, and heavy precipitation is discussed in Sect. 2.1.3.

Convective gusts

Virtually all thunderstorm systems are related to high wind velocities close to the surface, with extreme winds produced especially by supercells and MCSs. Wind speeds can exceed those observed for ETCs (see Sect. 2.1.1). Convective gusts are outflow-related damaging winds, with wind speeds exceeding $100\,\mathrm{km\,h^{-1}}$ that can occur locally or within gust fronts (Fujita, 1990). They are also referred to as straight-line winds (Houze, 1993). Gust factors (see Sect. 2.1.1) are also found to be higher for convective than for dynamic gusts (e. g., Bradbury et al., 1994; Mohr et al., 2017).

If straight-line winds extend over 400 km on one axis with gusts over $26\,\mathrm{m\,s^{-1}}$, they are called derechos (Markowski and Richardson, 2010; Gatzen et al., 2020). Furthermore, several spatially distinguished wind gusts exceeding 33 m $\mathrm{s^{-1}}$ must be reported to be classified as a derecho (Gatzen et al., 2020). Derechos occur through the progression of singular wind swaths or through a series of several swaths, which need to be attributed to the same event (Gatzen et al., 2020).

Convective gusts near the surface have two main causes, which can occur in combination, leading to an amplification. One mechanism involves downdrafts on the meso-γ-scale (see Fig. 2.1), triggered by precipitation (due to evaporation, sublimation, and friction of hydrometeors). Upon reaching the ground, a pressure dome forms, causing the downdraft to shift to horizontal directions. Given a high pressure gradient, it extends horizontally with high velocities. Downdrafts with limited horizontal extent ($\leq$ 10 km) are also called downbursts, as they create strong, often highly divergent horizontal winds near the ground. Downbursts with a particularly small spatial scale of $\leq 4\,\mathrm{km}$ are termed microbursts. The second mechanism occurs when cold pools associated with horizontal pressure gradients large enough to produce damaging winds; this happens on the meso-β-scale. Conditions favoring this development include the merging of several thunderstorm outflows, as this deepens the outflow and increases its surface pressure. This is also the case with MCSs.

If the virtual temperature of an air parcel is lower than that of its surroundings, it will descend. The energy released within this process can be described by the Downdraft Convective Available Potential Energy (DCAPE), which is formulated similar to the CAPE (Markowski and Richardson, 2010):

$$\mathrm{DCAPE} = g \int_{h}^{0} \frac{T_v' - T_v}{T_v}\, dz, \tag{2.16}$$

where T_v' equals the virtual temperature of the descending air parcel.

DCAPE quantifies the energy released by the descent of an air parcel in a saturated downdraft until it reaches the ground. First, it cools to the wet-bulb temperature at $z = h$ and becomes saturated. Then, it is brought to the surface ($z = 0$) first along the pseudo adiabats and then along the dry adiabats. The maximum speed of the downdraft can be derived from DCAPE as with CAPE (see above). However, as the elevation h can only be roughly estimated and not all processes are considered, DCAPE can only be a rough approximation of the downdraft and therefore its useability is limited. The downdraft can be enhanced by friction of falling hydrometeors (especially relevant with large hail) and latent thermal transitions (change of potential temperature) mainly through sublimation and evaporation (e. g., Houze, 2014).

Hail

Hail is a solid form of precipitation, in the form of irregular lumps or balls of ice, with a diameter of $\geq 5\,\text{mm}$ (AMS, 2024a). Particles below this diameter are referred to as graupel (Markowski and Richardson, 2010). Individual hail units are called hailstones, which consist of frozen water with small air inclusions. These air inclusions vary in concentration, leading to a lower density than that of pure ice (0.7–0.9 $\text{g}\,\text{cm}^{-3}$ for hail vs. ~0.9 $\text{g}\,\text{cm}^{-3}$ for pure ice, Pruppacher et al. (1998)). For small hail, the density is found to be lower and more variable. Hail can have different forms, from round to conical up to serrated forms. Therefore, the hail diameter also largely varies. The terminal velocity of hail v_{hail} is approximated by the velocity resulting from the balance between friction, gravitation and updraft forces. It depends on the diameter d of the hail, air density ρ, ice density ρ_{ice}, size and shape (Markowski and Richardson, 2010):

$$v_{\text{hail}} = \sqrt{\frac{4g\rho_{\text{ice}}d}{3c_d\rho}}, \tag{2.17}$$

where c_d is a dimensionless drag coefficient, depending on the shape and smoothness of the hydrometeor and accounting for air resistance. Eq. 2.17 shows that v_{hail} rises with a higher ice density and diameter, but weakens with increasing air density and drag coefficient. The drag coefficient c_d varies largely due to the variety in hail shapes, which is why it (and therefore also v_{hail}) cannot be determined exactly. However, the relationship between hail diameter and v_{hail} has been estimated empirically, usually assuming a value of $c_d \approx 0.4 - 0.5$ (Heymsfield and Wright, 2014). An estimate is, for example, $v_{\text{hail}} \approx 9d^{0.8}$ (Auer, 1972; Pruppacher et al., 1998) resulting in a terminal velocity of 32.6 $\text{m}\ \text{s}^{-1}$ for a hail diameter of 5 cm, showing the high vertical velocities required for the formation of large hail (Markowski and Richardson, 2010).

Various spatial scales are relevant for the formation of hail, including microphysical processes in cold clouds as well as mesoscale dynamics such as strong updrafts, wind shear, and storm organization. Hail only occurs in organized convective systems, where a large number of unfrozen liquid droplets (that is, *supercooled* droplets) and a small number of ice crystals exist (see Sect. 2.1.3). When supercooled water droplets rime on ice crystals, hail embryos in the form of graupel can form. Subsequently, hail is formed

from graupel (or large frozen drops), mainly by riming, which is the freezing of supercooled droplets by contact with ice particles.

Two regimes of hail growth exist, depending on the surface temperature T_s of the hail: dry growth (leading to opaque layers) and wet growth (clear layers). The dry growth regime occurs at $T_s < 0\,^{\circ}\mathrm{C}$, when riming may include air entrapments. In contrast, in the wet growth regime, as $T_s \approx 0\,^{\circ}\mathrm{C}$, the surface of the hailstone is covered by liquid water, which enters the pores of the rimed layer. This leads to an almost transparent layer. During the growth process both regimes can alternate, depending on the ambient conditions, mainly the concentration of supercooled droplets and the temperature, leading to changing layers.

Hail growth conditions are ideal when the difference between v_{hail} and updraft velocity w is large, or where a large concentration of supercooled liquid water and ice particle occurs. A long residence time of hailstones in regions with a high liquid water content allows for growth to large diameters. The updraft should neither be too strong nor too weak, as the hailstone can be ejected or fall out prematurely, respectively (Markowski and Richardson, 2010). Therefore, the main factors favoring hail growth are assumed to be a long lifetime of the hailstorm, high vertical velocities and a high liquid water content.

The relatively short lifetime of single cells does usually not permit the production of hailstones (Markowski and Richardson, 2010). When hail forms in multicells, it is assumed to be transported across multiple single cells. In supercells, a high graupel concentration prevails on the backside and in the upper part of the updraft, while in the updraft, the concentration of supercooled droplets is high (Browning and Foote, 1976). When hail embryos enter the margin of the updraft, supercooled droplets can accrete to the hail embryos. If hail embryos enter the rotating updraft in the center, they are transported upwards, where they can develop to large hailstones. Due to the vertical wind shear, hailstones are transported to the front of the updraft, where they start to fall. However, this process of hail formation is the subject of ongoing research.

Damage potential of convection

SCSs occur frequently and, while the number of injuries and fatalities are relatively low and mainly related to lightning, they are associated with high annual losses. Globally, these events have become established as the second largest hazard with regard to losses after tropical cyclones (Swiss Re, 2024). In the period 2013–2024, SCSs accounted for more than 32 % of total annual insured losses from natural hazards, which is a significant increase compared to preceding decades (Swiss Re, 2024). SCSs-related losses in Europe, and specifically Germany, are also of major relevance. These are discussed later in this section and in detail in Chapter 5.

Hail damage

Damaging hail is caused by the high kinetic energy and terminal velocity of solid hailstones. While terminal velocity increases linearly with hailstone size (e. g., Auer, 1972, see Sect. 2.1.2), kinetic energy has been found to increase with the hailstone size raised to the power of 2–4 (Gessler, 2013; Grieser and Hill, 2019). Therefore, most of the hail damage is caused by a few heavy storms (e. g., Küpfer et al., 2024), and hailstone size, together with the size of hail streaks, are major determinants of damage in general (see also below). The largest hailstone worldwide had a diameter of 20 cm (South Dakota, USA, 2010), 19 cm in Europe (Italy, 2023, Eisenbach, 2023), and 14 cm in Germany (Undingen, 2013, Kreibich et al., 2014).

Hail can impact agricultural crops or fruit, cars, or buildings (e. g., Púčik et al., 2019). Global insured losses of SCSs are dominated by hail, accounting for about about 50–80 % (Swiss Re, 2024). Single events, such as a major event in southwest Germany on 28 July 2013, can be associated with losses in the scale of billions (Kunz et al., 2018). Germany is a hot spot for hail losses in Europe, with the highest number of major loss events across Europe in the past decades (see Fig. 2.10c, Púčik et al., 2019). However, this is likely also influenced by the distribution of assets across Europe. Between 1986 and 2008, around 40 % of the insured building losses in southwest Germany have been attributed to hail (Kunz and Puskeiler, 2010). Including more recent data, hail also plays a major role in southwest Germany, as seen in Chapter 5. When comparing direct thunderstorm impacts, hail damage is much larger than wind gust damage (Calotescu et al., 2024), and the effort required by insurance companies to deal with the damage is much higher for hail than for other hazards (Kantonale Gebäudeversicherungen, 2015).

Hail damage to buildings depends, among others, on hailstone size, wind speed and direction, and building material (Brown et al., 2015). Many studies have found building damage to increase exponentially with hail size. For example, Púčik et al. (2019) evaluated the conditional probability of different types of hail damage in Europe given the hail size. They found that the probability of damage to houses, especially roofings, increases exponentially and more strongly than all other types with hail size, with the steepest increases occurring between hail diameters of 4–5 and 8–9 cm (see Fig. 2.9a). Roofings are among the building components most affected by hail (Kantonale Gebäudeversicherungen, 2012; Brown et al., 2015). A sigmoid increase is found for the percentage of damaged buildings (insured assets affected) and the corresponding losses, with the maximum expected severe hail size (MESHS) measured from radar data (see Fig. 2.9b, Schmid et al., 2024). Hohl et al. (2002) also found a sigmoid-shaped relationship between the total loss ratio of residential buildings and kinetic energy. Lastly, the probability of failure of roofing (in North America, where roof shingles are common) was also found to increase in a sigmoid pattern with the hailstone diameter (Li et al., 2024). The percentage of damaged buildings (Schmid et al., 2024), roofing failure probability (Li et al., 2024), and share of a building affected (Hohl et al., 2002) increase most strongly with diameters of 4–6 cm. If the primary wind direction is vertical,

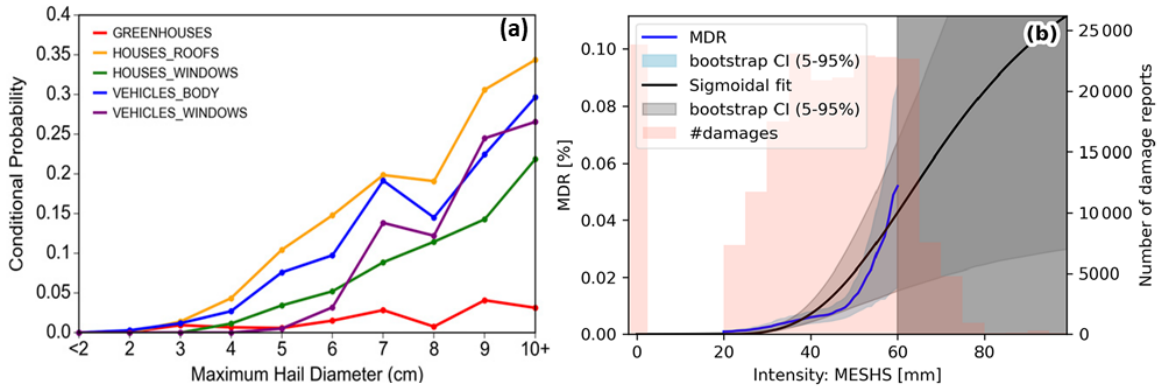

Figure 2.9.: Damage to buildings as a function of (maximum) hail size: (a) Conditional probability of different types of hail damage as a function of maximum hail diameter for living and nonliving objects, from Púčik et al. (2019): *Large hail incidence and its economic and societal impacts across Europe.* ©American Meteorological Society. Used with permission. (b) Impact function for damage sums in CHF, with the empirical mean damage ratio (MDR) in blue, calibrated with data from 2002 to 2021. In black, a sigmoidal fit is shown. The grey shaded area indicates maximum expected severe hail size (MESHS) values without sufficient data points for a meaningful empirical fit, from Schmid et al. (2024), their Fig. 6, Copyright ©2024 T. Schmid et al., licensed under a Creative Commons Attribution 4.0 License (`http://creativecommons.org/licenses/by-nc-sa/4.0/`), cropped to (b).

mainly the roof will be affected, whereas horizontal winds may lead to hailstones propelling at an angle (Changnon et al., 2009), which can lead to impacts on facades, shutters, windows, or doors, as well as thermal insulation layers (Schuster et al., 2006; Calotescu et al., 2024). In southwestern Germany, a hail risk model finds walls or ceilings most affected, with roofings only being the second highest affected building part, together with windows and doors (Schmidberger, 2018). Higher wind speeds may lead to a higher kinetic energy, increasing the impact (Brown et al., 2015).

With respect to building material, metal and wood roofs have shown to be much more susceptible to hail than tile or asphalt shingle roofs (Brown et al., 2015). In the United States, roofing material may be classified by impact resistance , where roofing is tested for impacts simulating hail with steel balls, for example (Brown et al., 2015).

Other potentially influencing factors for hail damage include hailstone hardness, sheltering of buildings (or crops) by trees or other buildings (Brown et al., 2015), material age (materials becoming brittle, Brown et al. (2015)) or building age (newer buildings being more susceptible, Schmid et al. (2024)). Regarding shutter damage, the timing of the event matters, where events during nighttime may lead to a higher share of damage (Kantonale Gebäudeversicherungen, 2015). While additions to roofings, especially solar panels, can increase the damage (e. g., Swiss Re, 2014), they are generally excluded from the building insurance in Germany according to the general insurance conditions (GDV (2023), Sect. 7.6.1). Convective systems in central Europe generally occur during the summer half year (Punge and Kunz, 2016; Púčik et al., 2019), with the highest mean damage between mid-June to mid-August, as found in a study on hailstorms in Switzerland (Hohl et al., 2002). This reflects the fact that supercells

preferentially occur during this period in central Europe. In a study on France, Belgium, Luxembourg and Germany based on large hail reports (2005–2014), large hail occurs most often from May to July (Kunz et al., 2020). During 1980–2018, large hail reports were most frequent in June across the majority of central Europe, whereas in western Germany, large hail was most often reported in July (Púčik et al., 2019). Seasonally differing impacts also occur with crop impacts (Changnon, 1971).

Water infiltration can exacerbate the damage, which has been shown for a specific hail cell, where the combination of hail and rainfall significantly amplified losses (Hohl et al., 2002). In industrial buildings, water infiltration can damage e. g., machinery, which may even lead to the halting of production (Schmidberger, 2018). Impacts of combined extremes, including hail and flooding, will be discussed in Chapter 6.

Damage from straight-line winds

Due to the high velocities of convective gusts, they have a considerable damage potential. The globally strongest gust ever observed was recorded during a microburst with a peak of $67\,\mathrm{m\,s^{-1}}$ (United States, 1983, Fujita (1990)). In Germany, the strongest convective gust in the past decades was recorded in Zinnwald-Georgenfeld (Saxony) on 25 July 2005 with $52.6\,\mathrm{m\,s^{-1}}$ (Mohr et al., 2017). However, there is a lack of consistent observation data, as the network of weather stations has a low density and is unable capture local phenomena comprehensively; therefore, gust fronts have a larger probability of being detected than, e. g., microbursts (Mohr et al., 2017). The data used to identify convective gusts in this work are introduced in Sect. 3.2. Convective gusts can impact, for example, wind-sensitive systems and structures, such as buildings, trees, wind-turbine towers (Bradbury et al., 1994; Baniotopoulos, 2007), or stages of outdoor open-air festivals (e. g., Deutsche Welle, 2024; De Meutter et al., 2015).

How convective gusts impact buildings is hard to capture, due to their localized and short-lived nature (Calotescu et al., 2024). Recently, wind-induced damage from thunderstorms has been observed by roofing system failures in Romania, often related to sheet metal and clay tiles (Calotescu et al., 2024), the latter of which is common and prone to damage in Germany as well (e. g., Swiss Re, 2014). Other structures vulnerable to wind damage include windows and doors and the connection between the roof and the lower structure (Calotescu et al., 2024). Downbursts or microbursts in particular also pose a risk for aviation during take-off and landing, due to sudden changes in wind direction. The research by T. Fujita, who discovered and proved the existence of downbursts and microbursts in the 1970s–1980s, trigggered the improvement of warning systems using Doppler radars and training of pilots that helped to prevent many airplane crashes (Wilson and Wakimoto, 2001).

Tornado damage

Tornadoes are assumed to be the most destructive meteorological phenomena as they can reach wind speeds of up $500\,\mathrm{km\,h^{-1}}$ or even higher (Mitchell-Wallace et al., 2017). The damage potential is assumed to increase with the cube of maximum wind speed (Dotzek et al., 2005). Because of their local

occurrence, they contribute only to ~20 % of all SCSs-related damage (Mitchell-Wallace et al., 2017). Tornadic damage is commonly evaluated with the Enhanced Fujita (EF) Scale, a modification of the original Fujita Scale (Fujita and Pearson, 1973; Fujita, 1981). The EF Scale consists of distinct classes from EF0 (29–38 m s^{-1}) to EF5 (> 90 m s^{-1}, McDonald and Mehta, 2006; Potter, 2007). Although damage from tornadoes in Germany has been relatively minor in the past in comparison to other natural hazards, the occurrence of tornadoes in Europe should not be underestimated (e. g., Dotzek, 2001; Antonescu et al., 2017). Examples in Germany include a very damaging F4 tornado in Pforzheim, a city in southwestern Germany, in July 1968. The tornado led to two fatalities, more than 200 injuries and an economic damage which would amount to about € 300 million (inflation-adjusted) as of today (Sävert, 2024). A more recent example is an F2 tornado in May 2022, which occurred around Paderborn, leading to 47 injuries and total economic losses of more than € 200 million (Möller, 2023).

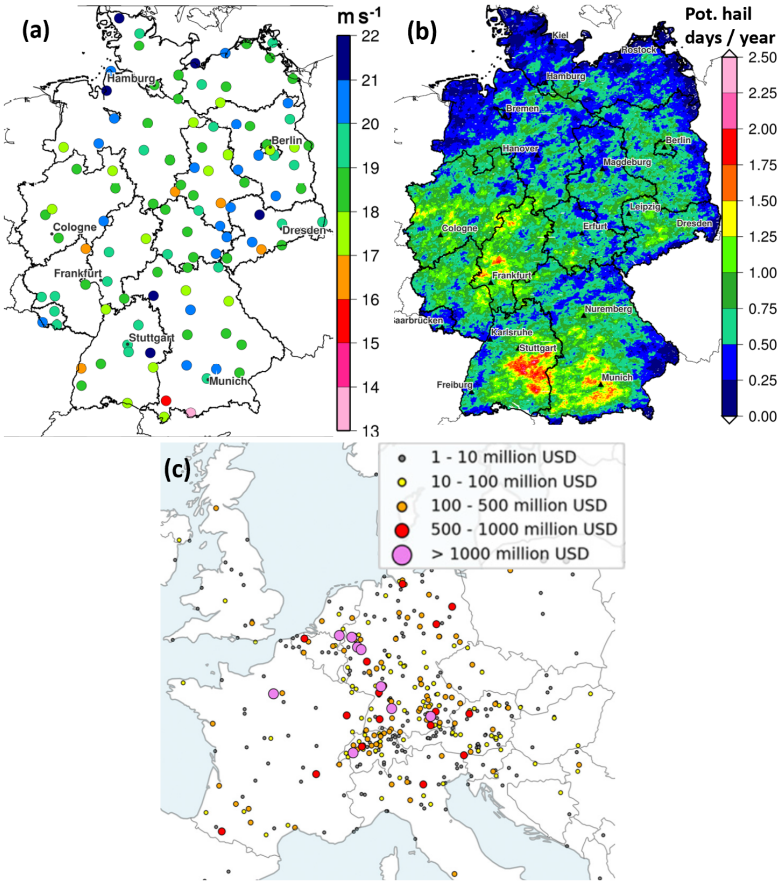

Figure 2.10.: Spatial distribution of extreme events from severe convective storms: (a) Spatial distribution of the 95 % percentiles of a convective gust sample (1992–2014), from Mohr et al. (2017), their Fig. 2b,: ©2017 S. Mohr et al.: *Statistical characteristics of convective wind gusts in Germany*, licensed under Creative Commons Attribution 3.0 License (`http://creativecommons.org/licenses/by/4.0/`); cropped to (b), (b) Number of days with severe thunderstorms / hail per year in Germany between 2005 and 2023 for areas of 1 x 1 km^2, from Kunz (2024), (c) Hail-related losses exceeding $1 million (USD) from 1980 to 2018, from Púčik et al. (2019): *Large hail incidence and its economic and societal impacts across Europe*. ©American Meteorological Society. Used with permission.

Spatial distribution and trends of SCSs

Regarding thunderstorm days in general, a distinct north-to-south gradient can be observed across Germany. Compared to the north, southern Germany experiences more thunderstorm days based on lightning data (Piper and Kunz, 2017; Augenstein et al., 2024), and a higher number of annual lightning and hail hours is observed based on a combination of lightning and ESWD data (Taszarek et al., 2020). With respect to severe weather, southern Germany also experiences more convective gusts (lower threshold of $18\,\mathrm{m\,s^{-1}}$), but not regarding the most extreme ones: Extreme wind speeds of $\geq 30\,\mathrm{m\,s^{-1}}$ do not show any spatial patterns, but have a similar occurrence probability across Germany (see Fig. 2.10a, Mohr et al., 2017). Gatzen et al. (2020) also find a north-to-south gradient regarding derechos, with a maximum density in southern central Germany. Hail streaks, which are areas of continuous hail occurrence (Changnon, 1970), extend about 47 km on average in Germany (Puskeiler et al., 2016). The probability of hail days (based on radar data) also shows a gradient from north to south, with hotspots in Baden-Württemberg, the Bavarian pre-alps and parts of Hesse (see Fig. 2.10b, Kunz, 2024). The hot spot for hail frequency in Germany is in Baden-Württemberg, downstream of the Black Forest, the Neckar valley and the Swabian Jura. Major loss events (> $1 billion) are also found to cluster in southern Germany and in urban centers (see Fig. 2.10c, Púčik et al., 2019). In this work, regional differences with respect to losses from SCSs are discussed in Sect. 5.3.

There is a generally high annual and decadal variability in thunderstorm and hail occurrence in Germany (Mohr et al., 2015a; Piper and Kunz, 2017). Due to the scarcity of direct measurements and the small-scale nature of convective systems, trends are hard to assess reliably. Although vertical wind shear is expected to change little, a higher moisture content at lower levels increases the potential of all convective weather phenomena, as found in a study based on climate model data (Rädler et al., 2019). In the past decades, the number of thunderstorm days has decreased in parts of central Europe, as shown in an analysis based on lightning data (Augenstein et al., 2024). However, regarding periods with convective gusts, Rädler et al. (2018) found an increase by 56 % in the past decades based on a statistical model, mainly due to an increase in moisture, which leads to a higher instability. With respect to losses, these trends will be discussed in Sect. 5.4. Studies show a rise in hail occurrence and potential in Germany over the past 30 years. For example, Rädler et al. (2018) estimated an 86 % increase in hail potential since the 1980s, mainly in northern Germany, while Púčik et al. (2019) found a near doubling of large ($\geq 2\,\mathrm{cm}$) and very large hail ($\geq 5\,\mathrm{cm}$) probabilities since 1990, based on ESWD reports and loss data. Another recent study modeled a significant increase (1950–2021) in hail occurrence across most of Europe, attributing it to rising low-level moisture (Battaglioli et al., 2023), based on lightning observations, reanalysis data and hail reports. However, this is not visible in direct observation data (e. g., Manzato et al., 2022). Future projections using proxy data (e. g., Mohr et al., 2015b; Rädler et al., 2019) indicate a slight increase in hail-prone conditions, but trends remain uncertain due to a high year-to-year variability and differences in climate models and scenarios. Until 2050, projected changes are weak and often insignificant, as

outlined in a review by Raupach et al. (2021), due to the high annual variability of SCSs. By the late 21st century, the occurrence of hail ($\geq 2\,\text{cm}$) is expected to increase, with very large hail ($\geq 5\,\text{cm}$) potentially becoming twice as frequent (Rädler et al., 2019).

2.1.3 Precipitation and flooding

Precipitation is typically defined as liquid or frozen hydrometeors large enough to fall, that is, 'precipitate', as a result of gravity (AMS, 2021). Hydrometeors are any result of atmospheric water vapor condensation or deposition, water or ice particles, formed in the atmosphere or on Earth's surface (AMS, 2024b). This includes rain, drizzle (diameter < 0.5 mm), snow, graupel (diameter < 0.5 cm), hail and settled precipitation such as rime. The International Cloud Atlas as well as a vast amount of literature classifies these hydrometeors and their corresponding clouds (WMO, 2017). Precipitation is typically measured as the water amount reaching the ground; typical measurement instruments are rain gauges. The dimension of precipitation intensity is length divided by time, with the most common units being liters per square meter ($\text{l}\,\text{m}^{-2}$), or mm with a reference period (e. g., 1, 6, or 24 h).

Formation and microphysics of cloud and precipitation particles

Cloud particles are water droplets or ice crystals small enough to be held in suspension in the atmosphere (radius of ~1–100 µm, Houze (2014)). They are formed by heterogeneous nucleation, that is, the formation of hydrometeors from water vapor with the inclusion of an aerosol. The aerosol is either a cloud condensation nucleus (CCN) for liquid water or an ice forming nucleus (IN) for ice nucleation. IN need to have specific properties and are scarce; therefore, in cold clouds, supercooled droplets coexist with ice particles at temperatures down to -38 °C (Houze, 1993).

When water droplets or ice nuclei reach a radius of more than 100 µm, they are called precipitation particles, with an observable sedimentation speed. Precipitation particles develop from cloud particles in warm clouds by diffusion or collision and coalescence (Langmuir process). In mixed-phase clouds, where ice particles and droplets occur simultaneously, precipitation particles can form very effectively through the Wegener-Bergeron-Findeisen (WBF) process. By this process, water vapor diffuses from liquid particles to solid ones, because of the higher water vapor pressure over liquid than over ice. This leads to a rapid growth of ice crystals at the expense of liquid water droplets (Storelvmo and Tan, 2015).

Types of precipitation

Precipitation can be related to lifting caused by fronts, horizontal flow convergence, convection (see Sect. 2.1.2) or orography (forced lifting). In the mid-latitudes, precipitation can be distinguished into two main types, depending on their spatial and temporal extent: Stratiform precipitation is caused by large-scale

lifting and is characterized by low vertical velocities of about ~0.05-0.5 m s^{-1} and an extensive horizontal extent (Houze, 1993). The latter can be seen, for example, in radar echoes: Stratiform precipitation exhibits broad horizontal regions of maximum radar reflectivity around the melting level (see Fig 2.11). It is characterized by low to moderate and uniform intensities with a long duration (several hours to days).

Convective precipitation, in contrast, is caused by strong local vertical motion (Houze, 1993; AMS, 2025a). Updrafts in convective clouds are usually narrow (~1 km width), with well-defined vertical cores of maximum reflectivity in radar data. Convective precipitation usually is of short duration (~minutes), but higher intensity compared to stratiform precipitation. However, organized convection and mesoscale convective systems can lead to longer durations. Mixed precipitation, used as a category in this thesis, refers to mixed types of precipitation, such as embedded convection (see below).

Stratiform precipitation

As stratiform and convective precipitation differ in their vertical velocity scales, they are formally distinguished using the mean vertical air velocity w (Houze, 1993). Since a major part of precipitation develops from clouds above the 0 °C level and thus from ice particles, w is is typically compared to the terminal fall velocity of snow and ice crystals v_{ice} (~1–3 m s^{-1}). In stratiform precipitation, the magnitude of w is generally smaller than v_{ice} (Houze, 1993):

$$|w| < v_{\mathrm{ice}}. \tag{2.18}$$

Most stratiform precipitation falls from nimbostratus clouds reaching well above the 0 °C level (WMO, 2017). Ice particles can originate from within or outside the nimbostratus cloud and begin to grow once they are introduced into the cloud. Upward motions maintain saturation, which causes water vapor to condense and deposit onto ice particles (see Fig. 2.11a). For continuous growth, w must be large enough to maintain saturation. In the upper levels of the nimbostratus cloud, the ice particles must sediment, as they cannot be carried aloft by air motions anymore when growing bigger. These in-cloud air velocities in nimbostratus clouds are typically only a few tens of centimeters per second and therefore favor particle growth by vapor deposition. The higher the altitude at which the ice particles enter the cloud or are formed, the longer they can grow by deposition of vapor. This growth time is approximately 1–3 h for ice particles falling from the cloud top (Houze, 1993). When the particles approach the 0 °C level (~2.5–1 km above ground), they grow by aggregation to large snowflakes and by riming. Riming occurs since the vertical velocities of a few centimeters per second can be strong enough to keep a few liquid-water drops present alongside the falling ice particles. Aggregation becomes more frequent the closer the hydrometeors get to the 0 °C level, until they melt just below the 0 °C level, becoming large and rapidly falling raindrops.

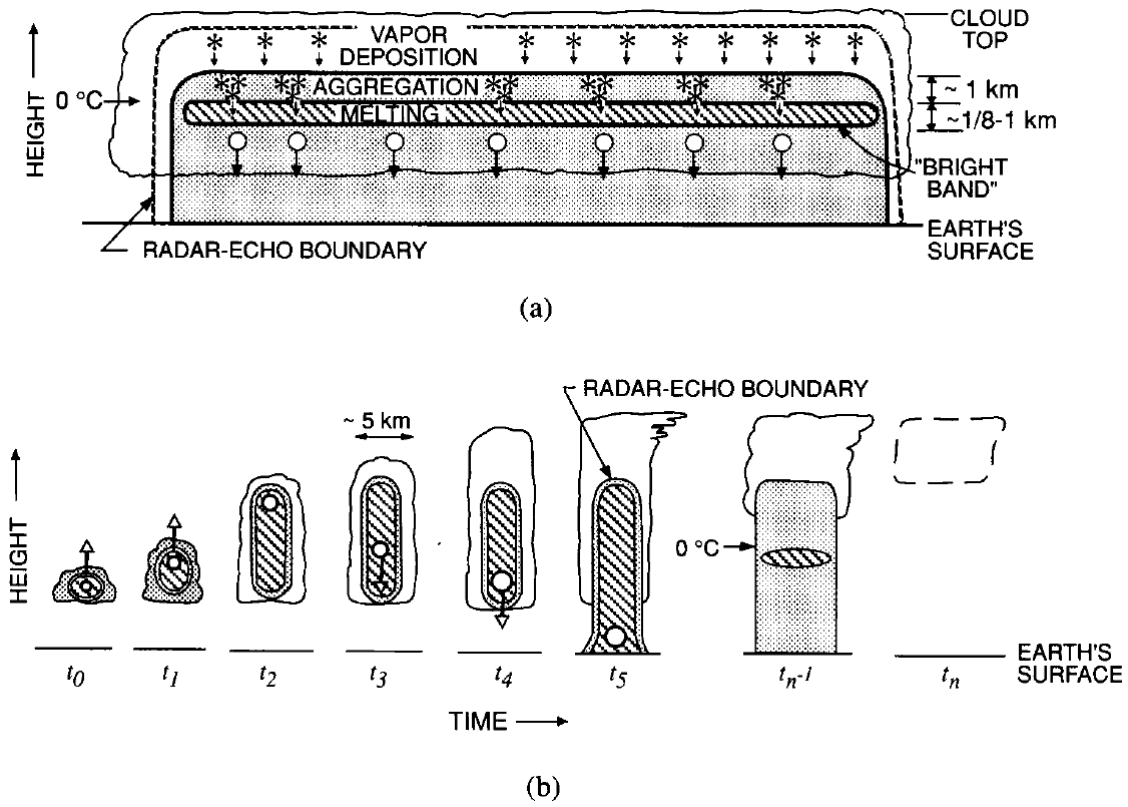

Figure 2.11.: Characteristics of stratiform (a) vs. convective (b) precipitation. Shading represents the radar echo, while hatching represents the strongest echo, and the dashed line indicates an evaporating cloud. (b) is shown during timesteps $t_0, \ldots, t_n$, which show growing particles carried upwards by updrafts until t_2, falling relative to the ground and reaching the surface just after t_5, and dissipating at t_{n-1} and t_n. Adopted from Houze (1993), their Fig. 6.1: Cloud Dynamics, Robert A. Houze, Jr, Copyright ©1993 by ACADEMIC PRESS, INC., Reproduced with permission of The Licensor through PLSclear.

Convective precipitation

In contrast to stratiform precipitation, convective precipitation is characterized by vertical velocities where condition 2.18 is not met (see also Sect. 2.1.2). The vertical velocity scale is ~1-10 m s^{-1}, encompassing typical fall speeds of ice crystals and snow. In extreme cases, vertical velocities of more than 50 m s^{-1} have been measured (Houze, 1993). These high vertical velocities are responsible for the high intensities and precipitation sums. When convective clouds dissipate (after t_5 in Fig. 2.11), the upward motions weaken and cannot carry precipitation particles upward anymore, thus precipitation can have a stratiform character (Houze, 1993).

Assuming complete saturation, the condensation rate is almost proportional to the vertical velocity. This leads to a production of a large number of liquid water or ice particles. In deep convective clouds, a high number of large precipitation particles can form by coalision and coalescence, as the mass changing rate of graupel and hail is proportional to the difference between vertical velocities and hydrometeors. An additional prerequisite for high intensities is a high moisture content of the incoming air masses. The highest precipitation intensities in the midlatitudes occur therefore when warm and humid air masses

Table 2.2.: Overview of the main characteristics distinguishing between convective and stratiform precipitation types, where w represents the vertical air velocity, and v_{ice} describes the terminal fall velocity of ice.

Form	Definition	Scale of w	Spatial Scale	Temporal Scale
Stratiform precipitation	$w < v_{ice}$	~0.05–0.5 m s^{-1}	~100–1,000 km	hours to days
Convective precipitation	$w > v_{ice}$	~1–10 m s^{-1}	~1 km	minutes

Form	Growth Mechanisms	Potential Hazards
Stratiform precipitation	deposition, aggregation	fluvial flooding
Convective precipitation	accretion, riming	pluvial flooding

prevail in the summer months. The strong updraft in the thunderstorm cloud enables a strong convergence close to the ground, which allows for a high moisture content in the cloud with sufficiently humid air masses.

Mixed precipitation

Within stratiform precipitation fields, convective cells may be embedded (Cannon et al., 2012). When this happens on a scale of thousands of square kilometers, the systems are termed MCSs (see Sect. 2.1.2). At the end of the lifecycle of convective cells, stratiform and convective precipitation can occur simultaneously. Furthermore, orographically triggered precipitation can be a result of both stratiform and convective processes, leading to high precipitation totals particularly over low mountain ranges (Kunz, 2011).

These hybrid forms of precipitation events will be referred to as 'mixed precipitation events' in this thesis.

Rainfall extremes

An extreme rain event is defined by a high intensity of rainfall, that is, a large precipitation amount per time unit (e. g., DWD, 2025c). Extreme rain often falls from convective clouds (see Sect. 2.1.3) and is by definition rare. There is no uniform quantitative definition of a heavy rain event, as rainfall characteristics depend largely on the geographic area and topography. Heavy rain can lead to high water levels, floods, and/or soil erosion.

For example, heavy rain in central Europe can be defined by the Wussow formula (Heyer, 1988), which relates the exceedance of a rain sum R to the duration t of an event:

$$R \geq \sqrt{5t - \left(\frac{t}{24}\right)^2} \quad \text{mm} \quad R \text{ in mm}, t \text{ in min.} \tag{2.19}$$

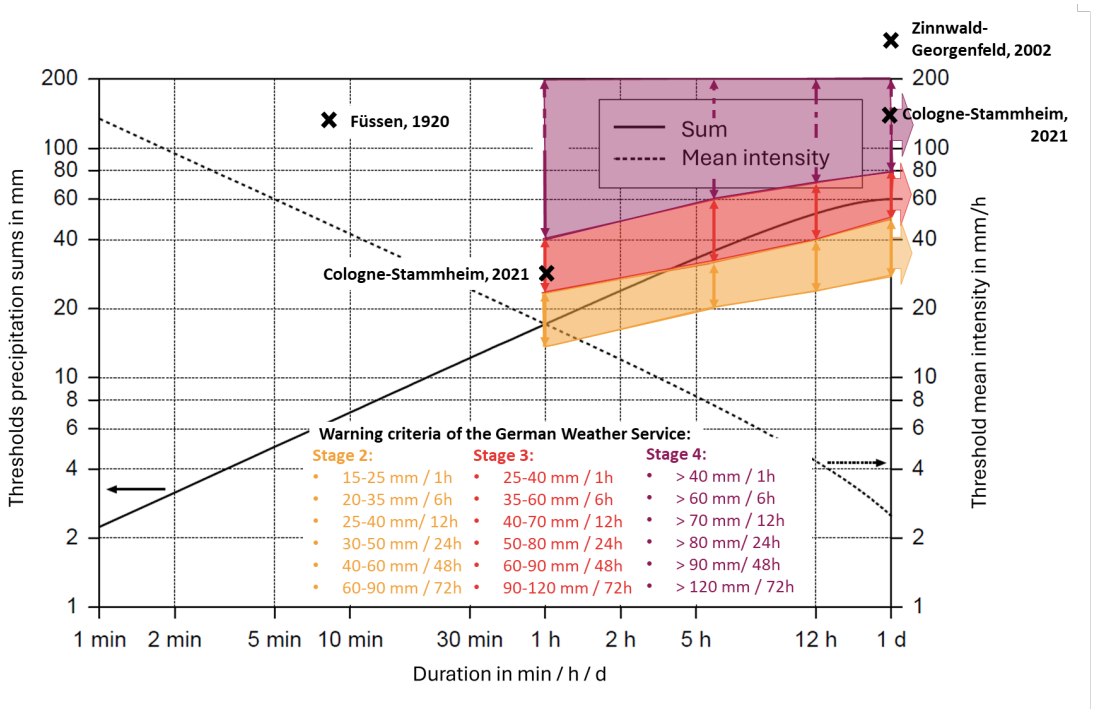

Figure 2.12.: Definition of heavy precipitation depending on duration after Eq. 2.19, resulting thresholds for precipitation sums (solid line) and mean intensities (dashed). In colors, the warning thresholds by the DWD are displayed. Crosses represent precipitation records (Becker et al., 2014; Junghänel et al., 2021) and recent events (Mohr et al., 2023) in Germany mentioned in the main text. Adapted from Kunz (2003) after Heyer (1988).

This definition takes into account that the mean intensity of a precipitation event decreases with its duration (see Fig. 2.12). With the Wussow formula, heavy rainfall as well as persistent rain up to 24h can be identified as extreme precitation, e. g., with a threshold of 7.1 mm with a duration of 10 min, a threshold of 17.1 mm with a duration of 1 h and a threshold of 60 mm with a duration of 24 h.

For statistical and other purposes, in research and practice, heavy rainfall is also defined as precipitation sums for certain return periods (e. g., 50 or 100 years) or at high percentiles (e. g., 95th, or 99th). A percentile-based approach is also taken in this work, however based on insurance loss data (see Sect. 4.2).

Rain extremes in Germany

The DWD issues weather warnings for heavy rain (in German: *Starkregen*, stage 3) for $>$ 25–40 mm h^{-1} or $>$ 35–60 mm within 6 hours (see Fig. 2.12). Above the upper thresholds of stage 3, a severe weather warning is issued (stage 4). The DWD differentiates heavy rain (duration up to 12 h) from persistent or continuous rain (from 12 h). Continuous rain often relates to a lower intensity and an extended field (that is, stratiform precipitation, see Sect. 2.1.3). For continuous rain, weather warnings (stage 3) are issued if 40–70 mm occur within 12 hours, $>$ 50–80 mm within 24 hours, $>$ 60–90 mm within 48 hours or $>$ 90–120 mm within 72 hours (see Fig. 2.12). Again, above the upper thresholds, a severe weather warning is issued (DWD, 2025b).

Precipitation records in Germany include one global record of a convective precipitation event in Füssen on 25 May 1920, with a total of 126 mm within 8 minutes (see Fig. 2.12, Junghänel et al., 2021). Further examples of German records include 312 mm within 24 h on 12–13 August 2002 in Zinnwald-Georgenfeld and 405 mm within 96 h in Aschau-Stein between 30 May and 2 June 2013 (Becker et al., 2014). For comparison, the devastating flood in western Germany between 13 and 15 July 2021 was associated with precipitation totals of more than 30 mm h^{-1} and 153.5 mm within 24 h in Cologne-Stammheim (Mohr et al., 2023). The long-term mean annual precipitation sums in Germany for the climate reference period 1960-1991 are about 789 mm (Friedrich et al., 2024).

Damage potential of extreme rain

A flood is commonly defined as the temporary overflow of water onto normally dry land, outside its normal confines (NOAA, 2025). From an insurance perspective, flooding is defined as the inundation of insured property (or directly adjacent land and soil areas, roads, footpaths, or cycle paths) by significant quantities of surface water, caused by an overflow of surface water or an escape of groundwater (GDV, 2023). Flooding has differing characteristics depending on its origin or geography (e. g., Klijn et al., 2009): Coastal or estuarine floods involve sea overflowing the land surface, while fluvial flooding occurs when rivers overflow their banks or river banks become breached. Areal flooding of catchments, urban areas or polders is typically triggered pluvially (i. e., related to abundant precipitation (AMS, 2021)) and due to insufficient drainage capacity of the soil. Finally, flooding from 'below' relates to groundwater flood or sewage overflow (Klijn et al., 2009). Another important distinction is based on the speed of onset, which differentiates flash floods with very fast onsets, caused by convective rainfall and characterized by short durations and high peak discharges, from other types that may persist for days or weeks (WMO, 2021; NOAA, 2025). Floods can also be triggered by mechanisms not primarily related to precipitation, such as volcanic flooding, tsunamis or lake outburst floods (Mitchell-Wallace et al., 2017). Since the focus of this work is on flood impacts in Germany fundamentally driven by precipitation, distinct flood types are summarized into the categories of pluvial and fluvial flooding (see Sect. 4.3.1), with a focus on characteristics in Germany.

Pluvial flooding

A pluvial flood occurs when rainwater accumulates at or near the point of rainfall, with rain falling faster than the drainage system to can remove it (WMO, 2021). Heavy and/or persistent precipitation becomes especially relevant when water masses concentrate in one or several areas due to persistence or orographic effects. Both effects can lead to strong increases in mean discharges and flow velocities, especially in small channels. Pluvial floods occur on the local scale, where they can lead to extreme damage, also because of a limited predictability, which impacts preparedness and precautionary measures. They may occur everywhere in Germany, albeit regions with a higher occurrence of SCSs (see above) are more

prone (Kreibich et al., 2014). A special case of flash floods is debris flows, where large amounts of debris are dragged within small channels or follow steep slopes (NWS, 2025), mainly in Alpine regions. Heavy rain, but also persistent rain within an MCS may also trigger landslides (Collins et al., 2020).

Fluvial flooding

Fluvial flooding occurs when discharges exceed the conveyance capacity and overtop river banks consequently (Kreibich et al., 2014). Fluvial flood regimes depend on catchment characteristics such as topography, hydro-morphologic structures and the general geographic situation (Kreibich et al., 2014). Meteorological conditions that triggered major flood events in Germany include interactions of upper-level pressure systems with associated surface lows and a persistent advection of warm and moist air masses over large distances (Schröter et al., 2015). Past severe floods in Germany often resulted from the so-called Vb weather pattern, which refers to a low-pressure system forming over the Mediterranean, and then moving (often slowly) with warm and moist air masses toward central and eastern Europe, causing heavy and persistent precipitation (DWD, 2024). Slightly modified Vb weather systems played a crucial role in the summer flood events of 2002, 2013, and 2024 (DWD, 2024).

Flood damage

Flooding is one of the most frequent and most damaging hazard globally, with an enormous damage potential both regarding loss of life and economic impacts. Flooding causes around a third of global economic losses from natural hazards (Mitchell-Wallace et al., 2017). In Germany, total economic direct and indirect flood losses are estimated to € 71 billion in the period 2001–2021 (Trenczek et al., 2022). Most direct economic losses occur to private household buildings, flood protection systems, infrastructure (e. g., transportation, power systems and water supply), and agriculture (Mitchell-Wallace et al., 2017; Trenczek et al., 2022). For the major flood events in 2002 and 2013 alone, flood damage to buildings and infrastructure amounted to about € 15 billion in Germany, and damage to commercial and industrial infrastructure amounted to € 4.7 billion (Trenczek et al., 2022). From 2007 to 2017, losses to residential buildings from precipitation extremes are estimated at € 6.7 billion, which equals an average loss of € 5,300 per building (GDV, 2019). The spatial and temporal distribution of insured flood losses in Germany are presented in Chapter 6.

Short-duration precipitation events cause the most damage to residential buildings, as can be seen by the claim frequency in residential building insurance, which is highest for 3-hourly events (2007–2017, see Fig. 2.13a). Continuous precipitation (duration > 12 h, see Sect. 2.1.3) is associated with lower damage, except if fluvial floods are triggered (GDV, 2019). Major trans-basin floods are especially damaging: If several catchments are affected at the same time, disaster management can be hindered, for example regarding the coordination of efforts. The insurance and reinsurance industry are also affected by trans-basin flood events due to the accumulation of losses (Uhlemann et al., 2010).

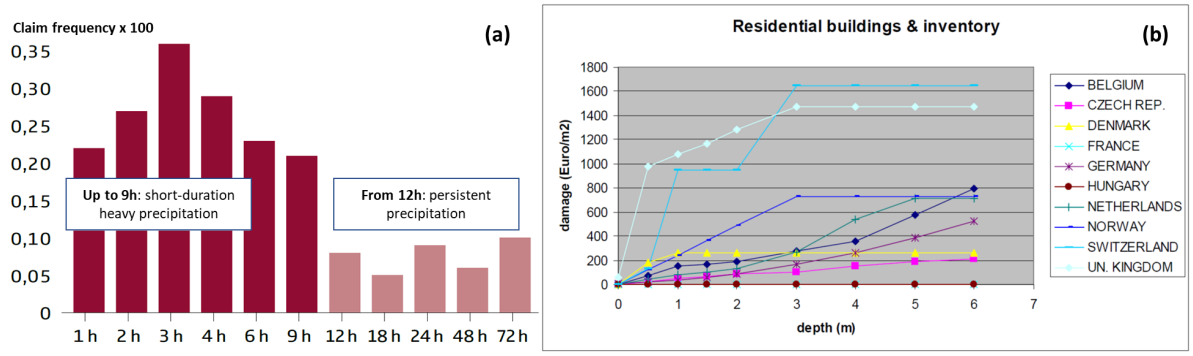

Figure 2.13.: (a) Claim frequency regarding flood damage in Germany depending on rainfall duration (2002–2017). The total number of claims amounted to 1.3 million. Adapted from GDV (2019) (Source: DWD/GDV). (b) Damage functions depending on the water depth and by country, adjusted for inflation with the consumer price index to the base year 2010, adopted from Huizinga et al. (2017), ©European Union 2017.

The degree to which individual buildings are affected by floods depends on several building attributes, such as the presence of a basement, building height and the use of the buildings in case of commercial or industrial properties. The type of building, its age, the standard of maintenance and the building materials can also play a role. Tangible flood damage is usually assessed based on water depth (White, 1942; Hammond et al., 2015), which can be amplified through flow velocity and duration, or sediments carried (Mitchell-Wallace et al., 2017). Since the water depth d can be recorded relatively easily through tide-line marks on trees or buildings and verified with historical data, flood severity is typically quantified as the function of maximum water depth d reached, by so-called depth-damage curves (see e. g., Fig. 2.13). The damage ratio, or fraction of the asset's value, is computed in relation to d. For example, Huizinga et al. (2017) developed flood damage functions with respect to residential buildings. They showed an almost linear function for buildings (including inventory) in Germany with a damage of about 500 € m^{-2} at a depth of 6 m (see Fig. 2.13b). Merz et al. (2004) criticized the focus of damage functions on water depth and building use, arguing that flood impacts on buildings are influenced by a range of factors, including flow velocity, sediment concentration, duration of the inundation, warning and response. Therefore, they argue, flood risk assessments based solely on water depth come with a large uncertainty. For a detailed review of factors contributing to flood damage, see Merz et al. (2010).

Flood severity can be assessed with the Flood Severity Index (FSI), an equivalent to the SSI (see Sect. 2.1.1): The FSI makes use of the 99.5th percentile of daily river discharges (Bloomfield et al., 2023). However, unlike for ETCs, the FSI is not widely used (yet). The variety of flood types and their spatial and temporal scales make the application of a uniform flood index challenging (Dacre and Pinto, 2020).

Spatial distribution and trends of flooding

Beurton and Thieken (2009) detected three regions with seasonally differing flood patterns, with western Germany being dominated by winter flood events of long duration and spatial extent, the east and

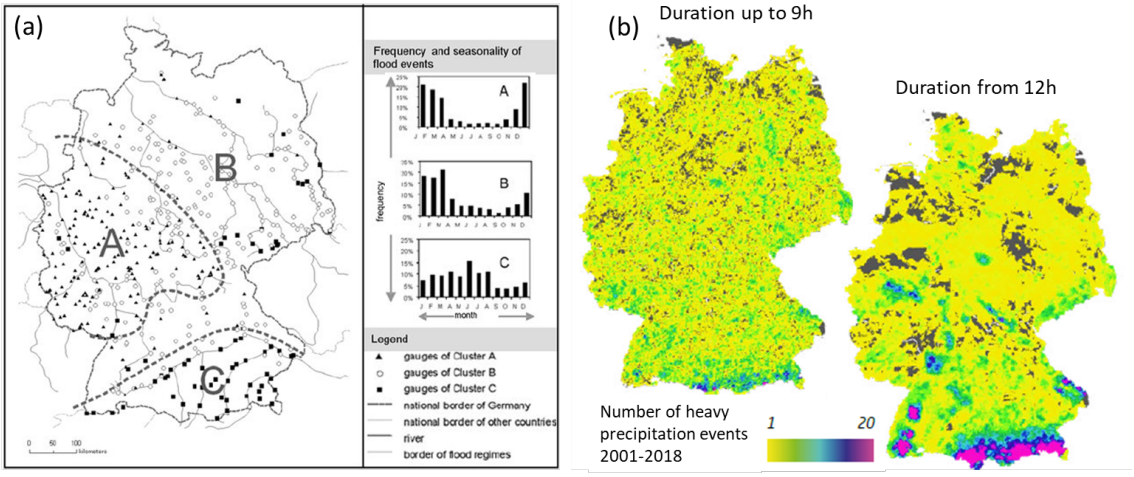

Figure 2.14.: Spatial patterns regarding precipitation extremes, (a) flood regimes adopted from Beurton and Thieken (2009), their Fig. 4: Seasonality of floods in Germany, Susanne Beurton and Annegret H. Thieken, Hydrological Sciences Journal, Copyright ©2009, reprinted by permission of Informa UK Limited, trading as Taylor & Francis Group, https://www.tandfonline.com, (b) number of heavy precipitation events 2001–2018, adapted from GDV (2019) (Source: DWD/GDV).

north of Germany also dominated by winter floods, but also some stronger spring or summer floods. Southern Germany has a multimodal distribution with snowmelt floods during spring and summer floods with local, but high discharges. When evaluated against the duration by using a radar climatology, heavy precipitation at time intervals of up to 9 h have similar probabilities across Germany, while heavy precipitation with a duration of 12 h and more is more likely in mountainous regions (see Fig. 2.14, GDV, 2019).

In Germany and central Europe, many studies have shown a significant increase in fluvial flood events in recent years, particularly in terms of damage (e. g., Becker et al., 2014; Paprotny et al., 2024). This is driven by changes in the hazard due to climate change, but also by changes in exposure and vulnerability such as settlement areas and land use, as well as by economic developments such as inflation. Regarding pluvial floods, an increasing trend (with outliers) can also be observed (GDV, 2019). When differentiating between the winter and summer half years, an increase in precipitation can be observed in the winter months, while a decrease is observed during summer (e. g., Kunz et al., 2023). In this work, trends with respect to past losses of floods are discussed in Sect. 5.4. According to the Clausius-Clapeyron equation, the saturation vapor pressure increases exponentially with temperature (e. g., Stull, 2017). Therefore, precipitation events and associated flooding are expected to become more severe in the future; however, these projections are associated with large uncertainty (e. g., Kunz et al., 2023).

In this section, individual meteorological phenomena and their associated hazards were introduced. An overview of the hazards discussed, including their main characteristics, can be found in Table 2.3.

Hazard	Underlying meteorological phenomena and typical timescales	Main drivers of damage	Strongest increase of building damage	Regions in Germany most affected	Trends past / future
Windstorms	ETCs: 1 day–2 weeks	Wind gust speed (m s^{-1})	Wind speeds $\geq$ 45 – 55 m s^{-1}, building construction type	Elevated areas, areas close to sea (northern Germany)	High annual and interannual variability / likely increase
Convective gusts	Convective systems: minutes	Wind gust speed (m s^{-1})	Wind speeds $\geq$ 45 – 55 m s^{-1}, Building construction type	Southern Germany (but not for most extreme ones)	High annual and interannual variability / uncertain
Hail	Convective systems: minutes	Hail size (cm)	Hail size $\geq$ 4-6 cm, wind speed, building material	Especially in southern Germany	Uncertain, probably more large hail
Pluvial flooding	Convective systems: minutes	Intensity (mm/h), Water depth (m)	Duration of 1 – 4 h, water depth of >1 – 2 m	Similar distributions	Increase in summer / increase (uncertain)
Fluvial flooding	Stratiform rain / ETCs: hours–days	Intensity (mm/h), water depth (m)	Duration of 1 – 4 h, water depth of > 1 – 2 m	Areas around river basins	Increase / increase (uncertain)

Table 2.3.: Overview of meteorological hazards discussed, their drivers, factors associated with strongest increases in (building) damage, main regions affected in Germany, and past and expected future trends.

2.2 Interactions between meteorological hazards

From single hazards to multi-hazards

Single hazards, their underlying atmospheric processes, and their impacts are well studied (Hillier et al., 2015) and have been the focus of research for many years. However, hazards frequently do not occur independently but can interact with each other across various spatial and temporal scales (Gill and Malamud, 2014). An independent view can lead to an over- or underestimation of risk (Hillier and Dixon, 2020), as hazard interactions may exacerbate impacts, making them greater than the sum of individual hazard impacts (Kappes et al., 2012). Therefore, in recent years, a branch of research has emerged in both climate and natural hazards research that takes into account interrelations between hazards and their drivers. For example, Zscheischler et al. (2018) argue that the predictability of extreme events like the 2010 heatwave in Russia could have been improved by taking into account the dependencies of climate drivers and/or hazards: the presence of high temperatures connected to the absence of precipitation, consequent drought, and an increased fire risk. Similarly, concurrent wind and precipitation extremes have dependent drivers in terms of wind speed, precipitation, orography, and the large-scale atmospheric circulation. The classification of possible hazard interactions, however, has several issues: There is a lack

of multi-hazard data records, interrelations can not always be categorized since physical interactions are complex, and the terminology is not fully clarified. More broadly, the dynamic feedback between hazard, exposure and vulnerability is hard to capture (see below).

Most databases, especially global ones, usually record (only) single hazards and do not account for any dependence between hazards. Therefore, also risk assessments typically examine individual hazards only (Ward et al., 2022). When interactions are recorded, this usually refers to spatial overlaps, although these overlaps are not required for an interaction of hazards to occur (Lee et al., 2024).

In insurance practice, catastrophe models use distinct methodologies depending on the hazard (or 'peril', in insurance language). The underlying key assumption is an independence of hazards, that is, hazards not being related with each other and not triggered by other hazards (primary hazards). Therefore, catastrophe models in the insurance industry usually assess hazards independently even in state-of-the-art models (Mitchell-Wallace et al., 2017). Increasingly, temporal and spatial hazard patterns within single hazard types get included in catastrophe models (e. g., Mitchell-Wallace et al., 2017). If several hazards are taken into account, they are commonly included in the form of secondary perils, that is, as a consequence of a primary peril (e. g., coastal surges produced by windstorms; Hillier et al., 2015). What is often not considered is the potential time delay between primary and secondary perils (e. g., earthquakes enhancing the landslide susceptibility), cascading impacts due to inter-dependencies in impacts, the potential dependence between primary perils, such as flood and storm events, or indirect effects by supply chain mechanisms, for example. Note, however, that the term *secondary peril* can also refer to small to medium perils in the insurance context (e. g., Swiss Re, 2021).

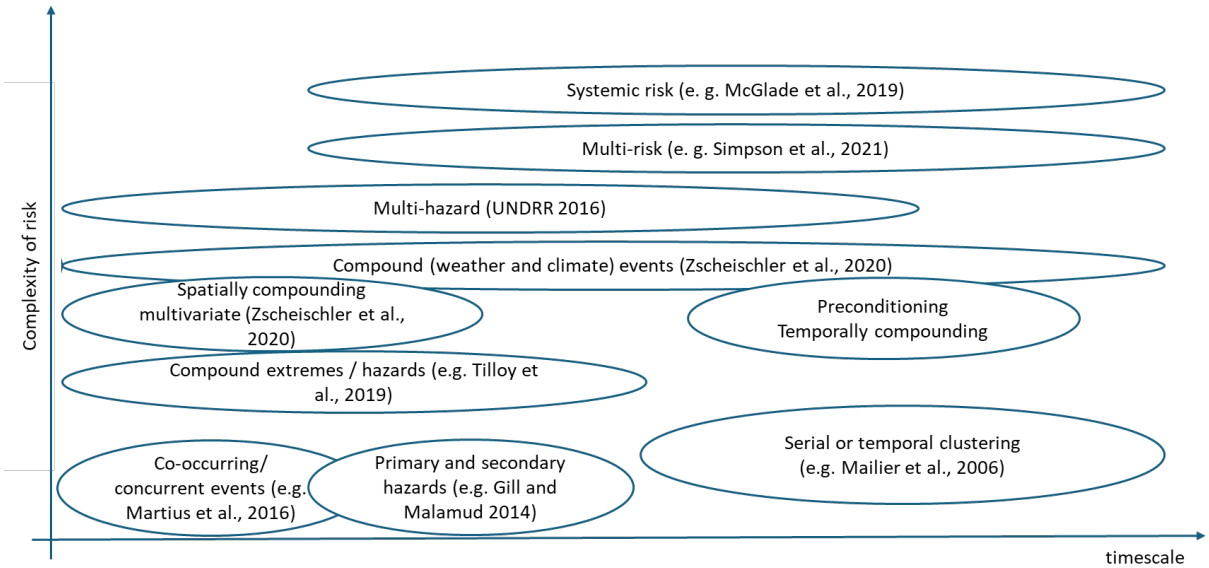

Figure 2.15.: Overview on the main hazard interaction terminology used in literature. The complexity of risk is shown on the x-axis, relating to the number of hazards or hazard types considered or the scope of hazard (natural vs. anthropogenic hazards). The y-axis points to the timescale of hazard interactions, from short timescales (that is, co-occurrence), to longer timescales, where hazards can be separated by, for example, weeks or even months.

Terminology and timescales: Compound and multi-hazard events

As seen in Figure 2.1, meteorological phenomena and meteorological hazards occur on a large range of spatial and temporal scales. Nevertheless, they partly can be related to each other. There is a variety of terminology describing those hazard interrelations. Figure 2.15 depicts the timescales of some of their most common applications. The interactions between hazards can be explored in various ways:

- Compound weather and climate events with a common distinction into four types: preconditioning, multivariate, temporally and spatially compounding (Zscheischler et al., 2020)
- Interactions between hazards with various interrelation classifications (Gill and Malamud, 2016; Tilloy et al., 2019; Simpson et al., 2021; Angeli et al., 2022), summarized, for example, using three categories: Triggering or cascading (one hazard causing another hazard to occur), amplifying (one hazard changing the likelihood or magnitude of another hazard) or compound relationships, which refers to two or more hazards affecting the same region and/or time period with impacts different than their sum (Gill et al., 2022)
- Primary and secondary hazards (Gill and Malamud, 2014; Hillier et al., 2015; Lee et al., 2024): Assuming simultaneous/cascading occurrence, primary hazards refer to hazards seen as unrelated to and not triggered by other hazards, as opposed to secondary hazards (Hillier et al., 2015), commonly used in insurance modelling.
- Temporal or spatial clustering of hazards: Hazard occurrence as such is viewed independently, but interrelationships can be found through analyses of clustering (see Sect. 4.5)

In our work, dependencies between different hazards are analyzed with respect to their temporal clustering (Chapter 6).

From multi-hazard to multi-risk

For risk assessment purposes, a multi-hazard approach is essential to capture a variety of risks. However, a holistic perspective is only possible when taking a multi-risk or systemic risk perspective. In the context of natural hazards in science and the insurance sector, risk is usually defined as the interplay between hazard, exposure and vulnerability (e. g., Zscheischler et al., 2018), where sometimes vulnerability is divided by capacity (Gill et al., 2022). However, these components are dynamic and interrelated, making risk assessments arising from natural hazards more complex. This complexity can be captured e. g., by including a time or response component to define dynamic risk and by taking into account dependencies between risk components and their drivers, as well as interactions between risks (e. g., Simpson et al., 2021). One type of complex risk is multi-risk, which refers to the risk from several hazards and the interrelationships between hazards and vulnerability (Simpson et al., 2021; Gill et al., 2022). The definitions of multi-hazard risk and multi-risk terms are largely ambiguous in the literature (e. g., Simpson et al., 2021).

2.3 Large-scale atmospheric circulation

As potential triggers of hydro-meteorological hazards are discussed within this work (see Chapter 7), large-scale atmospheric circulation patterns are introduced here. As seen in Sect. 2.1, atmospheric phenomena can occur on a range of timescales. This is because the atmospheric circulation exhibits substantial variability, which can last from the timescale of days (e. g., timescale of an ETC), over a few weeks, to a few months but also up to several years or even centuries, which would then characterize long-term climate change (CPC, 2008b). To allow for in-depth comparative analysis, this variability in the large-scale atmospheric circulation can be captured by a comparatively small number of states, such as teleconnection patterns described with indices (e. g., Barnston and Livezey, 1987), or weather regimes, where the large-scale configuration is categorized into typical recurring patterns (e. g., Michelangeli et al., 1995).

Teleconnection patterns are persistent, recurring large-scale patterns of pressure and circulation anomalies spanning vast geographical areas (Barnston and Livezey, 1987; CPC, 2008b). They typically last for several weeks to several months, but can also be dominant throughout several consecutive years. Therefore, they reflect the interannual and decadal variability of the atmospheric circulation. Many teleconnection patterns cover a planetary scale, often extending across entire continent or hemispheres. While some patterns span the entire North Pacific, others stretch from eastern North America to central Europe, for example (CPC, 2008b). These patterns are natural features of our chaotic atmospheric system, primarily emerging from internal atmospheric dynamics, and representing large-scale shifts in atmospheric wave structures and the jet stream (Barnston and Livezey, 1987).

Another way to capture specifically intra-seasonal variability of the atmosphere are so-called weather regimes. Weather regimes describe persistent, recurring and quasi-stationary circulation states aiming to reflect atmospheric variability over large geographic areas (e. g., Michelangeli et al., 1995). Many definitions of weather regimes exist, depending on the geographic area, time period, season and method used (e. g., Hannachi et al., 2017). Most of them are based on cluster analysis (e. g., Michelangeli et al., 1995) or Empirical Orthogonal Function (EOF) of geopotential height anomalies or Mean Sea Level Pressure (MSLP) (e. g., Grams et al., 2017). While a classification of four regimes is most commonly used in the North Atlantic-European region (e. g., Cassou, 2008) and many regime definitions cover a distinct season, a year-round regime definition was introduced for the North Atlantic-European region by Grams et al. (2017) and has been applied by many studies since (e. g., Barton et al., 2022; Hauser et al., 2023a).

Teleconnections exert widespread influence on temperature, precipitation, storm tracks, and the position and strength of the jet stream across vast regions (Hurrell, 1995). Both teleconnection patterns and weather regimes in Europe have been also shown to be connected to extreme weather events, such as windstorms (e. g., Donat et al., 2010; Priestley et al., 2017; Dacre and Pinto, 2020), heavy precipitation

(Villarini et al., 2011; Barton et al., 2022) and flooding (e. g., Zanardo et al., 2019), as well as convective extremes (e. g., Mohr et al., 2019; Piper et al., 2019; Augenstein, 2025). The influence of the large-scale circulation on these surface extremes is discussed in detail in Chapter 7. In addition, large-scale circulation patterns can also be related to other extremes, such as heatwave and drought events, as well as cold spells (e. g., Kautz et al., 2022).

Data used for the geopotential height anomalies, teleconnection patterns as well as weather regimes are introduced in Chapter 3. While teleconnection patterns used in this thesis have a monthly temporal resolution, the weather regimes data have a temporal resolution of 6 h. The weather regimes cover the North Atlantic and Europe, while teleconnection patterns have a broader spatial extent of the northern hemisphere.

2.4 Statistics

2.4.1 Parametric probability distributions

Parametric probability distributions are abstract mathematical forms that summarize data to represent variations in it (Wilks, 2006). A classic example of a parametric distribution is the Gaussian distribution, also called normal distribution, with a characteristic shape of a symmetric bell. Discrete probability distributions refer to random quantities that can only take on particular values, that is, finite or countably infinite values, whereas continuous probability distributions can take on any number within an infinite set (of a specific range) of real numbers. The specific nature of a parametric distribution is determined by its parameters, that is, particular values for its defining variables. Discrete parametric distributions include, among others, the binomial and negative binomial distribution, the geometric distribution, and the Poisson distribution (Wilks, 2006).

Poisson distribution

The Poisson distribution is a parametric discrete probability distribution that describes the number of discrete events in a series. Although it can be applied in space (e. g., the distribution of hailstones in a small area), this series is most commonly a timeseries, in which the counts represent discrete events. These events are assumed to be independent; this is a crucial concept for the assessment of clustering in this work. The rate of occurrence λ is the main parameter of the Poisson distribution, and for a given λ, the probability of particular counts depends uniquely on the size of the interval (usually the length of the timeseries). The rate of occurrence is independent of the number in other (non-overlapping) intervals, and of the specific timing of events within an interval. Therefore, events in a Poisson distribution are assumed to occur randomly, but with a constant average rate of occurrence. A sequence of such events is also referred to as a Poisson process. Of course, atmospheric phenomena do not strictly satisfy the

independence condition (or cannot be shown to do so), but Poisson distributions can serve as useful representations, when a low degree of dependence is assumed. This is given when the probability of simultaneous occurrence is very small. The probability mass function of the Poisson distribution links counts or number of occurrences x with their respective probability and is given by:

$$f(x) = \frac{e^{-\lambda}\lambda^{x}}{x!}, \quad x \in \Omega = \{0,1,2,\dots\} \tag{2.20}$$

with $\lambda > 0$. As shown by the probability mass function, the probability distribution depends on a single parameter only, the rate of occurrence λ, which is also called the Poisson parameter or intensity with the dimension of occurrence per time. The sample space of a Poisson process contains an infinite number of (counted) events. The Poisson distribution is fundamental to model the occurrence of randomly occurring events in time: With given λ and for independent events, the number of events occurring in a unit time interval is Poisson distributed with parameter λ (e. g., Coles, 2001):

$$E(X) = Var(X) = \lambda. \tag{2.21}$$

Eq. 2.21 shows that the expected value (E) of the Poisson distribution is equal to the variance (Var) in the distribution (equidispersion), which is described by λ. A deviation from a Poisson process may manifest, for example, as a variance that exceeds the mean (see Sect. 2.4.3).

The Poisson distribution is applied by fitting it to a sample of data. This involves finding the most suitable parameter λ for a given data set. This parameter can be easily estimated for Poisson distributions using the sample average of occurrences within a given time series (method of moments; Wilks, 2006).

Extreme-value distributions

Extreme-value theory is a probabilistic concept on the asymptotic behavior of extreme values. The extremal types theorem states that the largest of *m* independent observations from a fixed distribution will increasingly approximate a known distribution as *m* increases, regardless of the single distributions from which the observations originate. These known extreme value distributions are called Gumbel, Fréchet, and Weibull. They are generalized by the Generalized Extreme Value Distribution (GEV), described by the Cumulative Distribution Function (CDF)

$$G(z) = \exp\left\{-\left[1+\xi\left(\frac{z-\mu}{\sigma}\right)\right]^{-\frac{1}{\xi}}\right\}, \tag{2.22}$$

which has three fitted parameters: A location parameter μ ($-\infty < \mu < \infty$), where the distribution is centered; a scale parameter $\beta > 0$, which shows the spread in the distribution, and a shape parameter ξ

($-\infty < \xi < \infty$), showing the behavior of the distribution tail. These parameters are commonly estimated by the method of maximum likelihood (Wilks, 2006).

The three distribution families can be distinguished by the shape parameter ξ. The Gumbel distribution is frequently used to fit extreme data with exponential-type tails (e. g., Gaussian or gamma) follows for $\xi = 0$:

$$G(z) = \exp\left\{-\exp\left[-\left(\frac{z-\mu}{\beta}\right)\right]\right\}. \tag{2.23}$$

The Weibull distribution is defined by a bounded upper tail and a negative shape parameter ($\xi < 0$), whereas the Fréchet family is described by a heavy upper tail, with a positive shape parameter ($\xi > 0$). The GEV can be used to model the maxima of longer sequences, or, in other words, block maxima (see below) can be fitted to the GEV distribution. This is frequently applied to the statistical analysis of timeseries.

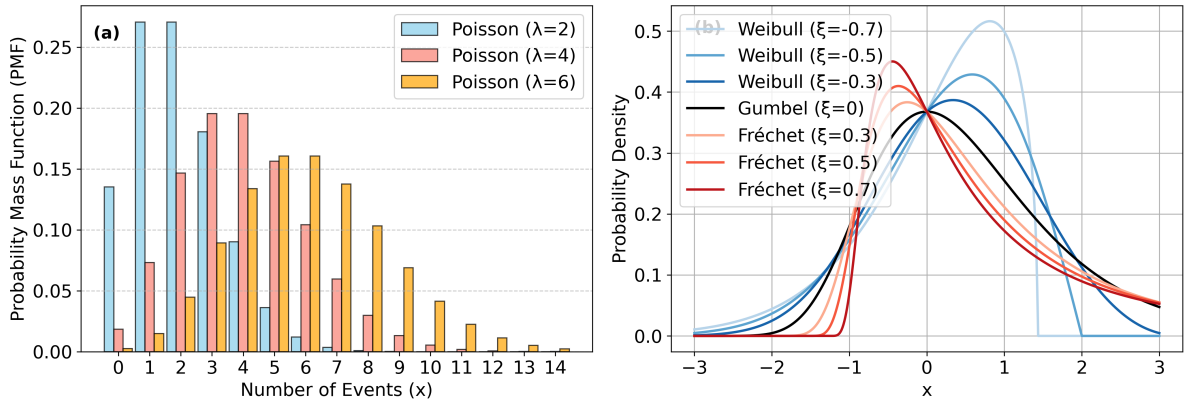

Figure 2.16.: (a) Sample Poisson distribution functions for different values of parameter λ. (b) General Extreme Value (GEV) distribution functions depending on the shape parameter ξ with distinct distributions for the families Weibull ($\xi < 0$), Gumbel ($\xi = 0$) and Fréchet ($\xi > 0$).

An inversion of Eq. 2.22 yields estimates of extreme quantiles of the annual maximum distribution:

$$z_p = \begin{cases} \mu + \dfrac{\beta}{\xi}\left((-\ln(p))^{-\xi} - 1\right), & \text{for } \xi \neq 0 \\ \mu - \beta\ln(1-\ln(1-p)), & \text{for } \xi = 0 \end{cases} \tag{2.24}$$

where $G(z) = 1 - p$. This yields the return level z_p with return period $1/p$. The level z_p is expected to be exceeded by the annual maximum in any particular year with the probability $1/p$, that is, on average every $1/p$ years. Return levels and return periods are commonly used to estimate the severity as a function of the probability of natural hazards. The return period is typically interpreted as the average time between the occurrence of two events of the same or higher magnitude (Wilks, 2006). Return periods with respect to clustered extremes will be examined in Sect. 6.3.2.

Two approaches: Block Maxima vs. Peaks over Threshold

A requirement for the use of the Poisson distribution, as well as for the application of extreme-value statistics, are independent events (e. g., Wilks, 2006). These can be modeled with two classical approaches, (1) block maxima and (2) the Peaks-Over-Threshold (POT) method. With block maxima, data are 'blocked' into sequences of observations of a specific length (see Fig. 2.17a); these blocks are usually considered independent (Coles, 2001). This length is often a year, for example, annual records of maximum sea levels. Block maxima can be fitted with the GEV distribution (Eq. 2.22). The second approach, the POT method, develops from threshold excess models, which become appropriate for modeling the extremes of data with a complete time series (for example, a daily temporal resolution). It is often applied in catastrophe models of insurances (Mitchell-Wallace et al., 2017). With the POT method, the largest n values, that is, values above threshold u, are chosen regardless of their blocks (for example, their year of occurrence, see Fig. 2.17b). Exceedances of this threshold can have a tendency to occur in groups with atmospheric data, which cluster on the temporal scale of synoptic systems. For example, an extreme cold day is likely to be followed by another, suggesting potentially strong dependence (Coles, 2001). Threshold excesses can be fitted with the Generalized Pareto Distribution (GPD), which is a variation of the Pareto distribution (Coles, 2001). The GPD has the following CDF (Coles, 2001):

$$H(x) = P(X < x | X > u) = 1 - \left(1 + \frac{\zeta(x-\mu)}{\beta}\right)^{-1/\xi} \quad \text{with} \quad \begin{cases} x > 0, & \text{when } \xi > 0, \\ x \in \left[0, -\frac{\beta}{\gamma}\right), & \text{when } \xi < 0. \end{cases} \tag{2.25}$$

with threshold u. Both the shape and scale parameters depend on u when modeling POT. In this work, the POT method is used to identify distinct events (alongside another method common in the insurance industry, see Sect. 4.2). The POT method is suitable, as clusters of events within a time series can only be investigated when looking at the complete time series instead of regular maxima.

The most widely adopted method to address dependence of events is declustering (see Sect. 4), which corresponds to the filtering of the (dependent) timeseries to obtain a set of approximately independent threshold excesses (Coles, 2001).

2.4.2 Poisson point processes

The extreme value behavior of a process can be modeled with a point process, which is a stochastic rule for the occurrence and position of point events on a set $\mathscr{A}$ (often a period of time). This allows to calculate the probability of a certain event within a specified period or the expected waiting time until the next event, given one event. A set of non-negative integer-valued random variables $N(A)$ for each $A \subset \mathscr{A}$

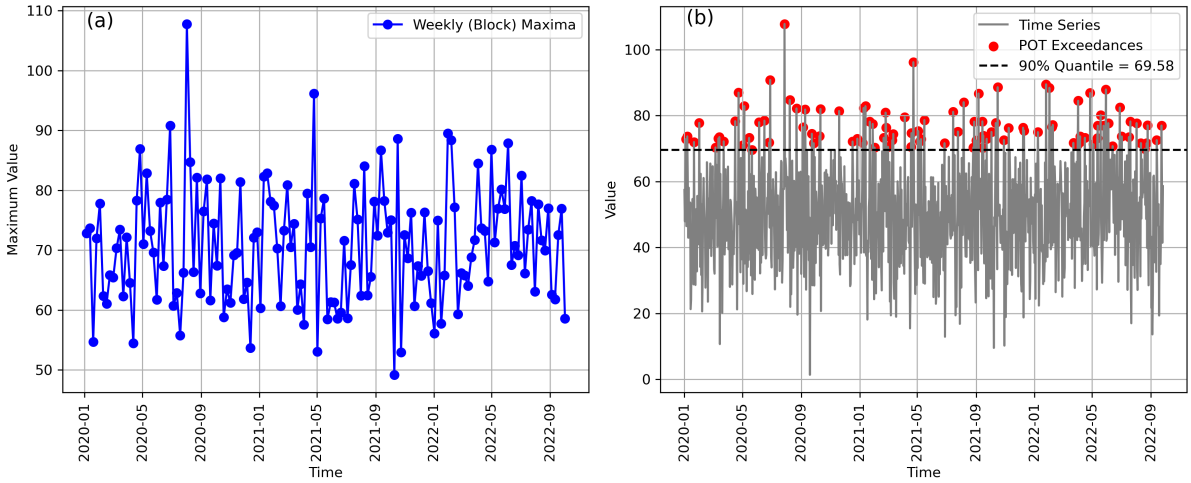

Figure 2.17.: (a) Block maxima method, applied here to a sample time series with a weekly resolution (weekly maxima). (b) Peaks-Over-Threshold (POT) method for a daily sample time, but with a threshold at the 90th quantile (90p). Values above 90p are selected (marked in red).

refers to the number of points in the set A. The probability distribution of each of the $N(A)$ determines the point process (N) characteristics. The intensity (Λ) of the point process is measured by

$$\Lambda(A) = E\{N(A)\}, \tag{2.26}$$

whose derivative function, assuming $A = [a_1, x_1] \times \cdots \times [a_k, x_k] \subset \mathbb{R}^k$, is

$$\lambda(\mathbf{x}) = \frac{\partial \Lambda(A)}{\partial x_1 \cdots \partial x_k}, \tag{2.27}$$

also called the intensity (density) function of the point process.

The standard point process is the one-dimensional homogeneous Poisson process (Cox and Isham, 1980). This is a process on $A \subset \mathbb{R}$ with parameter $\lambda > 0$, which satisfies

$$N(A) \sim \text{Poi}(\lambda(t_2 - t_1)) \tag{2.28}$$

for all $A = [t_1, t_2] \subset A$, and for all non-overlapping subsets A and B of $\mathscr{A}$, where $N(A)$ and $N(B)$ are independent random variables (Coles, 2001). This means that events (points) in a given time interval follow a Poisson distribution ('Poi'), where the mean is proportional to the length of the time interval, and the number of events in separate intervals is mutually independent. Therefore, the Poisson process with parameter λ is shown to be the appropriate stochastic model for points occurring randomly in time at a uniform rate of λ per unit time interval. The intensity measure is then described by $\lambda([t_1, t_2]) = \lambda(t_2 - t_1)$, and the intensity density function can be described by $\lambda(t) = \lambda$.

The homogeneous Poisson process (Fig. 2.18a) is often used to describe complete serial randomness, which means that the occurrence of a particular event is entirely independent of the occurrence of another event before or after, that is, events happen completely due to chance. This serial randomness is described by the simple homogeneous Poisson process, which is a one-dimensional process with a constant intensity λ. Although the number of events can vary throughout the process (see Fig. 2.18a), this is not a result of variations in the rate λ, but occurs by chance. With a constant rate λ, the number of events $N_{t_1} - N_{t_0}$ occurring in any time interval $\Delta t = t_2 - t_1$ are Poisson distributed with variance and mean $\mu = \lambda \Delta t$.

An inhomogeneous Poisson process (Fig. 2.18b) has the same properties for independent counts on non-overlapping subsets as the homogeneous one, but is described by

$$N(A) \sim \text{Poi}(\Lambda(A)) \tag{2.29}$$

for $A = [t_1, t_2] \subset \mathscr{A}$, where

$$\Lambda(A) = \int_{t_1}^{t_2} \lambda(t) dt. \tag{2.30}$$

The rate λ is therefore variable with a non-homogeneous Poisson process (see Fig. 2.18b). The counts of an inhomogeneous one-dimensional Poisson process can be modeled using Poisson regression, which is a class of a Generalized Linear Model (see e. g., Mailier et al. (2006)).

Lastly, a regular process (Fig. 2.18c) is characterized by (more) equal inter-arrival times compared to a simple homogeneous Poisson process, where an extreme example is the ticking of a clock (Mailier, 2007).

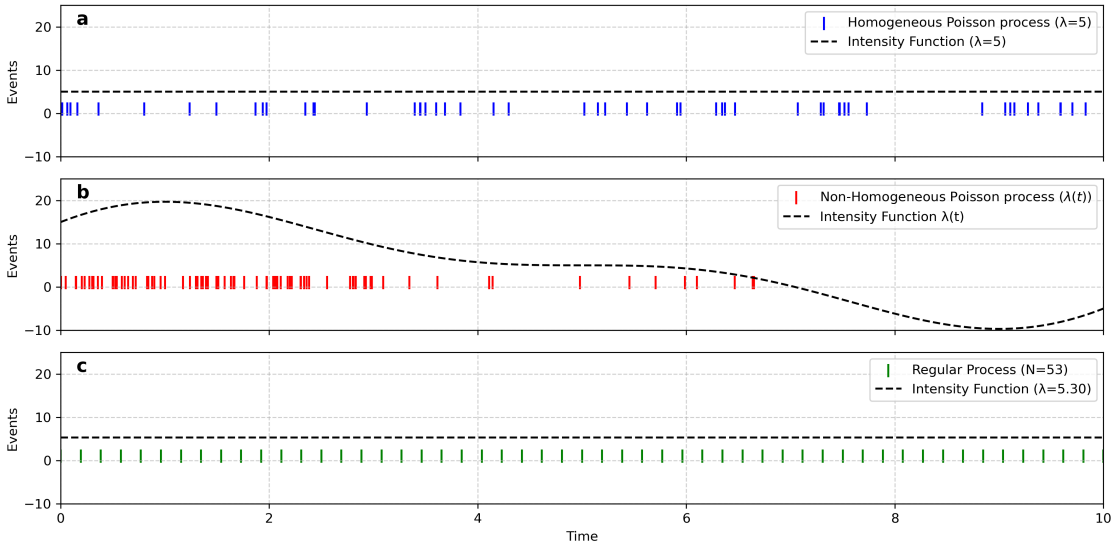

Figure 2.18.: Poisson point processes with (a) a homogeneous intensity λ and (b) a time-varying intensity λ. (c) shows a regular (underdispersed) Poisson process with a uniform rate of occurrence, created after Mailier (2007).

2.4.3 Detection of clustering

Poisson processes are intrinsically described by the independence of their points. This 'memoryless' property (Vitolo et al., 2009) allows their use as a measure of serial clustering, that is, the serial dependency between events (Mailier, 2007). Research on serial clustering of meteorological events was prompted by two series of windstorm events in 1990 (*Vivian* and *Wiebke*) and 1999 (*Lothar* and *Martin*). Various methods are used in this work to identify clustering, including an absolute frequency metric, a statistical tool, and impact methods. These methods are introduced in Sect. 4.5. Serial clustering, which is also called temporal clustering in this work, is investigated with respect to single and multiple hazards in Chapter 6.

3. Data

This chapter gives an overview of the datasets used within this thesis. The primary data source for extreme event identification is insurance loss data, which is presented first (Sect. 3.1). This is followed by a description of meteorological observation data used to categorize events into more accurate meteorological types (Sect. 3.2). Lastly, data used to investigate the relationship of extreme events and clusters with atmospheric circulation patterns are presented: ERA5 reanalysis (Sect. 3.3), teleconnection indices (Sect. 3.4) and weather regimes (Sect. 3.5).

The study area of this work is split into two regions: (1) BW, and (2) GER as a whole (see Fig. 3.1a). BW is a federal state in southwestern Germany with a size of approximately 36 000 km^2. Geographically, BW is structured with the broad Rhine valley to the west and the Neckar valley in the center, and the low mountain ranges of Black Forest and Swabian Jura from southwest to northeast. GER has a size of about 357 000 km^2 and a strong gradient in elevation from south to north, which borders to the North Sea and the Baltic Sea. The highest mountain ranges are the Bavarian Alps in the south, with further lower mountain ranges being the Bavarian Forest, the Ore mountains in the east, the Harz in the center, and the Eifel in the west of Germany.

This twofold focus makes effective use of comprehensive insurance loss data available and allows to look at differences in the impact at different spatial scales. While other types of impact data on extreme events are scarce and often not recorded in a consistent and comprehensive way, insurance loss data often constitute a reliable data source.

3.1 Insurance loss data

Insurance loss data are commonly used to assess impacts of extreme weather events or other natural hazards (e. g., Hillier et al., 2015), due to the frequent lack of uniform observation data. Given a high insurance coverage, insurance loss data capture the financial impacts of extreme events. In addition, they provide a relatively homogeneous, objective and reliable data source, in comparison to impact datasets collected by hand. Accordingly, in this work, hydro-meteorological extreme events from various hazards resulting in significant financial losses are identified through the analysis of insurance loss data. However, it needs to be noted that insurance loss data also come with uncertainties and caveats: They are typically biased towards regions with high insurance densities (urban areas, but also larger areas such as states, see below). This can also be dependent on the hazards, since they might be included in different insurance

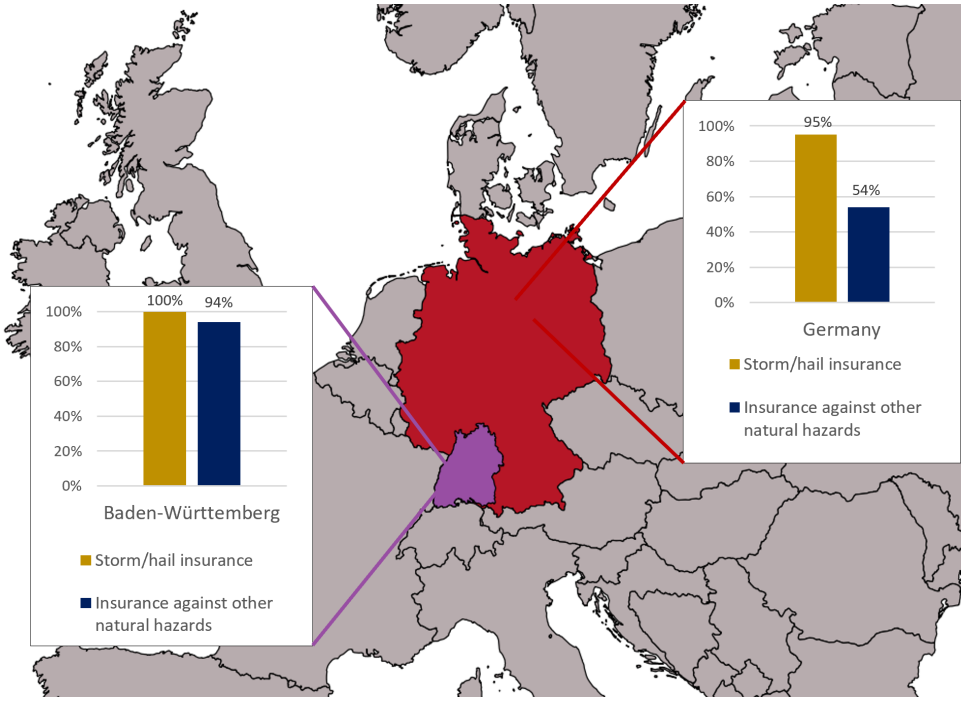

Figure 3.1.: Study areas and corresponding insurance density [%] against natural hazards as of 2023 (preliminary), based on GDV (2024b).

types. Temporal biases can also exist, for example on the scale of months, as the exact date of occurrence can not always be determined (see also Sect. 5). With regard to decadal variability, trends can be present in the data, for example due to economic developments, changes in exposure and in the hazard due to climate change (see Sect. 5.4).

Residential building insurance in Germany

In Germany, residential buildings can be insured against fire, lightning strikes, overvoltage caused by lightning, explosion, deflagration, implosion, impact or crash of an aircraft, vehicle impact, scorch damage, smoke and soot damage; piped water damage; and natural hazards (GDV, 2023). Natural hazards in this case include two categories: storm and hail as well as other natural hazards. Other natural hazards (in German also: *Elementargefahren*) include flooding, earthquakes, backwater, landslides, subsidence, snow pressure, avalanches and volcanic eruptions. The German Insurance Association *Gesamtverband der Deutschen Versicherungswirtschaft e. V.*, hereinafter GDV, defines storm and hail damage as follows: A storm is a weather-related air motion of at least wind force 8 on the Beaufort scale (wind speed of at least $62\,\mathrm{km\,h^{-1}}$). Hail is defined as solid precipitation in the form of ice grains (GDV, 2023).

The standard residential building insurance in Germany includes storm and hail damage, but for other natural hazards, an additional insurance component is required (in German: *Elementarschadenversicherung*). An increasing share of insurance companies offers this additional component (GDV, 2024b).

Table 3.1.: Overview of the datasets used; abbreviations are introduced in the main text.

Data type	**Dataset/Study area**	**Hazard type(s)**	**Resolution (spatial/ temporal)**
Loss data	State-wide insured losses and claims (Baden-Württemberg, SV, 1986–2023)	Storm, hail, flood	Federal state / daily
Loss data	Germany-wide insured losses and claims (GDV, 1997 – 2022 (storm/hail), 2002–2022 (other natural hazards))	Storm/hail; other natural hazards	Districts (Landkreise) / daily
Observation data	Atmospheric pressure gradients (synoptic stations from the Climate Data Center (CDC)/DWD)	Synoptic storms and convective gusts	Station-based / hourly
Observation data	Precipitation totals (HYRAS-DE-PR/DWD)	Fluvial, pluvial and mixed floods	Gridded / daily
Observation data	Cloud-to-ground lightning, European Cooperation for Lightning Detection (EUCLID)	Fluvial, pluvial and mixed floods	Gridded $(1 \times 1\ \mathrm{km}^2)$ / daily
Observation data	Severe hail reports (ESWD)	Hail	Reports (point data) / Daily
Reanalysis data	ECMWF Reanalysis 5 (ERA5) (ECMWF)	All	Gridded $(0.25^\circ \times 0.25^\circ)$ / three-hourly
Climate modes	Teleconnections: North Atlantic Oscillation (NAO), East Atlantic Patterns (EA), Scandinavian Pattern (SCAND), NOAA	All	Northern Hemisphere / monthly
Climate modes	Euro-Atlantic weather regimes	All	Northern Hemisphere / six-hourly

Insurance density across Germany

The density of the standard residential building insurance, including the hazards storm and hail, is estimated to be on average 95 % across Germany as of 2022 (see Fig. 3.1a, GDV (2024b)). The lowest density regarding storm and hail is found in Bavaria (88 %), followed by Rheinland-Pfalz and Hesse (91 % and 92 % respectively). In other federal states, the insurance density regarding storm and hail is 97 % or higher (GDV, 2024b).

As of 2023, on average, 54 % of buildings were insured against other natural hazards in Germany (GDV, 2024b). This proportion has increased significantly in recent decades. For example, in 2002 only 18.6 % of all buildings were insured against other natural hazards (GDV, 2023a). Differences between federal states are large, as published annually by the GDV (see Fig. 3.1b). By far the highest insurance density against other natural hazards exists in BW: While in BW 94 % of all residential buildings are insured

against other natural hazards, in many other federal states the coverage is less than 50 %. This high discrepancy between the federal states has historic reasons: In BW, from 1960 to 1994, an insurance obligation required building owners to insure against other natural hazards. This obligation was abolished in 1994 due to a guideline introduced by the European Union (Deutscher Bundestag - Wissenschaftliche Dienste, 2021).

In this work, two insurance loss datasets are employed, with one focusing on Baden-Württemberg (BW, Sect. 3.1.1) and another covering Germany as a whole (Sect. 3.1.2), but for a shorter time period (see below and Table 3.1). Both datasets include residential building losses (with deductible subtracted) and the number of claims with a daily temporal resolution, as well as some metrics to determine the coverage, such as the annual number of contracts or the sum insured.

3.1.1 Insurance loss data for Baden-Württemberg

For BW, data were provided from the *SV SparkassenVersicherung* for the time period between 1986 and 2023, covering about 70 % of residential buildings as of 2022 (pers. comm. SV 2022). The insurance loss data have a daily temporal resolution and were made available in an aggregated way for the whole portfolio of the insurance company, which includes Baden-Württemberg, Hesse and Thuringia.

Buildings can be insured against storm/hail and other natural hazards. However, the insurer (more specifically, the regulator, who is responsible for settling and adjusting insurance claims) categorizes the data into storm, hail and flood damage. Additionally, the number of contracts were made available from 1986 to 2023 (see Fig. 3.2). All contracts until 1994 include both insurance types (see above). An internal change in the system caused reliable data on the number of contracts regarding both insurance types to become available again in 2010. In Germany, hail occurs rarely between September and April, since convective systems mainly develop during the summer months (Kunz, 2007; Mohr et al., 2017). Therefore, hail damage is only considered between April and September. All other perils are considered for the entire year, although they also follow strong seasonal patterns (see Chapter 5).

An overview of the timeseries regarding the insurance loss data for BW is displayed in Figure 3.2a. Most remarkably, insured losses of certain events exceed those of others by far, such as a storm event in 1999 and a hail event in 2013 (see Chapter 5 for a detailed discussion). In general, the frequency of each category is quite similar, while storm and hail events are associated with higher losses. It is also visible that the frequency of significant losses in the second half of the time period exceed those of the early years, which can partly be attributed to economic developments (see Chapter 5) and that events occur with high decadal variability.

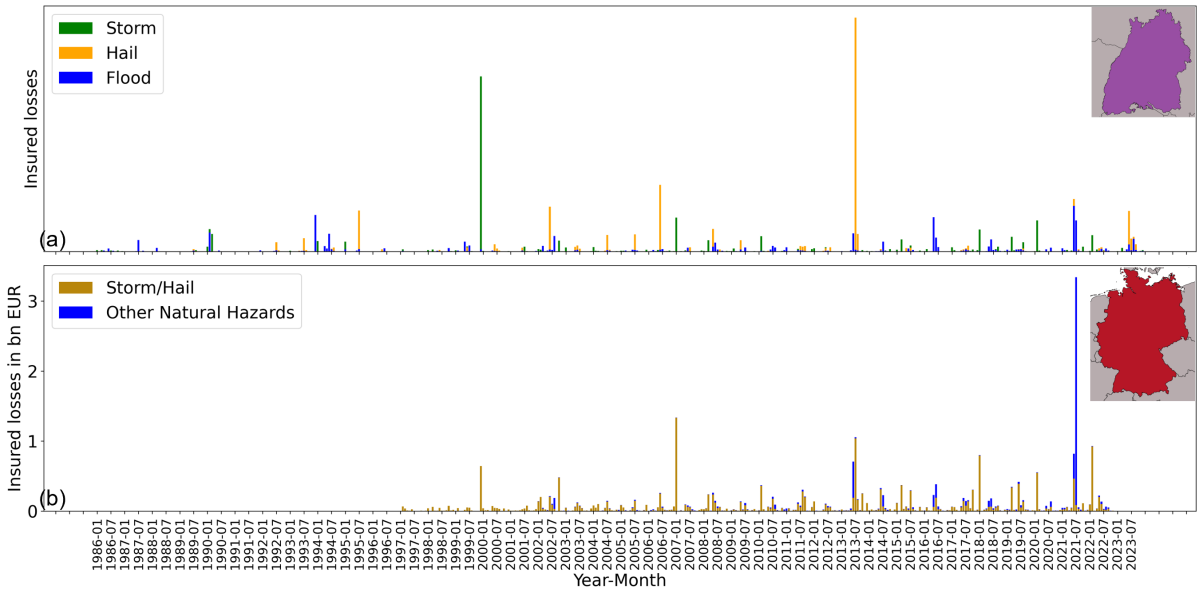

Figure 3.2.: Timeseries of the insured losses (a) regarding BW (scale omitted for confidentiality reasons) and (b) GER (in billion EUR) depending on the hazard type as recorded by the insurance company or association. For a detailed analysis including the naming of major events, see Chapter 5.

3.1.2 Insurance loss data for Germany

Residential building loss data covering Germany were made available from the GDV on the level of districts (*Landkreise*) and for two distinct categories: Data on the standard insurance contracts covering storm and hail were available from 1997 to 2022 and data regarding the insurance against other natural hazards were available from 2002 to 2022 (see Table 3.1). An overview regarding the timeseries for the insurance loss data for GER is shown in Figure 3.2b. As in Figure 3.2a, single events stand out. The dominating event in the study area of GER is the flood event in July 2021, with secondary peaks with two storm/hail in 2007 and 2013. In general, however, storm/hail events lead to significant losses more frequently. Furthermore, the number of events gradually increases throughout the timeseries.

3.1.3 Temporal variability

There is a high annual variability in the portfolio of SV SparkassenVersicherung and within the members of the GDV (see Fig. 3.3). Overall in Germany, there has been a continuous increase in both the sum insured as well as the number of contracts since 1997, with an especially steep increase of the sum insured in recent years. In contrast, for BW, there has been an almost continuous decline in the number of contracts. Again, this contradictory development is due to the abolition of the insurance obligation in 1994 and the use of data from one insurance company (BW) vs. a comprehensive dataset including about 95 % of insurance companies in Germany (pers. comm. GDV 2024).

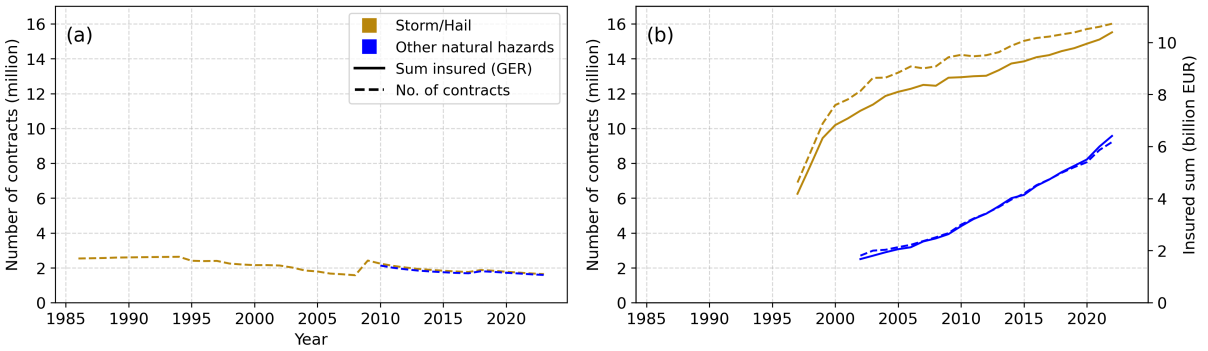

Figure 3.3.: Timeseries of the portfolio of study areas (a) Baden-Württemberg (BW) and (b) Germany (GER). Metrics are the number of contracts in millions (dashed line) and the sum insured in billion EUR (only available for GER, solid line) per hazard type. Regarding BW, the number of contracts by type of insurance are only available from 2010. Until 1994, all contracts include both storm and hail as well as other natural hazards due to the insurance obligation.

3.2 Meteorological observation data

The individual definitions of the three hazard types in the loss data (flood, storm and hail and storm/hail and other natural hazards, respectively) are not unambiguous. For example, the storm(/hail) category includes both winter storms and convective gusts. Given the different environmental conditions, which also lead to different temporal and spatial scales of the respective events, a further separation of the storm and flood categories according to their main characteristics was necessary (see Sect. 4.3). For this subdivision, meteorological observation data from the DWD as well as lightning data and severe weather reports were used.

3.2.1 Hydrometeorological raster data

The data most appropriate for a separation between precipitation-related hazards would be vertical velocities, cloud observations, or, most often used, radar data (maximum reflectivity). However, none of these data were available for a sufficient time period (starting from 1986), and with an adequate temporal resolution (1 day). Therefore, daily precipitation totals were used here from the *Hydrometeorologischer Rasterdatensatz Niederschlag für Deutschland* (HYRAS-DE-PR) dataset. HYRAS-DE-PR consists of station-based regionalized daily precipitation totals for Germany interpolated to the almost equidistant $1 \times 1\,\mathrm{km}^2$ grid of the *Regionalisierung der Niederschlagshöhen* (REGNIE) product (Rauthe et al., 2013).

Daily precipitation sums were interpolated from daily precipitation data observed at around 2,000 stations of the DWD (RR product, 6 UTC - 6 UTC of the following day). The spatial distribution of these daily precipitation sums is used to differentiate between precpitation types for BW (see Sect. 4.3.1).

3.2.2 Lightning data

Lightning data from the European Cooperation for Lightning Detection (EUCLID), which has been collecting standardized lightning data since 2001 (Schulz and Diendorfer, 2002), were used to identify convectively dominated precipitation events for Germany (see Sect. 4.3.1). Lightning strokes are detected by a combination of two techniques, namely time-of-arrival and direction finding (Poelman and Schulz, 2020). Time-of-arrival refers to the detection of lightning strikes due to the varying times at which the electrical impulse reaches different stations. Direction finding describes the ability of the stations to measure the angle by which the stroke arrives. By this method, the stroke can be geolocalized. Information on time, location, lightning type and intensity are available in the dataset. The EUCLID data were filtered using a rectangular box defined by the outermost coordinates of Germany in all directions. Furthermore, only cloud-to-ground strokes (as opposed to, for example, cloud-to-cloud or cloud-to-air strokes) with a current of >= 10 kA were considered. The latter filtering was performed to ensure temporal homogeneity, since strokes with lower amperage are prone to false classification (Augenstein et al., 2024).

3.2.3 Weather station data

To differentiate between storm hazard types (see Sect. 4.3.2), hourly measurements of surface pressure reduced to sea level (mean sea level pressure, MSLP) at selected stations from the Climate Data Center (CDC) of the DWD (`https://www.dwd.de/EN/climate_environment/cdc/cdc_node_en.html`) were employed. Since atmospheric pressure decreases with the height of the weather stations, MSLP is required to ensure a comparability of measurements. It is calculated from the surface pressure p_0 by use of the barometric formula (DWD, 2025a):

$$p_{\overline{z}} = p_0 \exp\left(\frac{-g(z-z_0)}{R_l \overline{T}}\right),$$

with $\overline{T}$ as mean temperature between p and p_0, and R_l as the universal gas constant for dry air (mean value = 287.15 J kg^{-1} K^{-1}). The geopotential height z (in m), at which the pressure is calculated, is adjusted by subtracting the geopotential height of the reference (ground) level z_0. Thereby, the hypothetical pressure is calculated at a uniform level of z_0.

3.2.4 Severe weather reports

As hail is not measured in a homogeneous and comprehensive way in Germany, severe weather reports from the European Severe Weather Database (ESWD; Dotzek et al., 2009) were used to identify hail events (see Sect. 4.3.3). The ESWD is a database operated by the European Severe Storms Laboratory, collecting reports of extreme weather, namely dust, sand- or steam devils, gustnadoes, large hail,

heavy rain, tornadoes, severe wind gusts, heavy snowfalls/snowstorms, ice accumulations, avalanches, and damaging lightning strikes (ESWD, 2024). As the database relies on crowd-sourced reports, they undergo quality control and are assigned with four different report statuses depending on the quality control level. It has to be noted that there has been a vast increase of reports in recent decades across Europe (Groenemeijer et al., 2017) and Germany (e. g., Schmidberger, 2018). Furthermore, with crowdsourcing data, there is a bias towards daytime, populated areas and the availability of portable telecommunication devices.

For this work, reports of large hail were used, which refers to hail with a diameter of more than 2 cm (Dotzek et al., 2009). Hail above this diameter is expected to cause building damage (Stucki and Egli, 2007). To ensure a high data quality, reports without a plausibility check (QC0) were excluded. Therefore, large hail data were extracted from the ESWD for the study area Germany with at least a plausibility check (QC0+, QC1, and QC2).

3.3 ERA5 reanalysis data

To investigate the relationship of clustered extremes with the large-scale atmospheric circulation, atmospheric reanalysis data provided by the European Centre for Medium-Range Weather Forecasts (ECMWF) were used (Hersbach et al., 2020). Reanalysis data are commonly used to investigate atmospheric dynamics and are based on data assimilation, which refers to the combination of observation data with weather prediction model forecasts to achieve the most accurate representation of atmospheric conditions. The latest reanalysis dataset by ECMWF is ECMWF Reanalysis 5 (ERA5), which uses an improved ensemble for data assimilation compared to its predecessor ERA-Interim (Hersbach et al., 2020). In this thesis, three-hourly reanalysis data from 1986 to 2021 are utilized. These data have been remapped to a regular latitude-longitude grid with a horizontal resolution of 0.5°.

From ERA5, we here use two variables which help to understand the relationship between the large-scale circulation and surface weather. A proxy for the location of high and low-pressure systems is the MSLP. In addition, Geopotential height at 500 hPa (Z500) is a common variable to study atmospheric circulation patterns (e. g., Grams et al., 2017).

To identify the difference of the actual geopotential height during an event from a mean state (= anomaly), the Z500 level was compared to the climatology. The climatology was computed with a 30-day running mean (1979-–2021) centered on the respective calendar day as in, for example, Hauser et al. (2023b). For example, for an event occurring on 1 July in a certain year, the climatology consists of all values from 16 June to 16 July each from 1980 to 2021. From this climatology, the anomaly was calculated (situation at event date - climatology). Composite plots were generated, which average the synoptic situation (MSLP and Z500 level) and the climatology anomalies over all event dates analyzed.

3.4 Teleconnection indices

Given the relationship between large-scale climate modes and the occurrence of damaging extreme events (e. g., Steptoe et al., 2018), the link between single and multiple hazards and several teleconnection patterns is investigated. Data on teleconnection indices, which describe teleconnection patterns, is continuously calculated and provided by the Climate Prediction Center (CPC) of the National Oceanic and Atmospheric Administration (NOAA) and the National Weather Service of the United States of America (CPC, 2008b).

Monthly teleconnection patterns are identified by a rotated EOF (Barnston and Livezey, 1987), which isolates the primary teleconnection patterns by months and thereby allows to construct time series for all patterns. The rotated EOF technique is applied to monthly mean standardized Z500 anomalies for the region 20°–90° N from 1950 to 2000. The standardization refers to the 1950–2000 base period monthly means and standard deviations. For each calendar month, the ten leading unrotated empirical orthogonal functions are determined from the standardized monthly Z500 anomaly fields from the month itself as well as the month before and the one after. A Varimax rotation (Kaiser, 1958) then yields the ten leading rotated modes and their time series. The resulting patterns are the North Atlantic Oscillation, the Pacific/North American teleconnection pattern, the East Atlantic Pattern, the West Pacific pattern, the East Pacific–North Pacific pattern, the East Atlantic/ Western Russia pattern, the Tropical/ Northern Hemisphere pattern, the Polar-Eurasian pattern, the Scandinavia pattern, and the Pacific Transition pattern. The indices for each of these patterns are obtained from Least Squares equations and represent the combination of teleconnection patterns accounting for the most spatial variance of the observed standardized anomaly map in the month (CPC, 2008c). For our analyses, monthly values of the North Atlantic Oscillation (NAO), the East Atlantic Pattern (EA), and the Scandinavian Pattern (SCAND) are employed, as these indices cover the Northern Hemisphere and have been shown to influence European weather (e. g., Hurrell, 1995). While the general patterns are similar throughout the year for each index, they differ in their intensity depending on the season. During wintertime, the index is often stronger (see below).

A positive NAO during wintertime is characterized by a strong dipole in geopotential height anomalies, with a negative anomaly over Greenland and Iceland, and a positive anomaly over the subtropical Atlantic and the Azores, extending to western Europe (Fig. 3.4a). In July, the pattern is similar but less organized. The positive Z500 anomaly is shifted northward, towards central and northern Europe (Fig. 3.4c). Positive Z500 anomalies are often associated with above-average temperatures and precipitation over northern Europe and Scandinavia in winter, and below average precipitation in southern and central Europe. With a negative NAO, this pattern is reversed (CPC, 2008a).

The EA is similar to the NAO, but shifted southeastward in comparison. In January, positive anomalies exist in a sustained belt over western and central Europe, while negative anomalies prevail in the Central

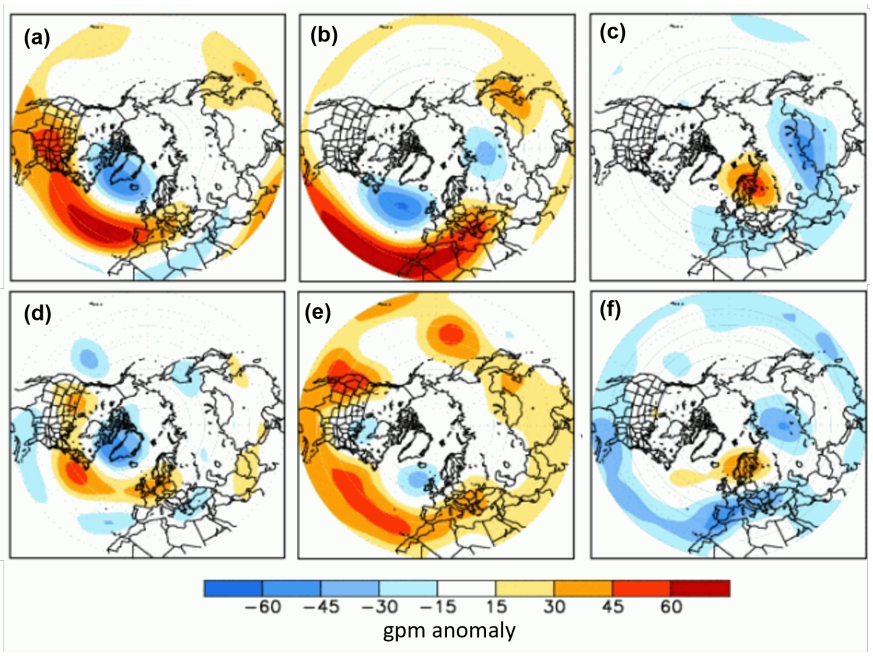

Figure 3.4.: Loading patterns (first leading mode of the rotated EOF analysis of monthly mean 500 hPa height during 1950-2000 period) for January (a–c) and July (d–f) for positive values of the NAO (a and d), EA (b and e), and SCAND (c and f). The plotted value at each grid point represents the temporal correlation between the monthly standardized height anomalies at that point and the teleconnection pattern time series valid for the specified month. Adapted from NOAA Climate Prediction Center (2005), reprinted in accordance with NWS requirements available at: `https://www.weather.gov/owlie/publication_brochures#reprint`.

North Atlantic (Fig. 3.4b). As with the NAO, the pattern is weakened in July (Fig. 3.4e). Weaker positive anomalies extend also to eastern Europe.

Regarding SCAND, there is a strong positive Z500 anomaly (ridge) over Scandinavia in January, surrounded by weaker negative Z500 anomalies in western Europe and Russia (Fig. 3.4c). In July, the ridge is weaker, with similarly negative anomalies over central and southern Europe (Fig. 3.4f).

3.5 Euro-Atlantic weather regimes

In addition, weather regimes were used to investigate the large-scale circulation with a finer temporal and spatial resolution. Based on Z500, year-round weather regimes were distinguished, originally by Grams et al. (2017) and adapted by Hauser et al. (2023b) to ERA5 data (see Sect. 3.3). They are defined over the North Atlantic–European domain (80° W–40°E, 30° –90°N), using 6-hourly data from January 1979 to December 2019 with a spatial resolution of 0.5°.

To retrieve the weather regimes, EOF analysis and k-means clustering are applied. The EOF is used in a year-round manner, as opposed to the calculation of teleconnection patterns (see Sect. 3.4). Anomalies of the 500 hPa geopotential height are calculated relative to a 90-day running mean of the climatology (1979–2019, Grams et al., 2017). After applying a 10-day low-pass filter (Duchon, 1979), which elim-

inates high-frequency fluctuations at synoptic timescales, anomalies were normalized for a year-round definition due to their seasonally varying intensities. To the seven leading EOFs, which describe 74 % of the variability, k-means clustering is applied (Hauser et al., 2023b). A weather regime is then identified as the cluster mean of one of seven clusters.

This results in a definition of seven distinct weather regimes. These include four cyclonic regimes (Zonal Regime (ZO), Scandinavian Trough (ScTr), and Atlantic Trough (AT)), and four anticyclonic regimes (Atlantic Ridge (AR), European Blocking (EuBL), and Scandinavian Blocking (ScBL)) with distinct patterns in Z500 geopotential anomalies (see Fig. 3.5). In addition to the seven regimes, a 'no-regime' category is defined, which represents a mean climatological pattern without distinct anomalies in Z500 (Grams et al., 2017).

For cyclonic regimes, negative Z500 anomalies dominate the large-scale atmospheric circulation. AT shows a strong negative Z500 anomaly west of the UK in the North Atlantic accompanied by a prevailing westerly upper-level flow across the North Atlantic-European region (Fig. 3.5a). Negative anomalies over Greenland and Iceland prevail for ZO, with a ridge over central Europe (Fig. 3.5b). The upper-level flow is westerly, with a diversion towards the north over northern Europe. ZO resembles the positive phase of the NAO (cf. Fig. 3.4a, d). ScTr is characterized by negative Z500 anomalies over Scandinavia, indicating an extensive trough spanning northern and eastern Europe (Fig. 3.5c). A weak ridge is indicated by a positive Z500 anomaly over the North Atlantic.

Since the anticyclonic regimes are dominated by positive Z500 anomalies, they are also referred to as blocked regimes. AR exhibits strong positive Z500 anomalies over the eastern North Atlantic, with a strong ridge blocking the westerly flow and causing northwesterly winds in northern and western Europe (Fig. 3.5c). EuBL is characterized by strong positive Z500 anomalies over the North Sea, implying a ridge which causes a blocking and therefore northwesterly flow over central and northern Europe (Fig. 3.5d). For ScBL, the block is shifted to the northeast compared to EuBL, with the strongest anomalies over northern Scandinavia (Fig. 3.5e). This is accompanied by negative Z500 anomalies over the eastern North Atlantic, and the upper-level flow is split into a poleward shifted flow and westerlies further south. Lastly, the Greenland Blocking (GL) shows a strong positive Z500 anomaly over Greenland, with a broad region of negative Z500 anomalies in broad regions of Europe (Fig. 3.5f).

The weather regime index I_{WR} (Michel and Rivière, 2011; Grams et al., 2017) allows to make quantitative statements regarding the similarity of a Z500 field to the seven weather regimes.

It is defined as

$$I_{WR}(t) = \frac{P_{WR}(t) - \overline{P_{WR}}}{\sqrt{\frac{1}{NT}\sum_{t=1}^{NT}\left(P_{WR}(t) - \overline{P_{WR}}\right)^2}} \tag{3.1}$$

with

$$P_{WR}(t) = \frac{\sum_{(\lambda,\varphi)\in \mathrm{EOF}} \Phi'(t,\lambda,\varphi)\,\psi_{WR}(\lambda,\varphi)\cos\varphi}{\sum_{(\lambda,\varphi)\in \mathrm{EOF}} \cos\varphi}. \tag{3.2}$$

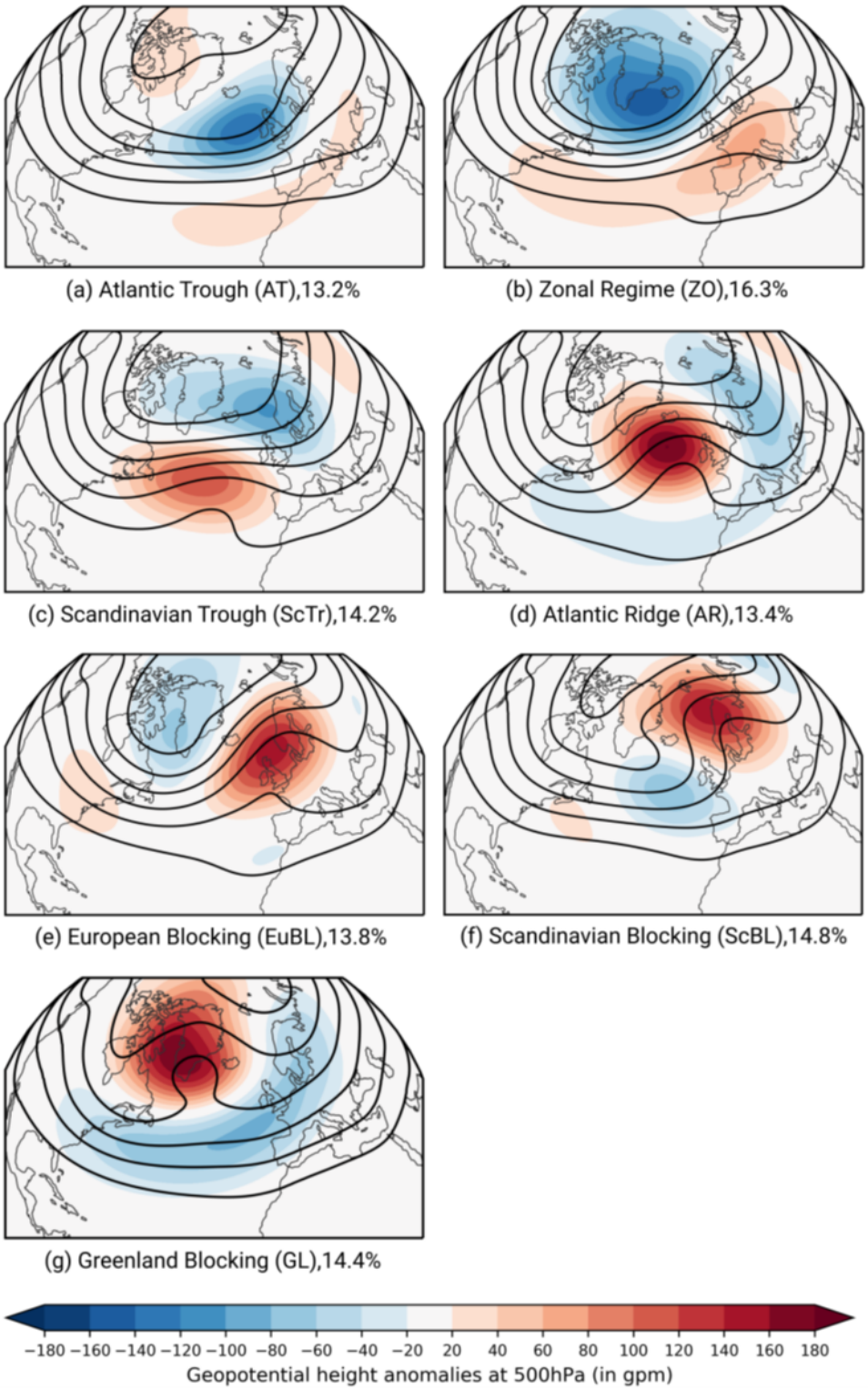

Figure 3.5.: The seven North Atlantic-European year-round weather regimes in ERA5. Mean low-pass filtered (10 days) Z500 anomalies (shading, in gpm) and mean absolute Z500 (in gpm, from 5300 to 5800 in steps of 100 gpm) based on the EOF clustering for the period 1979 – 2019. Regime names, abbreviations, and the explained variances (in %) are indicated in the captions of the subfigures. Adopted from Hauser (2023).

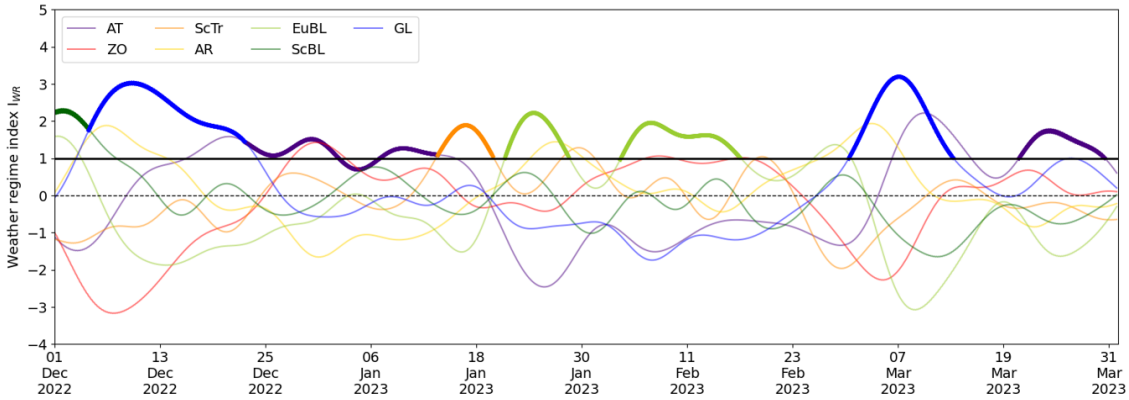

Figure 3.6.: I_{WR} for all seven weather regimes for the period 1 December 2022 -– 31 March 2023. Lines in bold indicate active regimes.

Here, (λ, φ) are the longitude and latitude coordinates within the EOF domain and NT is the total number of time steps within the climatological sample (1979-–2019). P_{WR} represents the projection of the filtered geopotential height anomaly in 500 hPa $\Phi'(t, \lambda, \varphi)$ to the EOF cluster mean $\psi_{WR}(\lambda, \varphi)$ within the EOF domain. $\overline{P_{WR}}$ is the climatological mean of $P_{WR}(t)$, and the denominator in Eq. 3.1 represents the standard deviation over the full time period. This means that I_{WR} is computed as the deviation of $P_{WR}(t)$ from the climatology, normalized by the standard deviation. Although the weather regimes were defined based on the 1979 – 2019 period, I_{WR} can also be computed beyond that period.

Objective life cycles and transition stages of weather regimes be identified from the temporal development of I_{WR} (Grams et al., 2017). An example time series is provided in Fig. 3.6 for the winter of 2022–2023. Regime life cycles are identified by various steps: At first, local maxima where $I_{WR} \geq 1.0$ are identified for each timestep as possible maximum stages of weather regimes life cycles. Second, preliminary regime onset and decay time steps are identified as the first and last time steps around the maxima where $I_{WR} > 1.0$. Lastly, a full regime life cycle is accepted if the time difference $\Delta t = t_{\text{decay}} - t_{\text{onset}}$ amounts to at least five days, so that a sufficient persistence of the regime is ensured.

In cases where multiple local maxima share the same onset or decay date (e. g., GL and AR in early December), a combined regime life cycle is created if each local maximum has $I_{WR} \geq 1.0$, and the time difference between the two maxima ($t_{\text{max1}} - t_{\text{max2}}$) is less than 100 days. The combined life cycle is then characterized by the earliest onset date and latest decay time, with the maximum stage corresponding to the highest I_{WR} during the combined life cycle period. Thereby, several regimes can exceed a value of 1.0 for more than five days, which is when they are called 'active'.

4. Methods

This chapter describes the adjustment of insurance loss data (Sect. 4.1), followed by an explanation of how major loss events were identified (Sect. 4.2) and categorized into meteorological hazard types (Sect. 4.3). The combination of different hazard types is then outlined (Sect. 4.4), and finally the methods used to detect clustering are explained (Sect. 4.5). An overview of the process steps can be found in Fig. 4.1.

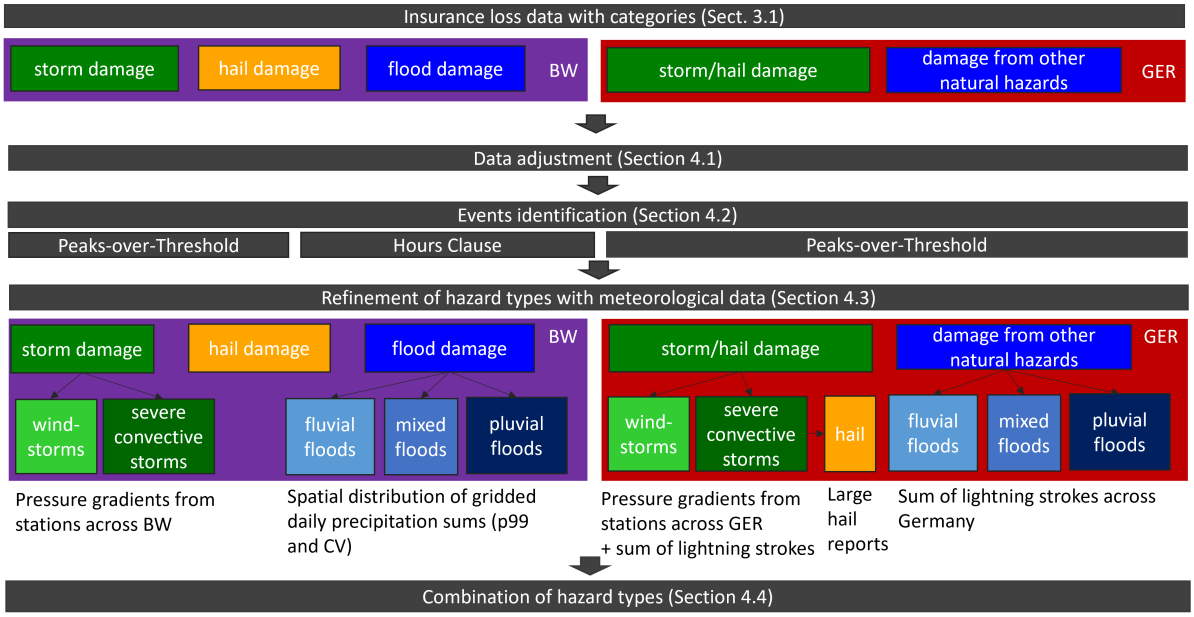

Figure 4.1.: Schematic overview of the methods section.

4.1 Loss data adjustment

Due to a high temporal variability in the insurance loss data (see Sect. 3.1) and the long time period considered, at first, the data needs to be adjusted. Therefore, the insurance loss data for both study areas, BW and Germany, were adjusted using a building-specific price index as well as for the annual variability of the portfolio.

> Inflation adjustment is performed to the base year 2022 using an adaptation factor including the so-called *Gleitender Neuwertfaktor* (glN), a factor commonly used in the German insurance industry (Dietz et al., 2015). The glN factor captures the development of construction prices as well as standard

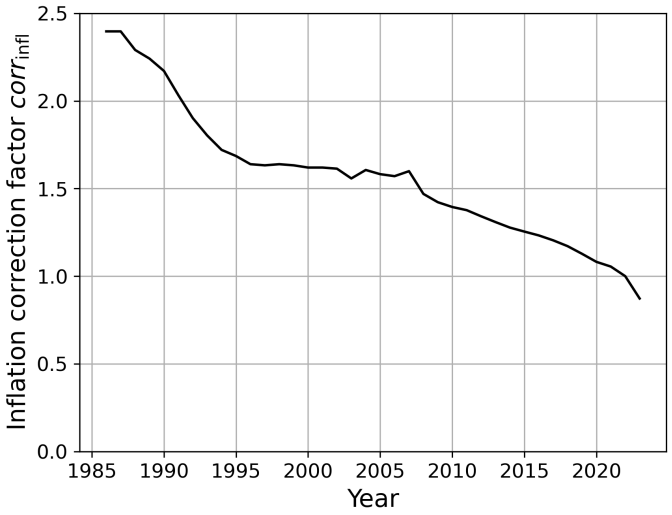

Figure 4.2.: Development of the adapation factor including glN (*gleitender Neuwertfaktor*, see main text, and Eq. 4.1).

wages and is made available to insurance companies annually by the GDV. This factor reflects the actual reconstruction costs, since it captures the development of construction prices as well as standard wages and is therefore a more accurate correction factor than the inflation correction factor as a whole. The adaptation factor is defined as:

$$corr_{\text{glN}}(year_x) = \frac{glN_{2022}}{glN_{\text{year}_x}}. \tag{4.1}$$

Daily insured losses are then multiplied by this factor for the respective year:

$$loss_{\text{adj}}(day_y) = loss(day_y) * corr_{\text{glN}}(year_x). \tag{4.2}$$

Due to the development of inflation and construction prices, glN has increased continuously, especially since 2007. Consequently, the adaptation factor has decreased, starting with a factor of 2.4 in 1986 (BW) and 1.63 in 1997 (Germany), respectively (see Fig. 4.2).

The annual variability of the portfolio was adjusted using the inflation-adjusted sum insured as well as the number of contracts per year: For the study area Germany, insured losses were adjusted with the following correction factor, where SI_{mean} refers to the mean sum insured over the entire time period, calculated separately for storm/hail and other natural hazards:

$$corr_{\text{a, portfolio}}(year_x) = \frac{SI_{\text{mean}}}{SI_{year_x}}. \tag{4.3}$$

A correction factor for the number of contracts (denoted by *NC*) during the course of time is created in an analogous manner:

$$corr_{\text{b, portfolio}}(year_x) = \frac{NC_{\text{mean}}}{NC_{year_x}}. \tag{4.4}$$

The number of claims for the study area Germany are therefore adjusted as follows:

$$claims_{\text{adj}}(day_y) = claims(day_y) * corr_{\text{b, portfolio}}(year_x), \tag{4.5}$$

as well as the losses incurred:

$$loss_{\text{adj}}(day_y) = loss(day_y) * corr_{\text{a, portfolio}}(year_x). \tag{4.6}$$

For the insurer providing data for BW, the portfolio has expanded during 1986–2023 through the merger with direct insurance companies from other federal states. Therefore, the dataset was corrected to determine the total loss for BW exclusively by filtering for the fraction of contracts in BW. Although the dataset may also contain events that did not affect BW only, this step is necessary to ensure comparability over the years. In addition, most of the contracts (around 85 % on average during the period under study) are from BW, so the resulting uncertainty is relatively low. As there is no consistent finer spatial information (such as on the municipality level, for example) available in the dataset, spatially aggregated losses per day were used for the whole region. Due to the limited size of BW, it is assumed that there was only a single synoptic event that caused loss at the same time. Since the sum insured is not available for the study area of BW, both damage claims and insured losses were adjusted using equation 4.4. Furthermore, the total number of contracts for both insurance types (storm/hail vs. other natural hazards) is used, i. e., the same adjustment is performed for all hazard types. This approach is justified by the similar contract numbers for both insurance types (see also Fig. 3.1) and data inconsistencies.

An investigation of the distribution of values throughout the year shows an unusually high accumulation of losses and claims on 1 January of every year. Since this is due to regulation and not due to meteorological reasons, values for 1 January were excluded in both study areas. A comparability across the time series is ensured using these adjustments for the temporal variability.

4.2 Identification of major loss events

As this work focuses on the temporal variability and clustering of major loss events, the daily loss data were filtered, to retain data above the 90th percentile (p90). Several percentiles were tested, ranging from p80 to p99, where p90 provided the best balance between severity and a sufficiently high number of events. A detailed sensitivity analysis regarding the percentile threshold is presented in Chapter 6. The percentile filter was applied to both damage claims and insured losses across the entire time series. Before

filtering, zero values representing losses below the deductible were excluded. By using a high percentile, only relevant meteorological hazards were captured. Note, however, that this percentile filtering scheme leads to a different number of events for each hazard type.

Furthermore, to analyze clustering of distinct events, the events are required to be independent. For example, in December 1999, two major windstorm events occurred within 36 hours, named Lothar and Martin in the German nomenclature[1]. This and other examples of windstorm clusters (see Sect. 2.4.1), challenge this independence assumption of extreme events. To address this, and to avoid clustering on the timescale of synoptic systems (around 5 days), clustering on the timescale of a few days needs to be removed (Wilks, 2006). This is called (runs) declustering (Coles, 2001) and means, for this work, that the daily data were aggregated to events with a length of either one or several days. Two different methods were used to define events: (i) the POT method, a standard method of extreme value theory (see Sect. 4.2.1), and (ii) the Hours Clause (HC) method (see Sect. 4.2.2), a method commonly used in the insurance industry (Mitchell-Wallace et al., 2017). We are not aware of any other study using the HC method or a comparison between POT and HC methods for insurance loss data.

4.2.1 Peaks-Over-Threshold

For the study area BW, the POT method is applied as follows, visualized in Figure 4.3:

1. First, the adjusted loss data were filtered for positive values, that is, only those days with insured losses and damage claims both larger than zero are kept. This ensures that major events are only identified from days with actual damage. From these values, the 90th percentile (p90) is used to retain only the most damaging events above threshold u. The p90 threshold is applied to both the number of claims and insured losses.

2. Days above the threshold u are identified by applying this combined percentile. For each pair of subsequent days t_i and t_{i+1}, the $\Delta t = t_{i+1} - t_i$ (in days) is computed. The maximum number of days r between two events to become one event is defined. This means that if two days are separated by less than $\Delta t = r$, they are considered as a single event. Values of r = 2 are common for central Europe regarding precipitation (Barton et al., 2016; Tuel and Martius, 2021b) and wind (Brabson and Palutikof, 2000) and therefore used in this work as well.

3. Events above u separated by less than r days (or, more generally, time steps) are aggregated and counted as single events. This is first applied for each timestep (t_i). If a specific event has a difference of less than two days to the next event ($t_{i+1} - t_i \leq r$), t_{i-1} is also evaluated with regard to the time difference to the next event. If this previous timestep is also separated by less than r from the t_i, that is, $t_i - t_{i-1} \leq r$ and $t_{i+1} - t_i \leq r$, all three days are counted as one event. As long

[1] Since the 1950s, the *Freie Universität Berlin* names high- and low-pressure systems in Europe. In even years, highs have male names and lows have female names; in odd years, the reverse is true. For more information see: https://www.wetterpate.de/ueber-uns/Geschichtliches/index.html

as $\Delta t \leq r$, the event is extended by including t_i, $t_{i+1}, \ldots, t_n$. Losses and claims of all participating days are cumulated to the resulting event. As a result, events lasting for one or several days are generated. Note that with this method, there is no upper limit for the duration of events, which means that in theory, events could last for as long as the timeseries is. However, in practice, the longest event lasts for 19 days. The resulting extreme events were mapped to a binary variable, with a varying start and end date for each event, which can then be used as an input for further analyses.

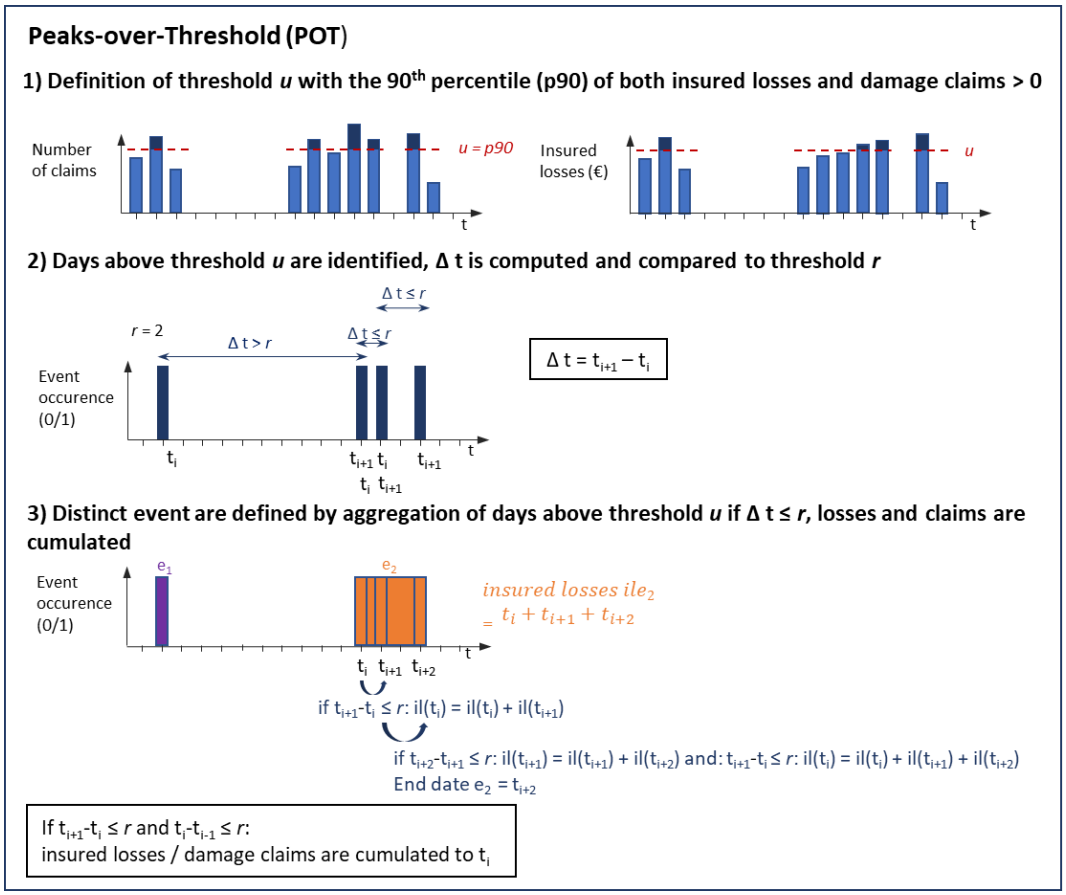

Figure 4.3.: Overview of the algorithm of the two Peaks-Over-Threshold method used for event identification for both the study areas of GER and BW.

For the study area Germany, the event definition using POT and 90th percentile (p90) of losses and claims was revisited. Due to the varying insurance density regarding other natural hazards, an extreme event definition using percentiles is biased towards BW, because of the high insurance penetration in this federal state. This does not (necessarily) reflect the occurrence of meteorological extremes for the whole of Germany. An alternative approach could be to use a high percentile of the daily loss ratio, calculated as the ratio of insured losses to the sum insured. However, this approach leads to a positive bias towards early years. In addition, errors in the data exist: For example, for some districts and certain days, the

insured losses with deductible subtracted exceed the sum insured. Therefore, as well as for consistency with the study area BW, the loss- and claims-based approach is preferred.

4.2.2 Hours Clause

The HC method is a commonly used method in the (re-)insurance industry to identify individual loss events. It relies on a pre-determined fixed event duration to obtain independent events, depending on the insurer as well as on the hazard type. The HC is a specific type of a nonproportional reinsurance contract (Mitchell-Wallace et al., 2017). Here, reinsurers do not cover a certain share of the loss but cover losses above an certain absolute limit, called attachment level. Commonly, in nonproportional reinsurance contracts, events with a certain duration and extent are defined with the HC, also called Loss Occurrence Clause. The insurer defines a time window over which losses are aggregated. This window is expressed in hours; common values are, for example, 72, 86, 168 or 504 hours, depending on the type of hazard and market. Retention, and therefore also coverage by the reinsurance, are applied separately for each event's losses. In case of event durations longer than these defined hours, the insurer will choose to aggregate their losses, that is, define the event, in the way that allows for the largest retention by the reinsurance. This is applied in this work by centering HC values on the maximum loss (see below). It is furthermore acknowledged by the industry that the HC does not capture the actual duration of events. For example, winter storms Lothar and Martin highlighted issues with HC, treating losses with a timespan of 72 hours as a single event (Mitchell-Wallace et al., 2017). Different event definitions may be used by different stakeholders.

To determine events using the HC method, an algorithm is applied to the loss data as follows (see Fig. 4.4):

1. First, a duration L (in days) is defined, depending on the event type. For precipitation-related events, an event duration of $L = 7$ days (168 h) is used, while for storm and hail events, $L = 3$ days (72 h) applies. These values are also used by the building insurance company providing the data for BW. Insured losses (*il*) and the number of damage claims (*dc*) are accumulated over the time period
$$\mathrm{il}(t_i) = \sum_{t_i-0.5d}^{t_i+0.5d} \mathrm{il} \quad \text{and} \quad \mathrm{dc}(t_i) = \sum_{t_i-0.5d}^{t_i+0.5d} \mathrm{dc}, \tag{4.7}$$
with duration $d = L - 1$, because t_i is not included. Running sums for losses and claims are therefore calculated over 3 and 7 days, respectively, depending on the hazard type.
2. From these cumulative sums, consecutive periods are extracted, during which values are continuously added until the time difference exceeds 1 day; this avoids event overlaps. If the duration of the consecutive periods $(t_{i+1} - t_i)$ equals L, the value in the center $(t_i + 0.5d)$ is chosen as event center regardless of the loss value, with start and end days being $t_i - 0.5d$ and $t_i + 0.5d$, respectively. For periods with loss records lasting longer than the predefined number of days, the day with the

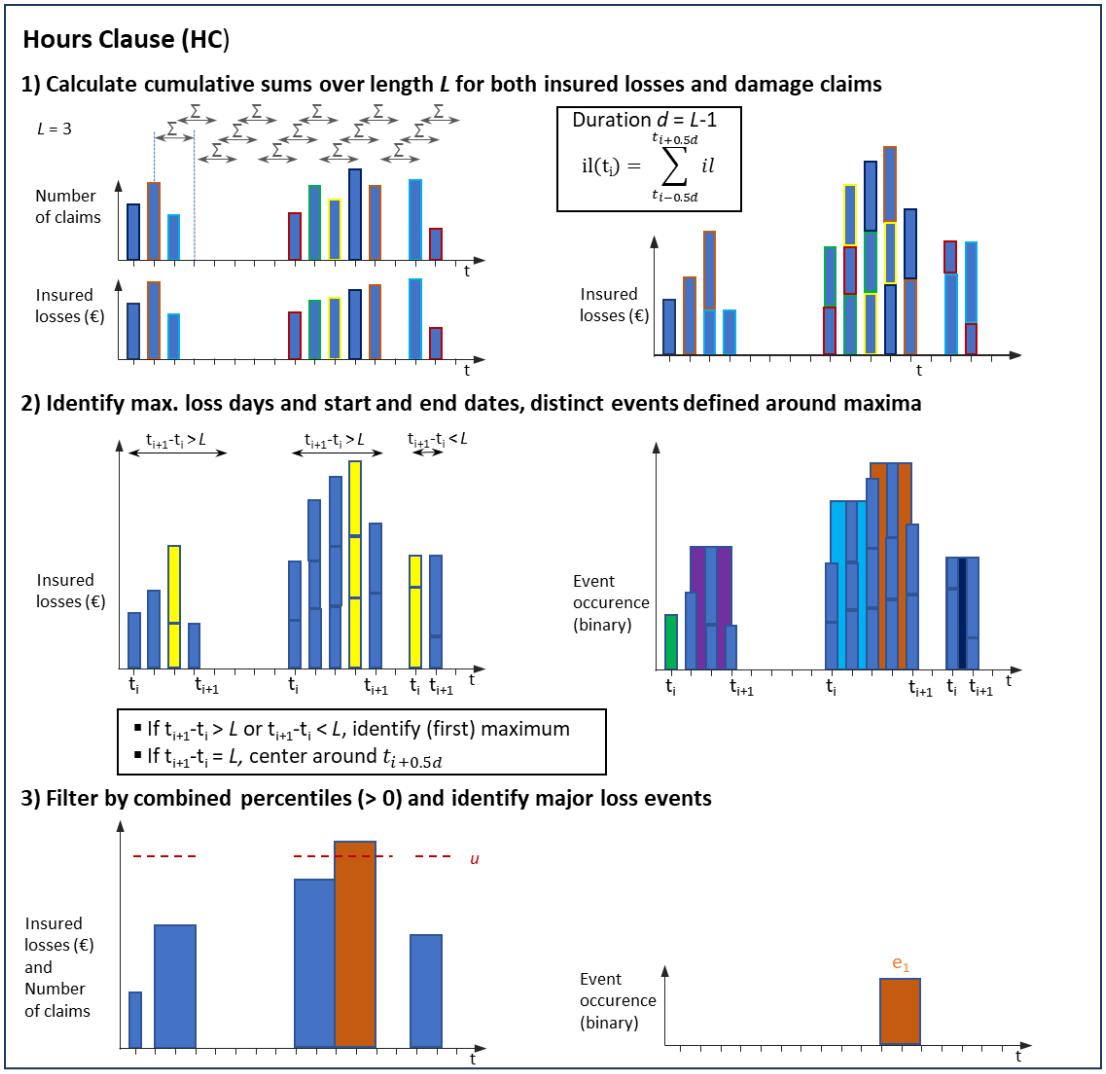

Figure 4.4.: Overview of the algorithm of the Hours Clause method for event identification for the study area of BW.

maximum loss is determined as the 'center day' of an event. Since storm and hail events defined with this method last for $d = 3$ days, the center day is the second day within the event. For flood events, where $d = 7$, the center day is day 4. In this case, the day with the maximum loss $t_{max(il)}$ within each consecutive period is identified. The first event is defined around $t_{max(il)}$ with start and end dates being $t_{max(il)} - 0.5d$ and $t_{max(il)} + 0.5d$. Potential further events are assigned around this event, preserving the fixed duration L (ending at t_{i-1} or starting at t_{i+2}) as long as the loss days continue. If there is only one further loss day before or after the event, the start date equals the end date and losses of this day are used (not cumulated).

3. Lastly, pre-defined events based on moving sums with values > 0 are filtered by the threshold u (see 4.2.1). Events above this threshold are mapped to a binary variable, representing the filtered

time series used for clustering analyses. By the use of this method, a sample of major damaging events for each type with a fixed duration is obtained.

The HC and POT methods identify differing numbers of events in some cases (see Figs. 4.3 and 4.4). For example, the severe winter storms Vivian and Wiebke in 1990 are combined to a single event with the POT method, but identified as two separate events with the HC method. Finally, it should be acknowledged that the HC method, due to its fixed duration, may classify certain days as extreme event days even if they are not. In Chapter 6, the degree of clustering in the data is evaluated and compared for both methods.

4.3 Categorization into meteorological hazard types

Different types of hazards, which are sometimes recorded within the same category by insurance companies, can occur at varying spatial and temporal scales (see Sect. 2, Fig. 2.1) and lead to varying damage patterns. These broad categories therefore do not represent accurate meteorological hazard types and need to be refined. The hazard types in the loss datasets are subdivided into more precise meteorological categories with a focus on their spatial scale, that is, large-scale events vs. local events. Both wind and precipitation extremes can be attributed to different underlying mechanisms. As seen in Chapter 2, convection-driven events and events triggered by large-scale lifting processes affect substantially different areas, a fact that has to be considered in the event definition and for the cluster analysis.

4.3.1 Flood damage events

> As seen in Sect. 2.1.3, a predominantly stratiform precipitation event is characterized by low to moderate rainfall intensities, a duration of several hours to days, and a large affected area, sometimes extending over several hundred kilometers (Houze, 1993). This can result in fluvial floods. By contrast, a convection-dominated precipitation event is characterized by high rainfall intensities combined with a short duration of a few minutes to a few hours, and has a small spatial footprint. This can result mainly in pluvial floods. However, a clear separation between these two hazard types is not always possible, in particular for mesoscale convective systems, for clustered convective events with a mixture of stratiform and convective precipitation primarily toward the end of the life cycle (Houze, 1993); or for orographic precipitation. The latter can attain very high precipitation totals, particularly over the Alps and over low mountain ranges such as the Black Forest (Kunz, 2011).

Therefore, three categories were defined: Predominantly stratiform, predominantly convective and mixed precipitation, typically leading to fluvial, pluvial and mixed floods respectively. Note that convective systems can also contribute to fluvial flooding. For simplicity, flooding resulting from convective precipitation events is termed pluvial flooding within the scope of this thesis.

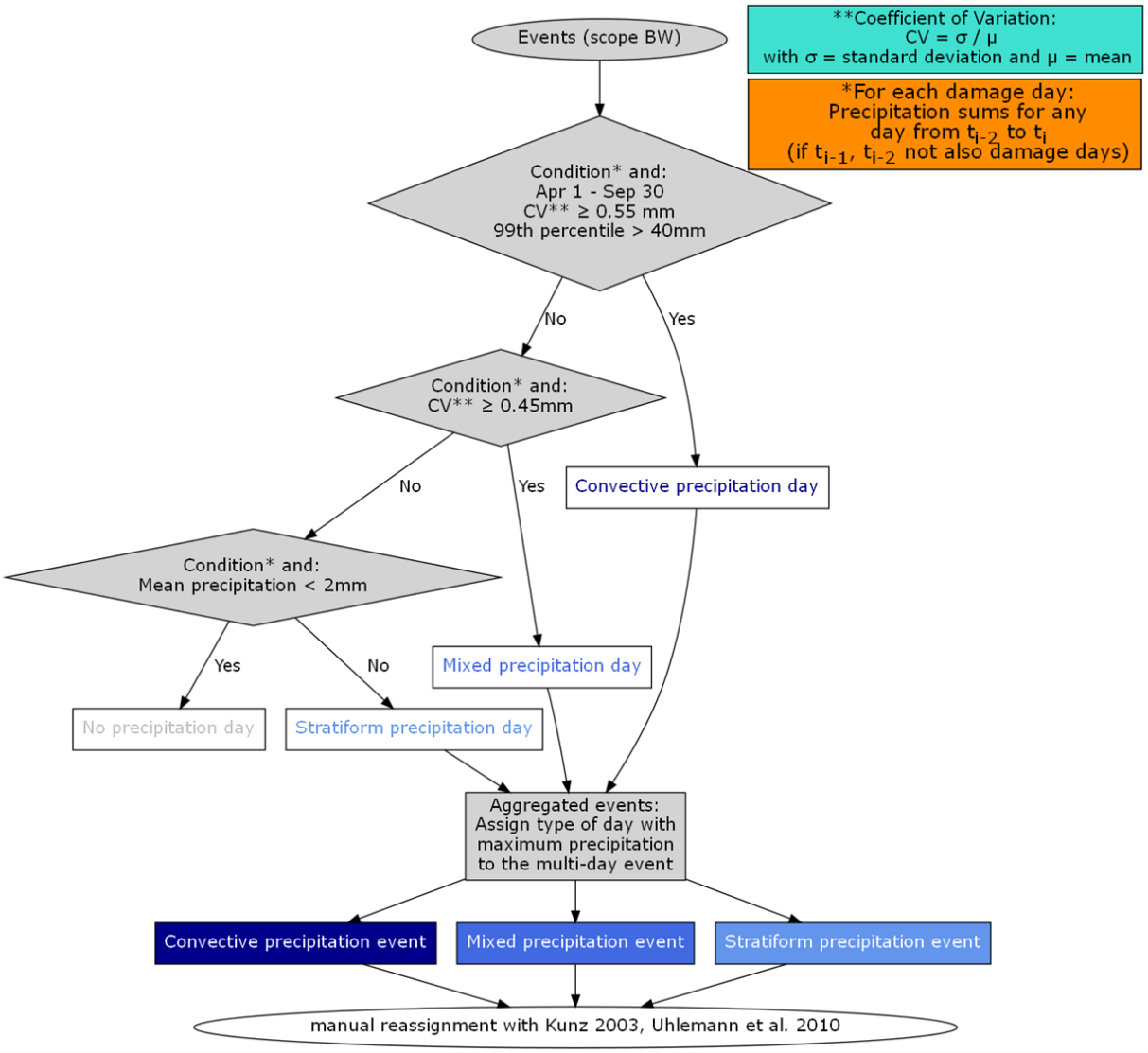

Figure 4.5.: Workflow for categorizing flood damage events in the insurance loss data into stratiform, mixed, and convective precipitation events in Baden-Württemberg.

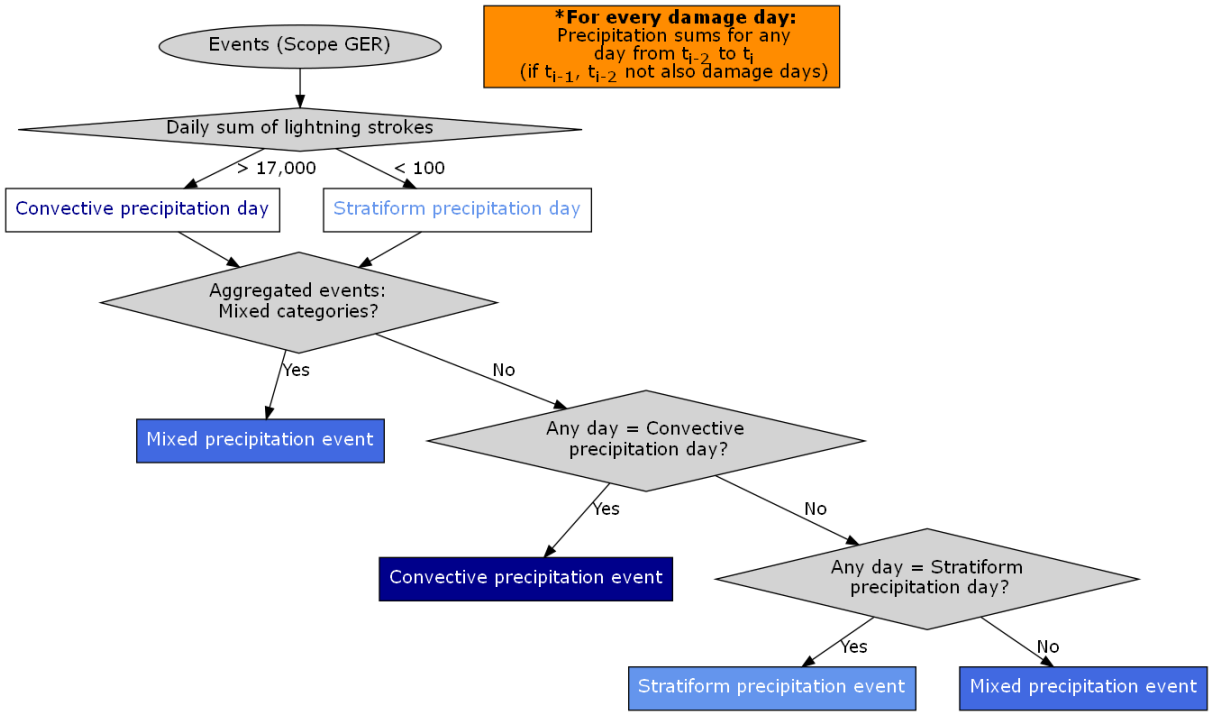

Figure 4.6.: Workflow for categorizing flood damage events in the insurance loss data into stratiform, mixed and convective precipitation events in Germany.

The most straightforward method to distinguish between these precipitation types would rely on radar data (e. g., Wang et al., 2021). However, radar data are not available for the entire period under study.

For the study area BW, therefore, gridded daily precipitation totals (see Sect. 3.2.1) during identified insurance loss events are used (see Fig. 4.5). Two metrics are considered for the separation between the precipitation types: the 99th percentile and the coefficient of variation (CV) of daily gridded precipitation totals (calculated in space). The CV is defined as the ratio between standard deviation σ and mean μ (Abdi, 2010):

$$CV(t) = \frac{\sigma}{\mu}.$$

For $CV(t)$, only grid points with precipitation (that is, >0 mm) are considered. As depicted in Figure 4.7a, in order for a day t to be classified as convection-dominated (associated with mainly pluvial flooding), the following conditions must be met: (i) the spatial 99th percentile of daily precipitation totals exceeds 40 mm for any day from t_{i-2} to t_i, (ii) $CV(t_i)$ is larger than or equal to 0.55 mm, and (iii) t is between 1 April and 30 September, since convective storms primarily occur during the summer months in Germany (Kunz, 2007; Mohr et al., 2017). Applying condition (i) from t_{i-2} to t_i allows to consider a potential time lag between the precipitation and the flood damage, particularly in case of a stratiform-dominated event or for heavy rain around midnight. Days not meeting these conditions are categorized as mixed precipitation days if $CV(t_i) > 0.45$ mm, and otherwise as stratiform-dominated (fluvial flood) events if the mean precipitation totals for all grid points are larger than 2 mm for that day. These thresholds were

extensively tested by comparing with radar images from DWD (available after 2005), especially with events from May to July 2021 as well as with the most extreme precipitation events in the timeseries.

Of course, the above described criteria do not distinguish all events clearly. Therefore, events that could not be clearly categorized – mainly those around the two defined thresholds – were visually checked and reassigned using expert knowledge, partly in combination with existing literature (Kunz, 2003) and taking into account the terrain height (e. g., Brommundt and Bárdossy, 2007). For multi-day events, the hazard type was determined by the hazard assigned to the day with the highest precipitation totals within the (spatial) 99th percentile of the precipitation fields.

For the study area Germany, due to the larger area and higher spatial heterogeneity of precipitation events, a different approach was taken (see Fig. 4.6). For example, a precipitation event could occur over northern Germany with the south being not affected at all. The CV across the study area as well as a spatial quantile are therefore not applicable at this study area. Therefore, cloud-to-ground lightning data were used to differentiate between precipitation types. The cumulative number of strokes across Germany (box-filtered) was computed for each day. If this number exceeded 17,000 strokes on a day, the day was defined as a convectively-dominated precipitation day. If the number of strokes was below 100, it was defined as a stratiform precipitation day. For values in between, no assignment was done. For aggregated events containing both categories (that is, days with a very high number and a very low number of strokes), a mixed precipitation event was defined. If there were no mixed categories for an aggregated event, the event was assigned a convective precipitation event if any day was defined as convectively-dominated (lightning-rich). On the other hand, if there was a stratiformly defined (lightning-scarce) day within the event, the entire events got defined as a stratiform event. If neither a lightning-scarce nor a lightning-rich day existed within the event, it was assigned a mixed precipitation event.

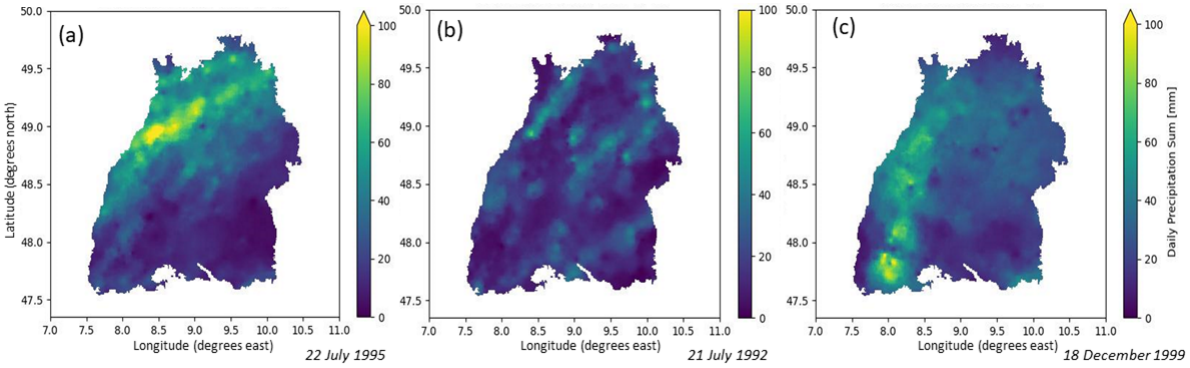

Figure 4.7.: Examples of (a) convectively-dominated, (b) mixed and (c) stratiformly-dominated precipitation events in Baden-Württemberg identified from gridded daily precipitation sums, computed based on HYRAS-DE-PR (see Sect. 3.2.1)

Having categorized precipitation events, they were labelled according to the (main) associated hazards in the following: Stratiform-dominated events are referred to as fluvial floods, mixed flood events as mixed floods and convection-dominated flood events are referred to as pluvial floods.

4.3.2 Storm damage events

> As seen in Chapter 2, damaging hazard types related to the storm category are typically either so-called windstorms or extratropical cyclones that extend on the synoptic scale (around 1,000 km), or (severe) convective gusts that have much smaller spatial scales (tens of km) (Markowski and Richardson, 2010). As with precipitation, insured losses categorized as storm damage can also result from the interaction of local- and large-scale processes. During the passage of cold fronts of winter storms, for example, convection can strengthen surface winds by convection-driven downbursts (Markowski and Richardson, 2010; Mohr et al., 2017). In case of convective gusts, the vertical transport of horizontal momentum increases convective gusts at the surface. However, all these processes occur on a local scale and cannot be simply estimated from available observation data. In addition, our main purpose here is to separate between damage created by the different triggering mechanisms, which presumably feature different clustering characteristics. For these two reasons, we only distinguish between synoptic- and convection-driven storms and do not consider a mixed class for storm events as we do for the flood hazard.
>
> To differentiate between these two main storm hazard types, we used the method of Mohr et al. (2017) based on the MSLP gradient between selected weather stations. We consider hourly MSLP observations from six DWD weather stations available from the CDC for the entire investigation period. This includes taking to account potentially varying locations of the stations, since some changed locations throughout this long time period.

For the study area of Germany, the specific stations were adopted from Mohr et al. (2017): Schleswig, Nordeney, Hannover, Berlin-Tempelhof, Frankfurt/Main, and Hof (see Fig. 4.10). Since the loss data were available on the scale of districts, for each storm event, the district with the maximum insured losses were identified. The weather station w_{maxloss} closest to this most affected district was then evaluated in comparison to the other stations. The MSLP gradient, i. e., the ratio of the difference in MSLP to the distance between the stations, was computed between w_{maxloss} and all other stations. For the study area BW, station pairs were created on three axes: north-south (stations Michelstadt-Vielbrunn and Konstanz), northwest-wortheast (stations Karlsruhe/ Rheinstetten and Weißenburg-Emetzheim), southwest-southeast (stations Freiburg and Lechfeld). These station pairs were chosen based on data availability for the entire time period and their location, so that they are geographically well distributed across BW. For these three station pairs, the MSLP gradient was computed.

The algorithm for the categorization of the storm events is visualized in Figure4.8 and Figure4.9. If any pair (BW) or at least combinations (GER) of the hourly MSLP gradients exceed a threshold of 3 $\mathrm{Pa\,km^{-1}}$

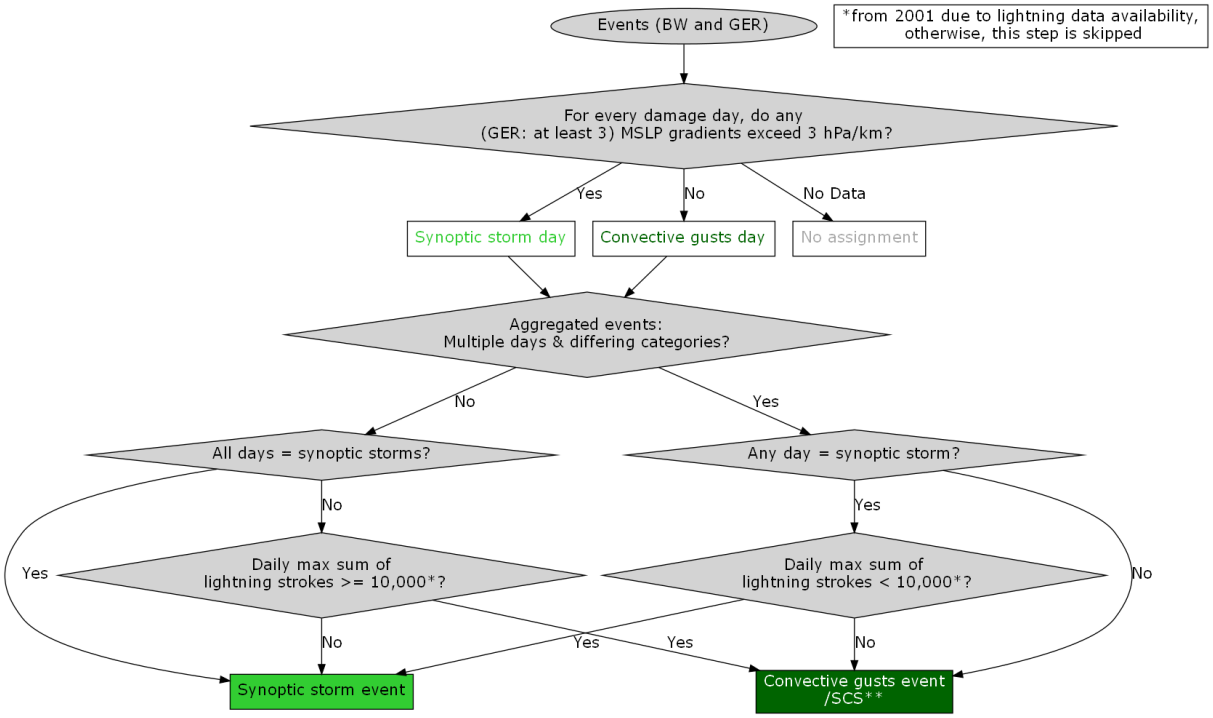

Figure 4.8.: Workflow for categorizing of storm damage events in the insurance loss data into synoptic storm events, convective gust events and hail events in Baden-Württemberg.

at any time on a specific day, the day is defined as a synoptic storm day. Otherwise, it is classified as a convective gusts day. The threshold was slightly reduced compared to Mohr et al. (2017) after testing with severe winter storms in recent years. For example, storm Victoria in 2020 shows maximum gradients of only 3.44 Pa km^{-1}.

For aggregated (multi-day) events starting from 2001, the process is as follows: If all days were classified as synoptic storm days and the daily maximum sum of cloud-to-ground lightnings across the study area does not exceed 10,000 strokes, it is defined as a synoptic event, otherwise, it becomes a convective gust event. If there are differing categories for multi-day events and any day is classified as a synoptic storm day, the multi-day event is classified as synoptic if the daily maximum sum of cloud-to-ground lightning is below 10,000. Otherwise, it is classified as a convective gust event (BW) or as a severe convective storm event (GER), which is later separated into convective gust events and hail events (see Sect. 4.3.3). This procedure ensures a robust classification, also in the case of missing data.

In the following, storms with a synoptic trigger are referred to as large-scale storms (LS) and convection-driven storms as convective gusts (CG).

4.3.3 Hail damage events

For the study area Germany, hail events are distinguished from convective gust events by using hail reports from the ESWD (see Fig. 4.9). For each damage day, if at least one hail report falls within 10 km

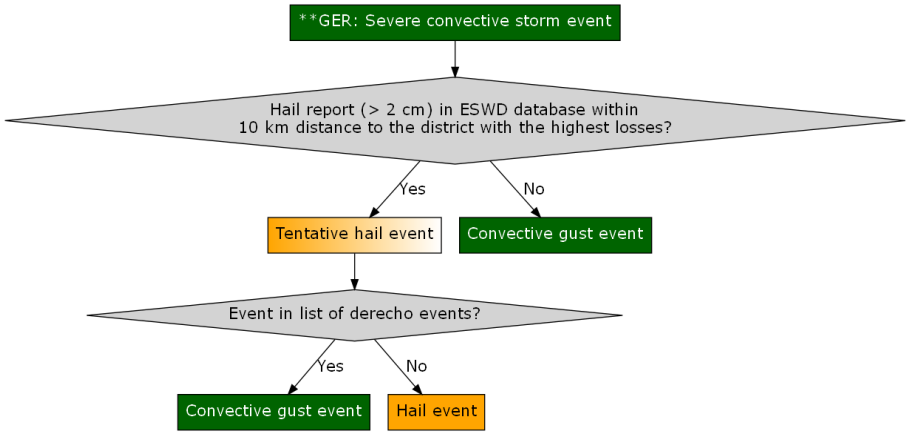

Figure 4.9.: Addition to Figure 4.8: regarding the categorization of storm damage events in the insurance loss data into the categories of synoptic storm events, convective gust events and hail in Germany.

distance of the district that recorded the highest losses in Germany on that day, the event is assigned to the hail category. If multiple days of one event fall into differing categories, they are assigned to the hail category, assuming that hail drives the damage during the event. However, if the event can be classified as a derecho event (see Sect. 2.1.2), the classification is revisited. Therefore, to separate derechos from hail events, a list of derechos over Germany identified by Gatzen et al. (2020) is employed. Due to the high impact in the case of a derecho, the damage is assumed to be driven by the gusts.

For the study area BW, distinct categories of storm and hail are defined by regulators, but hail events are only considered between 1 April and 30 September. Furthermore, verification with ESWD reports is not useful because of the longer time period, and the large increase in reports over the last two decades.

4.4 Combination of hazard types

> When events of different hazard types are combined, they again need to be declustered to avoid artificial clustering of events from the same meteorological driver (see Sect. 4.2 for declustering of single hazard types). We perform the following procedure: First, overlaps of events are identified. If events from different hazard types have the same start date or one event is fully contained by another event, only the event with the highest losses is kept. Of the deleted events, however, the type, insured losses and number of claims are added up to the maximum loss event. Keeping all hazard types is important since thereby both hazard types can potentially lead to clustering of multiple hazard types (for example, if a hail event and convective gust event occur on the same day and another convective gust event occurs within the clustering window, this is defined as a combined cluster of hail and convective gusts only because both types are retained).

For the statistical clustering analyses of multiple hazard types, two additional conditions are required. For a multi-hazard combination to be analysed, the maximum number of events from the most dominant

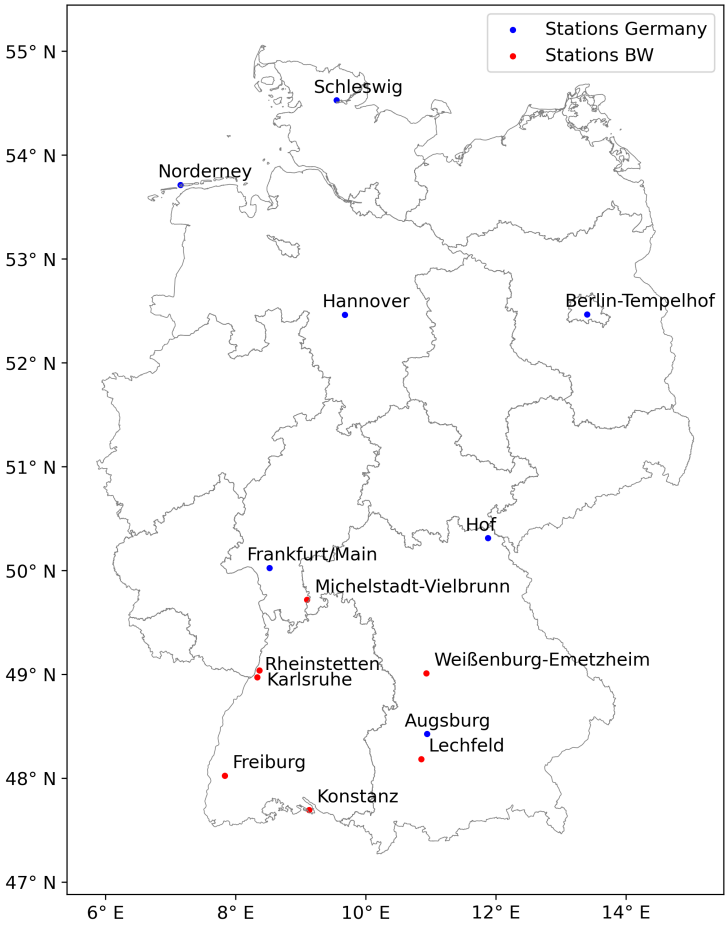

Figure 4.10.: Distribution of the synoptic weather stations selected from the Climate Data Center of the DWD across Germany (blue) and BW (red).

hazard type within a seasonal timeseries is 80 %. This prevents a particular type of hazard from dominating the cluster. On the other hand, each hazard type must account for at least 10 % of the total event count (per season). This ensures that all hazard types, especially in the combination of three hazard types, are relevant in the time series.

4.5 Clustering methods

Serial clustering of single- and multi-hazard events is assessed with mainly two methods, namely a counting method (Sect. 4.5.1) and the metric Ripley's K (Sect. 4.5.2). The former is used to identify time periods with an accumulation of extremes of single and multiple hazard types, while the latter is used to assess the degree of clustering by quantifying the deviation from a homogeneous Poisson process

(see Sect. 2.4.2). Impact metrics are used alongside these methods (Sect. 4.5.3). As the spatial extent of the study area is rather small, clustering is exclusively investigated in the temporal dimension.

4.5.1 Counting method

Individual clustering episodes can be identified using count-based algorithms (Kopp et al., 2021), recently employed by Bevacqua et al. (2021) with respect to precipitation events preceding landslides and by Kopp et al. (2021) and Tuel and Martius (2021a) for heavy precipitation events, as well as by Barras et al. (2021) for hail. For ETCs, e. g., Pinto et al. (2014) also implemented a count-based method. Bevacqua et al. (2021) employed given event numbers, and Hillier et al. (2025) used the term episodes, referring to a group of hazardous events within a selected spatial domain.

To detect clustering episodes, we use a counting algorithm based on Kopp et al. (2021), who originally developed this algorithm with respect to precipitation sums. This algorithm filters episodes of a predefined length (e. g., sub-seasonal scales) containing a certain number of events from a given time series. Typically, the time periods with the highest number of events for time windows of a given length are extracted. Thereby, these time periods are identified as cluster periods, which is important, for example, when analyzing the relation to the large-scale atmospheric circulation (see Chapter 7).

The detailed steps of the algorithm we adapted from Kopp et al. (2021) are as follows: First, the number of (filtered) events $n_{\mathrm{w}}(t)$ is computed for each hazard type and their respective combinations as well as their corresponding accumulated insured losses $il_{\mathrm{w}}(t)$ within leading windows of a fixed length w (w = 14, 21 or 28 days) for each day t of the time series Y_t ($t = 1, \ldots, N$). Naturally, clusters need to consist of at least two events over time period w and those need to have hazard types of the respective combination. Subsequently, an algorithm is applied that identifies cluster periods as follows (see Fig. 4.11, from top to bottom):

1. All counted time periods across the dataset with the maximum number of event counts, that is, $n_w(t_0) = \max_{t \in Y_t} n_w(t)$, are identified.
2. Within the subset of the maximum counts, the counted time period with maximum il_{w} is identified, which is the first cluster period. For that cluster period, the cluster start (t_0) represents the day on which the first event within the cluster starts. The end of the cluster period is defined by $t_0 + w$, independent of how many further events occur during this interval.
3. To avoid overlapping clusters, all potential further events within $t_0 + w$ and $t_0 - w$ are removed. If there are further periods for which $n_w(t_0) = \max_{t \in Y_t} n_w(t)$, the second cluster is identified with the second highest il_{w}, and so forth.
4. If no clusters of $\max_{t \in Y_t} n_w(t)$ remain, the subsequent cluster is identified at $\max_{t \in Y_t} n_w(t) - 1$. This procedure is continued until no further clusters can be identified, that is, $\max_{t \in Y_t} n_w(t) < 2$.

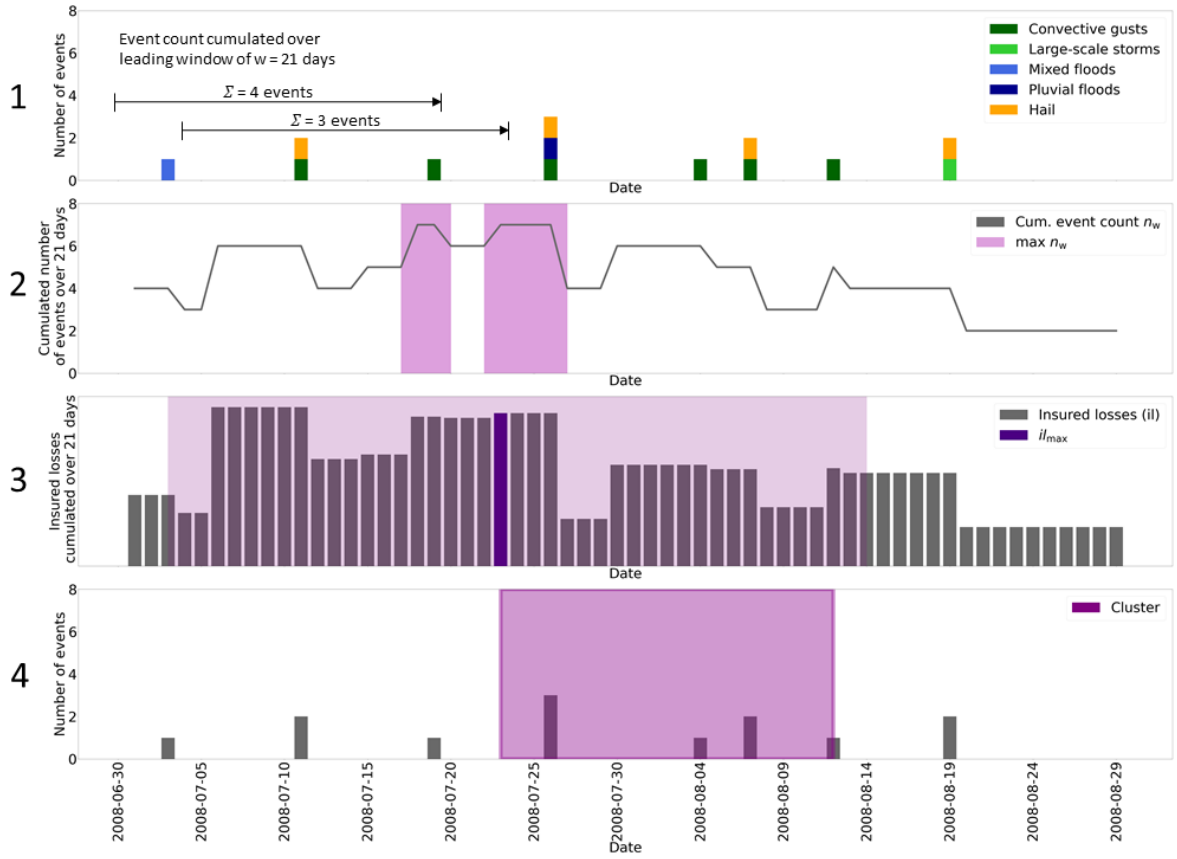

Figure 4.11.: Schematic depiction of the counting algorithm, adapted from Kopp et al. (2021), from top to bottom: At first, a joint timeseries with all hazards is created. Second, the number of events over a leading time window w is computed and maximum periods are extracted. Third, from the identified maximum cumulative events, the maximum accumulations of insured losses across w are identified. Last, the first maximum is the start of the first cluster period.

4.5.2 Ripley's K

To quantify the degree of clustering, we employ a second method, the statistical tool Ripley's K (Ripley, 1981). The function $K(t)$ introduced by Brian D. Ripley (Ripley, 1976, 1981) is a tool originally developed to quantify the clustering of point patterns at varying spatial scales, commonly referred to as Ripley's K (e. g., Mailier, 2007). It can be used to estimate parameters (e. g., intensity), fit models, or test hypotheses. Ripley's K can describe characteristics of a point process at various distance scales. Ripley's K has also been applied to one-dimensional time series of meteorological or hydrological extremes (e. g., Barton et al., 2016; Tuel and Martius, 2021b,a; Brunner and Stahl, 2023). For a time series and clustering window w, Ripley's K is defined as the average number of events $E(w)$ within a time window w (here in days) around any event in the time series:

$$K(w) = E(w), \tag{4.8}$$

and can be estimated, for example, by:

$$\hat{K}(w) = \left[\frac{1}{N} \sum_{n=1}^{N} \sum_{k=-w}^{w} Y_{t+k} | Y_t = 1 \right] - 1, \tag{4.9}$$

as in Barton et al. (2016), where Y_t refers to the binary time series and N is the total number of events. Ripley's K therefore quantifies the average number of events (major loss events in our case) within $\pm w$ days of an event. We let the time window w range from the timescale of a few days (note that due to the identification of independent events, $K = 0$ for the first few days) up to the seasonal level (w = 45 or w = 60, depending on the length of the season). Clustering on the seasonal level in our case compares the occurrence of events between different years.

As in Barton et al. (2016) and Tuel and Martius (2021b), the statistical significance of the clustering was tested by a comparison with a random homogeneous Poisson process (see Sect. 2.4.2). It was simulated here by 1,000 Monte Carlo runs with the same probability of occurrence (or: average density of events) as the observed extremes. These simulations were also declustered, using POT for both methods of event identification. Due to the strong seasonality present in the data (see Sect. 5.2), each month was simulated separately. For each w where the observed $K(w)$ exceeded the 95th percentile of the simulated $K(w)$, the data were treated as significantly clustered. Conversely, where the observed $K(w)$ was lower than the 5th percentile of the simulated $K(w)$, the data were significantly regularly spaced (Barton et al., 2016). Otherwise, the series could not be statistically distinguished from a homogeneous Poisson process.

Since the Ripley's K function can only take one event date per event as input, the start of each event (identified with POT or HC) was used as an input timeseries to Ripley's K. We took only hazard types with > 20 events throughout the time series into consideration. To avoid artificial clustering caused by the recurring seasonal patterns (see Chapter 5), we analyzed the data for specific seasons separately: May to August and December to February.

This work includes analyses with Ripley's K from Küpfer et al. (2024), where Ripley's K is applied to different types of extremes, and extends them with another dataset (see Chapter 6).

4.5.3 Impact metrics

Lastly, impact-oriented clustering metrics, such as the storm and flood severity indices (Priestley et al., 2018; Dacre and Pinto, 2020; Bloomfield et al., 2023), assess how clustering relates to event impacts. A common practice with insurance loss data is to assess loss clustering by comparing the losses of the most damaging event to the total losses of all events during that time period (e. g., Priestley et al., 2018; Dacre and Pinto, 2020). Towards this end, the Occurrence Exceedance Probability (OEP) is defined as the loss of the main (maximum) event in a year or season, and Annual Exceedance Probability (AEP) as the total losses in a year or season (Priestley et al., 2018). Loss clustering is assessed by dividing OEP by AEP,

where a large ratio indicates the dominance of a single event during the season, and a lower ratio points to the contribution of several events to the damage. A large ratio may be interpreted as loss clustering, although it is also possible that these events are randomly distributed. This metric is employed in Sect. 6.3.2.

5. Loss distribution analysis

A meaningful interpretation of the results presented in Chapters 6 and 7 requires an overview of the damage distribution, especially with regard to its relevance for impact assessment. Towards this end, this chapter provides an overview of the loss distribution, regarding their impact relevance (Sect. 5.1), their seasonality (Sect. 5.2), spatial patterns (Sect. 5.3) and trends (Sect. 5.4). If not stated otherwise, the events discussed here are identified by using the POT method. The resulting extreme events in GER range from losses of more than € 700 000 (flood hazards) and € 2 million (SCSs and windstorms, see Fig. A1) to approximately € 2 billion (see Fig. 5.4). Regarding BW, due to confidentiality restrictions, publication of this information is not permitted.

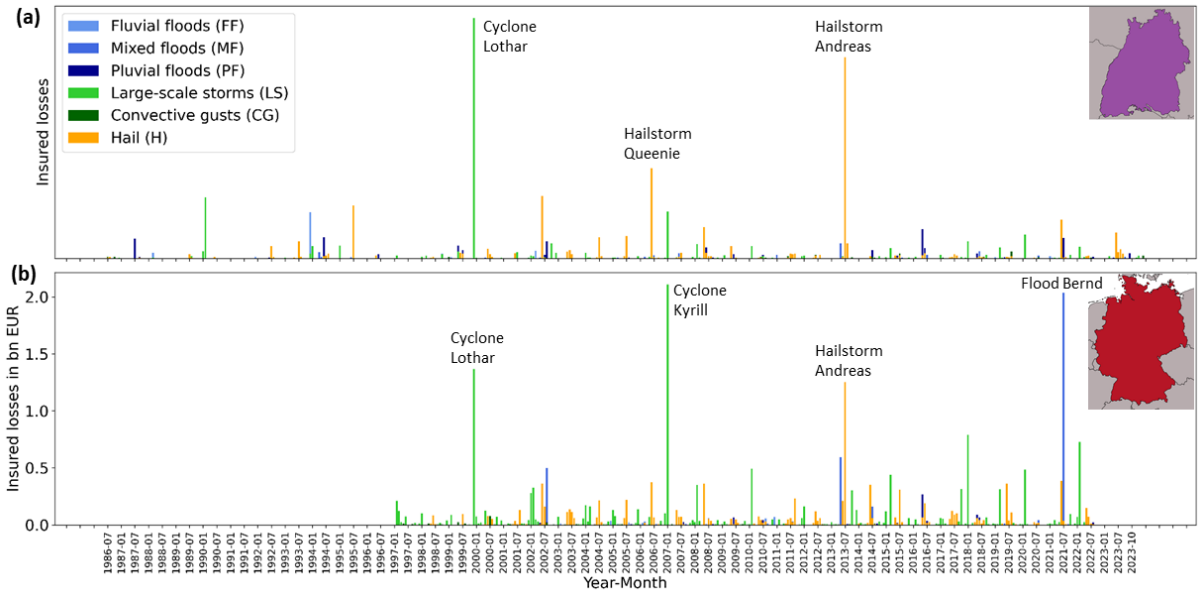

Figure 5.1.: Timeseries of insured losses regarding (a) BW (scale omitted for confidentiality reasons) and (b) GER (in bn EUR) adjusted for inflation to the base year 2022 and the temporal variability of the portfolio and separated into different meteorological hazard types.

5.1 Impact relevance of different hazards

After adjustment and categorization into meteorological hazard types, windstorms are among the major loss events both in the study areas of GER and BW (see Fig. 5.1). Major convective gusts events are not visible in the timeseries. In contrast, with respect to flooding, several flood hazard types seem to cause

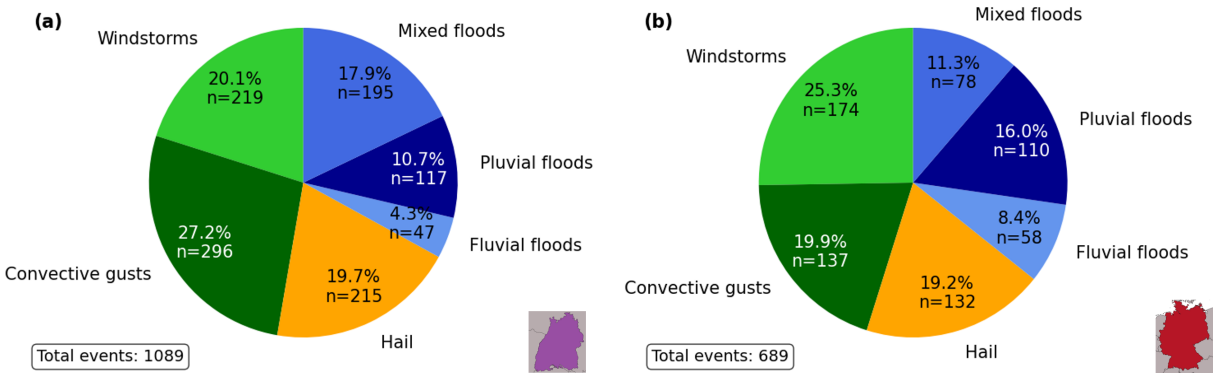

Figure 5.2.: Number of events per hazard type in (a) BW, 1986–2023 and (b) GER, 1997–2022. Added text refers to the total number *n* of events for the specific hazard type in the dataset, and the share of the occurrence of the respective hazard type with respect to all hazards.

major losses, clearly dominated by the 2021 western Germany (mixed) flood, triggered by low *Bernd* in July in GER. Hail events appear to be more relevant in BW than in GER. Note that the loss ranking of major events is changed compared to the unadjusted data (cf. Fig. 3.2).

Event occurrence

The number of events resulting from the p90 filter of the total losses is, due to the longer time period considered, higher in BW than in GER (Fig. 5.2). The average annual occurrence of events is comparable in BW and GER (see Fig. A2), as p90 is applied to both datasets. Therefore, the events are not directly comparable with regard to their severity, as BW only comprises an area of about 10 % of GER. Furthermore, note that since BW lies within the study area of GER, it represents a subsample of GER for the period 1997 – 2022.

Approximately half of all damaging hydro-meteorological events were associated with wind. In both GER and BW, around one quarter of all events was related to windstorms and convective gusts, around one third was a flood event, and around one fifth was damaging hail. While convective gusts were the most frequent hazard in BW, windstorms were more common in GER. Mixed flood types were the most common flood hazards in BW, while in GER, pluvial floods were more common. For comparison, analyses based on the comprehensive EM-DAT[1] show that Germany has been affected most frequently by storm events (53 events), followed by flood events (19 events) and extreme temperatures between 1950 and 2013 (Kreibich et al., 2014) and also between 1990 and 2024 (Thieken and Keyserlingk, 2025). These studies provide evidence that a similar ranking in the frequency of different hazard types exists also when using data independent of economic losses. The number of events per year is however lower with the (strong) criteria in EM-DAT (0.5 and 1.5 events p. a. vs. 5–8 events p. a. in our data, see Fig. A2).

[1]EM-DAT includes events if one of the following criteria is fulfilled: (1) At least 10 fatalities; (2) at least 100 people affected; (3) a state of emergency has been declared or an international appeal for help has been issued. See `https://doc.emdat.be/docs/protocols/entry-criteria/`.

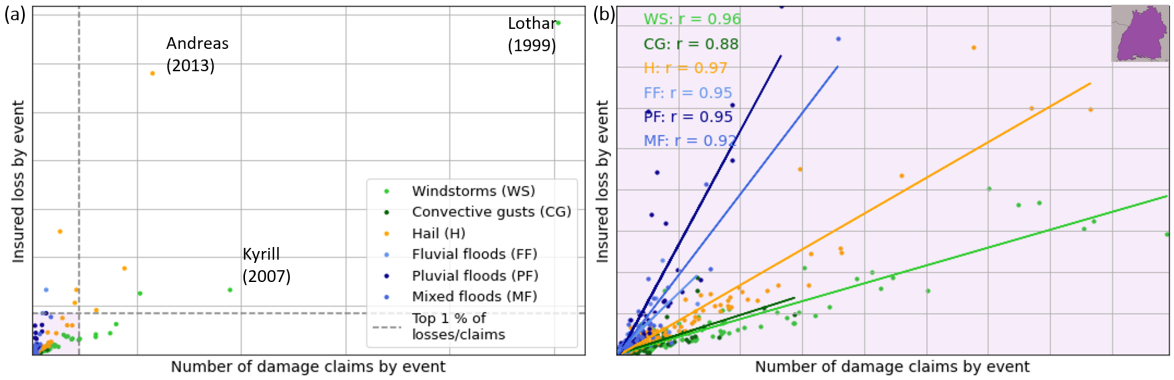

Figure 5.3.: Study area BW: (a) Total insured losses versus number of claims for building insurance regarding different hazard types (colors), from 1986 to 2023; events defined and aggregated using p90 and POT. Three of the most damaging events in terms of losses and/or claims are indicated (*Andreas*, *Lothar*, and *Kyrill*). (b) As in (a), but without major damaging events, including linear fit and Spearman correlation coefficients for the respective hazard type (all significant at $p < 0.05$).

Major events and skewness

In BW, windstorm *Lothar* (storm-force winds from 25 to 27 December 1999, event defined by high claim and loss values between 25 and 29 December 1999) and hailstorm *Andreas* (storm-force wind on 27 and 28 July 2013, event defined by high claim and loss values between 24 and 28 July 2013) were the major loss events in the past decades (see Fig. 5.3a). These two events were responsible for 21 % of the total cumulative insured losses in the entire period (17 % of all claims). When taking into account further events, hailstorm *Queenie* (28–29 June 2006) and two other hail events (19–24 June 2002 and 22 July 1995), the Christmas flood of 1993 (20–22 December), and windstorm *Kyrill* (17–19 January 2007) dominate, together with the hailstorm *Andreas* and the windstorm *Lothar*, overall losses and claims. Both major windstorms were associated with a particularly high number of damage claims, whereas the hail events triggered higher losses (see Fig. 5.3a). In GER, high losses were also dominated by several major events (see Fig. 5.4). Before adjustment for inflation and the annual changes of the portfolio, the 2021 western Germany flood, triggered by low *Bernd* was the single major event (cf. Fig. 3.2). After adjustment, losses of flood event *Bernd* and windstorm *Kyrill* are comparable (14 % of cumulative losses). Among the most severe events in Germany are hailstorm *Andreas* and windstorm *Lothar*, which also affected BW, and rank third and fourth nationwide in terms of losses. Additionally, a series of flood events during the end of May and the beginning of June in 2013 (low-pressure systems *Christoph, Dominik, Frederik and Günther*), as well as a series of windstorms from 14 to 19 February 2022 (*Dudley, Eunice, Franklin*) and a single windstorm from 15 to 20 January 2018 (*Friederike*) triggered major losses.

The loss distribution in the dataset is strongly right-skewed. The Gini coefficient, which is a statistical measure for inequality of a statistical distribution (1 relates to perfect inequality) equals 0.85 (BW) and 0.79 (GER) when comparing insured losses per day throughout the dataset. In general, the top 1 % of all events in BW (area without shading in Fig. 5.3a) were responsible for 45 % of the insured losses

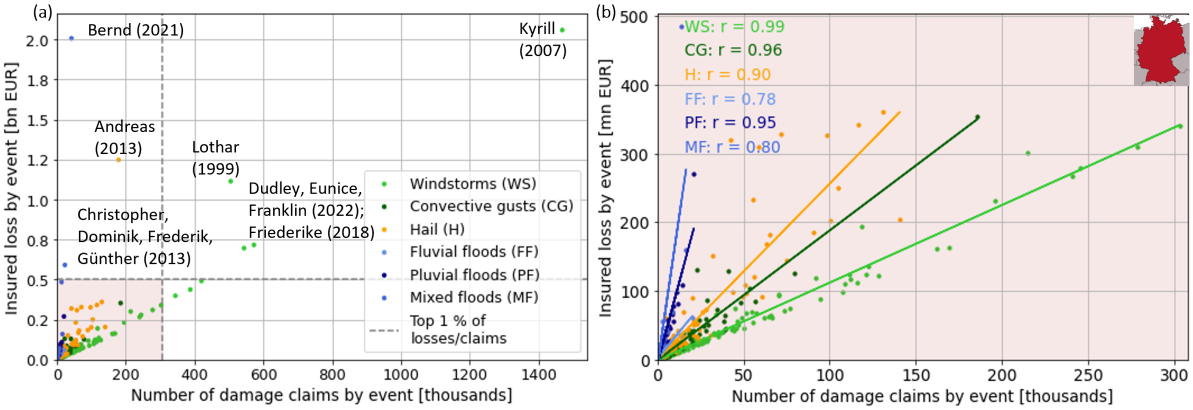

Figure 5.4.: Same as Fig. 5.3, but for the study area GER (1997/2002–2023).

throughout the time series. In Germany, 1 % of events caused only one third (34 %) of overall losses. To address this skewness, data is often log-transformed (Wilks, 2006), as is done here for some analyses (see this chapter and Chapter 6). Other studies on natural hazard losses in Europe find a similarly skewed loss distribution. A study by the European Environment Agency (EEA) showed that 1 % of weather- and climate-related extreme events accounted for 28 % of insured losses in Europe between 1980 and 2022 (EEA, 2023). Flood and windstorm losses in the UK (1998–2013) were shown to be dominated by single events as well (Hillier et al., 2015). With respect to hail, Schmid et al. (2024) found almost log-normally distributed values between building value and damage sum in Switzerland (2002–2021), where 90 % of the total damage to buildings was caused by the strongest 30 hail events, and a single event (28 June 2021) caused 35 % of the total losses.

Annual and mean losses

Average annual losses from hydro-meteorological hazards in GER and BW are dominated by windstorms and hail events (see Fig. 5.5). BW was most affected by hail losses, reflecting hail occurrence (see Sect. 2.1.2 and below) and windstorms, while annual insured losses in GER were primarily driven by windstorms. The influence of major events is also evident in annual losses – about half of all windstorm losses in GER were caused by the top 1 % of events, and even more than half in BW. Three quarters of average annual losses from mixed flooding in GER were caused by the top 1 %, which mainly include *Bernd* and the flood series of 2013 (see Fig. 5.4a). Most fluvial flood losses and more than half of annual hail losses are attributable to the top 1 % of events in BW (but not in GER). Comparative analyses using EM-DAT identified flooding and storm events, presumably including SCSs, as the main drivers of economic losses from natural hazards in Germany between 1990 and 2024 as well (Thieken and Keyserlingk, 2025). Between 1950 and 2013, floods caused more than half of the total losses in Germany, and storm events contributed to about 45 % (also based on EM-DAT, Kreibich et al., 2014). Across EU member states (1980–2020), economic losses from weather- and climate-related extreme events were

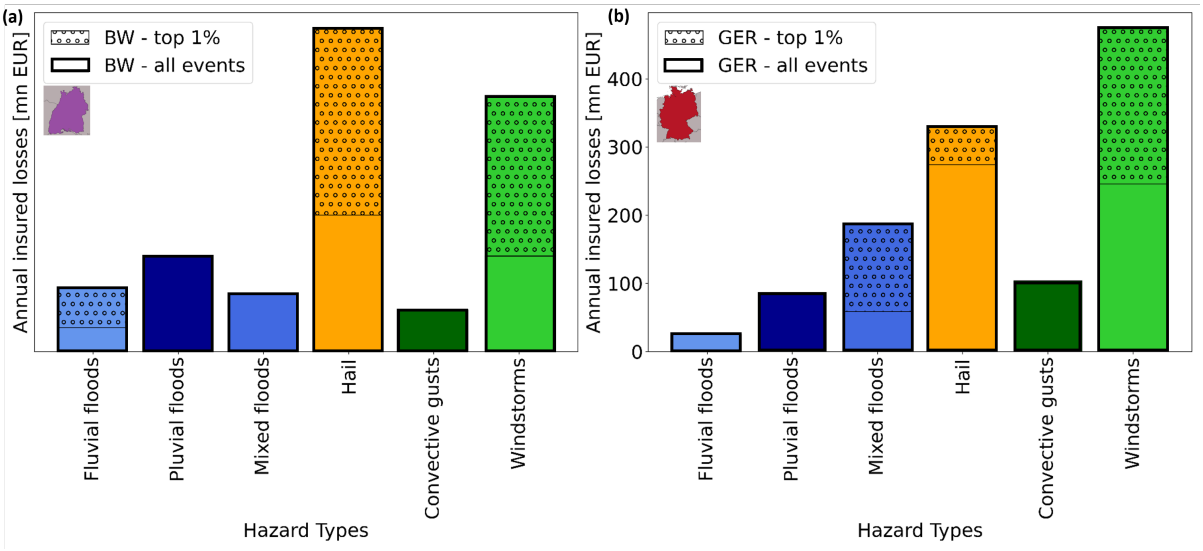

Figure 5.5.: Average annual losses by hazard type for (a) BW (1986–2023, scale omitted for confidentiality reasons) and (b) GER (1997/2002–2022), where the whole bar represents all events, and hatched parts represent the top 1 % of losses and claims.

roughly evenly split between (according to their definition) meteorological events – presumably primarily windstorms and SCSs – and hydrological events, such as floods, with each category contributing more than one third to total losses. The remaining losses were attributed to heatwaves and other climatological events. In contrast to total economic losses, insured losses were dominated by storm damage: up to two-thirds were attributable to meteorological events, while hydrological events accounted for less than 30 % of insured losses (EEA, 2023). The difference can be explained by the lower insurance density for flood risks compared to storms also in Europe, which was estimated at less than 27 % in the European Union (1998–2018; Insurance Europe, 2018). This dominance of insured losses by windstorms and SCSs is also apparent from our data, particularly when excluding flood event *Bernd*. In BW, insured losses were primarily driven by windstorms and SCSs, with major hail events being the dominant contributors. However, the results of the studies regarding Europe, and the limited insurance density regarding flooding suggest that total economic losses are driven by flooding and storm damage mutually.

Although losses were clearly dominated by single exceptional events, considering medium- and small-scale events is necessary, for example, to fully evaluate climate change impacts and support adaptation (EEA, 2023). Furthermore, severe impacts do not always result in extreme losses, particularly in the case of smaller-scale events. The reason for this is twofold: Firstly, insurance density varies, and secondly, we only consider losses relating to building insurance. When excluding the top 1% of loss and claim values (bars without hatching in Fig. 5.5), losses of different hazard types are within a similar range, with hail and windstorms still being associated with the highest annual losses (around € 250 million in GER). Without these major events, the amount of insured losses is strongly correlated with the number of damage claims per hazard type (see Fig. 5.3b and Fig. 5.4b). The relationship between claims and

losses can be described by a linear function for each hazard type, which allows insurers to estimate financial risk more reliably and consequently to set risk premiums, for example. The linear relationship also implies that the mean loss per claim for each hazard type remains relatively stable, regardless of the magnitude of the event, even in cases where events impact a large area (that is, a high number of claims). Consequently, the number of damage claims can be used to estimate total damage when absolute loss amounts are unavailable due to, for example, privacy issues. In addition, mean loss patterns, defined as losses per damage claim, differ substantially depending on the hazard type. For both study areas, floods cause the highest mean losses of all hazard types, while convective gust events and mainly large-scale storms cause the lowest mean losses (without major events, compare regression lines in Figs. 5.3b and 5.4b).

One potential explanation for the observed differences in mean losses is the type of damaging hazard: Large-scale storms affect a large area, much of which only suffers low-level damage, such as some removed roof tiles. By contrast, hail events occur locally and have a higher potential for damage. More parts of a building become susceptible (Stucki and Egli, 2007). Hail damage can result from pierced roof tiles, roof windows, solar installations, façades, shutters or winter gardens (see Chapter 2). If the roof is damaged, additional damage can result from subsequent rain events (even of moderate intensity), where water can enter the building through the roof (Stucki and Egli, 2007). Floods are more likely than hail or storm events to damage not only the exterior, but also the interior of a house, which is why the highest mean losses result from flood events. Once the water has entered, entire floors can get flooded (Merz et al., 2010), and reconstruction is a tedious and expensive undertaking (e. g., Mohr et al., 2023). This is particularly relevant given that insurance against floods for residential buildings is not mandatory in Germany (GDV, 2023b).

For the flood hazard types, pluvial events caused the highest mean losses (without major events, Fig. 5.3b) and annual insured losses in BW (Fig. 5.5a), although mixed floods were the most common flood hazard. By contrast, fluvial floods played only a minor role due to the absence of an extreme fluvial flood event during the considered period. Since other regions in Germany have experienced severe floods in recent decades (e. g., the Elbe flood in 2002 or the flood of the Ahr and other rivers in western Germany in 2021), BW appears to be an exception in this regard. However, the most severe fluvial flood events, including the Christmas flood of 1993, also contributed more than half of the total losses from fluvial flooding. In GER, mixed floods were associated with the highest mean and annual losses (Fig. 5.5b), while pluvial floods were associated with the highest losses excluding the top 1% of events. Therefore, while damage from the top 1 % of events was mainly caused by the mixed flood event *Bernd* in GER and by the fluvial flood during Christmas 1993 in BW, average annual losses of the remaining events were – due to their frequent occurrence – dominated by pluvial floods both in BW and GER (see Fig. 5.2b).

Within storm damage events, cumulative losses – both with and without major events – were higher for windstorms than for convective gusts by a factor of two (without major events) and more than five (with major events) in BW and GER (see Fig. 5.2). Convective gusts, however, occurred more frequently than windstorms in BW (see Fig. 5.5). When excluding major events, convective gusts were associated with higher mean losses than windstorms in both domains. Hail caused losses comparable to those from windstorms in both GER and BW, which even exceeded those of windstorms in BW. Without major events, hail caused the highest losses of all hazards in both regions.

In summary, a relatively small number of major large-scale (or mixed) flood and storm events caused the largest amount of total damage in Germany in the past 25–35 years. Regarding convective hazards, pluvial floods and convective gusts only become relevant after excluding major events in BW and GER. In this regard, hail hazard constitutes an exception, with the potential for extreme losses, particularly in BW, caused by a small number of major loss events.

5.2 Seasonality in hazard occurrence

A strong seasonality of all hazards is evident in both BW and GER, highlighting a shared pattern between the two regions (see Fig. 5.7). The majority of events occurred between May and August, with a second peak between December and January. The remaining seasons, autumn and spring, were less relevant in terms of incurred damage. Throughout the time period considered, most major damaging hazards occurred in December and January as well as in June and July (see Fig. 5.6).

All convection-driven hazard types, that is, hail, convective gusts, and pluvial floods, occur mainly between May and August. This seasonal occurrence is due to the predominance of convective systems in central Europe during the summer half-year, when atmospheric conditions favor the formation of deep moist convection (see Chapter 2; Punge and Kunz, 2016; Púčik et al., 2019). The number of events peaks in June or July, with significantly fewer events in August and even fewer in May, coinciding with the start of the convective season. Previous studies also found peaks of SCSs in June or July: Large hail reports are most frequent in June in central Europe (in July in western Germany, Púčik et al., 2019), whereas hail damage occurs most often between mid-June and mid-August (see also Chapter 2, Hohl et al., 2002). The highest convective gust activity is also observed in June and July, with the absolute maximum in the second half of June and in July (e. g., Dotzek et al., 2009; Mohr et al., 2017). Flood damage between April and September is dominated by mixed floods in BW, while in GER, damage in June and July specifically is driven by pluvial floods. Mixed flooding occurs mainly between May and August as well, but with a less pronounced seasonality compared to the convection-driven events. Across Europe, precipitation extremes also show a strong seasonal cycle, peaking in June and July (Barton et al., 2022). Major fluvial and flash flood disasters in Europe occurred most frequently in autumn from 1950 to 2005, followed by the summer months as the second most common period (Barredo, 2007).

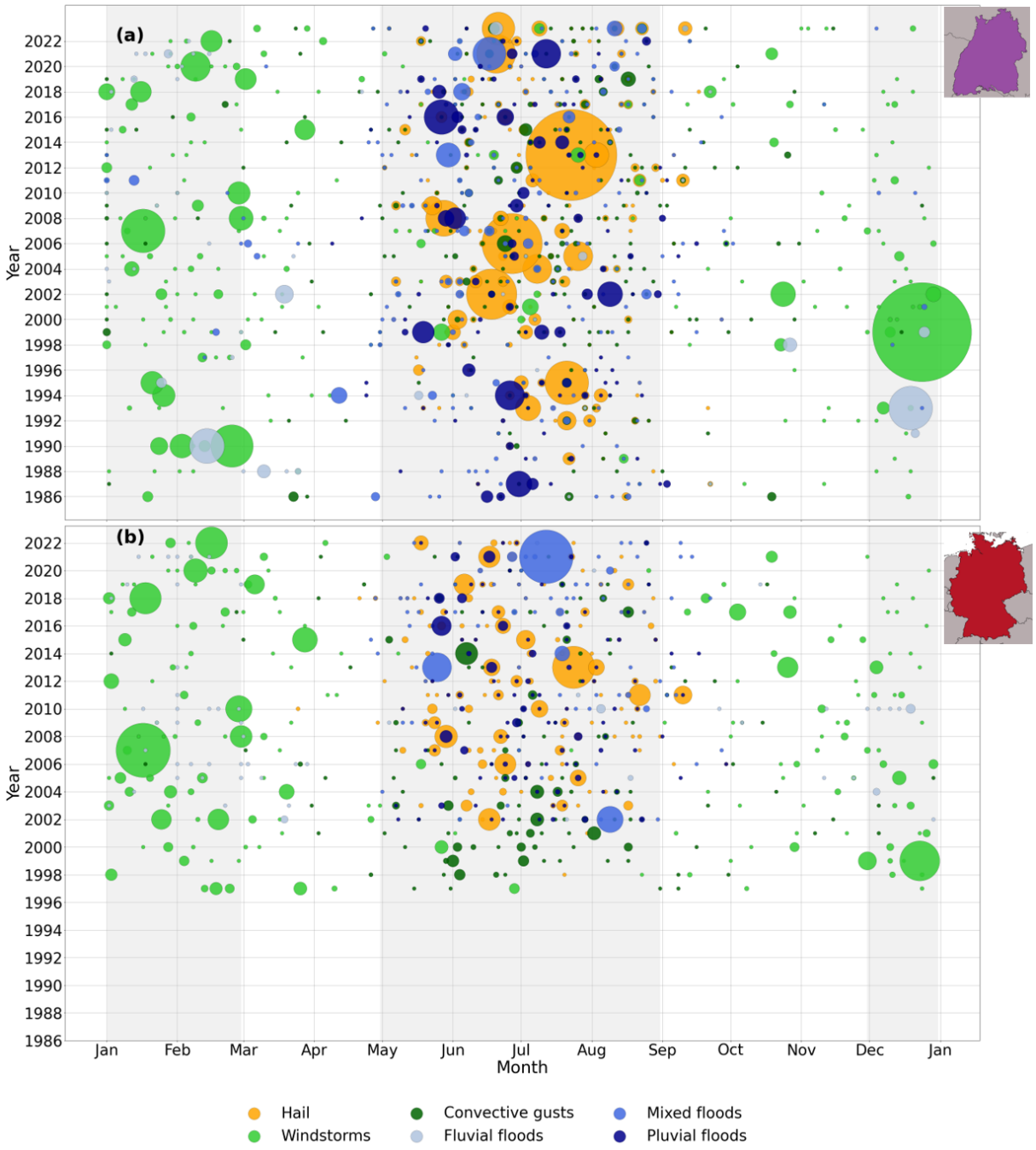

Figure 5.6.: Distribution of events throughout the year and across the years in (a) BW and (b) GER, where the size of the dots represents losses (different scales for (a) and (b) for better distinction). Grey areas represent the months with the highest occurrence (May–August and December–February).

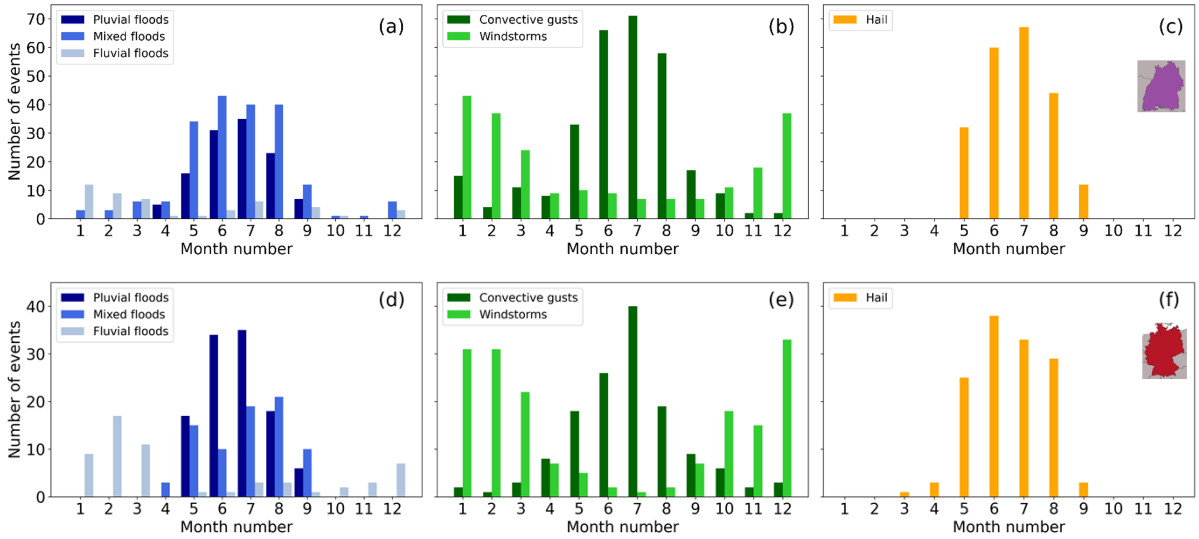

Figure 5.7.: Distribution of events identified for the study areas BW (upper panel) and GER (lower panel) with POT in p90 aggregated by month from 1986 to 2023 (BW, upper panel) and from 1997 to 2022 (GER, lower panel), regarding damage by (a)+(d) flooding triggered by pluvial, fluvial and mixed floods, (b)+(e) large-scale storms and convective gusts, and (c)+(f) hail.

During the winter months, mainly windstorms and fluvial floods are responsible for damage in BW and GER, but with a lower frequency (especially in case of fluvial floods) than the convective extremes in summer. Most fluvial floods occur between January and March both in BW and GER. Across Europe, secondary peaks in precipitation extremes can also be observed in December and January (Barton et al., 2022). In a study on trans-basin floods in Germany (1952–2002), the major part (64 %) was recorded in hydrological winter, with the most severe events also being winter events (Uhlemann et al., 2010). Damaging windstorms show a peak in December (GER) and January (BW), but the fluctuations during winter are marginal. The distribution throughout the winter follows the general seasonal distribution of extreme wind speed (Gliksman et al., 2023).

In summary, a strong seasonal pattern in the occurrence all hazard types is evident in both GER and BW. While a smaller number of large-scale events (windstorms and fluvial floods) is dominant in the winter months (December–February), a higher number of local extremes (pluvial flooding, convective gusts and hail) become relevant between May and August.

5.3 Spatial distribution of hydro-meteorological hazards across Germany

The impact of natural hazards depends heavily on the region in Germany, with some regions being significantly more affected by certain hazard types than others. In the following, the hazard types are compared based on the loss ratio, which equals the total sum of (normalized) losses by district divided by the total sum insured for each district. This approach is taken because of the varying insurance density

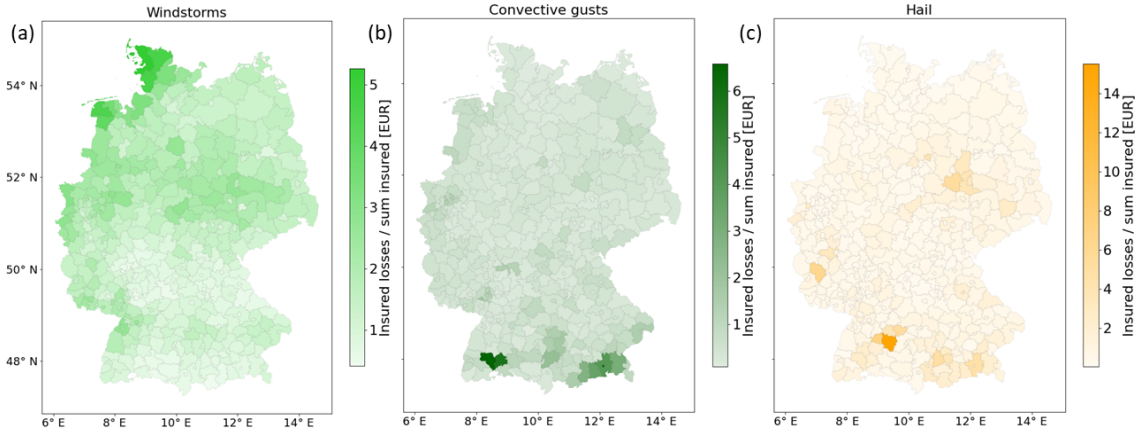

Figure 5.8.: Loss ratio (total insured losses divided by the insured sum) cumulated over 1997-2022 per administrative district in GER with respect to (a) windstorms, (b) convective gusts, and (c) hailstorms. Note that the scales of the color bars differ in order to visualize differences for all hazard types; for a comparison of losses between hazards see Fig. 5.5. Data for the administrative districts ©GeoBasis-DE / BKG 2023, License dl-de/by-2-0, available at `www.govdata.de/dl-de/by-2-0`.

across Germany. An analysis with respect to absolute insured losses can be found in the Appendix (Fig. A5).

The spatial distribution of windstorm losses across Germany shows a strong gradient from north(-west) to the south (Fig. 5.8a). As expected, losses are highest at the coast of the North Sea, due to higher wind speeds because of the smaller distance to the North Atlantic storm tracks and the lower friction over the water (see Sect. 2.1.1). Local-scale variations due to orography, as described, for example, in Hofherr and Kunz (2010), are not visible. However, the limited spatial resolution at the level of administrative districts (about 1 000 km^2 on average) may obscure finer-scale loss patterns and localized hazard dynamics, particularly in topographically complex regions. As seen from other studies, the northwestern coast is also the area with the strongest gusts (Fig. 2.6a), the highest wind loads (Fig. 2.6b) and the highest losses in Germany as estimated from building footprint data and damage curves (Fig. 2.6c, Koks and Haer, 2020). Secondary loss hot spots are Baden-Württemberg and the Altmark (southwest of Berlin). However, when considering absolute losses, the latter area is less affected (see Fig. A5). When the metric is changed to absolute insured losses, the western part of North Rhine-Westphalia, bordering the Netherlands, becomes more prominent.

With respect to losses from convective gust and hail events, southern Germany was most affected in the 25-year-period considered. Previous studies have also found a north-to-south gradient with respect to potential hail days and hail losses (Sect. 2.1.2; e. g., Puskeiler et al., 2016). However, the loss distribution is more skewed than what is found by the literature regarding the occurrence of convective gusts (Fig. 2.10a), potential hail days (Fig. 2.10b) and even loss data based on NatCatSERVICE (1980–2018), a database of Munich RE (Fig. 2.10c). For example, Bavaria seems to be less affected by losses from

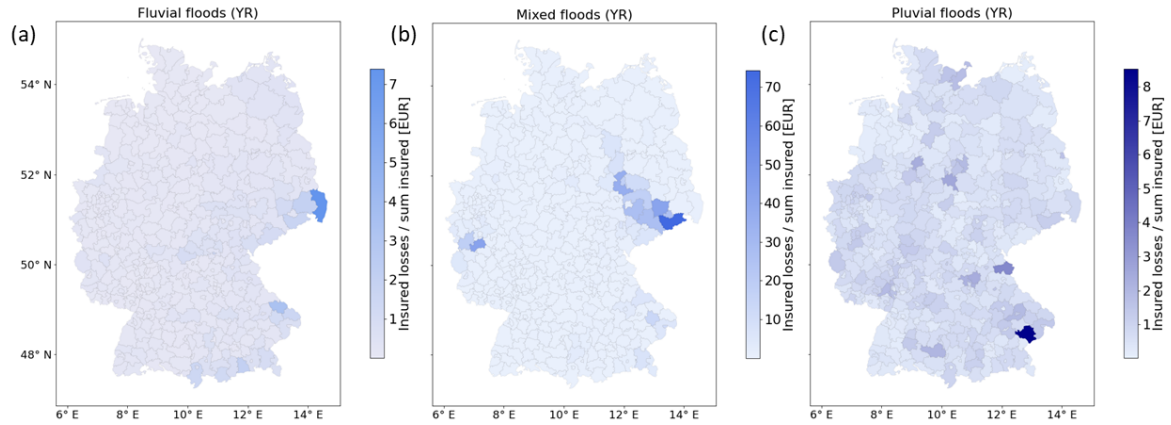

Figure 5.9.: Loss ratio (total insured losses divided by sum insured) cumulated over 1997-2022 per administrative district in Germany with respect to (a) fluvial, (b) mixed, and (c) pluvial flooding. Note that the scales of the color bars differ in order to visualize differences for all hazard types; for a comparison of losses between hazards see Fig. 5.5. Data for the administrative districts ©GeoBasis-DE / BKG 2023, License dl-de/by-2-0, available at `www.govdata.de/dl-de/by-2-0`.

SCSs in the present data than what has been shown in previous studies (Sect. 2.1.2; e. g., Mohr et al., 2017). One potential reason is that the famous Munich hailstorm in 1984, the most damaging event in the last 30 years (GDV, 2024d), is not part of the present dataset. Within our dataset, the district of Reutlingen (center of BW, at the eastern edge of the Swabian Jura) clearly stands out, which is due to the exceptional hail event *Andreas* (28 July 2013, see also above; Kunz et al., 2018) hitting this district particularly badly. These findings show that also the losses on a district-level can be dominated by single events. Excluding the top 1 % of losses (not shown), the most affected district is the Salzlandkreis (south-west of Berlin), also dominated by a single event on 11 September 2011. Convective gust events led to the highest damage in the pre-alpine regions in the southeast of Bavaria (specifically Upper Bavaria and Chiemgau). The literature also shows a north-to-south gradient regarding convective gusts (see Chapter 2; Mohr et al., 2017; Gatzen et al., 2020), but this hot spot in Upper Bavaria is not visible in observation data, which could have its cause in the limited spatial resolution of the weather station network. Total insured losses from convective gusts are highest in southeast Bavaria, Berlin and North Rhine-Westphalia (Fig. A5), which is likely due to higher insured values (cf. Fig. A3).

With respect to the loss ratio, fluvial and mixed flood losses mainly affected eastern Germany and especially Saxony (see Fig. 5.9a, b). For fluvial flooding, an east-to-west gradient in severity is apparent. A building-level study found the highest number of affected properties of flood-affected properties also in Saxony, with almost 3 % of properties located in flood-prone areas (GDV, 2024a). Absolute mixed flood losses (see Fig. A5) are dominated by the 2021 western Germany flood, triggered by low *Bernd*, with the highest losses in the Eifel region (districts of Ahrweiler and Euskirchen). Similar to hail, the loss ratio for pluvial floods in a single district far exceeds that in other districts. The pluvial floods loss ratio is also dominated by a single event, namely a regional flash flood during the end of May and beginning of

June in 2016 (Passau, eastern Bavaria). Absolute pluvial flood losses are highest in BW, with a second hot spot in North Rhine-Westphalia. This spatial pattern closely mirrors the total insured values with respect to other natural hazards (see Fig. A3), indicating that differences in pluvial flood damage are rather caused by differences in the insurance density than by meteorological variations. A recent study based on the same data and short-duration rain events (that is, mainly pluvial flooding) also shows the random occurrence (see Fig. 2.14, GDV, 2019), and finds the highest losses in western Germany. However, the study finds a bias towards elevated areas for longer events, which is not visible on the district level for any flood type. The variation in flood impacts across Germany can partly be explained by differences in population density and settlement patterns. For example, in the Mecklenburgische Seenplatte district in northeastern Germany, there is a high density of water bodies but a relatively low population density, resulting in a relatively small number of flood-prone properties. In contrast, areas with dense settlement along rivers, such as the Mosel and the Ahr (e. g., the districts of Cochem-Zell and Ahrweiler), or along the Elbe in Dresden, show much higher exposure (GDV, 2024a).

In summary, Germany can be split into four broad regions regarding the most prominent hazards: While windstorms primarily affected the northwest of Germany in the 25-year time period considered, the south(west) was most affected by losses from SCSs. Flood losses (normalized) were highest in eastern Germany, except during the exceptional flood event in western Germany in 2021 (low *Bernd*). These findings can be explained meteorologically and is in line with expectations (see also Chapter 2): the northwest is relatively flat and often affected by low-pressure systems, making it more susceptible to windstorms; SCSs occur most frequently in the southwest, as shown by radar-based statistics (e. g., Puskeiler et al. (2016)); and the east is prone to flooding due to Vb low-pressure systems.

5.4 Trends in the occurrence of different hazards

Trends regarding annual losses were investigated by hazard type for GER (see Fig. 5.10) and BW (see Fig. A7). Losses were adjusted for inflation (see Sect. 4.1) and here refer to cumulative losses above p90. All hazard types generally show a high annual variability, in particular hail events and windstorms.

Windstorm losses showed no clear trend in Germany over the past 25 years (Fig. 5.10a). The lack of a trend is in agreement with other studies, who have also found high annual and decadal variability in the occurrence of windstorms in Europe (see Chapter 2.1.1; Feser et al., 2015; Cusack, 2023). Since the 1990s, there has been a decline in damaging windstorms, which is also reflected in European normalized windstorm losses (1979–2014, Dawkins et al., 2016; Cusack, 2023).

Convective gust losses across Germany also decreased over the past decades, with the reduction being statistically significant (Fig. 5.10b). Considering the longer time period in BW, however, there is a slight but significant increase from 1986 to 2023 (see Fig. A7), pointing to the regional differences in the hazard. In turn, hail losses have increased both in Germany and in BW (both not significant). Other studies

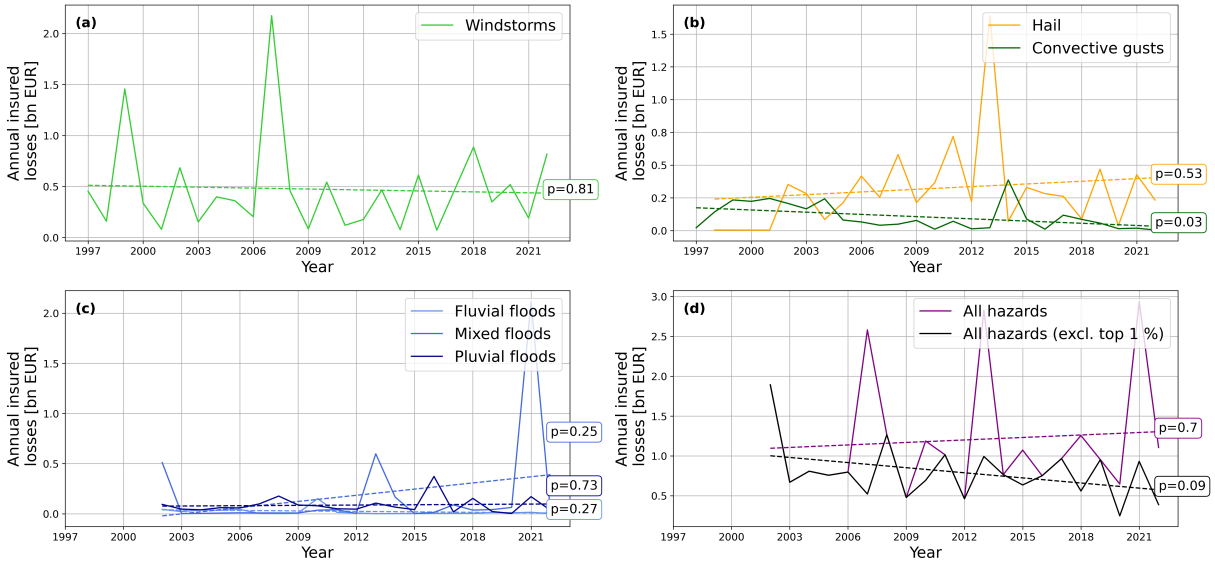

Figure 5.10.: Total losses across Germany by hazard type and year (1986–2023), for (a) windstorms, (b) convective gust events and hail, (c) flood events and (d) all hazards with and without the top 1 % of losses and claims.

also found contrasting trends with respect to the occurrence and occurrence potential of past SCSs: While the frequency of conditions favoring hail have increased over the past decades (see Chapter 2.1.2; e. g., Rädler et al., 2018), observation data do not show this clear increase but rather a high variability (Mohr et al., 2017; Piper and Kunz, 2017) or even negative trends (Augenstein et al., 2024). Global and European SCSs-related losses have increased in recent decades, where each of three recent years (2021–2023) exceeded $USD 5 billion (approx. € 4.4 billion), which can mainly be attributed to macroeconomic factors such as inflation (Swiss Re, 2024). Without adjusting for inflation and considering a longer time period, an increasing trend can also be found in Germany regarding storm and hail losses (1976–2023, GDV, 2024b).

Regarding flood events (Fig. 5.10c), no consistent trend is found. Mixed flood losses have increased, but this increase is only significant for BW (not GER). In contrast, both pluvial and fluvial flood losses have decreased in GER, while pluvial flood losses increased in BW, again pointing to the localized nature of extremes (both not significant). In central Europe, an increase in flood-related hazards is observed, particularly in terms of damage (see Chapter 2.1.3, Becker et al., 2014; Paprotny et al., 2024), which has been mainly attributed to increased exposure (Paprotny et al., 2024). However, when considering a longer time period and exposure-adjusted losses, no upward trend in flood losses is evident in Europe as well (Barredo, 2009; Paprotny et al., 2018). Some studies even indicate a decrease in recent decades (Paprotny et al., 2018). Global flood damage does not show a clear trend either (1984–2023, Swiss Re, 2024).

When considering all types of hazards in combination (Fig. 5.10d), there is a slight upward, but not significant trend in overall annual losses (both GER and BW). This trend becomes weaker in GER when

the top 1 % of events are excluded. In BW and for the longer time period, the increase corresponds to approximately € 1.5 million per year (adjusted for inflation to the base year 2022). Trends for overall Europe in economic losses from weather- and climate-related events between 1980 and 2020 also differ depending on the data source, which can partly be explained by substantial year-to-year fluctuations and the impact of implemented adaptation measures (EEA, 2023).

In summary, no clear upward trend is visible for losses from individual hazards, with a high annual and multi-annual variability and some regional differences regarding convective hazards. These findings are consistent with other studies. Considering all hazard types together indicates a slight upward trend, which is, however, likely influenced by socio-economic factors. The contribution of socio-economic factors to trends has been acknowledged in the context of flooding (Paprotny et al., 2024), windstorms (Barredo, 2010), and SCSs (Swiss Re, 2024). With respect to building insurance, additional factors may include shifts in public behavior, regulatory changes, and evolving building vulnerability due to changes in construction materials.

5.5 Conclusions

This chapter presented the loss distribution of major hydro-meteorological hazards in GER (1997/2002–2022) and Baden-Württemberg (1986–2023). It was evident that few events with extreme losses dominate the overall annual losses, but relationships between losses and claims remain constant when excluding the top 1 % of events. All hazards follow a strong seasonality, particularly in GER, with windstorms and fluvial floods mainly occurring between December and February. Convective extremes peak in June or July and are expected between May and August. A distinct pattern was also visible in the regional distribution of hazard types: While impacts of windstorms dominate in the northwest, the east is characterized by higher flood damage, and southern Germany is more prone to damage from severe convective storms. Across the time series, no consistent trend is found by hazard and for all hazards. This shows that while regional differences and the intra-annual variability of damaging hydro-meteorological hazard can be captured well, longer-term trends remain unclear. Sub-seasonal variability will be examined in the next chapter (Chapter 6).

6. Temporal clustering of multiple hazards

This chapter presents results regarding the temporal clustering of loss-related extreme weather events in Baden-Württemberg (BW) and Germany (GER). For BW, the two methods of event definition, Peaks-Over-Threshold (POT) and Hours Clause (HC), are compared. For Germany, only the POT method is applied. First of all, Sect. 6.1 answers the question of when clusters occur, with respect to calendar years and sub-seasonal clustering periods identified by the counting method (see Sect. 4.5.1). Subsequently, Sect. 2.4 discusses when clustering is significant by investigating which sub-seasonal clusters deviate significantly from a homogeneous Poisson process (see Sect. 4.5.2). Sect. 6.3 then examines the clustering of losses by comparing isolated and clustered events, as well as annual loss clustering metrics. Finally, Sect. 6.4 presents the temporal development of clusters.

6.1 Random clustering: When do clusters occur?

This section examines the distribution and clustering of events throughout the years as well as during May–August (MJJA) and December–February (DJF) for both single hazard types and combinations of different hazard types.

6.1.1 Clustering on the timescale of calendar years

Analyzing temporal clustering of damaging events in BW on the timescale of calendar years with POT (Fig. 6.1a) reveals that the number of events varies substantially over time. Most conspicuous is a pronounced peak in the early 2000s for both storm hazards, a peak between 2017 and 2019 for hail events, a smaller number of storm and hail events before 1998, and an especially high inter-annual variability of the flood hazard types. Due to the fixed and therefore on average longer duration (see also Sect. 6.2.1), the HC event definition (Fig. 6.1b) generally identifies a smaller number of events than POT, although the general distribution of events throughout the years is similar. The variability is comparatively high with the HC definition. This may be explained by events being more concentrated in time with a fixed method and the stronger effect of small changes. For both definitions, we see a recurring pattern throughout the years, with some years showing an exceptionally small number of events. This pattern could be related to decadal variability, which is a well-known pattern with respect to windstorms (e. g., Feser et al., 2015) and hail (Mohr et al., 2015a).

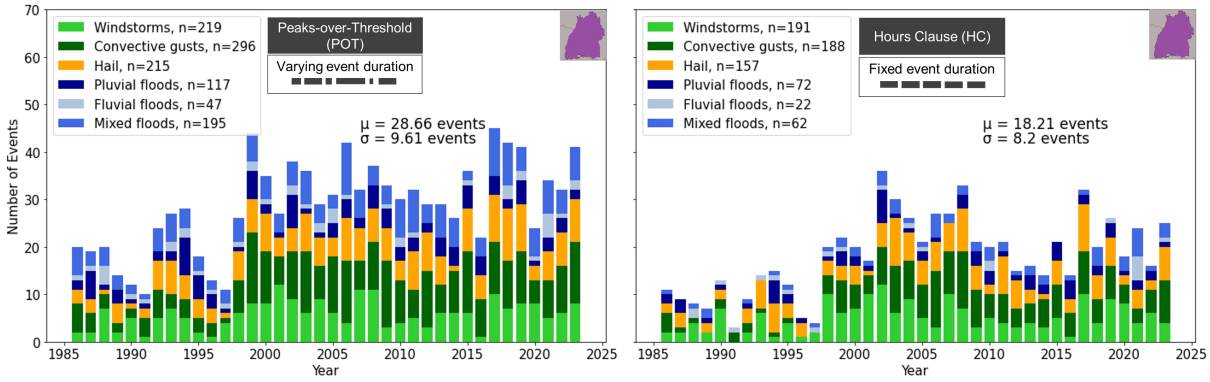

Figure 6.1.: Study area BW: Number of events per hazard type and year with (a) event definition with POT, (b) event definition with HC, for events defined by the 90th percentile of losses and claims (see Sect. 4.2). Mean event numbers per year (μ) and the standard deviation of event counts (σ) are annotated.

For the study area of Germany with events identified by POT (see Fig. 6.2), a recurring pattern is also visible, especially with an increase in storm damage events from 1997 until 2001 (note that the data for the flood hazards were only available as of 2002). The distribution of events between 2002 and 2008 is also similar in both study areas. 2010 stands out in GER, with a very high number of flood events, which constitute more than half of all events. The highest event numbers were recorded in the periods 2009–2011 (GER) and 2017–2019 (GER and BW with POT), which can be identified as clustered years. The mean number of events defined by POT is similar for both study areas, with slightly fewer than 30 events occurring each year. However, the range and the variability in GER is generally lower than in BW (compare standard deviation σ in Figures 6.2 and 6.1). The lower variability of event occurrence across the larger study area suggests that the regional differences (see Sect. 5.3), also in event timing, lead to temporal clustering effects canceling out when averaged over the larger region.

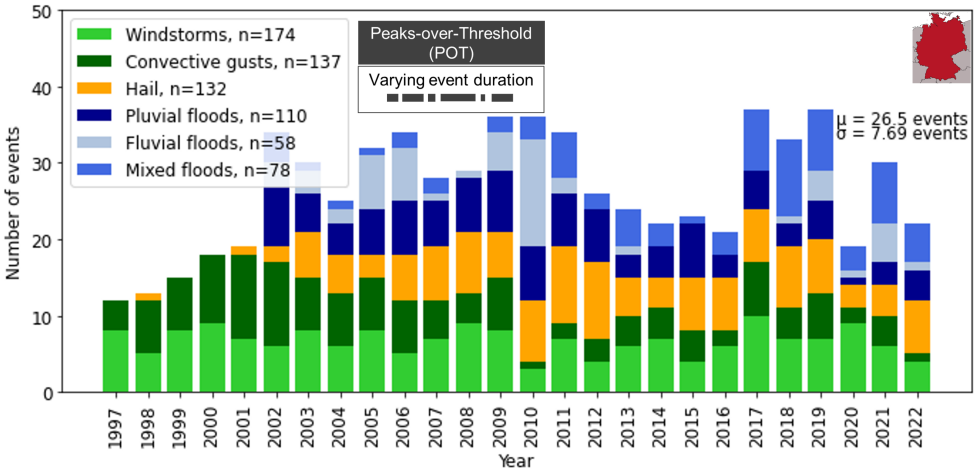

Figure 6.2.: Same as Fig. 6.1a, but for GER.

6.1.2 Sub-seasonal clustering: Counting

To investigate also multi-hazard clusters, the hazard types were combined as described in Sect. 4.4. The combinations between events of different hazard types are referred to by acronyms that combine those of the single hazard types (Pluvial Floods (PF), Mixed Floods (MF), Fluvial Floods (FF), Large-scale Storms (LS), Convective Gusts (CG), and Hail (H)). A combination of pluvial floods, convective gusts and hail, for example, is therefore referred to as PF-CG-H. All combinations between the three flood hazards and the two storm hazards as well as hail were computed. Within the storm and flood hazard types, no combinations were analyzed, since the goal is to investigate the combination of fundamentally different hazard types.

Figure 6.3 shows the resulting cluster periods for (a) single and (b) combined extremes for a clustering window of $w = 21$ days and events identified by POT for BW. The 21-day window is well suited for the quantification of subseasonal clustering, as it includes hydrologically relevant durations. It has been used by a range of studies, such as, for example, Kopp et al. (2021), Tuel and Martius (2022), or Hillier et al. (2025). It furthermore is the longest time period of event identification with HC we are aware of (see Sect. 4.2.2). It is evident that most clusters occur during MJJA, consistent with the seasonal distribution of the events (see also Fig. 5.7). Clusters occurred most frequently in July, followed by June and May. Clusters of convective gusts or combinations of multiple hazard types such as MF-CG and CG-H were most frequent in that period (see Fig. B1). The most damaging combinations were PF-H, followed by CG-H and PF-CG-H. This shows that combinations involving hail are most damaging, while not being most frequent, which can be attributed to the damaging nature of hail (see also Fig. B1). In winter (DJF), we see a much lower number of clustered events, with most clusters starting in December. Predominant in this season are clusters of large-scale storms and FF-LS, which also aligns with the seasonal cycle of these hazards. Fluvial flood clusters are detected less frequently, as the sample is much smaller compared to the other hazards.

Throughout the years, we see a peak of clusters between May and August of the early 2000s, and a secondary peak in recent years, which resembles the general pattern of event occurrence (see, e. g., Fig. 6.1). The early 2000s are also the time period with most damaging clusters (see Fig. 6.5a, and the period with the maximum number of clusters when reducing events to 99th percentile (p99)). This shows that within the time period of 1986–2023, the early 2000s stand out in their clustering behavior, potentially related to decadal variability. Interestingly, the peak of clustering in the early 2000s does not apply to the winter months. Winter clusters were most frequent, and also most damaging, in the 1990s as well as since 2017. Major damaging events often occurred together with other hazards, such as *Lothar* (FF-LS) and *Andreas* (PF-CG-H, see Fig. 6.5a). This is robust to a reduction in event numbers to p99. This shows that while those major loss events drive the damage, they can also be accompanied by other moderately severe events which can exacerbate their damage (e. g., by rain entering a storm-damaged roof).

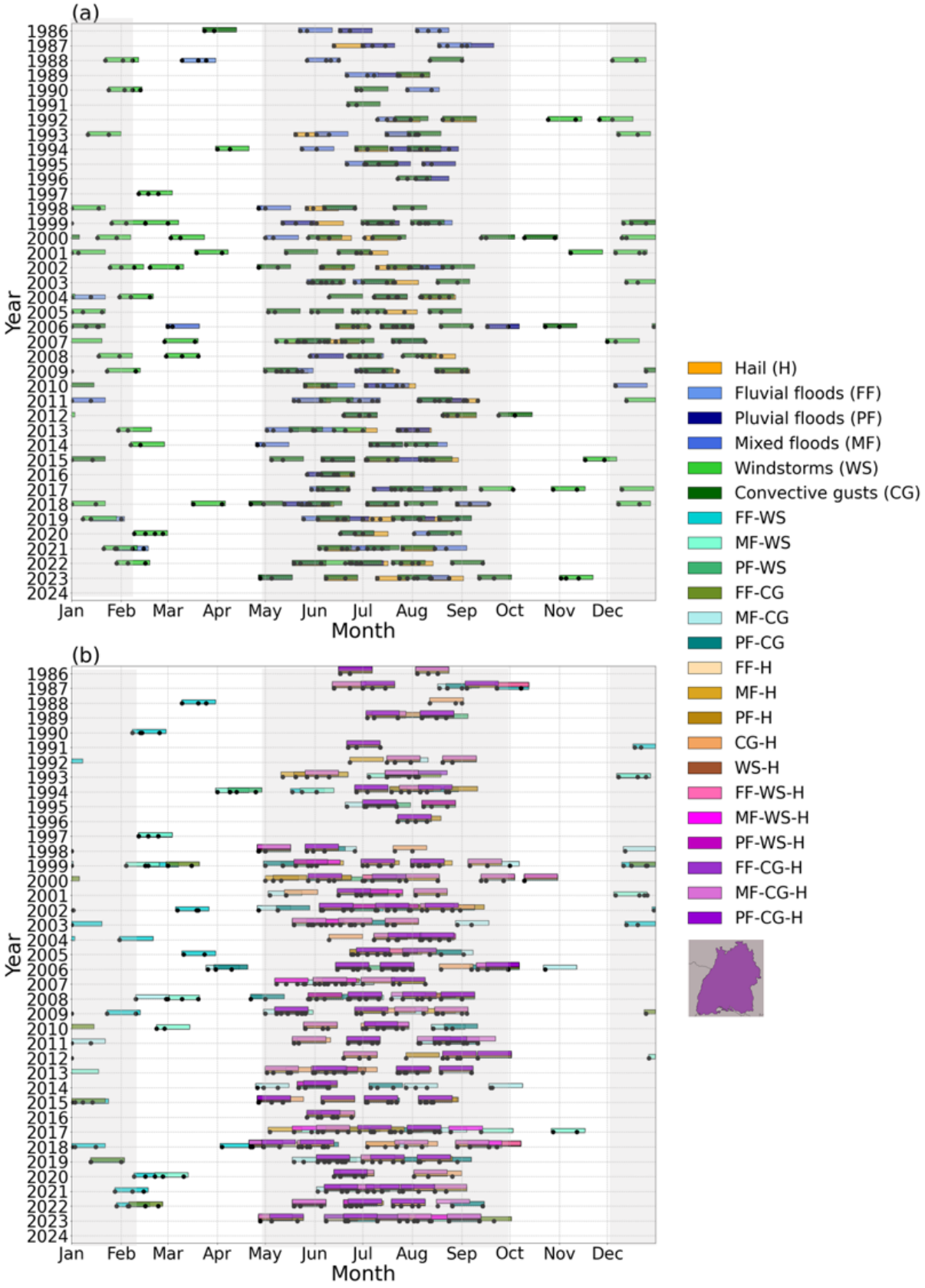

Figure 6.3.: Study area BW: Cluster start by the day of the year plotted against the corresponding year, identified by the counting method with a clustering window *w* of 21 days for (a) single and (b) combined hazard types (p90, POT method). The length of the bars represent the clustering window of 21 days and black dots relate to individual events within them. Grey areas show the seasons May–August and December–February.

> Considering different hazard types, there were very few clusters in winter between 2005 and 2018, which did not relate to a generally lower event number (cf. Fig. 6.1). The number of clusters in summer is also quite low in some of those years, for example, in 2014 and 2015. Seasonal patterns are visible even more clearly with clusters of different hazard types (Fig. 6.1b) than with single-hazard types clusters (Fig. 6.1a). There are almost no clusters between mid-March and mid-April, and similarly very few clusters between the end of September and the end of November. Furthermore, it can be seen that many of the single-type clusters also occur in multi-hazard clusters, particularly the most damaging ones. This shows that many clusters consist of multiple hazard types, but also include multiple occurrences of a single hazard type. Note that the number of events is much higher when assessing clustering with multiple hazard types, that is, naturally, a higher number of clusters can be found.

> When events are identified using the HC method instead of the POT, the number of clusters is reduced (not shown), since the number of events is also lower. However, this mainly relates to the least damaging clusters; the most severe clusters are similar to those detected with the POT method. Using the HC method, some additional clusters are detected, such as a mixed flood cluster in 2021 and several multi-hazard clusters in 2001. CG-H clusters are most frequent as well as those clusters leading to the highest cumulative losses when events are identified by HC.
> These results are tested for robustness by increasing the clustering window w. For $w = 28$ days, for example, the number of clusters is higher in summer, and slightly shifted to earlier start dates in winter.

In GER, most patterns look similar (see Fig. 6.4). Generally, the seasonal occurrence of clusters is even more pronounced compared to BW, with a low number of clusters from March to May and September to November. The large number of clusters in recent years, as in BW, cannot be seen in GER. A low number of winter clusters is also found between 2005 and 2018, but only for multi-hazard combinations. The most frequent clusters in winter consist of windstorms. Windstorm clusters are the most damaging clusters of all combinations in GER (in contrast to BW; see Fig. B2). This shows that windstorms and especially windstorm clusters drive insured losses in GER to a large extent. From around 2015, these winter clusters of large-scale storms have shifted to later start dates. In summer, combinations of convective events (PF-H, CG-H and PF-CG) cluster most frequently in GER and involve the highest losses (see Fig. B2). Considering clusters with high losses specifically (see Fig. 6.5b), it is visible that the most damaging events occurred in multi-hazard clusters, as in BW. While *Kyrill* was in a FF-LS cluster, hailstorm *Andreas* occurred in close succession with a pluvial flood event (PF-H), and the 2021 western Germany flood triggered by low *Bernd* was within a cluster of MF-CG-H. Apart from these major events, years such as 2002 or 2013 showed a particularly high number of damaging clusters.

The mean start date for convective clusters both in BW and GER is in June, while in BW, this is slightly shifted towards later dates (see Fig. B3). This might be related to the southward shift of the study area. For the winter extremes, this pattern is reversed: Fluvial floods, which mainly occur during DJF, have

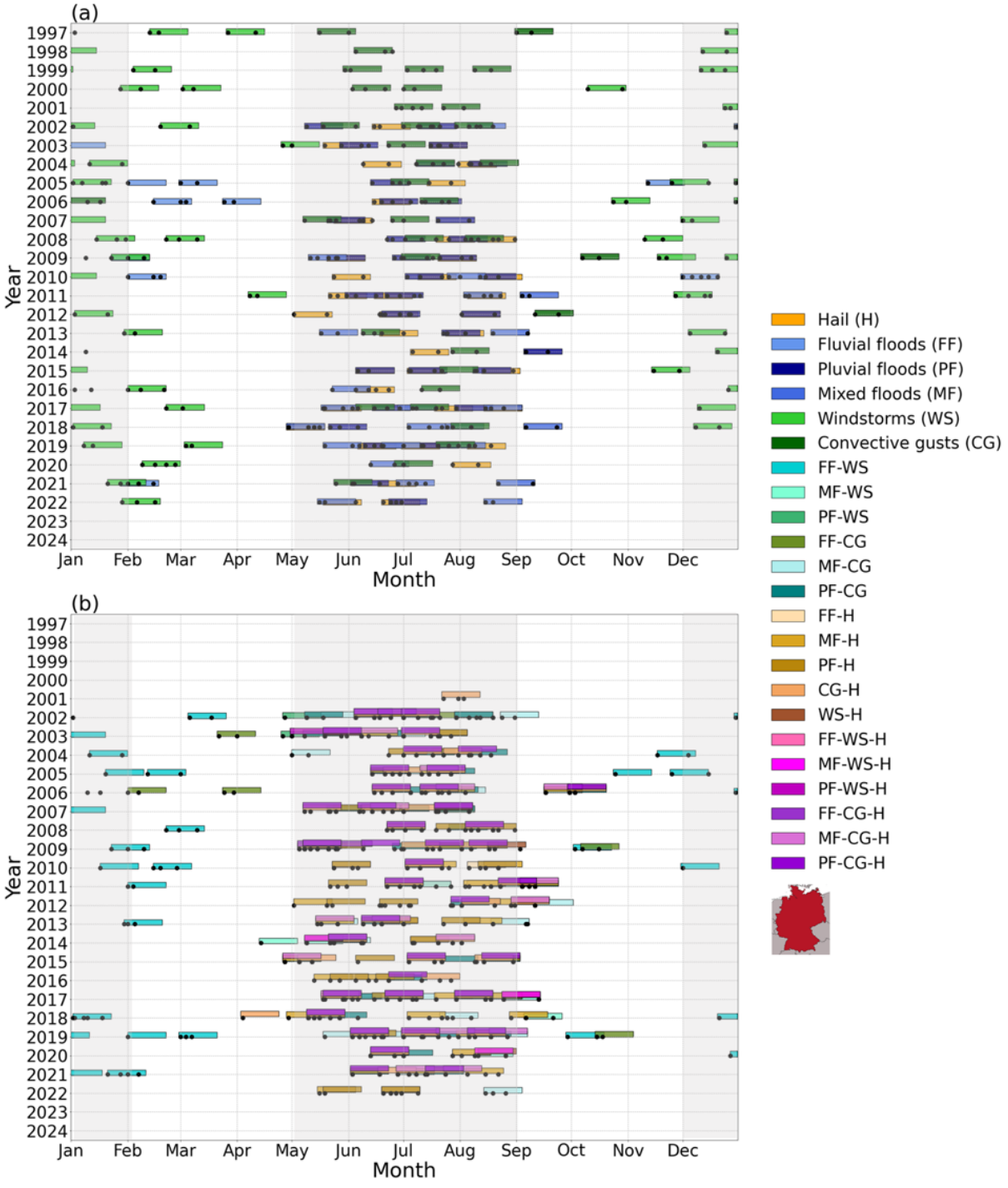

Figure 6.4.: Same as Fig. 6.3, but for the study area of GER.

an average start day at the end of January for BW, but a much later one in GER. This points to more winter-season events in GER during the end of the calendar year compared to BW. As the spread of events throughout the year is lower in GER, these findings can also help explain the lower variability found in GER (Fig. 6.2).

In summary, a high year-to-year variability is found in both study areas, with a recurring pattern where most events are found in the early 2000s, and a lower variability with the larger spatial scale of GER. Counted 21-day clustering periods follow this pattern, with many clusters detected between 2002 and 2010 (both study areas) as well as in recent years (BW), and most multi-hazard clusters occurring between May and August. Major damaging hazards were shown to occur in single- or multi-hazard clusters as well.

6.2 Statistical clustering: When is clustering significant?

The deviation of clusters from a homogeneous Poisson process is investigated using the statistical tool Ripley's K (see Chapter 4). Due to the seasonal occurrence of loss events, clustering would always be found in the summer months (MJJA) as well as the winter months (DJF) when taking a year-round perspective. Therefore, the seasons must be analyzed separately.

> The number of events influences the degree of clustering in a time series (recall the differences in event numbers between POT and HC, see Fig. 6.1). Therefore, when applying Ripley's K, the number of events identified by POT for each hazard type are reduced, using a ranking of insured losses, until the number of events identified by HC for that hazard type is reached.

6.2.1 Clustering of single hazard types

> Due to the seasonality of the events (see Sect. 5.2), we investigate large-scale storms and fluvial floods in winter (DJF) and convective gusts, pluvial and mixed floods as well as hail in summer (MJJA). Generally, Ripley's K for events identified by the HC method (K_{HC}) is significant on a broad range of timescales compared to a random series. It is also higher than Ripley's K for events identified by the POT method (K_{POT}; Fig. 6.6). In the following, statistical clustering is first evaluated for BW and then for GER.
>
> Regarding BW, the strongest clustering, significant at the 95 % confidence level of a Monte Carlo sample (hereinafter: significant), is found for convective gusts during MJJA with K_{HC}: At a seasonal timescale, more than four additional convective gust events can be expected around a random convective gust event. However, for K_{POT}, that is, a flexible event definition, the time series of convective gusts is within the 95 % confidence interval on almost all timescales and only slightly exceeds it around the seasonal scale. Pluvial floods do not cluster significantly during MJJA with both methods (POT and HC). Hail clusters are significant on all timescales with K_{HC}, but only from the timescale of 30

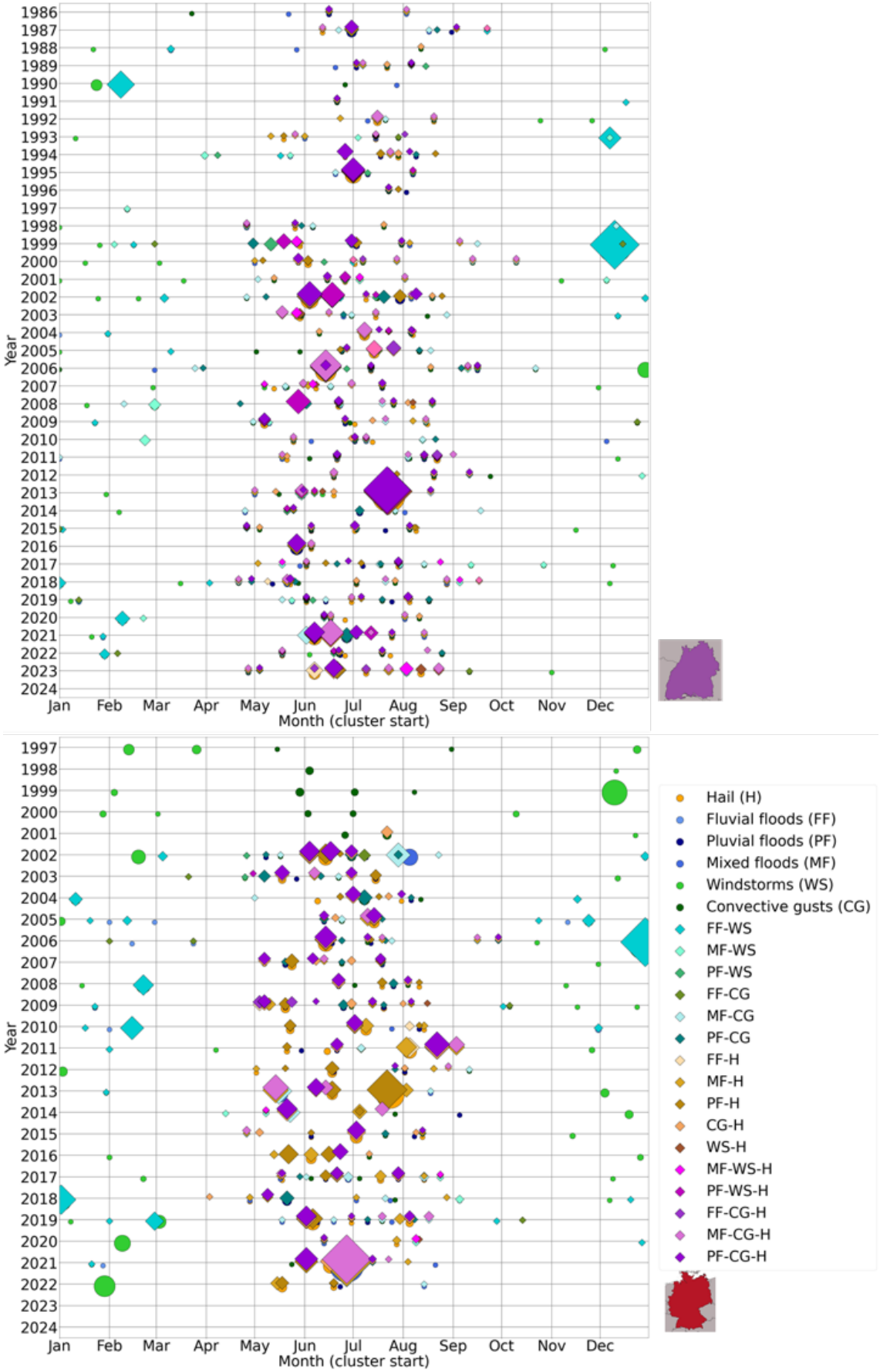

Figure 6.5.: Same as Fig. 6.3, but including losses: The size of the circles relates to the loss corresponding to each cluster (normalized) for single (circles) and combined (diamonds) hazard types for (a) BW and (b) GER.

days to seasonal level for K_{POT}. During DJF, large-scale storms cluster significantly on all timescales with K_{HC}, and are significant with K_{POT} starting from about 20 days, but with a low difference from the 95% confidence interval.

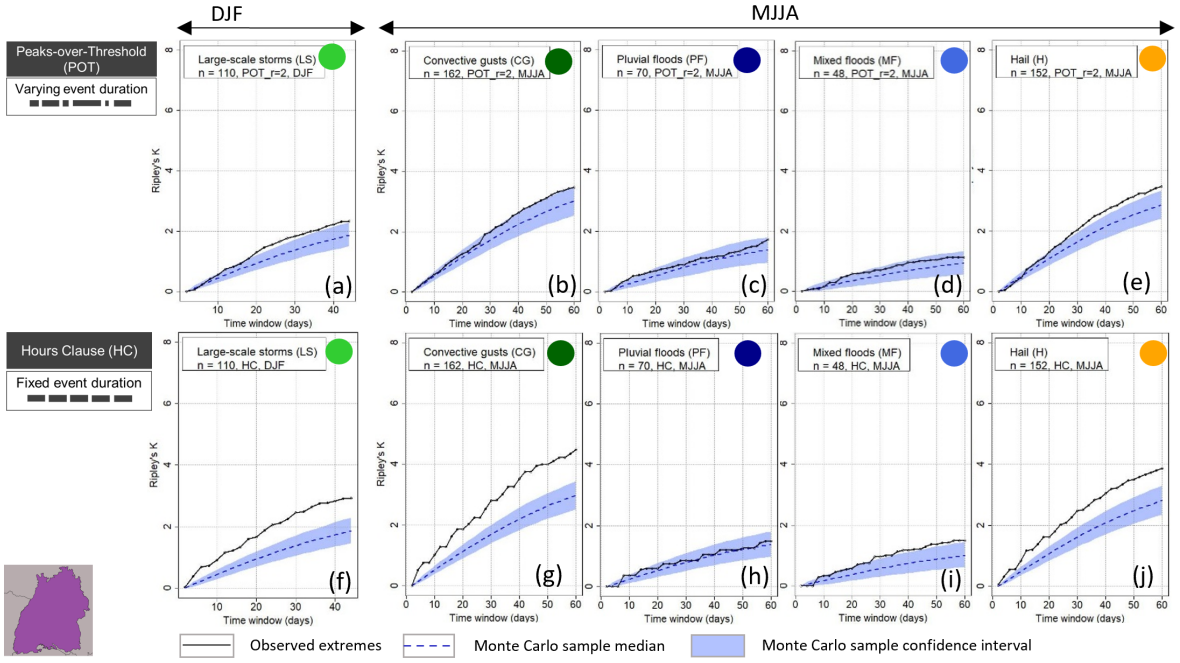

Figure 6.6.: Study area BW: Clustering results using Ripley's K for single hazard types: large-scale storms, pluvial floods, convective gusts, fluvial floods, mixed floods and hail damage, depending on the season (columns) and method of events identification (rows).

To assess the robustness of the results, we systematically changed various variables. Changing the seasonal focus from MJJA to only June–August (JJA), K_{POT} is not significant for convective gusts and hail. This implies that the occurrence in JJA follows a homogeneous Poisson process, but clusters in those months if May is added. Interestingly, when events are identified using the 95th percentile (p95) instead of p90, we see an increased degree of significant clustering for hail and convective gusts with K_{POT}, but a decreased degree of clustering for K_{HC}. For the flood hazards, there is only little change. If no declustering is applied, events do cluster significantly in both seasons and for all original hazard types as defined by the insurance company (storm, hail and flood). This shows that clustering occurs at short timescales, which is why declustering is needed. The results do not change when increasing the number of simulations for the significance test.

One reason for the increased number of significant results concerning clustering of events defined with the HC method is the duration of events. Due to the definition of HC, the duration of any event cannot be less than three days (or seven days for flood events). However, the average duration for events identified by the POT method is 1.9 days in BW and 2.3 days in GER (see Fig. B4). This on average

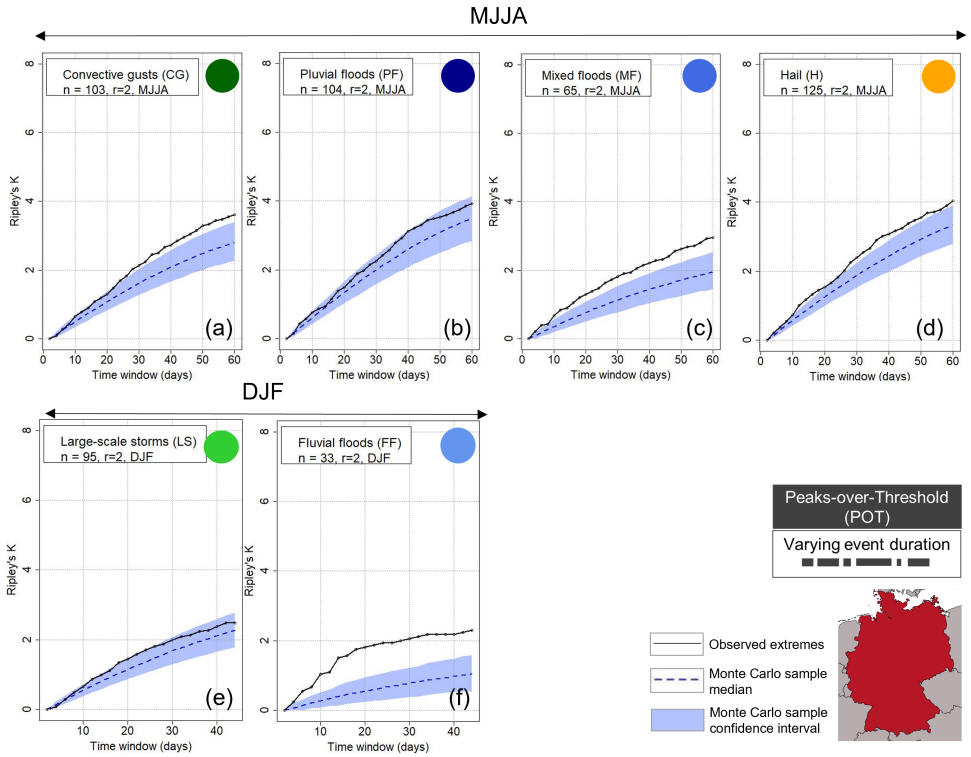

Figure 6.7.: Study area GER: Clustering results using Ripley's K for single hazard types: large-scale storms, pluvial floods, convective gusts, fluvial floods, mixed floods and hail damage, depending on the season (columns) and method of events identification (rows).

> much lower duration of events identified by POT compared to those identified by HC influences the degree of clustering. Although both methods can only approximately reproduce the actual duration of events, because of the only daily temporal resolution of the underlying loss data, it should be noted that POT is clearly more accurate because of its flexible nature. We therefore argue that by using HC, the degree of clustering is often overestimated. This furthermore proves that the (multi-day) events identified are not resulting from the same weather systems, since the degree of clustering is higher with longer durations (HC) than with shorter ones (POT).

Ripley's K results for GER were only analyzed with respect to the POT method (see Fig. 6.7). When comparing the results for the study area of GER to the ones in BW during MJJA (Fig. 6.6a–e versus Fig. 6.7), the significance of clustering both regarding pluvial floods and hail does not change. The significance of convective gust events becomes more robust, that is, covers more timescales, and mixed floods become significantly clustered. This partial change in results can be explained by the fact that hail and pluvial flood losses – which show a similar clustering tendency – are predominantly caused by events occurring in Baden-Württemberg (see also Fig. 5.9), whereas losses from other hazards are more regionally distributed across Germany. Regarding wintertime extremes, the significance of windstorm clustering is reduced in GER compared to BW. This is somewhat surprising given the strong south-to-

north gradient of windstorm losses in GER (see Sect. 5.3). Fluvial floods during DJF cluster significantly in GER, while they were not analyzed in BW due to their low sample size. The degree and significance of clustering (with the exception of windstorms) generally increases in GER compared to BW. This shows that the size of the study area matters for the investigation of sub-seasonal loss clusters.

> Previous studies have assessed clustering with respect to different hydro-meteorological hazards: In their global analysis of precipitation extremes, Tuel and Martius (2021b) find low values of Ripley's K for European regions and detect significant clustering over Europe only for a few grid cells for both DJF and JJA. For heavy precipitation events in Switzerland, defined using POT from gridded daily precipitation data, Barton et al. (2016) show similar results. For DJF and JJA, they find no significant clustering on the seasonal timescale for p95 when declustering is applied. Tuel and Martius (2021a) similarly detect low values of Ripley's K and no significant clustering of heavy precipitation for most Swiss regions during DJF and JJA. This is in line with our results for southwestern Germany, where we detect low and not significant values of Ripley's K for all three flood hazards during MJJA.

However, regarding GER and DJF, temporal clustering is also found for events from 1952 to 2002 in another study, with the highest number of events occurring in western and central Germany (Uhlemann et al., 2010). This is consistent with our findings for GER, which show significant clustering in DJF.

> Clustering of extratropical cyclones has not yet been assessed with Ripley's K to our knowledge, but is mainly investigated using the dispersion statistic. A statistically significant overdispersion, indicating clustering, is identified specifically in northwestern Europe, over the exit region of the North Atlantic storm track (e. g., Mailier et al., 2006; Vitolo et al., 2009), summarized in Dacre and Pinto (2020). However, the geographical area in question does not clearly extend to Germany. Dacre and Pinto (2020) also highlight that in Europe, more intense extratropical cyclones tend to cluster more frequently than larger samples of cyclones including also less intense ones in Europe, as shown across multiple studies. We find contrasting results: when we decrease our sample size towards more extreme large-scale storms in BW, we find a decreased degree of clustering. For hail events, to our knowledge, there is no systematic assessment of temporal clustering on the seasonal scale.

In summary, clustering is only detected for some hazards compared to a random Poisson process, when POT is used, in both study areas. While the results generally do not differ significantly between the two study areas, the reduced clustering of windstorms in GER compared to BW is striking. With HC, robust clustering is detected for all hazard types in BW.

6.2.2 Clustering of multiple hazard types

When applying Ripley's K to a combination of two hazard types, no combination may consist of more than 80 % of a single hazard type throughout the (seasonally filtered) time series. This prevents a particular type of hazard from dominating the cluster. With this condition, the combinations PF-CG, MF-CG, CG-H, MF-H), PF-H, PF-LS are feasible for MJJA. For DJF, the combinations LS-MF and LS-PF are feasible. For combinations of three hazard types, we introduce an additional condition: each hazard type must account for at least 10 % of the total event count (per season) of all three hazard types. Without this requirement, the combination could comprise a small number of events from a single hazard type, resulting in clustering outcomes that essentially mirror only events from the remaining two hazard types. The combinations MF-CG-H, MF-LS-H, PF-CG-H and PF-LS-H fulfill this condition within MJJA in BW.

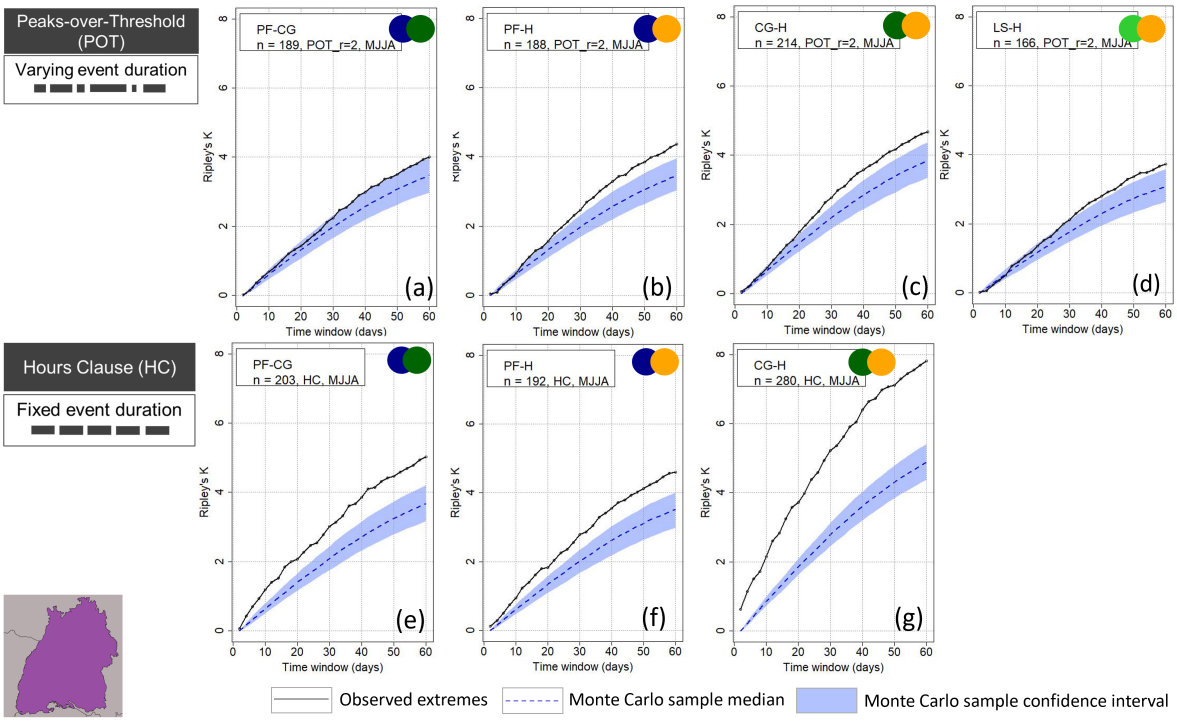

Figure 6.8.: Study area BW: Clustering results using Ripley's K depending on the method of events identification (rows) and during MJJA for the combination of two hazard types including pluvial floods (PF), mixed floods (MF), large-scale storms (LS), hail (H) and/or convective gusts (CG) (part 2).

Clustering of two hazard types

Ripley's K results for BW (Figs. 6.8 and 6.9) show that K_{HC} is significant for all feasible event combinations during MJJA for all timescales from a few days up to a season, with the exception of PF-LS. The degree of clustering is highest for CG-H. On average, eight events are found around a random event in the time series at the seasonal scale, which significantly deviates from a homogeneous Poisson

process. This is probably due to the strong degree of clustering of convective gusts (see Fig. 6.6), but also due to the strong clustering of hail. Convective gusts and hail often occur in close succession if an unstable air mass prevails for several days. The significance of K_{POT} is more pronounced when two hazard types are combined compared to the single hazard types. K_{POT} is significant for PF-H and CG-H from the timescale of about 20 days, but not for PF-CG (see Fig. 6.9). K_{POT} for MF-CG and PF-LS, respectively, does not significantly differ from a homogeneous process. For the combination of MF-H, LS-H, and MF-LS (see Fig 6.8), K_{POT} is significant from about 30 days. Clustering of FF-CG during winter is significant for HC only (not shown).

For GER, less combinations of two hazards are feasible during MJJA (see Fig. 6.10). However, all of the feasible combinations show significant clustering, in most cases more pronounced than in BW. Combinations involving hail also show the strongest degree and significance in clustering. FF-LS clusters in winter show significance until about 35 days.

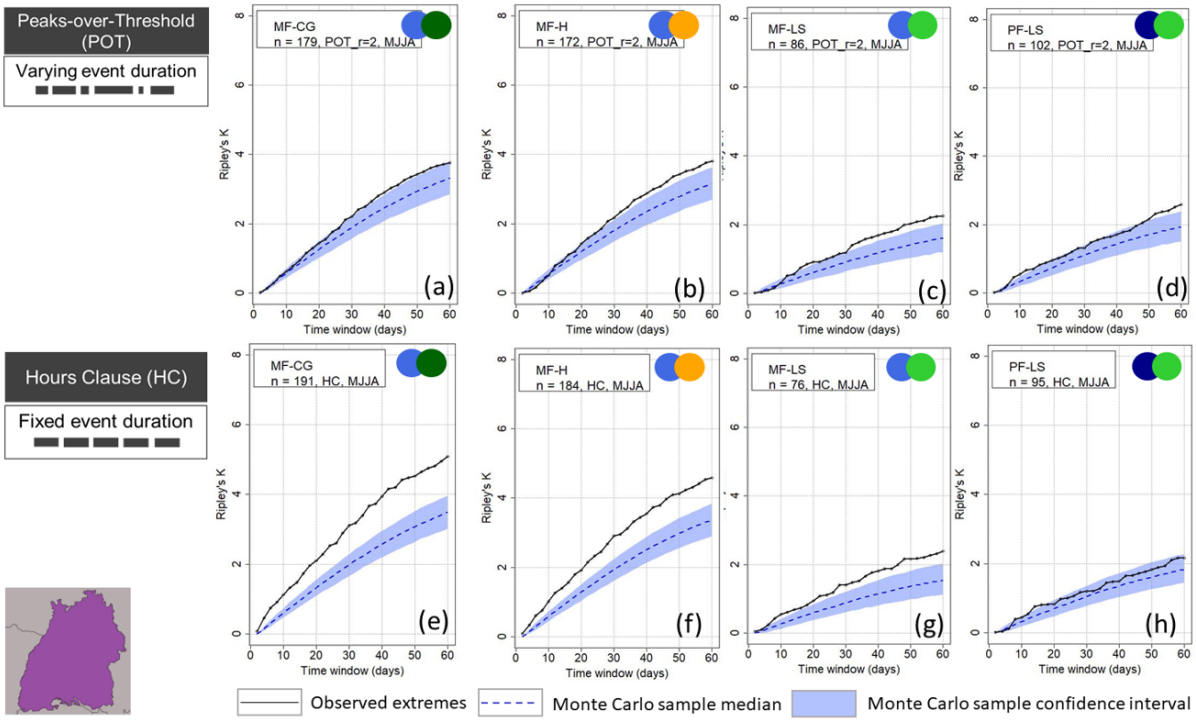

Figure 6.9.: Study area BW: Clustering results using Ripley's K depending on the method of events identification (rows) and during MJJA for the combination of two hazard types including pluvial floods (PF), hail (H) and/or convective gusts (CG) (part 1).

In summary, significant clustering can be found for all feasible combinations of two hazards in MJJA for K_{HC} in BW. Concerning K_{POT}, the results suggest that combinations of two hazard types involving hail lead to clustering. In GER, clustering is robust for all feasible combinations of two hazards, also without the involvement of hail. This shows that in contrast to the similar patterns for single hazard types in BW and GER, clustering becomes more robust in GER when considering two hazard types together. When

decreasing the number of events to the 95th percentile (in BW), the degree of clustering decreases, as with the single hazard types.

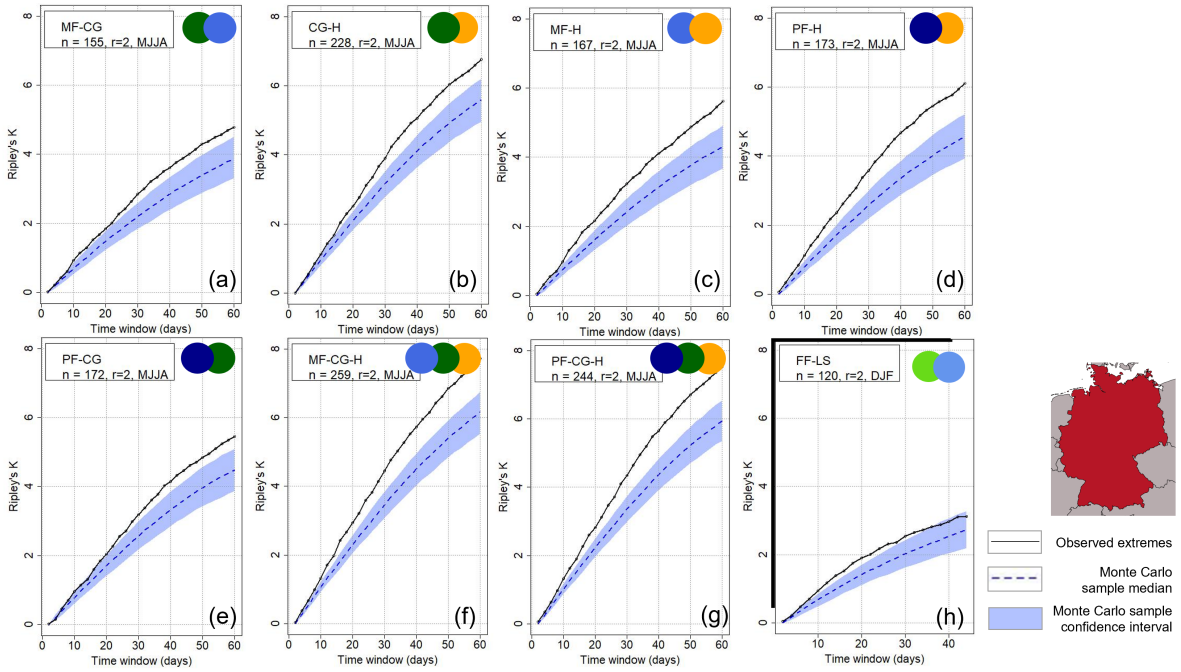

Figure 6.10.: Study area GER: Clustering results using Ripley's K depending on the method of events identification (rows) and during MJJA for the combination of two hazard types including pluvial floods (PF), mixed floods (MF), large-scale storms (LS), hail (H) and/or convective gusts (CG) (part 2).

Clustering of three hazard types

> As with the combination of two events, K_{HC} in BW is higher and more often significant than K_{POT} in almost all cases, especially where convective gusts and hail are involved (Fig. 6.11). For the POT method, we also find significant clustering for all combinations of three hazard types, at least at the seasonal scale and starting from 10 to 30 days. The occurrence of combinations of three damaging hazard types during MJJA therefore differs significantly from a homogeneous Poisson process at timescales of 30 days up to a season, regardless of the definition of events. When reducing the number of extremes to p95, the degree of clustering remains similar.

In GER with POT, the degree and significance of clustering for the two feasible combinations of three hazard types, namely MF-CG-H and PF-CG-H, exceed those observed in BW (cf. Figures 6.10 and 6.11). For both combinations, clustering is significant for all timescales up to the seasonal scale. On the latter, almost eight additional events can be found around a random extreme event of mixed or pluvial flooding, convective gusts or hail. However, since clustering is assessed for the entire study area of GER,

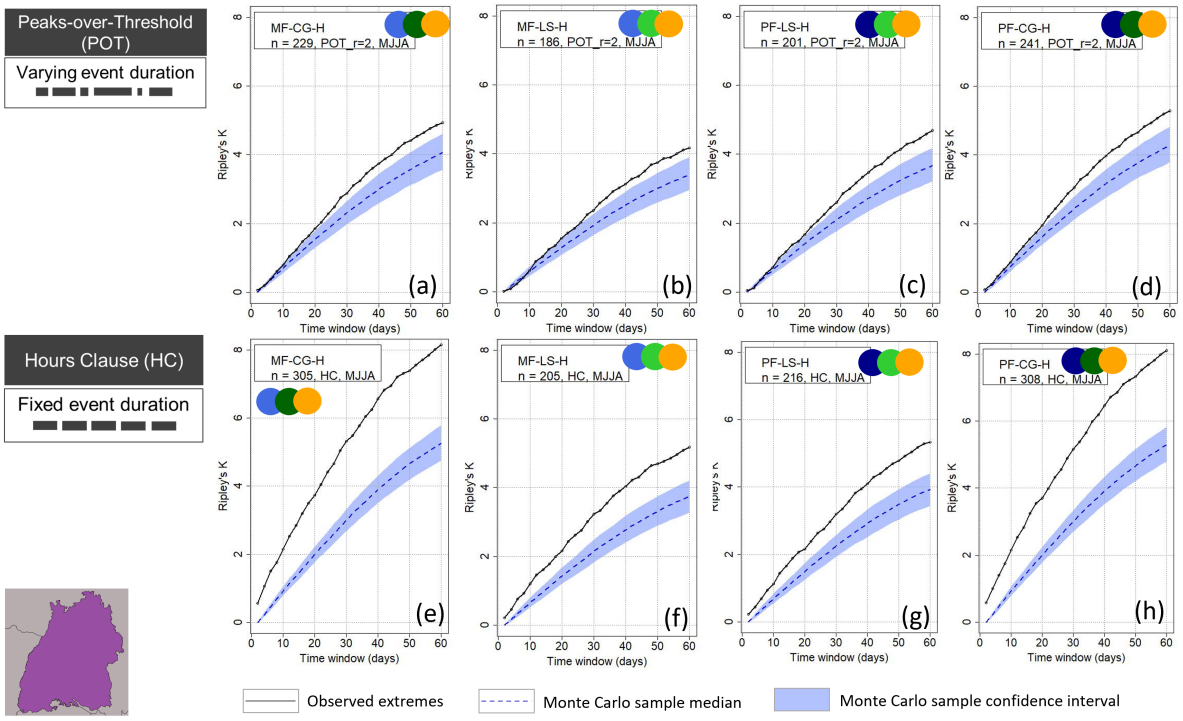

Figure 6.11.: Study area BW: Clustering results using Ripley's K depending on the method of events identification (rows) and during MJJA for the combination of three hazard types including pluvial floods (PF), mixed floods (MF), hail (H), large-scale storms (LS) and/or convective gusts (CG).

events in clusters could also result from distinct weather situations, especially due to their convective and local nature.

Figure 6.12 summarizes the results for Ripley's K using POT for BW and GER (Figures 6.6–6.11) for a fixed clustering time window of 21 days, in contrast to the variable windows discussed before. Bloomfield et al. (2023) show that correlations between wintertime storm and flood events are highest at a monthly scale in Germany (impacted by storm clustering). Therefore, utilizing a 21-day window should allow the majority of clusters to be identified. Summary figures with respect to other timescales can be found in Appendix B (Figs. B5–B7). It can be seen that for K_{POT} both in GER and BW and a window of 21 days, where large-scale storms, convective gusts, pluvial floods and mixed floods do not cluster significantly (upper panel, black framed boxes), the combination with other hazard types increases their degree and, most importantly, significance of clustering. Although Ripley's K is lower during DJF than during MJJA, it remains statistically significant. Furthermore, as more hazards are added, the robustness of clustering significance increases. Focusing solely on individual hazard types therefore may overlook significant clusters that become evident only when multiple hazards are considered together.

We expect that these results are robust with regard to the choice of input data for both regions, as we can assume that a large part of all major natural hazards are included in our impact datasets for the following reasons: In BW, firstly, the population density exceeded 100 inhabitants km^{-2} for all districts in BW as

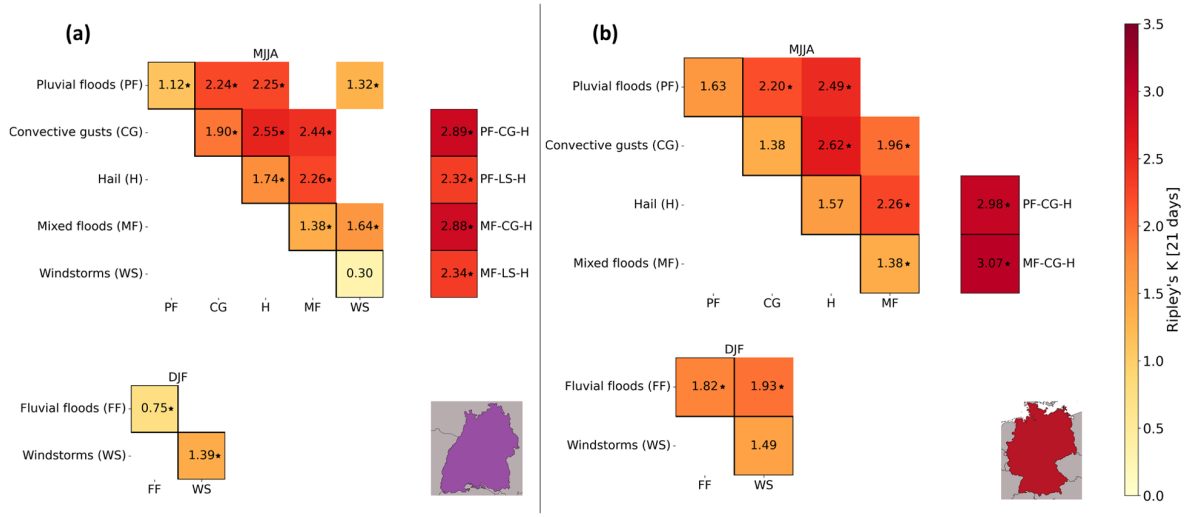

Figure 6.12.: Summary of Figures 6.6–6.11 for a time window of 21 days. Heatmap for hazard pairs in BW and (b) GER including Ripley's K results with a time window of 21 days, that is, the average number of events within 21 days before and after a random extreme event in the time series. Stars behind the numbers indicate significance compared to a random process. This is evaluated for May–August (top panel) and December–February (lower panel). Squares with black edges relate to combinations of single types, while squares without edges represent combinations.

of 2022 (Statistisches Landesamt Baden-Württemberg, 2022). Secondly, insurance coverage against all hazards included in this analysis is very high across BW, and the SV Sparkassenversicherung has a high market share (see Sect. 3.1). Finally, by using the 90th percentile across all years, we include a large number of events (see e g., Fig. 6.1 and 6.2). Thereby, a major part of meteorological hazards in BW is assumed to be included, also in less densely populated regions with lower insured losses. Regarding GER, the GDV covers more than 95 % of residential building insurance with respect to storm and hail (Burghoff, 2024). Although p90 covers more severe events in GER due to the larger area, we argue that regarding windstorms and SCSs, major events are included due to the arguments above. Regarding flooding, this cannot be guaranteed due to the highly fluctuating insurance density across Germany (see Chapter 3).

6.3 Clustering and losses

This chapter so far has focused on the clustering of extreme events using their frequency of occurrence. However, since this work is based on insured losses, three additional analyses are conducted here: First, events in 21-day clusters are investigated in more detail with respect to the losses they entail, compared to isolated events (Sect. 6.3.1). Second, clustering of losses idependent of the event occurrence, but by quantifying the contribution of the largest event, can be of interest (Sect. 6.3.2). Lastly, return periods of identified 21-day clusters are evaluated (Sect. 6.3.2). This shift to insured losses allows for a more

impact-oriented perspective, highlighting how not only meteorological intensity but also exposure and vulnerability shape clustering patterns – which may differ from purely physical event clusters.

6.3.1 Losses of clustered and isolated events

The loss distribution of clustered and isolated extremes differs heavily, depending on the hazard type. Therefore, the loss distribution of 21-day clusters vs. events not within clusters (= isolated events), is investigated. A focus is set on frequent clusters in winter (FF-LS) and summer (PF-CG-H).

Clusters during December–February

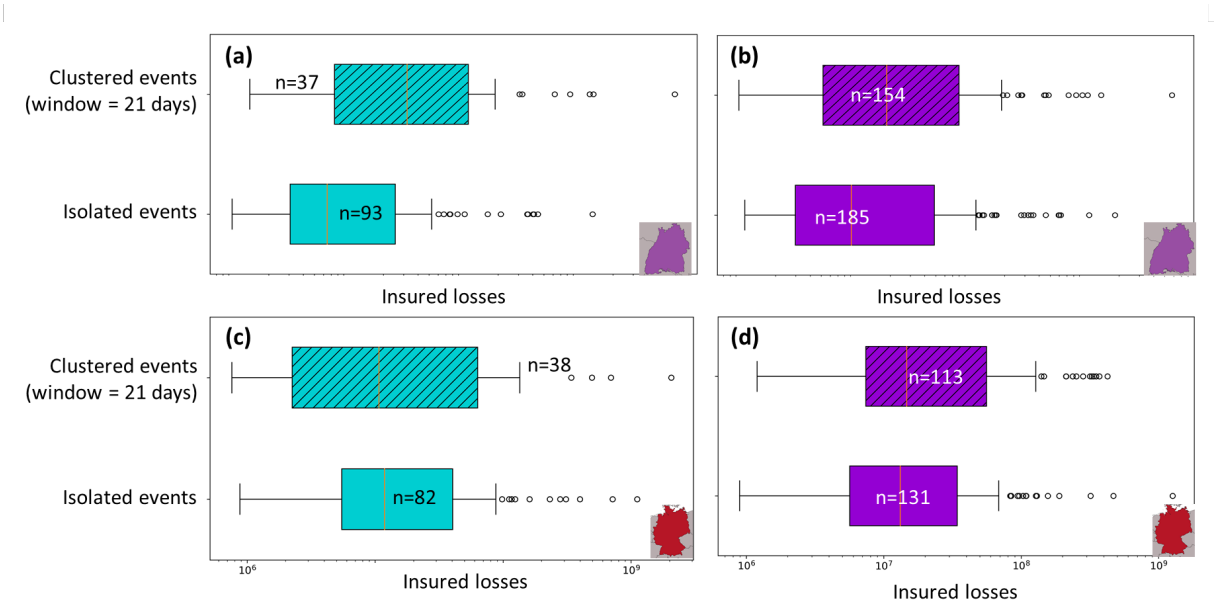

Figure 6.13.: Insured losses (logarithmic) of events within clusters vs. isolated extremes within a clustering window of 21 days in BW (a and b, loss amounts are not shown due to their confidentiality) and GER (c and d). The left panel (a and c) displays the combination of FF-LS, while the right panel shows PF-CG-H.

In BW, for large-scale storms and fluvial floods during DJF, the median loss of events occurring within clusters of 21 days (n = 37) exceeds the median loss of isolated events (n = 93) by a factor of 5 (see Fig. 6.13a, scale omitted for confidentiality reasons). Note that losses of clustered events are not accumulated; each event is a separate data point and only categorized into either an isolated or clustered occurrence. These results are robust to sensitivity testing: When changing the clustering window to 14 or 28 days or when excluding major loss events (only events of < € 5 million), the median loss of clustered events still exceeds the one of isolated ones. This highlights that multi-hazard clusters lead to higher losses during DJF compared to isolated hazards. In GER, the pattern is less clear (Fig. 6.13c), with a similar median for both clustered and isolated events. However, in an analysis on the co-occurrence of wind and precipitation extremes in winter, Xoplaki et al. (2025) reveal a significantly higher loss ratio

for residential buildings in Germany with respect to co-occurring extremes compared to their isolated occurrence (DJF, 1997-2016). When we change the metric from insured losses to the loss ratio, clustered events also involve higher losses per claim than isolated events, robust to a change in clustering window. The differing results depending on the metric demonstrate the influence of the varying insurance density. On the other hand, it can be concluded that the loss ratio of combined wind and precipitation extremes exceeds the loss ratio of isolated events on various timescales. This has also been investigated in other European countries: For the UK, Hillier et al. (2015) showed, based on rail data, that interactions between floods, winter storms and shrink-swell subsidence events increase insured losses by up to 26 % per year.

For convective clusters (PF-CG-H) during MJJA, clustered losses also exceed isolated ones in BW (Fig. 6.13b). The double median losses were caused by clusters of PF-CG-H, compared to the isolated occurrence of any of these hazard types. Note that this specific hazard combination also leads to the highest degree of clustering (see Fig. 6.12). The most damaging clustered events include, for example, the hail event *Andreas* on 28 July 2013 (see e. g., Fig. 5.1), which was accompanied by pluvial flood damage and preceded by another pluvial flood as well as convective gust events on 23 July 2013. Another cluster with high losses includes the hail event *Queenie* on 28 June 2006, which was accompanied by a pluvial flood, and preceded by convective gust events and hail on 25 June 2006. The median losses of clustered events also exceed those of isolated ones in GER, but with a less pronounced difference (see Fig. 6.13d).

Other clusters of multiple hazards show similar patterns in BW (Fig. 6.14a). For almost all combinations, clustered events are associated with higher losses. However, this is not the case for clusters involving only a single hazard type (lower part of Fig. 6.13a). Compared to clustered single hazard types, isolated events of the particular hazard are associated with higher losses during MJJA, even when major loss events (> € 5 million) are removed. In GER, the differences between clustered and isolated extremes are generally lower (Fig. 6.14b). Most multi-hazard clusters are associated with higher losses compared to the isolated occurrence. However, in contrast to BW, clustered individual hazards are associated with higher losses than isolated ones.

In summary, multi-type clusters systematically cause significantly higher median losses compared to isolated events in BW and, with a weaker signal and not for all types, in GER. When comparing single-type clusters to the isolated occurrence of (single) hazards, the result depends on the study area considered, with isolated events being more damaging in BW and clustered extremes more damaging in GER. This difference between BW and GER suggests that in BW, damage is mainly amplified by interactions between multiple hazard types, while in GER, even repeated occurrences of the same hazard can substantially increase losses, possibly due to the larger spatial aggregation at the national scale.

These findings with respect to multi-hazard clusters align with recent studies emphasizing the relevance of multi-hazard interactions. For instance, Jäger et al. (2024) find that hazard pairs in EM-DAT often

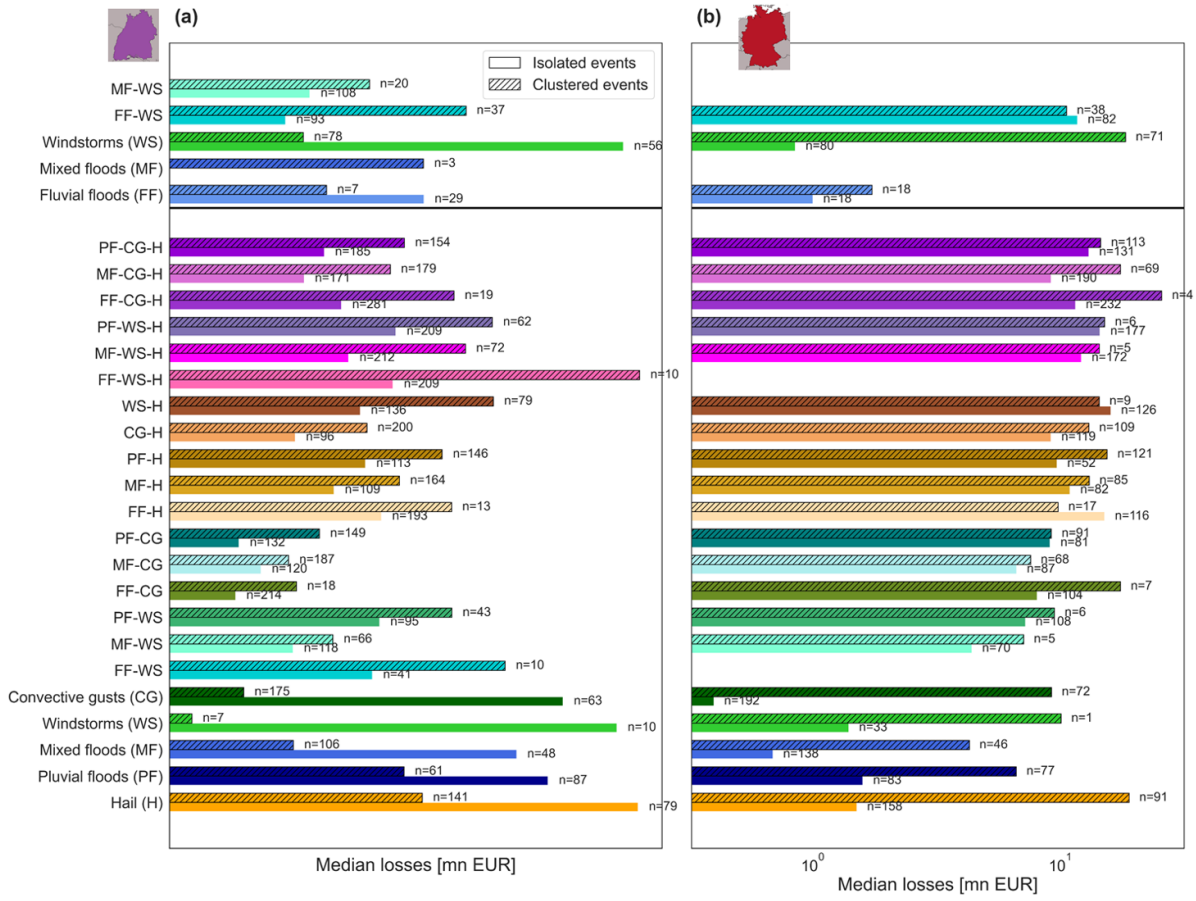

Figure 6.14.: Median insured losses (logarithmic) of clustered (hatched) vs. isolated extremes in (a) BW and (b) GER within a clustering window of 21 days, for events during DJF (upper parts, above the grey line) and MJJA (lower parts). Clusters involving single hazard types can be found at the bottom of the graph (the first five groups counted from below). Loss amounts are not shown for BW due to confidentiality of the data.

have at least as much, or even more, impact than two isolated single-hazard events. Similarly, Mohamed et al. (2024) point out that the joint occurrence of hail, wind, and flooding tends to be underestimated, highlighting the need to account for such compound events in risk assessments. The substantial amplification of losses by clusters from different hazard types shows the importance of considering this effect in applications such as risk modeling. This is particularly relevant as different damaging hazard types frequently occur in close succession during persistent synoptic settings or weather patterns, such as blocking, or an extended Atlantic trough (Grams et al., 2017), which can trigger multiple extremes.

6.3.2 Impact metrics

Loss clustering can also be assessed by comparing annual losses to major loss events. This is particularly common with respect to windstorms, for which the storm severity index has been developed (see Sect. 2.1.1).

Overall and annual exceedance probability

To assess loss clustering, we employ the ratio of the annual maximum loss event (OEP) to the total annual losses (AEP, see Chapter 2.4; e. g., Dacre and Pinto, 2020).

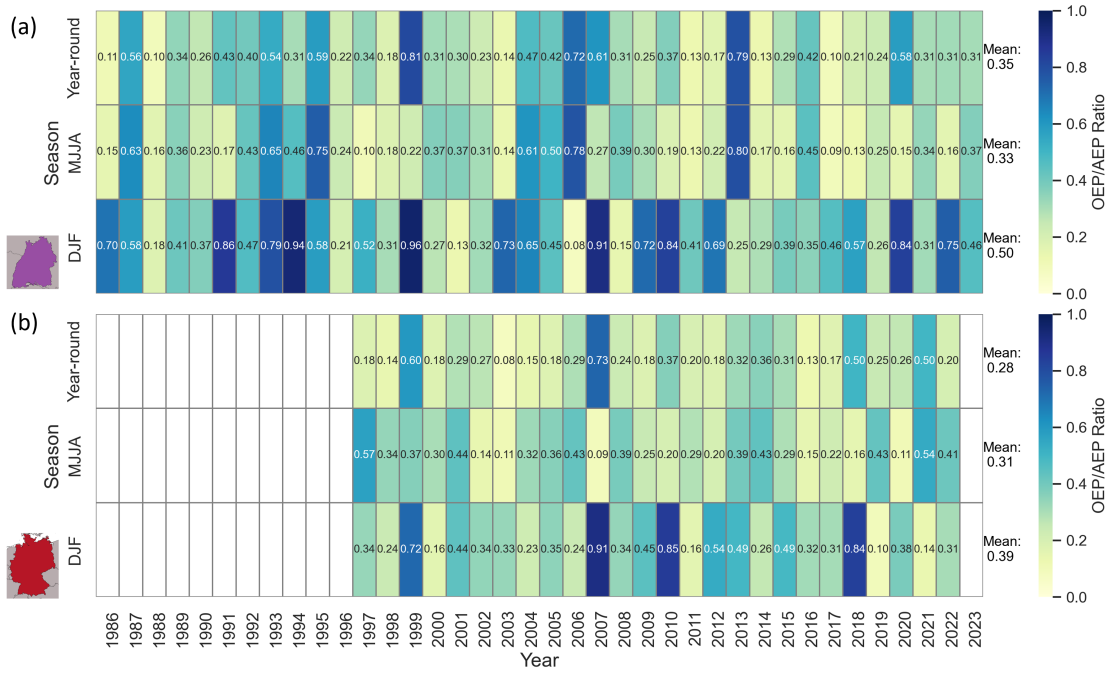

Figure 6.15.: Clustering measure of the main event contribution vs overall losses: Occurrence Exceedance Probability (OEP), relating to the maximum loss event in a season, vs. the Aggregate Exceedance Probability (AEP), that is, the total annual losses (upper row) or total seasonal losses, between May and August (middle row) and (c) December–February (bottom row) in (a) BW and (b) GER.

We assess the ratio of OEP to AEP separately for calendar years, for May–August, and for December–February (see Fig. 6.15). As explained in Sect. 2.4, a low ratio indicates clustering, as the contribution of the most severe event is limited. A high ratio then demonstrates the dominance of a single event in contributing to aggregate annual losses.

In contrast to other studies, OEP and AEP are applied to aggregate losses across hazards in this work. Note that while this metric is usually applied to a 72 h HC, we apply it to daily losses due to our method of event definition.

In BW, it is evident that in certain years with major events (e. g., 1999, 2013, see also Fig. 5.3), the ratio of OEP/AEP in a year-round perspective is about 0.8, showing a large contribution of a single event (*Lothar* and *Andreas*) and thus a low degree of clustering. The mean ratio of yearly OEP/AEP across 1986-–2023 however equals 0.35, which means that, on average, the contribution of several events is relevant to annual losses. Loss clustering may be present, for example, from 2011 to present, with the exception of 2013 and 2019. It is also visible that the degree of clustering as measured by OEP/AEP

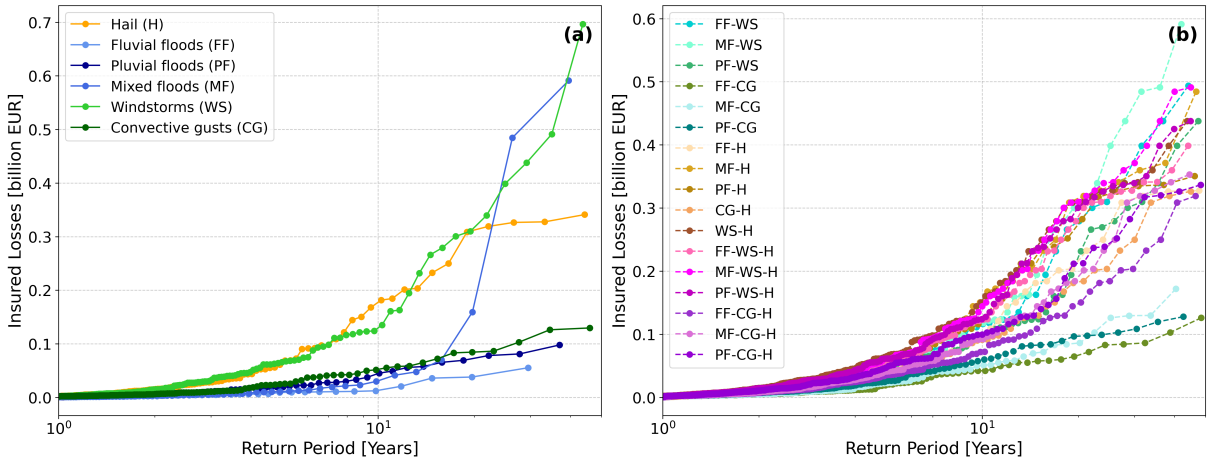

Figure 6.16.: Study area GER: Return period of events (logarithmic scale) vs. insured losses caused by (a) single-hazard and (b) multi-hazard clusters.

is, on average, 20 % higher during DJF than during MJJA. In certain winters, such as 2020/2021, for example, losses were dominated by more than 80 % by single loss days.

In GER (Fig. 6.15b), the mean of year-round OEP/AEP is lower than in BW, which can be attributed to the larger geographic area, and to extremes in the winter, where clustering is much stronger compared to BW. Therefore, loss clustering exists throughout the timeseries of GER, with the exception of only some years. The higher contribution of single loss days during winter, and the higher ratio in GER compared to BW is as expected due to the nature of the extremes: While convective extremes during summer affect smaller areas, they are less likely to dominate aggregate losses in GER compared to windstorms or flood events affecting broad regions. This investigation into loss clustering clearly showed that single events dominate losses during many winters, particularly in the smaller study area of BW, and can even dominate overall annual losses. The summer is generally characterized by a higher loss clustering, that is, multiple events contributing to seasonal losses. This is also in line with our results regarding Ripley's K (see e. g., Fig. 6.12), where stronger clustering is detected in summer than during winter.

Return periods of clusters

A common metric to assess the severity of extreme events is the use of return periods (see Sect. 2.4), which can be evaluated with respect to the losses of the events. This means that losses of clusters are investigated as a function of their return periods (see Fig. 6.16). Towards this end, we rank the events by losses, then calculate the exceedance probability, and lastly calculate the return periods based on the exceedance probabilities. Higher loss events have lower ranks, resulting in lower exceedance probabilities and thus longer return periods.

In GER, frequent clusters with return periods of up to 10 years cause minor insured losses across all hazard types. Regarding single-type clusters (Fig. 6.16a), windstorm and mixed flood clusters are associated

with the highest insured losses at longer return periods, while hail drives losses of moderate frequencies (≈ ,10 years). Although losses of pluvial flood and convective gust clusters still show noticeable growth at moderate return periods, the increase in losses from hail clusters is stronger. Windstorm and mixed flood losses show a tail risk behavior with their exponential increase from about 20 years. Combinations of three hazards (e. g., PF-Windstorms (WS)-H, FF-CG-H, or MF-WS-H) dominate loss magnitudes at the highest return periods. Comparing single-hazard and multi-hazard clusters, the latter show an exponential increase from return periods of 10–20 years, while some single-hazard clusters show an only gradual increase in losses. While differences are minor at shorter return periods, multiple hazards disproportionately worsen losses with rarer events at higher return periods.

In BW, the pattern is similar. Some single hazard clusters show an exponential increase in losses with higher return periods, whereas multi-hazard clusters robustly show exponential increases (see Fig. B8). In contrast to GER, the major hazard in BW with long return periods are hail and windstorms and the spread is lower. These results highlight the amplifying effect of multi-hazard interactions. When neglecting these interactions, potential losses for long return periods could severely be underestimated.

6.4 Clustering and trends

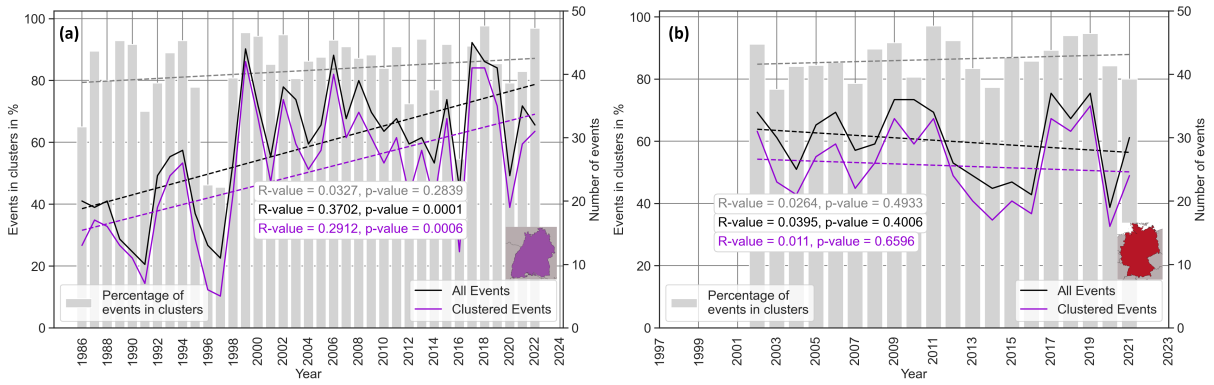

Figure 6.17.: Time series of the percentage of meteorological hazards in clusters (clustering window = 21 days) as well as the number of all resp. clustered events, including trend lines and significance, for (a) BW during 1986–2023 and (b) GER during 2002–2022.

In BW, the number of damaging extremes has increased significantly from 1986 to 2023, and the same can be said for clusters of damaging extremes (see Fig. 6.17). Note that the upward trend is clearly significant (p-value < 0.0001 for all events, p-value = 0.0001 for clustered events). This upward trend is also significant with events that occur in clusters of 14 days. When investigating all multi-hazard clusters separately, there is a significant increase in clusters consisting of MF, CG, MF-CG, MF-H, and MF-CG-H. The number of clustered events of other hazard types or combinations does not increase significantly throughout the time frame. Note however that these upward trends are also governed by increasing values of the objects and vulnerable extensions, such as winter gardens or solar panels.

> Additionally, throughout the entire period, both the reporting and regulation of claims have undergone substantial changes.
> Since all of the natural hazards under consideration occur seasonally, the share of events within clusters compared to all events within a year is quite high (65 % with a clustering window of 14 days, 83 % with a window of 21 days, and 86 % with a window of 28 days). However, certain years stand out: In 1996, 1997 and 2016 only half or less of the events occurred within clusters of 21 days. This share of clustered extremes compared to all extremes has increased throughout 1986–2023 by about 8 %, even though this increase is statistically not significant.

For GER, trends can only be assessed for a time period of 20 years (Fig. 6.17b). Throughout this time, a slight insignificant decrease is found for all events as well as for events in clusters (robust to a change in clustering window). There is no clear trend with respect to the percentage of events in clusters, which fluctuate around 80 % throughout the years with a 21-day window (with a 14 day window, values get as low as 60 %). This shows that particularly in recent years, no consistent trend over both study areas can be found. This applies to all events (Sect. 5.4), and also to clusters.

6.5 Conclusions

The analyses in this chapter revealed that loss-related extreme events in BW and GER cluster most between May and August, particularly in the early 2000s. A high year-to-year variability is found particularly in BW. Major events are found to be part of multi-hazard clusters. Comparing these clusters to a random occurrence, sub-seasonal clustering is robustly significant for many combinations of (convective) hazards, mainly between May and August, as well, especially when a fixed event definition (K_{HC}) is used, and more robustly for GER compared to BW. These multi-hazard clusters are often involved with higher losses than isolated events, and lead to especially steep increases in losses with increasing return periods. Loss clustering can be expected rather in summer than in winter, as winters are more likely to be dominated by single event days. Especially in GER, the dominance of single summer events rules out with the larger study area. The number of clustered hazards has not increased significantly in GER (2002–2022), but in BW over the past 35 years (1986–2023). This shows that sub-seasonal clustering of multiple hazards is a relevant phenomenon, particularly in summer.

7. Multiple hazards and the large-scale atmospheric circulation

Chapters 5 and 6 outlined the damaging nature of various hazards, especially when they occur in clusters. These findings raise questions about the underlying drivers. What mechanisms lead to the formation of single- and multi-hazard clusters, and which large-scale synoptic conditions enable these events to unfold? Improving our understanding of these large-scale drivers is essential for two reasons: first, to improve the predictability of extreme events; and second, to anticipate future developments, given that the prediction and projection of damaging hazards are both subject to high levels of uncertainty. The aim of this chapter is therefore to identify patterns in the large-scale circulation with respect to the clustered and isolated occurrence of single and multiple hazards.

Towards this end, this chapter contextualizes the results of Chapter 6 with respect to potential large-scale atmospheric triggers of these clustered and isolated events. The 21-day cluster periods identified (see Sect. 6.1.2), called 'clusters' in this chapter, are investigated separately for winter (December–February (DJF), Sect. 7.1) and extended summer (May–August (MJJA), Sect. 7.2). For all events, large-scale flow patterns are examined, complemented with an analysis of teleconnections and weather regimes. Composite flow patterns are computed by hazard type, depending on their occurrence in clusters or in isolation. For each of the individual hazards and their combinations, relevant teleconnection indices are analyzed, and the prevailing weather regimes are determined. If not stated otherwise, the results refer to the study area of Germany (GER), due to the larger spatial scale considered.

7.1 Winter extremes: December–February

During the winter months, the most frequent extreme weather events in Germany are windstorms and fluvial floods (see Chapter 5). Consequently, the focus of this section is on clusters of these hazard types and their combinations.

7.1.1 Windstorms

The mean large-scale flow during clustered windstorm events during DJF is characterized by an intensified jet stream with dominating zonal (i. e., west-to-east) orientation, as visible from the composites in Fig. 7.1a. The Z500 composite indicates a typical pattern with lower geopotential heights over Svalbard (in German: *Spitzbergen*), while the MSLP composite shows a pressure minimum over southern Norway. Relative to the climatology (Fig. 7.1b), this pattern reflects a strong negative anomaly of up to 200 gpm.

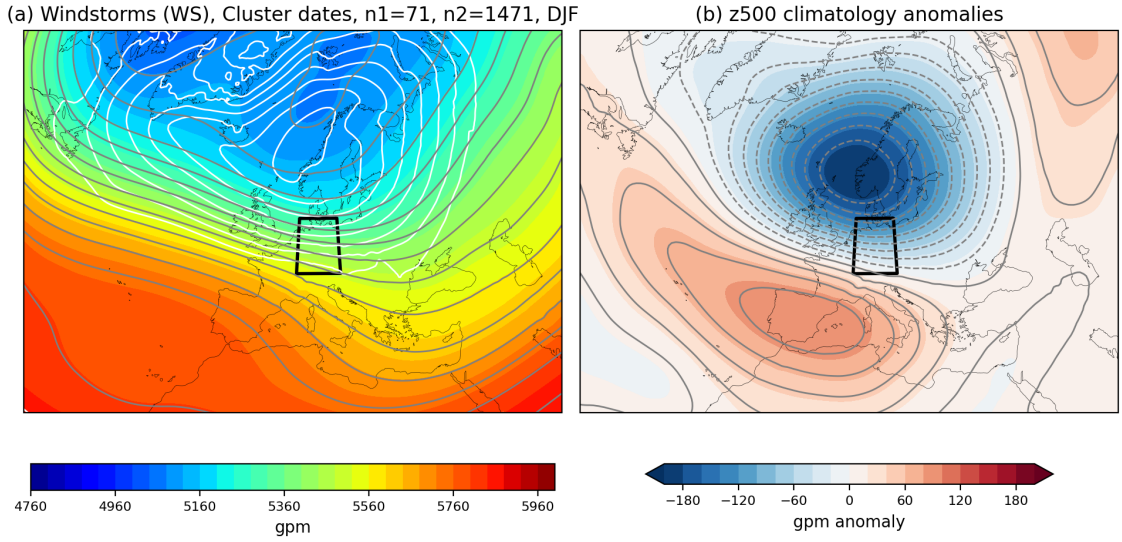

Figure 7.1.: (a) 500 hPa height composite for clustered windstorm events in GER. Colors and grey contours refer to the Z500 level ranging from 4760 gpm to 6000 gpm in steps of 40 gpm. White lines denote MSLP ranging from the minimum value to the 60th percentile of values over the domain in steps of 10 gpm. The bold black rectangle denotes the study area of Germany. *n1* is the number of distinct events and *n2* refers to the number of timesteps (3-hourly) which are included in the composite. (b) as (a); but related to the anomaly with respect to the climatology in gpm, ranging from -200 to +200 gpm in steps of 15.

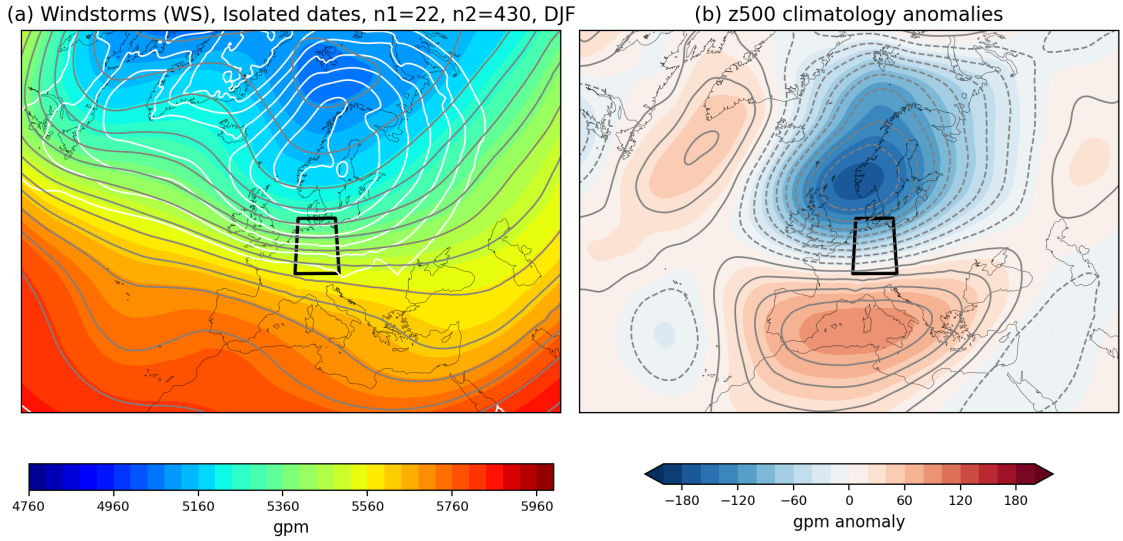

Figure 7.2.: Same as Fig. 7.1, but for isolated windstorms.

In the mean fields, Germany lies near the southern edge of the low-pressure anomaly, within the transition zone toward a positive geopotential height anomaly over southwestern Europe. While many historical severe windstorms have followed storm tracks associated with a southwesterly flow over the North Atlantic (see Chapter 2, Fig. 2.4; Roberts et al., 2014), the composite for clustered storm events in our dataset – also including less intense storms – suggests a more northwesterly jet stream orientation toward Germany. The anomaly pattern appears weaker than during individual severe windstorms such as *Lothar* or *Kyrill*, which is expected given that the composite reflects the mean of 71 distinct events; individual storms may exhibit much stronger deviations from the climatology. Isolated windstorms (see Fig. 7.2), here windstorms separated by more than 21 days, exhibit a circulation pattern that is similar to that of clustered windstorms. The composite flow at 500 hPa is more zonally oriented, indicating a slight shift in wind direction over Germany – from a northwesterly direction during clustered events to a more southwesterly one during isolated events. In addition, the negative geopotential height anomaly over Scandinavia is slightly weaker compared to clustered windstorms. This weaker anomaly with isolated events suggests that an intense low-pressure system is conducive to windstorm clustering.

When reducing the clustering window to 14 days, the negative geopotential height anomaly associated with clustered extremes is enhanced in the mean fields, whereas an extension to 28 days weakens the anomaly pattern (not shown). The intensified anomalies with a shorter clustering window suggest that a smaller sample of windstorm clusters occurring in close succession, for example cyclone families, tend to be more severe than windstorms separated by longer intervals. This interpretation, combined with the intensified anomalies for clustered compared to isolated extremes, can serve as an explanation for findings from the previous section: In Sect. 6.3, we showed that windstorm clusters cause significantly higher losses than isolated events in GER (cf. Fig. 6.14b); these more severe events may be caused by more intense negative geopotential height anomalies.

Furthermore, the patterns in geopotential height anomalies remain robust when considering the longer time series of BW for windstorm clusters (not shown). While the anomaly pattern of clustered extremes closely resembles that of the GER time series, there is little difference between the patterns of clustered and isolated windstorm events. Notably, losses associated with clustered events do not exceed those of isolated ones for windstorms in BW (Fig. 6.14a). A plausible explanation lies in the higher frequency of windstorms (and associated losses) in northwestern Germany compared to the south (see Fig. 2.6). This suggest that windstorm clustering is driven by the events in the northwest of Germany and is most relevant in this region.

Periods of cyclone clustering in Europe have been shown to be associated with a pronounced North Atlantic jet stream (Dacre and Pinto, 2020). The strong jet is often accompanied by Rossby Wave-Breaking (RWB), which describes the irreversible overturning of large-scale atmospheric waves, on either one or both sides of the jet (e. g., Dacre and Pinto, 2020). RWB determines the location of windstorm occurrence and thus facilitates the clustering thereof (Priestley et al., 2017; Dacre and Pinto, 2020). RWB

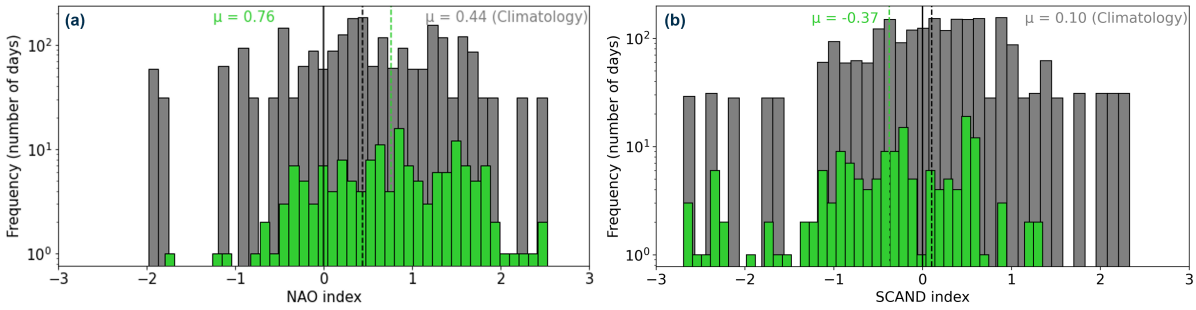

Figure 7.3.: Number of days within windstorm clusters (green) and corresponding indices of (a) NAO and (b) SCAND, compared to the climatology (grey).

at both sides of the jet, anticyclonic to the south and cyclonic to the north, is associated with increased cyclone clustering at 55° N, including northern Germany (Dacre and Pinto, 2020). Further south (45° N, including southern Germany), cyclonic RWB and a zonal jet are associated with increased cyclone clustering (Priestley et al., 2017). It is argued that a persistence of these dynamical conditions over a longer period of time causes clustering by the formation of cyclone families (see Chapter 2, Priestley et al., 2018; Dacre and Pinto, 2020): After cyclogenesis of the first cyclone, RWB increases, which increases the jet speed and decreases stability near the surface, providing ideal conditions for additional cyclones in a similar area. Consequently, it can be assumed that a strong jet including RWB on both sides, drives clustering of extreme windstorms in – mainly northwestern – Germany, although this is naturally not visible in the composites including a large sample of windstorms.

Teleconnections

The average flow pattern during windstorm clusters exhibits some similarity with regard to a positive NAO (cf. Fig. 3.4a), which is reflected in a more positive mean NAO index compared to the climatology, which consists all NAO values within the season of DJF over the time period provided (1997–2022 in the case of windstorms; Fig. 7.3a). A larger similarity is exhibited to the negative phase of SCAND, with a slight northeastward shift (cf. Fig. 3.4c). This is also reflected in a significantly lower mean SCAND index compared to the climatology (Fig. 7.3b).

Many studies have investigated the relationship between windstorms (and even windstorm clusters) and the NAO (e. g., Donat et al., 2010; Dawkins et al., 2016; Walz et al., 2018; Priestley et al., 2023). Positive phases of the NAO are found to be drivers of an increased storm activity north of the eastern North Atlantic storm track (Dacre and Pinto, 2020) and in Central Europe (Priestley et al., 2023). With regard to the inter-annual variability in windstorm occurrence (that is, clustering), the main drivers are found to be SCAND and NAO (Steptoe et al., 2018; Walz et al., 2018). Nevertheless, it has also been shown that the NAO does not explain the entire variance of windstorm occurrence (Mailier et al., 2006). Other studies, however, found that the variability in the NAO explains clustering as identified by overdispersion (Economou et al., 2015). Pinto et al. (2016), for example, showed that 20 %-60 % of the clustering

variability, depending on the cyclone tracking algorithm used, can be explained by the NAO. Our results suggest that damaging windstorms in Germany are more closely associated with SCAND than with the NAO, in accordance with other studies on European windstorm clustering (e. g., Walz et al., 2018).

Weather regimes

During both NAO+ and SCAND-, the negative geopotential height anomalies are centered over the high-latitude North Atlantic sector. This is most closely resembled by ScTr, which is the dominant weather regime during cluster occurrences (see Fig. 7.4a). Relative to the climatology – calculated as the relative frequency of each regime being dominant compared to all days within the specified season – this regime exhibits a frequency anomaly of +20 % during clustered events. The second most frequent regime is ZO, occurring approximately 10 % more often compared to the climatology. Notably, these two regimes are also most common during isolated windstorm events (see Fig. 7.4b). While for clustered events, the maximum anomaly within the ±10-day window is centered on the start day of each windstorm event (day 0), the frequency anomalies for ScTr and ZO tend to increase after the occurrence isolated events, suggesting a gradual build-up of the flow configuration, from which the winter storms then preferably arise. The stronger dominance of specific regimes during clustered events highlights the more pronounced large-scale flow patterns associated with them. In BW, the most frequent regimes relative to the climatology are ScTr and AT (not shown). The higher frequency of these regimes can be explained by a southward shift of the jet stream during AT, implying stronger wind speeds over the south of Germany compared to, for example, ZO.

With regard to European windstorm clusters, cyclonic regimes have shown to be dominant in northern Europe, with anticyclonic regimes being more relevant in southern Europe during cyclone passages (DJF, 1979–2019, Hauser et al., 2023a). This pattern is also evident in our data (see Fig. 7.1). Hauser et al. (2023a) further found ZO and ScTr to occur most frequently during clustering episodes, with regimes establishing prior to the clustering period and persisting beyond it. Similarly, our results show that ScTr is most frequent compared to the climatology as early as four days before the events (cf. Fig. 7.4a). The alignment of our results with studies based on meteorological data only demonstrates the reliability of our mainly loss-based analysis, and shows that our results are applicable in a broader context.

7.1.2 Fluvial floods

The mean large-scale flow during fluvial flood events differs strongly from the strong westerly flow of windstorms, both with regard to their clustered and isolated occurrence (see Fig. 7.5a and b). A negative Z500 anomaly with regard to clustered fluvial floods is found, in the mean fields, over the eastern North Atlantic, the UK, the Netherlands and northwestern Germany, while a strong positive Z500 is found over Greenland. Isolated fluvial floods show much weaker anomalies (see Fig. 7.5b), which indicates a greater variability in synoptic patterns during isolated flood events. This greater variability suggests that these

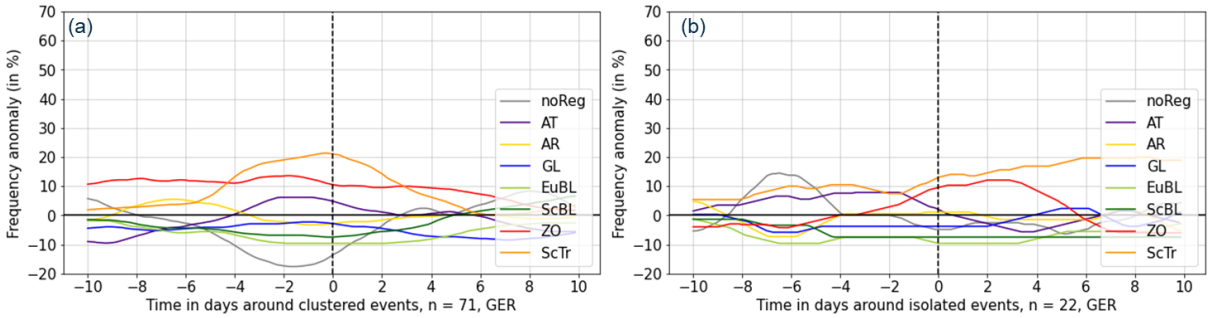

Figure 7.4.: Anomaly in the frequency of weather regimes in the 10 days before and after (a) windstorm events in clusters and (b) isolated windstorms, where day 0 relates to the start date of the event.

events were associated with diverse atmospheric conditions without the presence of a clear pattern. This finding is supported by a sensitivity analysis with clustering windows of 14 and 28 days, which identifies differing and weak patterns with respect to isolated events. Clustered extremes, in turn, show a strong association with a positive anomaly over Greenland robustly to the clustering window.

In BW, the mean flow and anomaly patterns for clustered fluvial floods look similar, with a strong ridge over Greenland and two centers of negative geopotential height anomalies, one over the North Atlantic and one over Poland (see Fig. C1). In the context of isolated fluvial floods, the ridge tends to be weaker, but a strong negative geopotential height anomaly over Scandinavia prevails, which is similar to the windstorm anomalies (Fig. C2). The findings are consistent across different clustering window lengths. These events in BW might be dominated by accompanying windstorms and also less damaging overall (recall that the same filter is applied to both loss datasets). The results that fluvial flood clusters are robustly governed by a ridge over Greenland, whereas isolated floods show no clear pattern (GER) or resemble the windstorm anomaly pattern (BW, ScTr / NAO+ / SCAND-), implies that flood clusters in Germany are characterized by distinct large-scale meteorological conditions (GL / NAO-), regardless of the study area and time period considered.

Teleconnections

As with windstorms, the NAO is also commonly used to investigate heavy precipitation or flooding. The correlation between NAO and precipitation in Europe shows distinct patterns during summer and winter (Zanardo et al., 2019): During wintertime, a positive NAO is related to increased rainfall and hydrological peaks in northern Europe (including northern Germany), as strong westerly winds lead to the advection of warm and moist air masses from the Atlantic. A relationship between a positive NAO and extreme precipitation has been found with respect to extreme winter rainfall in central and northern Europe (e. g., Steptoe et al., 2018), and also in smaller regions like western Austria (Villarini et al., 2011). This positive NAO is also correlated to losses from flood events in Germany, however including mixed signals (Zanardo et al., 2019).

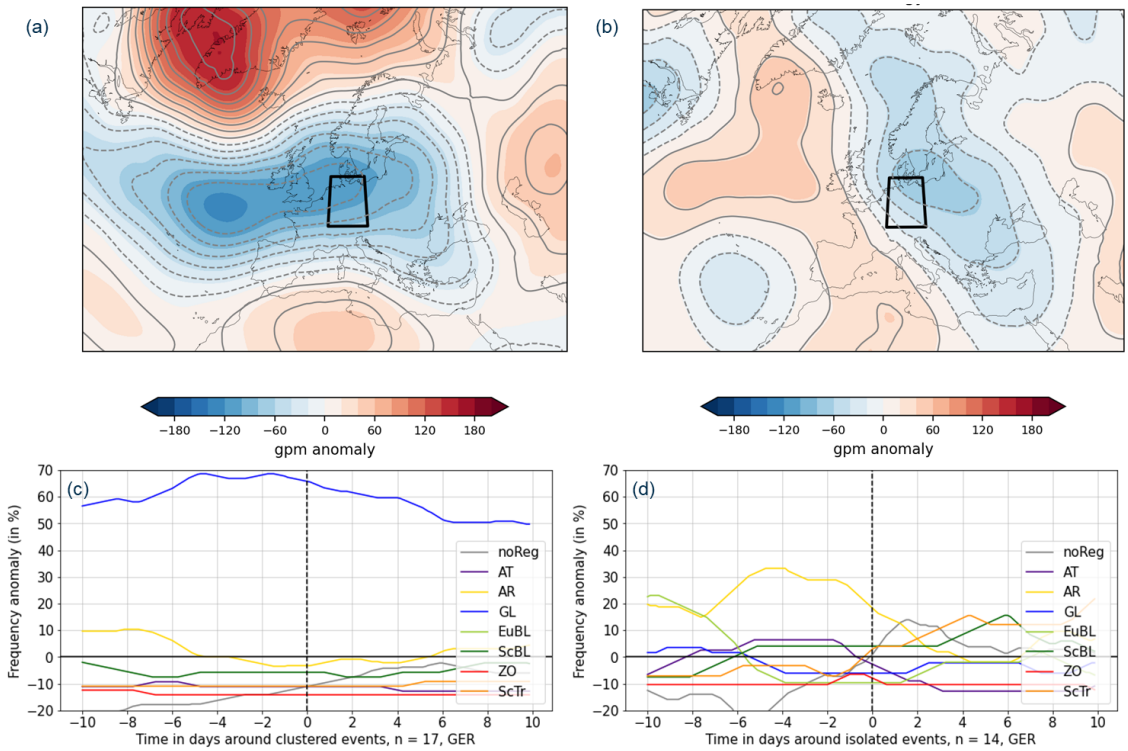

Figure 7.5.: Upper panel: Same as Fig. 7.1b, but for (a) clustered fluvial floods and (b) isolated fluvial floods. Lower panel: Same as Fig. 7.4, but for (c) clustered and (d) isolated fluvial flood events.

In our data, this positive relationship between the NAO and flood events is not visible. Clustered fluvial flood events are associated with a strongly negative NAO both in BW and GER (see Fig. 7.6a). This differs from windstorms and isolated fluvial floods in GER and contrasts with what is found in previous studies. Fluvial floods (both isolated and clustered) are also associated with a more negative EA index compared to the climatology (not shown).

Weather regimes

From a weather regimes perspective, the negative NAO phase during fluvial flood clusters corresponds to the GL regime. This regime exhibits clear persistence before, during, and after flood clusters, with a markedly elevated frequency anomaly of 50–70 %, beginning 10 days prior to the events and continuing for 10 days afterward (Fig. 7.5c). This persistence supports the hypothesis that sustained large-scale circulation regimes steer the clustering of surface extremes, at least in the case of fluvial flooding. In contrast, isolated flood events display much greater temporal variability in the dominance of regimes, with the AR regime being most frequent (Fig. 7.5d).

Lenggenhager and Martius (2019) also found a relation of blocking with heavy precipitation in winter. They found a significant increase in the odds of moderately extreme events of a duration of 1–5 days in parts of Central Europe, including southern Germany, during blocking in the western North-Atlantic sector (between 60° W and 30° W). As the block is located close to Greenland, our findings are consistent

with this study. Another study on heavy precipitation and weather regimes, Barton et al. (2022) found AT explaining the highest share of clustering probability in all seasons throughout most of western Europe, including western Germany as well. Note that AT and GL are somewhat similar (cf. Fig. 3.5), with negative anomalies over northern and central Europe (strong for AT, weak for GL) and a positive anomaly over Greenland (weak for AT, strong for GL. They however find the other zonal regimes (ZO and ScTr) also associated with an enhanced clustering during winter, whereas the blocked regimes (EuBL and ScBL) tend to inhibit clustering (Barton et al., 2022).

The contrasting patterns of flood clusters compared to most other studies on both weather regimes and teleconnections can possibly be explained by the following arguments: First, our study area is much smaller compared to studies covering larger parts of Europe (Barton et al., 2022; Zanardo et al., 2019). Second, clustered fluvial floods both in GER and BW include only a limited number of events (17 and 14 events, respectively), albeit with a robust result, and are potentially dominated by specific winters (see case study below). Towards this end, the sensitivity was tested by excluding some winters, which yielded no significant changes. Third, due to the insurance type for 'other natural hazards' (see Chapter 3), the damage categorized as fluvial floods may include snow pressure events as well. This applies only to GER, as the data for BW were already pre-filtered. Excluding named snow pressure events (provided by the GDV) did, however, not change the general geopotential height anomaly pattern. Fourth, identifying extreme event days using loss data directly may conceal other drivers leading to the damage, such as topography, previous conditions, or socio-economic factors, for example. Lastly, cyclone clustering has shown to be associated with increasingly blocked patterns with decreasing latitudes (Hauser et al., 2023a). Due to the anomalously high insurance density in BW, the identification of flood events in winter may be disproportionately influenced by precipitation events affecting mainly BW (see also Chapter 6 for a discussion). GL is associated with strong westerlies and negative anomalies over central and southern Europe (cf. isohypses in Fig. 3.5g). Therefore, this southward shift in event occurrence could be related to a southward shifted jet stream and thus an increased GL dominance. Thus, we argue that this pattern of GL / NAO- with fluvial flood clusters can assumed to be robust for the given time period and particularly for southern Germany. However, further investigations covering a longer time period with more events, and a broader geographic area covered, would help to confirm or challenge our findings.

7.1.3 Multi-hazards: Windstorms and fluvial floods

The mean geopotential height anomaly pattern associated with clustered fluvial flood and windstorm events closely resembles that of clustered windstorms (Fig. C4). This similarity is expected, as windstorms are initiated by strong cyclonic systems that dominate the large-scale circulation (e. g., Bloomfield et al., 2024). The anomaly pattern for clustered compound extremes is typically somewhat weaker than for windstorms alone (as the fluvial flood events with a strong GL dominance are also included), whereas it is slightly more pronounced in the case of isolated events.

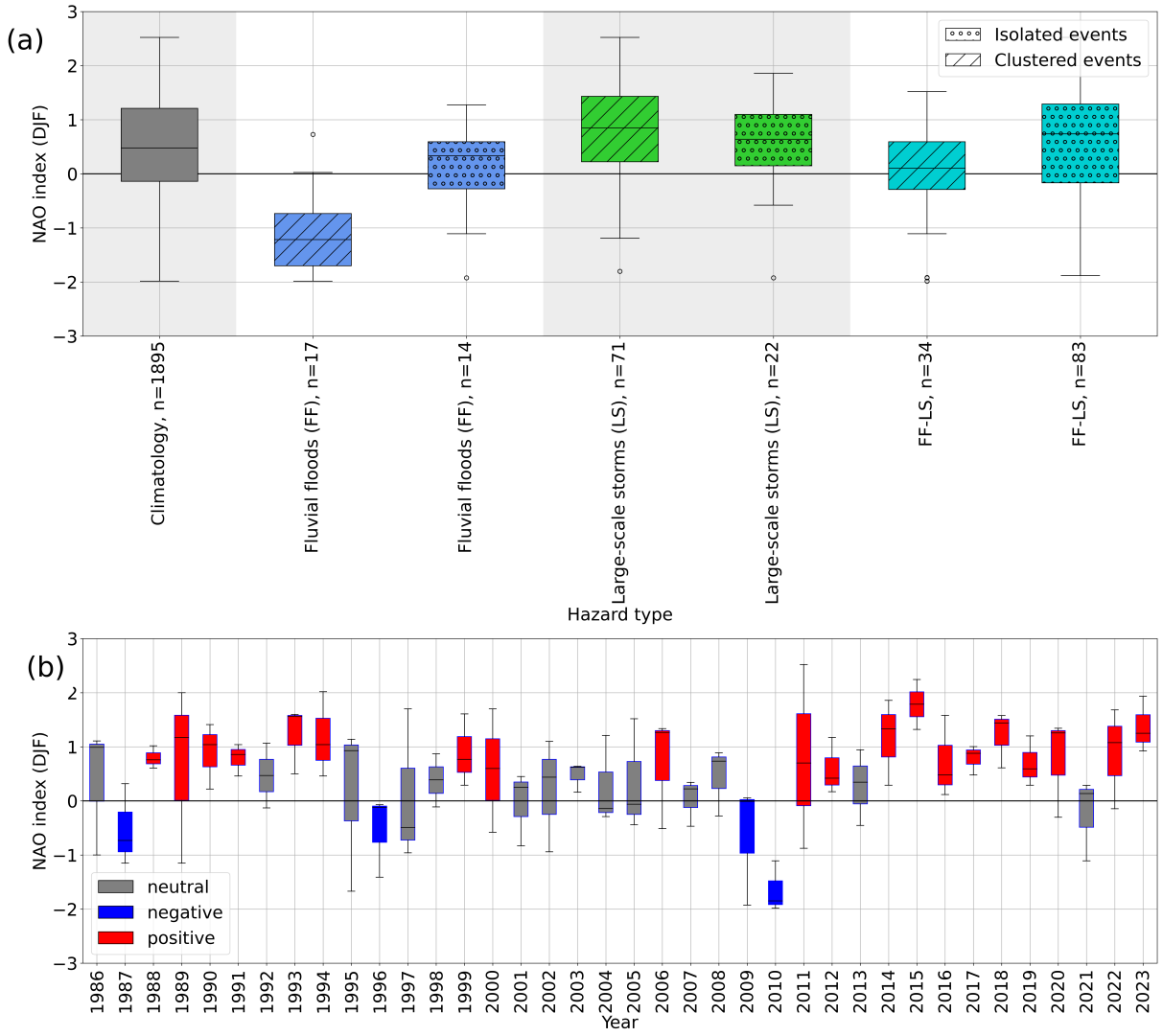

Figure 7.6.: December–February: (a) Distribution of monthly NAO values during 1986–2023, depending on the event type (colors), isolated occurrence or occurrence in clusters (hatches), (b) monthly mean NAO values from 1986 to 2023. Positive NAO values are detected if mean values > 0.5 and max values > 0.75. Negative values relate to mean values < -0.5 and max values < -0.75. Neutral years are all years neither classified as positive nor as negative.

The NAO index also reflects the similarity in large-scale circulation anomalies between compound windstorm–fluvial flood events and windstorms alone, with only a slightly weaker signal for the compound events (Fig. 7.6a), indicating a comparable synoptic-scale setup (compare also Figs. 7.1 and C4). While there is a high annual and multiannual variability in the NAO index, a range of winters in past decades were dominated by cyclonic regimes and a positive NAO (see Fig. 7.6b). This pattern is especially pronounced in the most recent decade, where the windstorm clusters of 2018, 2020, and 2022 occurred.

From a weather regimes perspective, however, GL becomes dominant when clusters are combined (see Fig. C5a). This is noteworthy given the substantially higher number of circulation-dominating windstorm events, which are associated with a pronounced ScTr anomaly (cf. Fig. 7.1). An explanation for these differences in NAO and weather regime anomalies is the way of calculation: While the NAO is represented by a standardized monthly index based on pressure differences, weather regimes are identified from 6-hourly anomaly patterns relative to the climatological mean. This climatology of the weather regimes is dominated by zonal regimes in winter (Grams et al., 2017), which is why the anomaly is stronger for blocked regimes. Note that daily NAO values are also available from the NOAA; a sensitivity test with monthly averages based on a 15-day rolling window yielded only minor changes. A different result could be expected when using daily values of the NAO index.

Previous studies also found compound wind and precipitation extremes in northern and central Europe to be associated with positive NAO values (Bloomfield et al., 2024; François et al., 2024). Bloomfield et al. (2024) furthermore found cyclonic patterns as the main relevant patterns during daily extreme compound events in the UK, with the highest risk of co-occurrence in January and February. They suggest that in a future climate, these extremes may happen in a larger variety of weather patterns (Bloomfield et al., 2024). Others suggest that combinations of teleconnection patterns could explain a larger share of the variability (François et al., 2024).

In summary, while persistence matters for the occurrence of single-hazard clusters, the large-scale circulation patterns differ heavily comparing fluvial flooding and windstorms. The strong difference in patterns between clustered fluvial flood and windstorm events suggests that persistent, but different synoptic conditions favor the occurrence of the most extreme flood and windstorm extremes in winter. The prevalent pattern during windstorms, a slightly shifted zonal flow (moderate NAO+, ScTr as dominant regime), is often accompanied by (moderate) precipitation as well, and NAO+ is therefore also the dominant pattern during compound flood-wind clusters. In contrast, flood clusters alone are related to a contrasting pattern, dominated by NAO- and GL. This contrasts findings from most other studies, and therefore requires further investigation with meteorological data and a larger sample size for a more robust assessment.

7.1.4 Analysis of three selected winters

To understand the temporal development of multiple hazard clusters (including windstorms and fluvial floods) in depth, we use three selected winters to illustrate how specific circulation patterns lead to the accumulation of extreme events over short periods. This can provide additional insights, as synoptic situations and their temporal progression are always distinct expressions of the large-scale configuration, which can deviate strongly from a mean state. As the winters of 2004/2005, 2009/2010, and 2020/2021 showed a particularly high number of clusters, and were characterized by different large-scale conditions, they are analyzed here in more detail.

The winter 2004/2005 was governed by both cyclonic and blocked regimes (see Fig. 7.7a), which was associated with a snowy conditions in Germany (DWD, 2005). Mainly cyclonic regimes were present during December and until mid-January, followed by a dominance of blocked regime during the second half of the winter. It is visible that the longer life cycles of ScTr and ZO associated with windstorm clusters were preceded by a short-lived blocking (EuBL). December 2005 may be therefore be an instance of blocking contributing to increased cyclone intensity: Blocking can contribute to establish strong near-surface pressure gradients, which imply strong geostrophic near-surface winds (Kautz et al., 2022). In January and February, AR and EuBL were associated with fluvial flooding, while ZO and ScTr were associated with a windstorm series (cyclones *Aloys* and *Erwin*, including gusts of up to $156\,\mathrm{km\,h^{-1}}$, Wettergefahren-Frühwarnung, 2005). Similar conditions occurred during a windstorm series in February 2020 including *Sabine*, for example (not shown). In February 2005, a combined cluster including fluvial floods and a windstorm in February was favored by a succession of zonal (ScTr) and blocked (AR and GL) regimes. This underlines the relevance of cyclonic regimes for windstorm clustering as pointed out in Sect. 7.1.1, in contrast to mainly blocked regimes for floods. While the composites demonstrate that for combinations of flood and windstorm clusters a cyclonic pattern is dominant, this temporal analysis reveals that the temporal succession of cyclonic and blocked regimes can play an important role. Note that both in mid-January and mid-February, the events occurred in the transition between ScTr and AR. It is furthermore evident that both hazards occurred predominantly after a build-up phase within the life cycle of each regime, suggesting that both regime types need to be well established for the occurrence of extreme events.

The winter of 2009/2010 was dominated by an exceptional negative NAO (see Fig. 7.6b), where many of the clustered fluvial flood events, likely including snow pressure events as well, occurred in GER. In general, this winter was characterized by abnormally cold and snowy conditions, with Germany experiencing the longest period of snow cover for at least 30 years (WMO, 2010). While the most frequent dominant regime was clearly GL, blocked regimes dominated throughout the entire winter (Fig. 7.7b). This corresponded to an anomalously long negative NAO phase (Osborn, 2011). During this winter, a persistent block extending to Scandinavia at around 60° N caused low cyclone numbers near Greenland and Iceland, but enhanced cyclone activity and strong mean winds spanning from the North Atlantic into

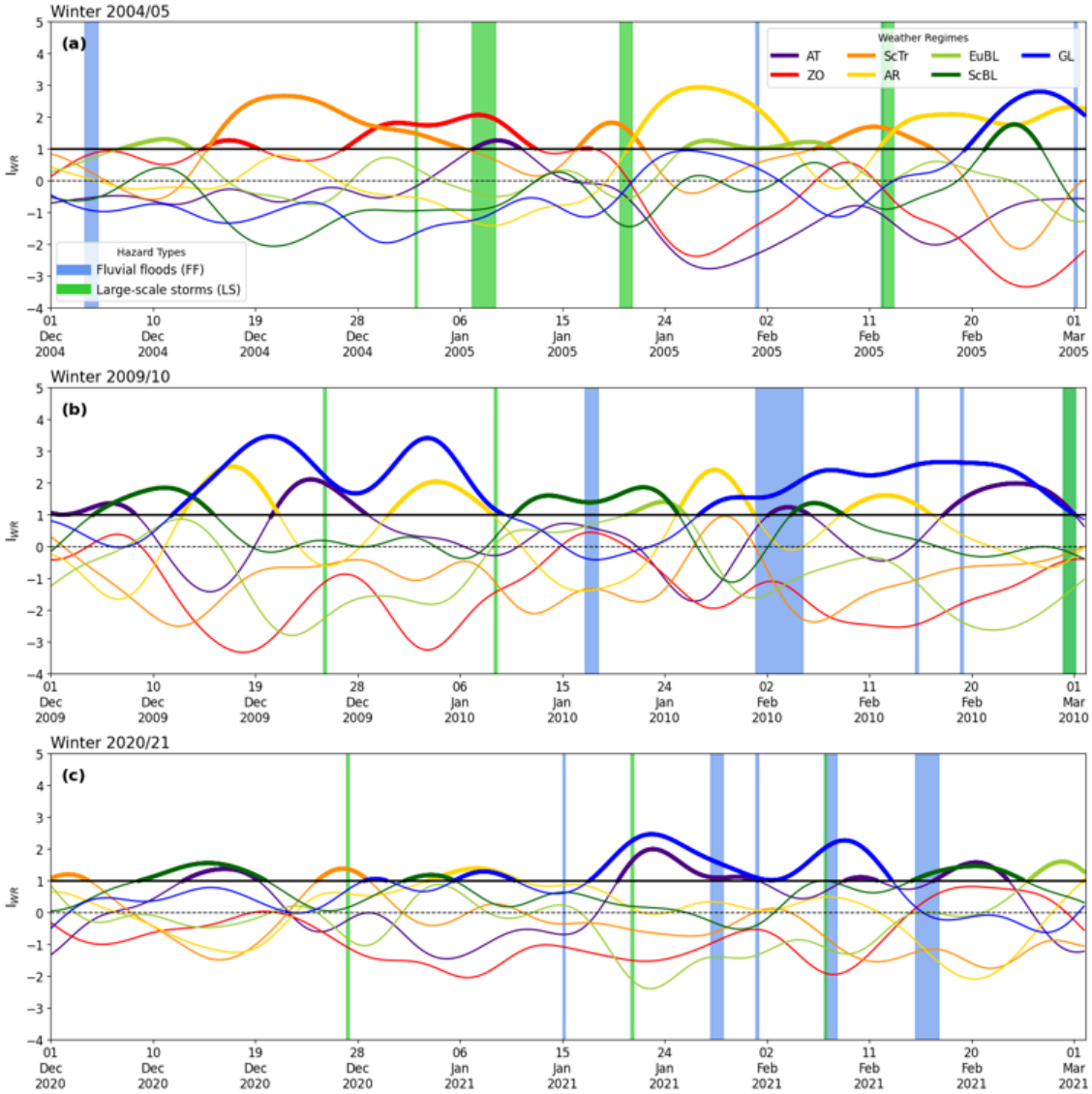

Figure 7.7.: Time series for example winters of (a) 2004/2005, (b) 2009/2010, and (c) 2020/2021, and their associated weather regime index. Colored horizontal lines represent I_{WR} for each of the weather regimes. An $I_{WR} > 1$ is denoted by thick lines. Vertical lines denote dates within clustering periods, where the color relates to the type of the cluster.

the Mediterranean at around 45° N (Kautz et al., 2022). The persistent GL was related to a windstorm cluster, with windstorms occurring in December 2009 and January 2010. On January 9-10, cyclone *Daisy* entailed heavy snowstorms and disruptions (DER SPIEGEL, 2010), succeeded by flood (or snow pressure) events and a combined cluster with fluvial flooding and a windstorm during February 2010 (cyclone *Xynthia* occurred between 26 February and 1 March, see also Sect. 2.1.1; Roberts et al. (2014)). Based on cyclone tracks, Hauser et al. (2023a) also found serial clustering of windstorms at 45 ° N (i. e., slightly south of Germany) in that winter, namely between 21 December and 31 December 2009 as well as during the end of February 2010. This shows that persistent GL can be associated with both an increased occurrence of flood and windstorm events: The first life cycle of GL was only associated with windstorms, while the second one mainly induced flood damage. As was the case in the winter of 2004/2005, it is evident that events took place a few days after the onset of a regime, with further events occurring within clusters throughout the life cycle of each regime.

The winter of 2020/2021 (Fig. 7.6b) was characterized by above-average temperatures but also by numerous surface lows advecting humid, often cold and wet air masses to Germany during December and January (DWD, 2021). These conditions led to snow abundance. During the end of January and in February, the onset of thawing weather led to the melting of the snow masses and heavy rainfall in the west and south causing major flooding (DWD, 2021). Regarding the large-scale circulation, this winter was also dominated by GL, however, for a shorter period compared to 2009/2010 (Fig. 7.7c). A series of windstorm and flood events occurred in close succession, almost exclusively within GL or a few days before and after. This was a classical case of rain-on-snow flooding, which can be classified as a preconditioning compound event and has been studied extensively (e. g., Bevacqua et al., 2021). This presence of GL in January 2021 shows a similar pattern as in December 2009, with a strong increase in the I_{WR} up to an index of about 2.5, followed by a decay after a few weeks, and another peak a few days later. In contrast to the winter of 2009/2010, this period was accompanied by surface extremes of both types, showing that GL can also favor the succession of multiple extremes. The winter of 2018/2019 shows a similar pattern (not shown): This winter was dominated by combined extremes which mainly occurred during AR, also a blocked regime. The high frequency of combined clusters underpins the relevance of weather regimes for multi-hazard events, and shows that extended periods with blocked regimes can favor their occurrence.

Several conclusions can be drawn from the analyses of these selected winters: First, consistent with what has been found for the whole sample in Sects. 7.1.1 and 7.1.2, longer life cycles of cyclonic regimes were often associated with windstorm clusters, and blocked regimes favor the occurrence of flood events in the case studies. Nevertheless, the sequence of weather regimes may also have an influence, and their transition may play an important role (winter 2004/2005). Furthermore, GL can also be associated with the occurrence of windstorm clusters only (winter 2009/2010), or with multi-hazard clusters (winter 2020/2021). This shows that GL is an important regime with respect to extreme events in winter, not

only with respect to flooding. In addition, the occurrence of almost all extremes was associated with the strong presence of a distinct weather regime, showing that clear distinguishable large-scale patterns help to explain surface extremes. However, it should be noted here that this is only exemplary evidence based on selected winters – naturally, statistical analyses across the full dataset provide stronger evidence for general patterns than individual case studies.

7.2 Summer extremes: May–August

The large-scale circulation during events in MJJA differs heavily from the prevailing westerly flow driving most events in the wintertime. Pressure differences are generally smaller in summer, due to smaller temperature differences between the North Pole and the Equator (see Chapter 2; e. g., Kraus, 2004). Therefore, the intensity of teleconnection patterns is weaker as well (e. g., Barnston and Livezey, 1987).

A prevailing southwesterly flow, typically reflecting a transition from a trough to a ridge, characterized the mean synoptic state over Germany during all major convective events (see, e. g., Fig. 7.8). This can be associated with atmospheric blocking, which is characterized by persistent positive geopotential height anomalies, e. g., over eastern Europe or Scandinavia. With blocking over Scandinavia or eastern Europe, the western flank of the blocking system lies above Germany, with the trough positioned west of the British Isles. In the area between the ridge and the trough, particularly on the forward flank of the trough, lifting is often initiated, and thereby convective extremes can be favored.

7.2.1 Pluvial and mixed floods

During pluvial flood events, the ridge is centered over eastern Scandinavia in a mean state (Fig. 7.8a), corresponding to a positive geopotential height anomaly (Fig. 7.9a). For isolated pluvial floods (Fig. 7.9d), this geopotential height anomaly is stronger than for clustered pluvial floods, representing the overall strongest anomaly compared to the other convective single hazards. This strong anomaly, indicating a weak geopotential gradient within the area it covers, may explain the presence of stationary thunderstorms, which can lead to a high cumulative precipitation. When reducing the clustering window (14 days), a secondary positive geopotential height anomaly evolves over Greenland, suggesting the presence of another Rossby wave (not shown). With an increased clustering window (28 days), isolated events are characterized by an even stronger secondary positive anomaly over the North Atlantic.

With mixed flooding, the positive geopotential height anomaly is shifted towards central Scandinavia, positioned even north of the negative geopotential height anomaly (not shown), which is robust for a change in the clustering window. Mixed flooding is characterized by a strongly positive EA index (see Fig. 7.13) and also a positive SCAND index, where mixed flooding stands out with positive values (not shown).

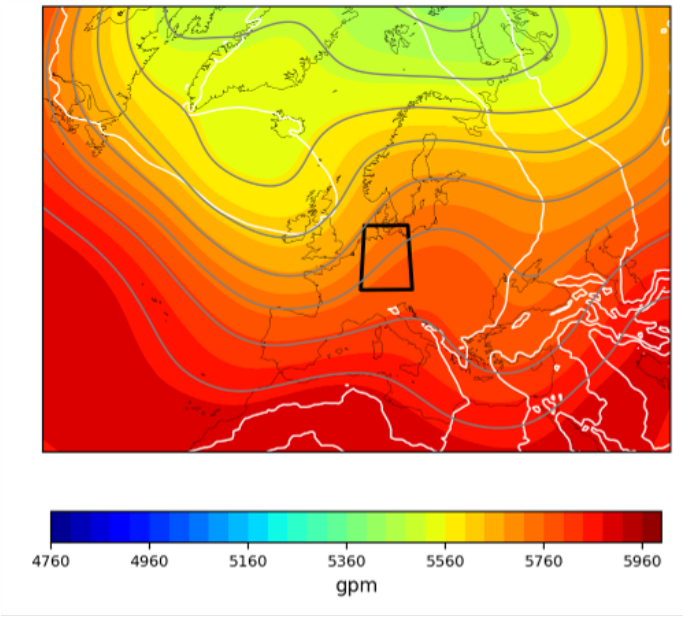

Figure 7.8.: Same as Fig. 7.1a, but for clustered pluvial floods during MJJA, with a sample of 77 events and 2045 time steps included.

It has been shown that thunderstorm frequency is increased with the occurrence of atmospheric blocking (Mohr et al., 2019), which also affects the frequency and distribution of convective precipitation and flash floods (Mohr et al., 2020; Kautz et al., 2022). For example, blocking is found to affect regional-scale heavy precipitation of short duration in Europe (e. g., Lenggenhager and Martius, 2019). While heavy precipitation is less likely within the blocked area, it tends to increase southeast and southwest of the blocking anticyclone (Lenggenhager and Martius, 2019; Kautz et al., 2022). With the typical geopotential height anomaly patterns found during convective extremes (Fig 7.9), this typically includes Germany, as the positive anomalies are located to the east of Germany.

Teleconnections and weather regimes

During the European summer, the NAO is much weaker than in the winter months (cf. Fig. 3.4), with a stronger influence in the north around 60 °N (e. g., Zanardo et al., 2019). Pluvial floods are associated with a NAO index similar to the the climatology (Fig. C8). A stronger signal is shown by the EA index (Fig. 7.13), which is higher (more positive) for clustered pluvial floods compared to their isolated occurrence.

The dominant weather regime during both pluvial and mixed floods is ScBL, with little difference between clustered and isolated events (see Fig. 7.10a and b). Note that ScBL is generally most frequent during MJJA (1979–2015, Grams et al., 2017), which is why a frequency anomaly of 20 % can be regarded as high. For pluvial floods, the frequency anomaly increases when ScBL begins to rise as early as eight days before the event, peaking approximately two days prior to the event. These findings suggest that pluvial flood events likely occur within a positive frequency anomaly of ScBL, which begins to de-

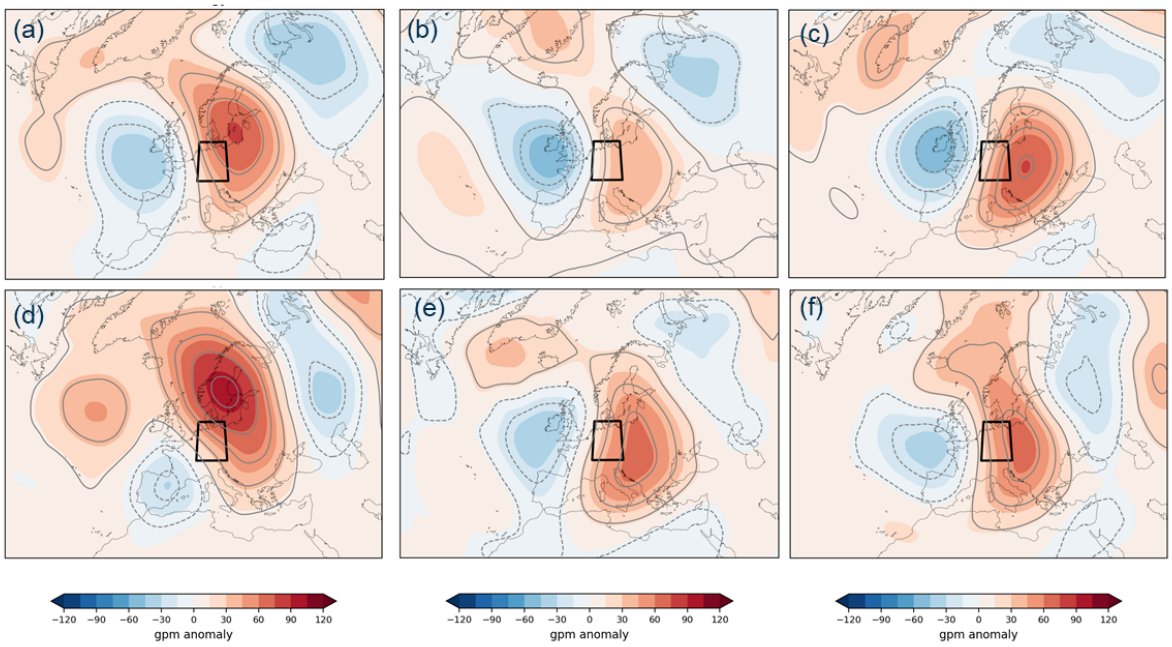

Figure 7.9.: Z500 anomaly (see Fig. 7.1) for (a and d) pluvial floods, (b and e) convective gusts, and (c and f) hail events, for clustered (upper row) and (lower row) isolated events. Note that the color bar is adjusted to a smaller range compared to DJF.

velop up to a week prior to the event and peaks shortly before the event. The frequency anomaly of ScBL decreases sharply until two to four days after the event, where GL emerges as the dominant regime. By contrast, mixed flood events are characterized by a single, persistent regime (ScBL), which builds up prior to clustered events. With regard to isolated events, ScBL occurs even more frequently around 10 days before events than during them. A potential explanation for these contrasting temporal patterns might be that for the occurrence of pluvial and mixed flood clusters, a longer and accumulating anomaly of ScBL is necessary to advect warm and moist air masses from the Mediterranean. Isolated mixed flood events, with a decreasing frequency anomaly of ScBL, would then rather be a result of stochastic synoptic processes (consider also the smaller sample), while the pure convective events associated with pluvial flooding also require an established ScBL.

Barton et al. (2022) also found a (slightly) positive effect of ScBL on precipitation clustering over Germany in summer, together with AT, which mainly increases the effect in the northwest. They explained the higher frequency of ScBL by an associated increase in atmospheric instability at the flank of the block, which is shifted northwards in summer. Consequently, precipitation extends further northwards as well compared to other seasons (Barton et al., 2022). The major flood events in 2002 and 2013 (see also Sect. 7.2.4), for example, were associated with a high blocking frequency prior to the event, providing wet and cool conditions over central Europe (Kautz et al., 2022). During the 2021 western Germany flood, triggered by low *Bernd*, a persistent ScBL was also present, favoring the formation of a series of cut-off lows, among which *Bernd* was notable (Barton et al., 2022). The positive relationship with AT

over northwestern Germany found in Barton et al. (2022) suggests a strong presence of the polar-front jet during precipitation clusters throughout the year. In our dataset, this high AT frequency is neither evident for pluvial nor for mixed flood events; however, this could be related to the relatively low insurance density in some regions (see Chapter 3 and Fig. A3), which does not guarantee that all relevant events are included, especially those in the northwest.

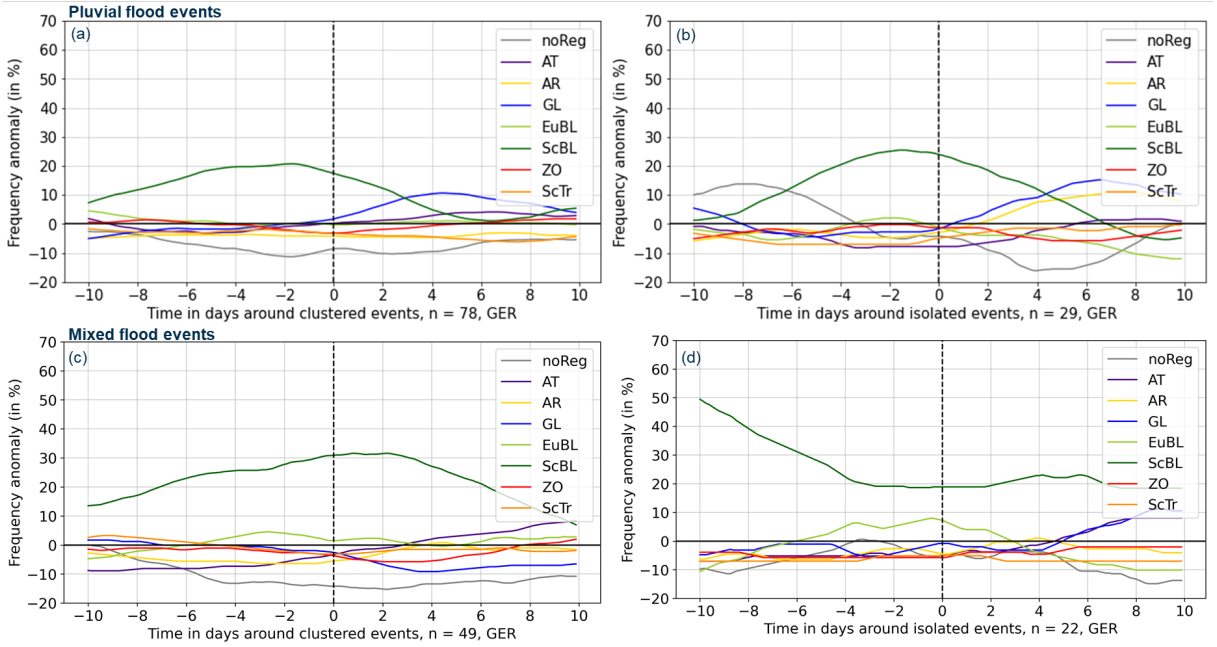

Figure 7.10.: As Fig. 7.4, but for pluvial (upper panel) and mixed (lower panel) flood events.

7.2.2 Convective gusts and hail

The Z500 anomaly patterns regarding pluvial floods are similar for convective gust and hail damage events (middle and right panels in Fig. 7.9), as all three phenomena are induced by convective systems. Compared to pluvial floods, the ridge is shifted to the southwest, with its center east of Germany. The positive geopotential height anomaly is weaker for convective gusts than for hail. These findings are robust to a change in clustering window (14 or 28 days). This suggests that more severe SCSs are favored by stronger ridges and therefore also troughs upstream, which in combination induce lifting in their transition area, creating favorable conditions for thunderstorms. For the longer timeseries of BW, the geopotential height anomaly patterns regarding convective gusts, hail, and pluvial floods resemble those in GER strikingly, reproducing the southwestward shift of the positive geopotential height anomaly within convective gusts and hail compared to pluvial flood events (not shown). This is expected, as studies relating thunderstorm occurrence probability to the large-scale atmospheric circulation showed no regional differences in thunderstorm probability during the occurrence of blocking over Scandinavia (Mohr et al., 2019; Augenstein, 2025).

Teleconnections and weather regimes

Convective gusts and hail events are associated with a negative NAO index, however without a visible deviation from the climatology (see Fig. C8). The clear dominant weather regime is ScBL, with little difference between clustered and isolated events and a generally high variability. However, in contrast to pluvial and mixed floods (and the events in winter), no regime exceeds a frequency anomaly of 15 % throughout the +/- 10 days before and after the event (Fig. C9).

In a study on the relation of blocking and thunderstorm activity in western and central Europe, it is found that thunderstorm occurrence shows the largest statistical increase with a block present over the Baltic Sea, by supporting the advection of unstable, warm, and moist air masses from the south into western and central Europe (Mohr et al., 2019). This finding is supported by another study showing that convection-favoring conditions, such as increased moisture, occur ahead of upper-level troughs (Piper et al., 2019). Comparing these findings to the geopotential height anomalies of SCSs in our data, convective gusts and in particular hail are dominated by blocking over the Baltic Sea, centered almost exactly over the location identified by Mohr et al. (2019). This demonstrates, as shown for the large-scale storms in winter, that the loss-based analysis is comparable to analyses based on meteorological data only, and that our findings, also related to large-scale triggers, are reasonable. The block over the Baltic Sea is more accurately depicted by the EA compared to the northward shifted NAO. Therefore, especially clustered hail and convective gust events, where the positive geopotential height anomaly is shifted farther south, show a higher EA index (Fig. 7.13).

Serial clustering of thunderstorms has also been investigated with regard to weather regimes (Augenstein, 2025). Blocked regimes were found to be more frequent during the occurrence of serial thunderstorm clusters compared to other regimes. Although the presence of blocked regimes during thunderstorm clusters might suggest a general increase in blocked regime frequency compared to isolated events, our data show no significant difference in blocking frequency between clustered and isolated events (compare left to right panel in Fig. C9).

7.2.3 Multi-hazards: Pluvial floods, convective gusts, and hail

When convective extremes are investigated together, clusters of pluvial flooding and hail (PF-H) seem to be dominated by the synoptic situation during pluvial flood events (not shown). This is not the case for clusters of pluvial flooding and convective gusts (PF-CG), and clusters of convective gusts and hail (CG-H) resemble the patterns during hail events, with a slightly stronger positive geopotential height anomaly. This indicates that the large-scale circulation patterns of either pluvial flood or hail events dominate the patterns of clusters. While isolated extremes again resemble the patterns of pluvial floods, with the ridge centered over Scandinavia (Fig. 7.12), clustered PF-CG-H are characterized by a strong positive geopotential height anomaly farther south, to the east of Germany (Fig. 7.11). This pattern, with

the strongest anomaly over Scandinavia, strongly resembles the mean pattern of hail and convective gust events. The patterns are robust to a change of the clustering window, with a slight weakening for the longer time period in BW.

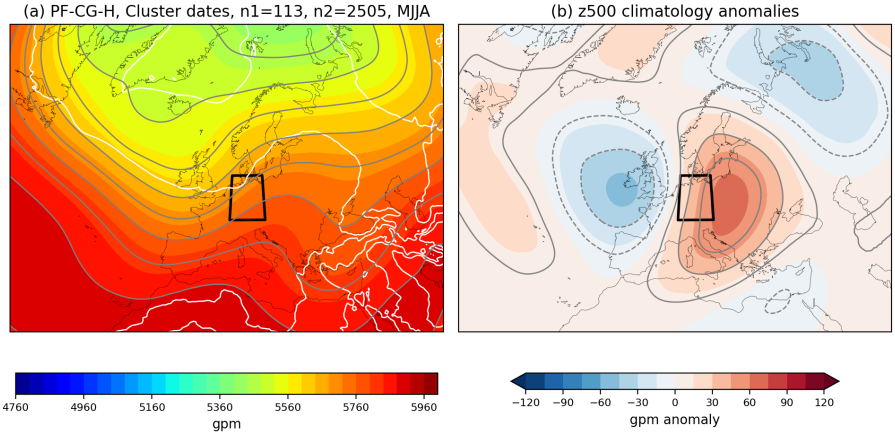

Figure 7.11.: Same as Fig. 7.1, but for clustered pluvial floods, convective gusts, and hail during MJJA. Note that the color bar is adjusted to a smaller range compared to DJF, ranging from -120 to 120 gpm with steps of 15.

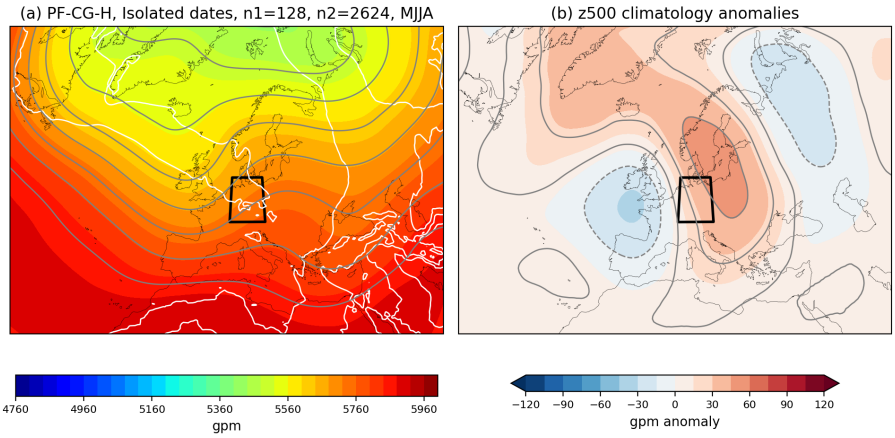

Figure 7.12.: Same as Fig. 7.11, but for isolated pluvial floods, convective gusts, or hail.

This shows that the distinct geopotential height anomaly over Scandinavia during pluvial flood events dominates the patterns when investigating conditions for isolated extremes of either SCSs or pluvial flooding (Figs. 7.11). Clustered events including all three convective extremes are characterized by a ridge centered over the Baltic Sea and Poland, which is dominant during hail events.

As seen above, the teleconnection pattern with the most pronounced differences during MJJA is the EA pattern. Many clustered multi-hazard combinations of convective hazards also show much higher positive values of the EA index compared to isolated ones (see Fig. 7.13a), which also dominated in recent summers (see Fig. 7.13b). With regard to weather regimes, all combinations (PF-H, PF-CG-H, PF-CG and CG-H) show a dominance of ScBL (Fig. C10). While clustered extremes involving hail

occur at the transition between a dominant ScBL regime to an anomalous AT occurrence, the dominance of ScBL is replaced by GL in the case of isolated extremes.

The difference in the EA index of clustered and isolated extremes as well as the distinct sequence of regimes during clusters and isolated extremes points to an influence of the large-scale circulation which is yet to be researched.

7.2.4 Analysis of three selected summers

As was done for winter (see Sect. 7.1.4), a detailed analysis of selected summer periods can similarly enhance our understanding of the influence of large-scale circulation patterns.

At first, the summer of 2009 is analyzed, a period with a particularly high number of events (see Fig. 7.14a). A variety of mixed flood, hail, and convective gust events occurred especially in May. This was followed by a relatively calm period until mid-June, after which a period of convective activity began and continued until the end of August. The DWD called it a 'diversified summer', where dry and warmer periods alternated rapidly with wetter, somewhat cooler phases (DWD, 2009). The warmer periods came with many severe thunderstorms and accumulated precipitation in the Alps (DWD, 2009). The convective hazards generally occurred at a variety of both blocked and zonal regimes. Most frequently, events were observable after the establishment of ScBL, GL and AT. Particularly late July was characterized by an $I_{WR} > 2$) regarding all three of the aforementioned regimes. It is also evident that all three convective extremes (pluvial flooding, hail, and convective gusts) often occurred in close succession. This suggests that, although convective extremes are more common during blocked regimes in the extended summer months, various regimes can occur during these extremes. This indicates the dominance of local processes.

The summer of 2013 (see Fig. 7.14b) is selected due to a sequence of particularly severe events that occurred in that year (see also Chapter 1 or Chapter 6): Severe flooding caused high damage at the end of May and beginning of June, which was followed by a severe hail event in July, and a heat wave in August. An analysis of the entire period from May to August with respect to weather regimes reveals the following: The summer was started by a continuous period of hail, convective gusts and the severe mixed flood events during the end of May and the beginning of June, where ScBL, AT and ZO were active. The heavy precipitation, causing major floods in 2013, was caused by cyclonic wave breaking on the flank of the block over Scandinavia, with associated southward ascending warm conveyor belts (Grams et al., 2014; Kautz et al., 2022). After a calmer period during the beginning of July, where EuBL was active, hail event *Andreas* was accompanied by pluvial flood and convective gust events. This period was characterized by a longer active period of ScBL, with southwest Germany located in the transition zone between ridge and trough during the hailstorm *Andreas* (Kunz et al., 2018). From this example, it can be seen that especially long periods of ScBL can favor surface extremes with particularly damaging

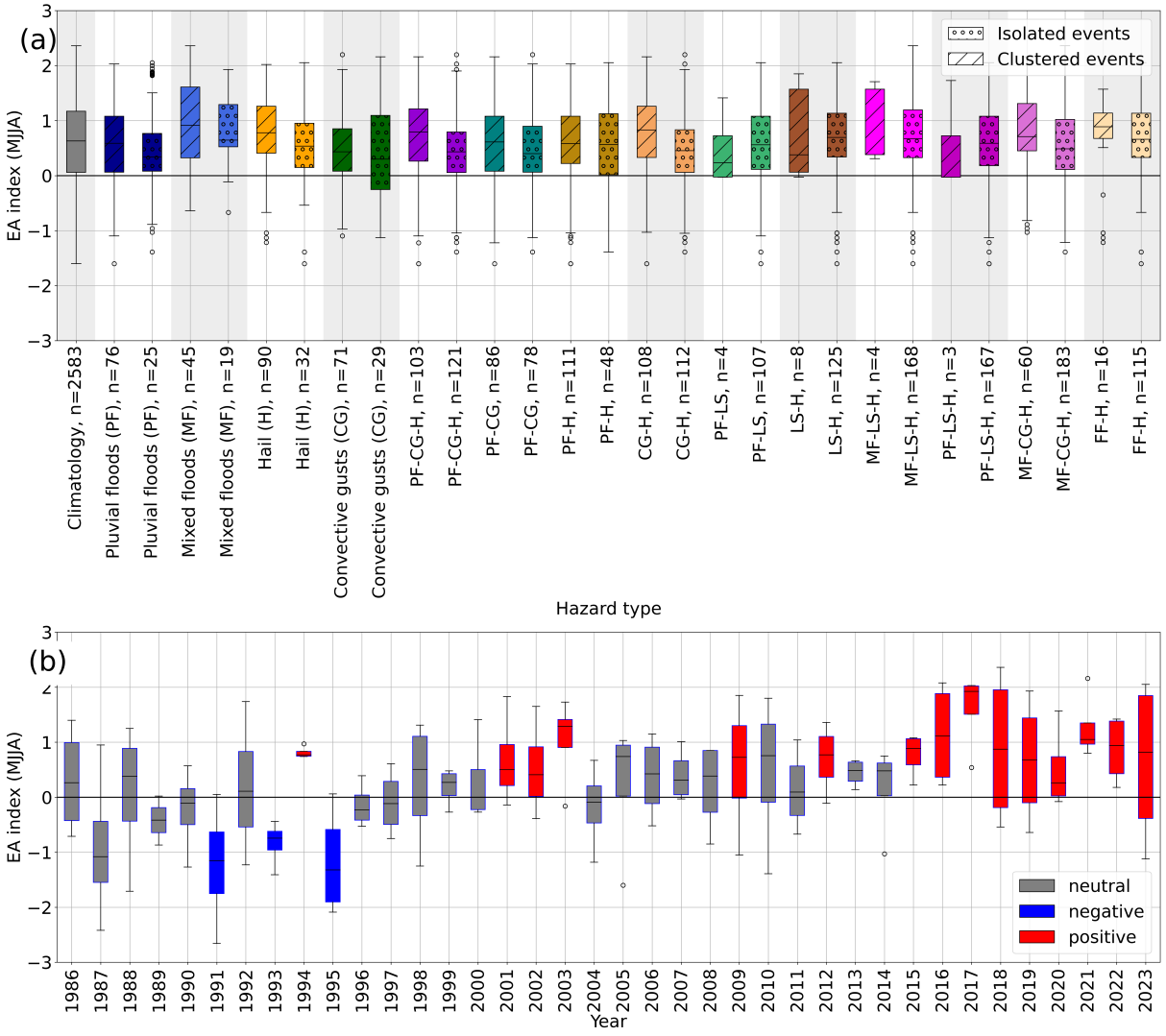

Figure 7.13.: May–August: (a) Distribution of monthly EA values during 1986–2023, depending on the hazard type (colors), isolated occurrence or occurrence in clusters (hatches), (b) monthly mean EA values from 1986 to 2023. Positive EA values are detected when with mean values > 0.5 and max values > 0.75. Negative values relate to mean values < -0.5 and max values < -0.75. Neutral years are all years neither classified as positive nor as negative.

impacts, and the succession of ScBL by AT might play a role. In addition, albeit being a blocked regime as well, EuBL seems to be less relevant for the convective extremes, even with a strong I_{WR}.

Lastly, as the highest number of clustered events were observable in 2019 (cf. Chapter 6, Fig. 6.4), the summer of 2019 was also chosen for a case study analysis (see Fig. 7.14c). While it was dominated by extreme heat, severe thunderstorms and flash floods were also responsible for high damage (DWD, 2019). 2019 was almost exclusively dominated by blocked regimes as well as AT. Several clusters of multiple convective extremes were present, for example in the beginning of June, and during the end of July. The thunderstorm period in June was particularly severe, with a synoptic pattern characterized by three extended troughs, including cut-off lows, and a ridge over Scandinavia (Wilhelm et al., 2021). Almost all of the thunderstorms in June and July were associated with a strong I_{WR} (up to 4) of ScBL, or an extended AR. As during July 2009, a strong dominance of GL, ScBL and AT was present during the end of July 2019, accompanied with a set of mixed flood events. Therefore, 2019 was a summer in which the increased extremes caused by blocking were evident: The presence of a block over Scandinavia was associated with the advection of warm and moist air masses, which were transported northward and favor strong convection over central Europe (Mohr et al., 2019; Wilhelm et al., 2021). Interestingly, the weaker I_{WR} of ScBL in June was related to more hail events than the strong I_{WR} in July. Therefore, this example suggests that a more pronounced blocking does not favor more intense thunderstorms.

In summary, these example summers manifest the findings that blocked regimes and AT, particularly ScBL, are most relevant for the occurrence of convective extremes in summer. On the other hand, severe convective events may also take place during cyclonic regimes, suggesting that smaller-scale processes can also enable the occurrence of extremes from SCSs, also when the synoptic conditions do not enhance lifting. On top of that, also in summer, the sequence of extremes can play an important role: Sequences of ScBL, AT and/or GL seem to be conducive to extremes. Note that in the analysis including all events, transitions in the frequency anomalies ScBL to AT (clusters) and of ScBL to GL are also found during extremes. This underpins the relevance of researching regime transitions. EuBL is found to be less relevant to extremes in Germany, which can be explained – as seen above, extremes are mainly found at the flank of a block (see Sect. 7.2.1), which lies north of Germany in the case of EuBL.

7.3 Conclusions

This chapter provided an overview of the large-scale atmospheric circulation during clustered and isolated events identified in the Chapter 6. In winter, a strong zonal jet, associated with a negative SCAND index, favors the occurrence of windstorm and combined windstorm-fluvial flood clusters. Fluvial flood clusters alone are characterized by different Z500 anomaly patterns, a dominant block over Greenland (GL) and a negative NAO, contrasting most literature findings. This suggests that combined clusters are mainly influenced by cyclonic patterns, but clusters of individual types occur under persistent, but

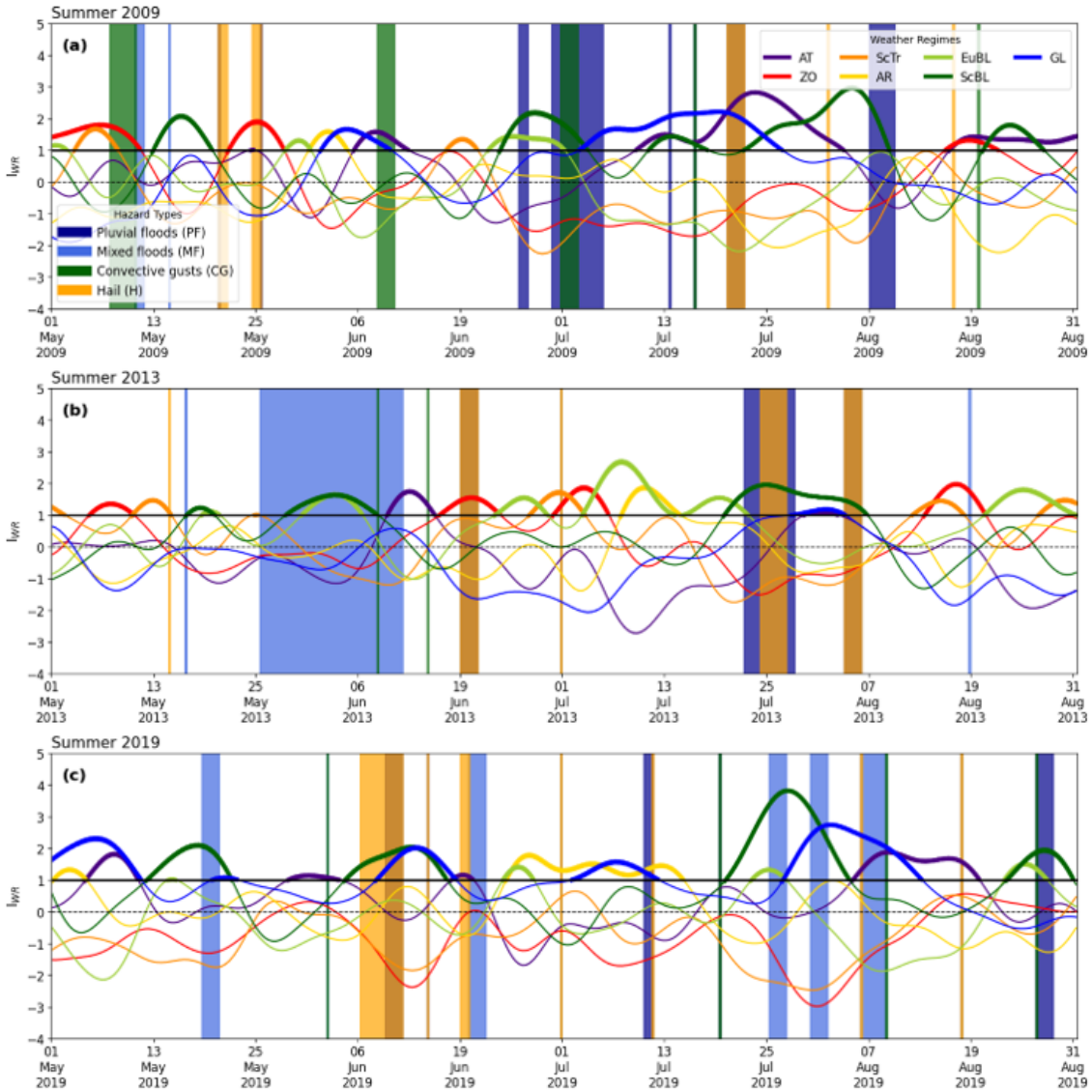

Figure 7.14.: Same as Fig. 7.7, but for the summers of (a) 2009, (b) 2013, and (c) 2019.

different conditions. From the analysis of selected winters, it could be seen that individual conditions are diverse, where many patterns can contribute to the occurrence of surface extremes. Furthermore, the transition between the regimes, particularly the contribution of a preceding blocking, may play an important role.

During summer, the mean fields are robustly characterized by a ridge over Scandinavia (pluvial flooding) or the Baltic Sea (convective gusts and hail), suggesting that atmospheric blocking plays a dominant role. Convective extremes often occur when a high-pressure ridge is positioned to the east of Germany, with the western flank of the ridge positioned above Germany, where lifting is initiated. These findings are consistent with what has been discussed in other studies. While teleconnections exert less influence on the occurrence of (smaller-scale) convective extremes compared to winter, most clusters are found to

occur within an enhanced EA index. Combined clusters of convective hazard types are mainly associated with blocking over the Baltic Sea, replaced by emerging other weather regimes with a westward shifted anomaly as time proceeds. The large-scale circulation pattern of convective gusts and hail therefore dominates also during combined convective clusters. Isolated events of either pluvial floods, convective gusts, or hail are characterized by a ridge centered over Scandinavia, which is dominant with pluvial flood events. The case studies for summer also reveal that the succession of regimes (ScBL and AT, ScBL and GL plays an important role particularly in summer. While zonal regimes can also be present during (less severe events), pointing to the dominance of local triggers, the block over Scandinavia is found to be present with particular damaging extremes.

Most of our findings, with the exception of fluvial floods in winter, are consistent with the consensus from other studies. Thus, it can be concluded that the present insurance loss data, when refined with meteorological observation data, reproduce meteorological patterns. This is remarkable considering the range of processes involved, from the formation of ridges and troughs to surface highs and lows and surface extremes, and ultimately the resulting damage. In winter, this includes the formation of cyclones from the jet, which can lead to heavy rainfall then invoking flooding, or to windstorms, directly involving (building) damage. In summer, atmospheric blocking involves the advection of warm and humid air masses, creating favoring conditions for thunderstorms that can include hail or convective gusts. Hail or convective gusts can lead to direct damage, while heavy precipitation creates damage through a flood, where other non-meteorological factors play a crucial role regarding its severity. To our knowledge, the direct link between the triggering large-scale circulation and losses resulting from hydro-meteorological extremes is rarely established.

8. Conclusions and Outlook

This thesis investigated the occurrence, impacts, and clustering of multiple loss-related hydro-meteorological hazard types (hail, pluvial, fluvial and mixed floods, convective gusts and windstorms) in Germany and Baden-Württemberg, as well as their relation to potential large-scale atmospheric triggers. To date, few studies have focused on a range of different hydro-meteorological hazards. The temporal dynamics of hazard combinations, especially with regard to their impact and triggers, have received less attention. Specifically, to our knowledge, temporal clustering has not been analyzed with regard to multiple hazard types. Based on building insurance loss data for the two study areas of Germany (1997–2022) and Baden-Württemberg (1986–2023), two event catalogs including a set of damaging hydro-meteorological hazard types were created. To identify extreme events, after an adjustment for inflation, the daily loss data was filtered by the 90th percentile of losses and claims. From this set of major loss events, hydro-meteorological hazard types including pluvial, fluvial and mixed flooding, hail, convective gusts, and windstorms were identified by the use of meteorological observation data.

This yielded a unique event catalog with a long timeseries including meteorologically categorized events and their losses, allowing for an in-depth analysis of their temporal dynamics. A skewed loss distribution was found, where a low number of severe events caused a high proportion of the overall losses, including the 2021 western Germany flood triggered by low *Bernd*, the hail event *Andreas* in 2013, and the windstorms *Lothar* in 1999 and *Kyrill* in 2007. It was found that flood events trigger the highest mean damage, and windstorms lead to the lowest losses per claim. In addition, damaging hazards follow strong seasonal patterns: While damaging convective hazards (pluvial floods, hail, and convective gusts) occur predominantly between May and August, windstorms and fluvial flooding primarily hit during December–February. Regional differences in the risk exist, with windstorms being most relevant in the northwest, hail and convective gusts predominantly hit the south(-west), and flooding affecting eastern Germany most. Losses from all hazards are subject to a high inter-annual and decadal variability, with a high number of events especially in the early 2000s, but no presence of clear and consistent trends, which can partly be explained by the dominance of few extreme loss hazards. With these insights, we contribute to research mainly by the comprehensiveness of our analysis: In contrast to many other studies mainly investigating impacts of single hazards, we provide a broad overview of impact patterns for a long time period and across Germany. We also demonstrate that, compared to broader insurance categories, more detailed meteorological categorizations are sensible: For example, windstorms and convective gusts, both part of the 'storm' category, entail entirely distinct impacts in space and time.

Subsequently, the degree and significance of clustering in the event catalog was investigated. It was shown that damaging hydro-meteorological hazards and their combinations exhibit random sub-seasonal clustering on timescales of two to four weeks, following the strong seasonality of individual hazards from May to August and December to February. Compared to a homogeneous Poisson process, clustering is significant for hail as well as for convective gust events for monthly to seasonal timescales from May to August (but not regarding pluvial floods) with events defined with a flexible duration both in GER and BW. Mixed results were found in winter, where clustering regarding large-scale storms (fluvial floods) is only significant for GER (BW) and on some timescales. These mixed findings partly align with existing literature regarding the detection of clustering among windstorms (e. g., Dacre and Pinto, 2020) and the detection of no significant clustering regarding precipitation (e. g., Tuel and Martius, 2021b) in Europe. Considering multiple hazards, the significance of sub-seasonal clustering is increased compared to single hazards, which is robust for all hazard combinations. The amplifying effect is much stronger for the convective hazards from May to August compared to the winter, where single loss events cause a high share of the total damage. This amplifying effect demonstrates that clustering of multiple hazard types, especially during the summer months, needs more consideration, as clusters of hydro-meteorological extremes can involve cascading impacts: Multi-hazard clusters within 21 days involve higher losses than isolated events for all hazard types in BW and for most hazard types in GER, in both summer and winter. This is a striking result: This thesis has newly shown that clustered extremes are involved with higher losses. Therefore, this thesis contributes to the existing literature with a robust assessment of the occurrence and degree of clustering of multiple hazards – temporal clustering has, to the best of our knowledge, not been assessed with respect to different hazards in previous studies. We find that they do cluster when combined, irrespective of the event definition and both for a smaller region, a federal state of 36 000 km^2, and for Germany with about the tenfold size. Thereby, we show that including multiple hazards makes a difference.

Furthermore, it was shown that the chosen duration of events matters for the degree of clustering, as two methods of declustering (= event definition) using a data-driven (Peaks-over-Threshold) vs. a pre-determined (Hours Clause) method were compared for BW. A fixed event definition is associated with a significant deviation from a homogeneous Poisson process in almost all cases. It should be noted here that events have varying characteristics and resulting durations; the Hours Clause method does therefore not necessarily reflect their true occurrence. Applications in the insurance sector, however, often use the Hours Clause method to define events. From the differing clustering results with varying durations, it can be seen that it is important to accurately assess the actual duration of extreme events. Lastly, while clustered extremes have increased significantly throughout the investigated time period of 38 years in BW, there is no clear increase throughout the shorter time period of 25 years in GER. It should be noted here that the increase detected in BW may be caused by a non-uniform reliability of the data.

The significant clustering of multi-hazard events on timescales of two to three weeks prompted an investigation into the drivers of multivariate hazards in the large-scale atmospheric circulation. In winter (December–February), 21-day clustering periods of fluvial flood events are characterized by a block over Greenland. In turn, clusters of windstorms as well as compound windstorms and fluvial flood events are associated with a strong, zonal jet and a positive index of the Scandinavian pattern. These findings underline what has been found in other studies, namely a strong jet and the presence of cyclones favoring compound wind and precipitation extremes (e. g., Martius et al., 2016). In summer (May–August), convective hazards are characterized by similar geopotential height anomalies involving blocking over Scandinavia or the Baltic Sea, which suggests that their occurrence in close succession is favored. Regarding all extremes, Germany is positioned at the flank of a trough, consistent with extreme-favoring locations found in the literature (Kautz et al., 2022).

As described above, damage tends to increase economically during clustered events; however, this is not reflected in the meteorological conditions, as there are no substantial differences between clustered and isolated events in terms of geopotential height anomalies or modes of variability (which however include stochastic variability). The results do not indicate fundamentally different flow configurations, stronger persistence, or altered temporal sequencing that would be visible through anomaly composites or modes of variability. Hence, greater damage does not necessarily result from more extreme meteorological conditions, but may arise from a variety of other factors. This interpretation is supported by trend analyses from recent years, which often identify increased exposure or vulnerability as key contributors to higher losses. Therefore, this thesis has newly shown that combinations of impact-related hazards can be explained by large-scale atmospheric circulation patterns. Although no pronounced differences exist between clustered and isolated patterns, establishing this link helps to improve our understanding of how hydro-meteorological events are related to damage.

This thesis is unique regarding the use of impact data to assess clustering with methods primarily used in hydrological research so far, and for long periods of 25–35 years. However, some limitations need to be taken into account: Insurance data are generally dependent on how claims are regulated. Although the losses are adjusted for inflation and the number of contracts, changes such as, for example, policy adjustments or changes in exposed assets (e. g., solar panels on roofs), and the susceptibility to hydro-meteorological hazards (Kron et al., 2019) cannot be taken into account. Furthermore, the damage regulation is biased towards the first day of the month, probably because of simplicity to damage regulators; this however is within the scope of the usual fluctuation for the most extreme events. A bias of insurance loss data to fraud is also possible; it is however assumed to be less relevant as only major loss events are evaluated.

While this thesis is based on comprehensive loss data, it focuses on a limited geographic area. It is therefore suggested to extend the spatial scope in future studies. Furthermore, the impact is purely insurance-related and therefore monetary. Damage to critical infrastructures or municipality assets are

not captured by the data. Due to a lack of comparable data, no societal impacts such as fatalities were included to measure impact. In addition, other hazard types such as cold spells, droughts or heatwaves, which usually do not cause high direct monetary (insured) damage attributed to the event, were not included. These events also usually occur on different timescales: Impact-relevant durations of those hazards range from about two weeks to two months (Polt et al., 2023) and hydrological droughts cluster most strongly on the annual time scale and generally from seasonal to 3-year time scales (Brunner and Stahl, 2023). Therefore, a comparison with the present hazard types with a mean duration of less than two days is not sensible. It should furthermore not be neglected that there is a stochastic element within impact data, which may lead to the effect that a meteorologically relevant event at the local scale is not captured due to low population density and therefore low losses. Arguably, these events are less relevant to the public, as they do not cause major damage. Nevertheless, future research could be directed at analyzing these clustering patterns with larger datasets and including larger geographic scopes. An interesting question would be to what extent the findings are robust for other regions in (central) Europe. On top of that, regional differences in the impact of extreme events were detected, but clustering was not investigated on a spatial scale. Ideally, impact data in a fine spatial resolution could be connected to gridded meteorological reanalysis data. Although the availability of consistent impact data on fine spatial scales is still limited, its potential is enormous: Given the relevance of clustered extremes and their impacts, an improved assessment of those is crucial.

The identification of atmospheric patterns linked to clusters of multivariate extremes offers potential for improving the prediction of conditions favoring these hazards as well as their temporal dependence. While the relationship between surface extremes and large-scale circulation patterns has been extensively studied with respect to many individual hazard types, the understanding of how modes of variability affect compound extremes is still limited (e. g., Steptoe et al., 2018). For example, it could be studied how transitions of dominating weather regimes affect the occurrence of single and multiple extreme events. Furthermore, the striking large-scale circulation patterns within fluvial floods deserve further consideration, for example, by extending the temporal or geographic scale of the analysis. Moreover, in our case, we make a direct link between large-scale circulation and extreme event impacts. Although we have shown that impact data reproduce results from purely meteorological approaches, the process chain of extreme event impacts includes many additional variables. For example, environmental variables from reanalysis data can help capture the meteorological conditions geographically closer to where the event occurs. This is particularly relevant for the period from May to August, where local processes can be dominating for the occurrence of convective extremes. In the case of flood events, factors such as the topography, but also socio-economic factors such as the effectiveness of a warning system, influence impacts. To investigate these factors, case studies that examine the entire process chain, from the large-scale meteorological trigger to the final impact, are presumably the most appropriate method of analysis. Additionally, as meteorological conditions do not reproduce the intensified losses with clustered events, potential causes could be investigated: What processes exert the biggest influence on the damage? As

seen in this thesis, impacts and trends are also influenced by macroeconomic factors, vulnerability, and exposure. Towards this end, the potential of climate adaptation to mitigate damage could also be investigated.

Another interesting topic for further research would be to investigate how the clustering of different types of hydro-meteorological hazards changes due to human-induced climate change. This has been investigated for windstorms, for example, where an increased cyclone clustering can be expected in central Europe (Dacre and Pinto, 2020). Climate modeling has started to consider multi-hazard relationships, where an increasing risk is found for compound flood-wind extremes in Great Britain, for example (Bloomfield et al., 2024; Hillier et al., 2025). Another interesting aspect from an impact-based view would be the extension towards non-meteorological hazards and impacts, for example, capacities of authorities and relief organizations. This would be a step towards the consideration of systemic risk.

This thesis generally argues for a holistic view of hazards, since a lot of research and its application follows a single hazard type approach. A comprehensive risk assessment ideally requires a multi-hazard perspective that accounts for all relevant hazard types, their interactions, and potential consequences – though implementing this in practice remains a significant challenge.

List of Acronyms

AEP Annual Exceedance Probability.

AR Atlantic Ridge.

AT Atlantic Trough.

BW Baden-Württemberg.

CA Coriolis Acceleration.

CAPE Convective Available Potential Energy.

CDC Climate Data Center.

CDF Cumulative Distribution Function.

CG Convective Gusts.

CIN Convective Inhibition.

CPC Climate Prediction Center.

DCAPE Downdraft Convective Available Potential Energy.

DJF December–February.

DMC Deep Moist Convection.

DWD Deutscher Wetterdienst.

EA East Atlantic Pattern.

ECMWF European Centre for Medium-Range Weather Forecasts.

EEA European Environment Agency.

EF Enhanced Fujita.

EL Equilibrium Level.

EM-DAT Emergency Events Database.

EOF Empirical Orthogonal Function.

ERA5 ECMWF Reanalysis 5.

ESWD European Severe Weather Database.

ETC Extratropical Cyclone.

EuBL European Blocking.

EUCLID European Cooperation for Lightning Detection.

FF Fluvial Floods.

FFD Forward Flank Downdraft.

GA Gravitational Acceleration.

GDV German Insurance Association.

GER Germany.

GEV Generalized Extreme Value Distribution.

GL Greenland Blocking.

GPD Generalized Pareto Distribution.

H Hail.

HC Hours Clause.

IPCC Intergovernmental Panel on Climate Change.

JJA June–August.

LCL Lifting Condensation Level.

LFC Level of Free Convection.

LS Large-scale Storms.

MCS Mesoscale Convective System.

MF Mixed Floods.

MJJA May–August.

MSLP Mean Sea Level Pressure.

NAO North Atlantic Oscillation.

NOAA National Oceanic and Atmospheric Administration.

OEP Occurrence Exceedance Probability.

p90 90th percentile.

p95 95th percentile.

p99 99th percentile.

PF Pluvial Floods.

PGA Pressure Gradient Acceleration.

POT Peaks-Over-Threshold.

RFD Rear Flank Downdraft.

RWB Rossby Wave-Breaking.

SCAND Scandinavian Pattern.

ScBL Scandinavian Blocking.

SCSs Severe Convective Storms.

ScTr Scandinavian Trough.

SSI Storm Severity Index.

SV SV SparkassenVersicherung.

UNDRR United Nations Office for Disaster Risk Reduction.

WS Windstorms.

Z500 Geopotential height at 500 hPa.

ZO Zonal Regime.

Bibliography

Abdi, H., 2010: Coefficient of Variation. *Encyclopedia of Research Design*, Salkind, N. J., Ed., SAGE Publications, Inc., Thousand Oaks, CA, USA, 169–171.

AMS, 2021: Precipitation. *Glossary of Meteorology*, URL: http://glossary.ametsoc.org/wiki/Precipitation, accessed: 2025-01-20.

AMS, 2024a: Hail. *Glossary of Meteorology*, URL: http://glossary.ametsoc.org/wiki/Hail, accessed: 2025-01-20.

AMS, 2024b: Hydrometeor. *Glossary of Meteorology*, URL: http://glossary.ametsoc.org/wiki/Hydrometeor, accessed: 2025-01-20.

AMS, 2024c: Mescoscale convective system. *Glossary of Meteorology*, URL: https://glossary.ametsoc.org/wiki/Mesoscale_convective_system, accessed: 2025-02-17.

AMS, 2025a: Stratiform. *Glossary of Meteorology*, URL: http://glossary.ametsoc.org/wiki/Stratiform, accessed: 2025-01-20.

AMS, 2025b: Thunderstorm. *Glossary of Meteorology*, URL: http://glossary.ametsoc.org/wiki/thunderstorm, accessed: 2025-01-20.

AMS, 2025c: Tornado. *Glossary of Meteorology*, URL: http://glossary.ametsoc.org/wiki/Tornado, accessed: 2025-01-20.

Angeli, S. d., B. D. Malamud, L. Rossi, F. E. Taylor, E. Trasforini, and R. Rudari, 2022: A multi-hazard framework for spatial-temporal impact analysis. *Int. J. Disaster Risk Reduct.*, 102829, DOI: 10.1016/j.ijdrr.2022.102829.

Antonescu, B., D. M. Schultz, A. Holzer, and P. Groenemeijer, 2017: Tornadoes in Europe: An Underestimated Threat. *Bull. Am. Meteorol. Soc.*, **98 (4)**, 713 – 728, DOI: 10.1175/BAMS-D-16-0171.1.

Auer, A. H., 1972: Distribution of Graupel and Hail with Size. *Mon. Weather Rev.*, **100 (5)**, 325 – 328, DOI: 10.1175/1520-0493-100-05-0325.

Augenstein, M., 2025: Variabilität, Trends und serielles Clustering schwerer Gewitterereignisse im Bezug zu großräumigen atmosphärischen Bedingungen. Ph.D. thesis, Karlsruher Institut für Technologie (KIT), URL: https://publikationen.bibliothek.kit.edu/1000179408.

Augenstein, M., S. Mohr, and M. Kunz, 2024: Influence of the North Atlantic Oscillation on annual spatio-temporal lightning clusters in western and central Europe. *EGUsphere [preprint]*, **2024**, 1–30, DOI: 10.5194/egusphere-2024-2804.

Banfi, F. and C. De Michele, 2024: Temporal Clustering of Precipitation Driving Landslides Over the Italian Territory. *Earth's Future*, **12 (5)**, e2023EF003 885, DOI: 10.1029/2023EF003885.

Baniotopoulos, C. C., 2007: Design of Wind-Sensitive Structures. *Wind Effects on Buildings and Design of Wind-Sensitive Structures*, Stathopoulos, T. and C. C. Baniotopoulos, Eds., Springer, Vienna, CISM International Centre for Mechanical Sciences, Vol. 493, 201–227.

Barnston, A. G. and R. E. Livezey, 1987: Classification, Seasonality and Persistence of Low-Frequency Atmospheric Circulation Patterns. *Mon. Weather Rev.*, **115 (6)**, 1083 – 1126, DOI: 10.1175/1520-0493(1987)115<1083:CSAPOL>2.0.CO;2.

Barras, H., O. Martius, L. Nisi, K. Schroeer, A. Hering, and U. Germann, 2021: Multi-day hail clusters and isolated hail days in Switzerland – large-scale flow conditions and precursors. *Wea. Clim. Dyn.*, **2 (4)**, 1167–1185, DOI: 10.5194/wcd-2021-25.

Barredo, J., 2010: No upward trend in normalised windstorm losses in Europe: 1970–2008. *Nat. Hazards Earth Syst. Sci.*, **10**, 97–104, DOI: 10.5194/nhess-10-97-2010.

Barredo, J. I., 2007: Major flood disasters in Europe: 1950–2005. *Nat. Hazards*, **42 (1)**, 125–148, DOI: 10.1007/s11069-006-9065-2.

Barredo, J. I., 2009: Normalised flood losses in Europe: 1970–2006. *Nat. Hazards Earth Syst. Sci.*, **9 (1)**, 97–104, DOI: 10.5194/nhess-9-97-2009.

Bartel, J. and P. Schubert, 2025: Engagement im Ernstfall – Zahlen und Fakten zu freiwilligem Engagement und zivilgesellschaftlichen Organisationen im Bevölkerungsschutz. ZiviZ-Sonderauswertung im Auftrag des BBK, URL: `https://www.bbk.bund.de/SharedDocs/Downloads/DE/Mediathek/Publikationen/Foerderung-Ehrenamt/sonderauswertung-ziviz_download.pdf`, accessed: 2025-05-10.

Barton, Y., P. Giannakaki, H. Von Waldow, C. Chevalier, S. Pfahl, and O. Martius, 2016: Clustering of regional-scale extreme precipitation events in southern Switzerland. *Mon. Weather Rev.*, **144 (1)**, 347–369, DOI: 10.1175/MWR-D-15-0205.1.

Barton, Y., P. Rivoire, J. Koh, M. Ali S., J. Kopp, and O. Martius, 2022: On the temporal clustering of European extreme precipitation events and its relationship to persistent and transient large-scale atmospheric drivers. *Wea. Clim. Extrem.*, **38**, 100 518, DOI: 10.1016/j.wace.2022.100518.

Battaglioli, F., P. Groenemeijer, T. Púčik, M. Taszarek, U. Ulbrich, and H. Rust, 2023: Modeled Multidecadal Trends of Lightning and (Very) Large Hail in Europe and North America (1950–2021). *J. Appl. Meteorl. Climatol.*, **62 (11)**, 1627–1653, DOI: 10.1175/JAMC-D-22-0195.1.

Becker, A., P. Becker, S. Brienen, A. Gratzki, G. Grünthal, V. Holzwarth, R. F. J. Hüttl, U. Kaminski, H. Kreibich, C. Koppe, G. Laschewski, J. Lauterjung, H. Lühr, G. Malitz, B. Merz, M. Rauthe, B. Rudolf, M. Rosenau, S. Roessner, M. Pilz, S. Parolai, C. Janssen, C. Haberland, A. Walter, T. R. Walter, B. Wichura, K.-P. Wittich, P. Becker, and R. F. J. Hüttl, 2014: *Forschungsfeld Naturgefahren*. DWD, GFZ.

Beurton, S. and A. H. Thieken, 2009: Seasonality of floods in Germany. *Hydrol. Sci. J.*, **54 (1)**, 62–76, DOI: 10.1623/hysj.54.1.62.

Bevacqua, E., C. De Michele, C. Manning, A. Couasnon, A. F. S. Ribeiro, A. M. Ramos, E. Vignotto, A. Bastos, S. Blesic, F. Durante, J. Hillier, S. C. Oliveira, J. G. Pinto, E. Ragno, P. Rivoire, K. Saunders, K. van der Wiel, W. Wu, T. Zhang, and J. Zscheischler, 2021: Guidelines for Studying Diverse Types of Compound Weather and Climate Events. *Earth's Future*, **9 (11)**, e2021EF002 340, DOI: 10.1029/2021EF002340.

Bloomfield, H. C., P. Bates, L. C. Shaffrey, J. Hillier, A. Champion, D. Cotterill, J. O. Pope, and D. Kumar, 2024: Synoptic conditions conducive for compound wind-flood events in Great Britain in present and future climates. *Environ. Res. Lett.*, **19 (2)**, 024 019, DOI: 10.1088/1748-9326/ad1cb7.

Bloomfield, H. C., J. Hillier, A. Griffin, A. Kay, L. C. Shaffrey, F. Pianosi, R. James, D. Kumar, A. Champion, and P. Bates, 2023: Co-occurring wintertime flooding and extreme wind over europe, from daily to seasonal timescales. *Wea. Clim. Extrem.*, **39**, 100 550, DOI: 10.1016/j.wace.2023.100550.

Brabson, B. B. and J. P. Palutikof, 2000: Tests of the Generalized Pareto Distribution for Predicting Extreme Wind Speeds. *J. Appl. Meteorl. Climatol.*, **39 (9)**, 1627–1640, DOI: 10.1175/1520-0450(2000)039<1627:TOTGPD>2.0.CO;2.

Bradbury, W. M. S., D. M. Deaves, J. C. R. Hunt, R. Kershaw, K. Nakamura, M. E. Hardman, and P. W. Bearman, 1994: The importance of convective gusts. *Meteorological Applications*, **1 (4)**, 365–378, DOI: 10.1002/met.5060010407.

Brasseur, O., 2001: Development and Application of a Physical Approach to Estimating Wind Gusts. *Mon. Weather Rev.*, **129 (1)**, 5–25, DOI: 10.1175/1520-0493(2001)129<0005:DAAOAP>2.0.CO;2.

Brett, L., H. C. Bloomfield, A. Bradley, T. Calvet, A. Champion, S. De Angeli, M. C. de Ruiter, S. B. Guerreiro, J. Hillier, D. Jaroszweski, B. Kamranzad, M. M. Keinänen-Toivola, K. Kornhuber, K. Küpfer, C. Manning, K. Mattu, E. Murtagh, V. Murray, Á. N. Bhreasail, F. O'Loughlin, C. Parker, M. Pregnolato, A. M. Ramos, J. Schlumberger, D. Theochari, P. Ward, A. Wessels, and C. J. White,

2025: Science–policy–practice insights for compound and multi-hazard risks. *Meteorological Applications*, **32 (2)**, e70 043, DOI: 10.1002/met.70043.

Brett, L., C. J. White, D. I. V. Domeisen, B. van den Hurk, P. Ward, and J. Zscheischler, 2024: Review article: The growth in compound weather events research in the decade since SREX. *Natural Hazards and Earth System Sciences Discussions*, **2024**, 1–35, DOI: 10.5194/nhess-2024-182.

Brito, M. M. d., J. Sodoge, A. Fekete, M. Hagenlocher, E. Koks, C. Kuhlicke, G. Messori, M. de Ruiter, P.-J. Schweizer, and P. J. Ward, 2024: Uncovering the Dynamics of Multi-Sector Impacts of Hydrological Extremes: A Methods Overview. *Earth's Future*, **12 (1)**, e2023EF003 906, DOI: 10.1029/2023EF003906.

Brommundt, J. and A. Bárdossy, 2007: Spatial correlation of radar and gauge precipitation data in high temporal resolution. *Advances in Geosciences*, **10**, 103–109, DOI: 10.5194/adgeo-10-103-2007.

Brown, T. M., W. H. Pogorzelski, and I. M. Giammanco, 2015: Evaluating hail damage using property insurance claims data. *Weather, Climate, and Society*, **7 (3)**, 197 – 210, DOI: 10.1175/WCAS-D-15-0011.1.

Browning, K. A., 1990: *Organization of Clouds and Precipitation in Extratropical Cyclones*, 129–153. Springer.

Browning, K. A. and G. B. Foote, 1976: Airflow and hail growth in supercell storms and some implications for hail suppression. *Q. J. R. Meteorol. Soc.*, **102 (433)**, 499–533, DOI: 10.1002/qj.49710243303.

Brunner, M. I. and K. Stahl, 2023: Temporal hydrological drought clustering varies with climate and land-surface processes. *Environ. Res. Lett.*, **18 (3)**, 034 011, DOI: 10.1088/1748-9326/acb8ca.

Burghoff, O., 2024: pers. comm., personal communication in an online meeting regarding GDV loss data, 22 August 2024.

Byers, H. R. and R. R. Braham, 1949: *The Thunderstorm: Report of the Thunderstorm Project*. US Government Printing Office.

Calotescu, I., X. Li, M. T. Mengistu, and M. P. Repetto, 2024: Thunderstorm impact on the built environment: A full-scale measurement and post-event damage survey case study. *J. Wind Eng. Ind. Aerodyn.*, **245**, 105 634, DOI: 10.1016/j.jweia.2023.105634.

Cannon, D. J., D. J. Kirshbaum, and S. L. Gray, 2012: Under what conditions does embedded convection enhance orographic precipitation? *Q. J. R. Meteorol. Soc.*, **138 (663)**, 391–406, DOI: 10.1002/qj.926.

Cassou, C., 2008: Intraseasonal interaction between the Madden–Julian Oscillation and the North Atlantic Oscillation. *Nature*, **455 (7212)**, 523–527, DOI: 10.1038/nature07286.

Changnon, S. A., 1970: Hailstreaks. *J. Atmos. Sci.*, **27 (1)**, 109 – 125, DOI: 10.1175/1520-0469(1970)027<0109:H>2.0.CO;2.

Changnon, S. A., 1971: Hailfall Characteristics Related to Crop Damage. *J. Appl. Meteorl. Climatol.*, **10 (2)**, 270–274, https://www.jstor.org/stable/26174912.

Changnon, S. A., D. Changnon, and S. D. Hilberg, 2009: Hailstorms across the nation: An atlas about hail and its damages. Tech. rep., Illinois State Water Survey.

Claassen, J. N., P. J. Ward, J. Daniell, E. E. Koks, T. Tiggeloven, and M. C. de Ruiter, 2023: A new method to compile global multi-hazard event sets. *Sci. Rep.*, **13 (1)**, 13 808, DOI: 10.1038/s41598-023-40400-5.

Coles, S., 2001: *An Introduction to Statistical Modeling of Extreme Values*. Springer Verlag, Berlin, Germany.

Collins, B. D., N. S. Oakley, J. P. Perkins, A. E. East, S. C. Corbett, and B. J. Hatchett, 2020: Linking Mesoscale Meteorology With Extreme Landscape Response: Effects of Narrow Cold Frontal Rainbands (NCFR). *J. Geophys. Res.: Earth Surface*, **125 (10)**, e2020JF005 675, DOI: 10.1029/2020JF005675.

Cox, D. R. and V. Isham, 1980: *Point processes*, Vol. 12. CRC Press.

CPC, 2008a: North Atlantic Oscillation (NAO). URL: https://www.cpc.ncep.noaa.gov/products/precip/CWlink/pna/nao.shtml, accessed: 2025-05-13.

CPC, 2008b: Northern Hemisphere Teleconnection Patterns: Introduction. URL: https://www.cpc.ncep.noaa.gov/data/teledoc/teleintro.shtml, accessed: 2025-05-02.

CPC, 2008c: Teleconnection Index Calculations. URL: https://www.cpc.ncep.noaa.gov/data/teledoc/teleindcalc.shtml, accessed: 2025-05-02.

Cusack, S., 2023: A long record of European windstorm losses and its comparison to standard climate indices. *Nat. Hazards Earth Syst. Sci.*, **23 (8)**, 2841–2856, DOI: 10.5194/nhess-23-2841-2023.

Dacre, H. F. and J. G. Pinto, 2020: Serial clustering of extratropical cyclones: a review of where, when and why it occurs. *npj Clim. Atmos. Sci.*, **3**, 48, DOI: 10.1038/s41612-020-00152-9.

Davies-Jones, R., 2015: A review of supercell and tornado dynamics. *Atmos. Res.*, **158-159**, 274–291, DOI: 10.1016/j.atmosres.2014.04.007.

Dawkins, L. C., D. B. Stephenson, J. F. Lockwood, and P. E. Maisey, 2016: The 21st century decline in damaging european windstorms. *Nat. Hazards Earth Syst. Sci.*, **16 (8)**, 1999–2007, DOI: 10.5194/nhess-16-1999-2016.

De Meutter, P., L. Gerard, G. Smet, K. Hamid, R. Hamdi, D. Degrauwe, and P. Termonia, 2015: Predicting Small-Scale, Short-Lived Downbursts: Case Study with the NWP Limited-Area ALARO Model for the Pukkelpop Thunderstorm. *Mon. Weather Rev.*, **143 (3)**, 742 – 756, DOI: 10.1175/MWR-D-14-00290.1.

DER SPIEGEL, 2010: Tief "Daisy": Rettungskräfte befreien Dutzende Autofahrer aus Schneefalle. `https://www.spiegel.de/panorama/tief-daisy-rettungskraefte-befreien-dutzende-autofahrer-aus-schneefalle-a-671060.html`, accessed: 2025-05-18.

Deutsche Welle, 2024: Slovakia: At least 15 hurt as storm hits music festival. DW News, URL: `https://www.dw.com/en/slovakia-at-least-15-hurt-as-storm-hits-music-festival/a-69653307`, accessed: 2025-02-19.

Deutscher Bundestag - Wissenschaftliche Dienste, 2021: Elementarschadenversicherung - Zur Frage der Einführung einer Versicherungspflicht. URL: `https://www.bundestag.de/resource/blob/855918/b60c095da0bb03d4a4b36f7cf279b809/WD-7-082-21-pdf-data.pdf`, accessed: 2025-01-15.

Dietz, H., S. Fischer, and C. Gierschek, 2015: *Wohngebäudeversicherung*. VVW GmbH.

DIN, 2010: DIN EN 1991-1-4:2010-12: Eurocode 1: Actions on Structures – Part 1-4: General Actions – Wind Actions; German Version EN 1991-1-4:2005 + A1:2010 + AC:2010. `https://www.baunormenlexikon.de/norm/din-en-1991-1-4/9ecef8e5-7d6d-4c9e-8409-338540ad9e72`, accessed: 2025-03-25.

Donat, M. G., G. C. Leckebusch, J. G. Pinto, and U. Ulbrich, 2010: Examination of wind storms over Central Europe with respect to circulation weather types and NAO phases. *Int. J. Climatol.*, **30 (9)**, 1289–1300, DOI: 10.1002/joc.1982.

Doswell III, C. A., 1987: The distinction between large-scale and mesoscale contribution to severe convection: A case study example. *Weather and Forecasting*, **2 (1)**, 3–16, DOI: 10.1175/1520-0434(1987)002<0003:TDBLSA>2.0.CO;2.

Dotzek, N., 2001: Tornadoes in Germany. *Atmos. Res.*, **56 (1)**, 233–251, DOI: 10.1016/S0169-8095(00)00075-2.

Dotzek, N., P. Groenemeijer, B. Feuerstein, and A. M. Holzer, 2009: Overview of ESSL's severe convective storms research using the European Severe Weather Database ESWD. *Atmos. Res.*, **93 (1)**, 575–586, DOI: 10.1016/j.atmosres.2008.10.020.

Dotzek, N., M. V. Kurgansky, J. Grieser, B. Feuerstein, and P. Névir, 2005: Observational evidence for exponential tornado intensity distributions over specific kinetic energy. *Geophys. Res. Lett.*, **32 (24)**, DOI: 10.1029/2005GL024583.

Duchon, C. E., 1979: Lanczos Filtering in One and Two Dimensions. *Journal of Applied Meteorology (1962-1982)*, **18 (8)**, 1016–1022, URL: https://www.jstor.org/stable/26179027.

DWD, 2005: Deutschlandwetter im Winter 2004/2005. Tech. rep., Deutscher Wetterdienst, https://www.dwd.de/DE/presse/pressemitteilungen/DE/2005/20050228_deutschlandwetter_winter.pdf, press release dated 28 February 2005.

DWD, 2009: Deutschlandwetter im Sommer 2009. Tech. rep., Deutscher Wetterdienst, https://www.dwd.de/DE/presse/pressemitteilungen/DE/2009/20090829_deutschlandwetter_sommer.pdf?__blob=publicationFile&v=2, press release dated 29 August 2009.

DWD, 2013: Pressemitteilung: Deutschlandwetter im Sommer 2013. accessed: 03 September 2024, URL: https://www.dwd.de/DE/presse/pressemitteilungen/DE/2013/20130829_DeutschlandwetterimSommer.html?nn=583156, accessed: 2024-08-23.

DWD, 2019: The Weather in Germany in Summer 2019. Tech. rep., Deutscher Wetterdienst, https://www.dwd.de/EN/press/press_release/EN/2019/20190830_the_weather_in_germany_in_summer_2019.pdf?__blob=publicationFile&v=2, press release dated 30 August 2019.

DWD, 2021: Deutschlandwetter im Winter 2020/21. Press release dated 26 February 2021, URL: https://www.dwd.de/DE/presse/pressemitteilungen/DE/2021/20210226_deutschlandwetter_winter2020_2021_news.html.

DWD, 2024: Dauerregenlage durch VB-Tief. Online article from Deutscher Wetterdienst, URL: https://www.dwd.de/DE/wetter/thema_des_tages/2024/5/30.html, accessed: 2025-02-26.

DWD, 2025a: Barometrische Höhenformel: Glossar - Deutscher Wetterdienst. URL: https://www.dwd.de/DE/service/lexikon/Functions/glossar.html?lv2=100310&lv3=100384, accessed: 2025-02-28.

DWD, 2025b: Warnkriterien. URL: https://www.dwd.de/DE/wetter/warnungen_aktuell/kriterien/warnkriterien.html, accessed: 2025-01-17.

DWD, 2025c: Wetter- und Klimalexikon. URL: https://www.dwd.de/DE/service/lexikon/Functions/glossar.html, accessed: 2025-01-16.

Economou, T., D. B. Stephenson, J. G. Pinto, L. C. Shaffrey, and G. Zappa, 2015: Serial clustering of extratropical cyclones in a multi-model ensemble of historical and future simulations. *Q. J. R. Meteorol. Soc.*, **141 (693)**, 3076–3087, DOI: 10.1002/qj.2591.

EEA, 2023: Economic losses from weather- and climate-related extremes in Europe. URL: https://www.eea.europa.eu/en/analysis/indicators/economic-losses-from-climate-related, accessed: 2023-12-04.

Eisenbach, S., 2023: Hail record broken again – 19 cm hailstone confirmed in Italy | European Severe Storms Laboratory. URL: https://www.essl.org/cms/hail-record-broken-again-19cm-hailstone-confirmed-in-italy/, accessed: 2024-11-05.

ESWD, 2024: URL: https://eswd.eu/, accessed: 2025-02-24.

Feser, F., M. Barcikowska, O. Krueger, F. Schenk, R. Weisse, and L. Xia, 2015: Storminess over the North Atlantic and northwestern Europe—A review. *Q. J. R. Meteorol. Soc.*, **141 (687)**, 350–382, DOI: 10.1002/qj.2364.

Feuerstein, B., P. Groenemeijer, E. Dirksen, M. Hubrig, A. M. Holzer, and N. Dotzek, 2011: Towards an improved wind speed scale and damage description adapted for Central Europe. *Atmos. Res.*, **100 (4)**, 547–564, DOI: 10.1016/j.atmosres.2010.12.026.

François, B., K. Teber, L. Brett, R. Leeding, L. Gimeno-Sotelo, D. I. V. Domeisen, L. Suarez-Gutierrez, and E. Bevacqua, 2024: Concurrent modes of climate variability linked to spatially compounding wind and precipitation extremes in the Northern Hemisphere. *EGUsphere [preprint]*, **2024**, 1–32, DOI: 10.5194/egusphere-2024-2079.

Friedrich, K., D. Niermann, F. Imbery, S. Haeseler, and M. Ziese, 2024: Klimatologischer Rückblick auf 2023: Das bisher wärmste Jahr in Deutschland. URL: https://www.dwd.de/DE/leistungen/besondereereignisse/temperatur/20240201_klimarueckblick-2023.pdf?__blob=publicationFile&v=3, accessed: 2025-02-12.

Fujita, T., 1981: Tornadoes and downbursts in the context of generalized planetary scales. *J. Atmos. Sci.*, **38 (8)**, 1511–1534, DOI: 10.1175/1520-0469(1981)038<1511:TADITC>2.0.CO;2.

Fujita, T., 1990: Downbursts: meteorological features and wind field characteristics. *J. Wind Eng. Ind. Aerodyn.*, **36**, 75–86, DOI: 10.1016/0167-6105(90)90294-M.

Fujita, T. T., 1992: Mystery of severe storms. *WRL Research Paper*, **239**, 298.

Fujita, T. T. and A. D. Pearson, 1973: Results of FPP classification of 1971 and 1972 tornadoes. *Eight conference on severe local storms*, 142–145, URL: http://hdl.handle.net/10605/261906.

Gall, M., K. A. Borden, and S. L. Cutter, 2009: When do losses count?: Six fallacies of natural hazards loss data. *Bull. Am. Meteorol. Soc.*, **90 (6)**, 799 – 810, DOI: 10.1175/2008BAMS2721.1.

Gatzen, C. P., A. H. Fink, D. M. Schultz, and J. G. Pinto, 2020: An 18-year climatology of derechos in germany. *Nat. Hazards Earth Syst. Sci.*, **20 (5)**, 1335–1351, DOI: 10.5194/nhess-20-1335-2020.

GDV, 2023: Allgemeine Wohngebäude Versicherungsbedingungen (VGB 2022 - Wohnflächenmodell) - Musterbedingungen des GDV. https://www.gdv.de/resource/blob/37090/85030e2f2518d

925d739fd751f523a5a/allgemeine-wohngebaeude-versicherungsbedingungen--vgb-2016---wohnflaechenmodell--data.pdf, accessed: 2024-11-11.

GDV, 2023a: Datenservice zum Naturgefahrenreport 2023. Tech. rep., Gesamtverband der Deutschen Versicherungswirtschaft e. V., https://www.gdv.de/resource/blob/154862/1e5f68dd03dbe238e8238632976dd59b/naturgefahrenreport-datenservice-2023-download-data.pdf, accessed: 2024-02-22.

GDV, 2023b: Nur die Hälfte der Gebäude in Deutschland ist richtig gegen Naturgefahren versichert. https://www.gdv.de/gdv/themen/schaden-unfall/nur-die-haelfte-der-gebaeude-in-deutschland-ist-richtig-gegen-naturgefahren-versichert-12176, accessed: 2023-07-17.

GDV, 2024a: Amtliche Zahlen zeigen: Mehr als 300.000 Adressen in Deutschland sind von Hochwasser bedroht. \protect\tolerance9999\emergencystretch3em\hfuzz.5\p@\vfuzz\hfuzzhttps://www.gdv.de/gdv/medien/medieninformationen/amtliche-zahlen-zeigen-mehr-als-300-000-adressen-in-deutschland-sind-von-hochwasser-bedroht-168828, accessed: 2025-04-23.

GDV, 2024b: Datenservice zum Naturgefahrenreport 2024. https://www.gdv.de/gdv/statistik/datenservice-zum-naturgefahrenreport, accessed: 2024-11-25.

GDV, 2024c: Hochwasser in Süddeutschland: Schäden um die zwei Milliarden Euro erwartet. accessed: 28 June 2024, URL: https://www.gdv.de/gdv/medien/medieninformationen/hochwasser-suedeutschland-schadenschaetzung-versicherer-178816, accessed: 2024-06-28.

GDV, 2024d: Teuerstes Elementarschaden-Jahr 1984 mit dem „Münchener Hagel“. https://www.gdv.de/gdv/statistik/datenservice-zum-naturgefahrenreport/autokasko/teuerstes-elementarschaden-jahr-1984-mit-dem-muenchener-hagel--139062, accessed: 2025-05-19.

GDV, S., Schweda, 2019: Forschungsprojekt Starkregen. https://www.gdv.de/gdv/themen/klima/forschungsprojekt-starkregen-52866, accessed: 2025-01-20.

Gessler, S. E., Shaun E. and Petty, 2013: Hail Fundamentals and General Hail-Strike Damage Assessment Methodology. *Forensic Engineering*, CRC Press.

Gill, J., M. Duncan, R. Ciurean, L. Smale, D. Stuparu, J. Schlumberger, M. de Ruiter, T. Tiggeloven, S. Torresan, S. Gottardo, J. Mysiak, R. Harris, E. Petrescu, T. Girard, B. Khazai, J. Claassen, R. Dai, A. Champion, A. Daloz, and P. Ward, 2022: MYRIAD-EU D1.2 Handbook of Multi-Hazard, Multi-Risk Definitions and Concepts. Tech. Rep. D1.2, H2020 MYRIAD-EU Project, Grant agreement number 101003276.

Gill, J. C. and B. D. Malamud, 2014: Reviewing and visualizing the interactions of natural hazards. *Rev. Geophys.*, **52 (4)**, 680–722, DOI: 10.1002/2013RG000445.

Gill, J. C. and B. D. Malamud, 2016: Hazard interactions and interaction networks (cascades) within multi-hazard methodologies. *Earth Syst. Dynam.*, **7 (3)**, 659–679, DOI: 10.5194/esd-7-659-2016.

Gliksman, D., P. Averbeck, N. Becker, B. Gardiner, V. Goldberg, J. Grieger, D. Handorf, K. Haustein, A. Karwat, F. Knutzen, H. S. Lentink, R. Lorenz, D. Niermann, J. G. Pinto, R. Queck, A. Ziemann, and C. L. E. Franzke, 2023: Review article: A European perspective on wind and storm damage – from the meteorological background to index-based approaches to assess impacts. *Nat. Hazards Earth Syst. Sci.*, **23 (6)**, 2171–2201, DOI: 10.5194/nhess-23-2171-2023.

Grams, C. M., R. Beerli, S. Pfenninger, I. Staffell, and H. Wernli, 2017: Balancing Europe's wind-power output through spatial deployment informed by weather regimes. *Nat. Clim. Change*, **7 (8)**, 557–562, DOI: 10.1038/nclimate3338.

Grams, C. M., H. Binder, S. Pfahl, N. Piaget, and H. Wernli, 2014: Atmospheric processes triggering the central European floods in June 2013. *Nat. Hazards Earth Syst. Sci.*, **14 (7)**, 1691–1702, DOI: 10.5194/nhess-14-1691-2014.

Grieser, J. and M. Hill, 2019: How to Express Hail Intensity - Modeling the Hailstone Size Distribution. *J. Appl. Meteorl. Climatol.*, **58 (10)**, 2329 – 2345, DOI: 10.1175/JAMC-D-18-0334.1.

Groenemeijer, P., T. Púčik, A. M. Holzer, B. Antonescu, K. Riemann-Campe, D. M. Schultz, T. Kühne, B. Feuerstein, H. E. Brooks, C. A. Doswell, H.-J. Koppert, and R. Sausen, 2017: Severe convective storms in Europe: Ten years of research and education at the European Severe Storms Laboratory. *Bull. Am. Meteorol. Soc.*, **98 (12)**, 2641–2651, DOI: 10.1175/BAMS-D-16-0067.1.

Gyakum, J. R. and R. E. Danielson, 2000: Analysis of meteorological precursors to ordinary and explosive cyclogenesis in the western North Pacific. *Mon. Weather Rev.*, **128 (3)**, 851–863, DOI: 10.1175/1520-0493(2000)128<0851:AOMPTO>2.0.CO;2.

Hammond, M., A. Chen, S. Djordjević, D. Butler, and O. Mark, 2015: Urban flood impact assessment: A state-of-the-art review. *Urban Water Journal*, **12 (1)**, 14–29, DOI: 10.1080/1573062X.2013.857421.

Hannachi, A., D. M. Straus, C. L. E. Franzke, S. Corti, and T. Woollings, 2017: Low-frequency nonlinearity and regime behavior in the Northern Hemisphere extratropical atmosphere. *Reviews of Geophysics*, **55 (1)**, 199–234, DOI: 10.1002/2015RG000509.

Hauser, S., 2023: A Novel Quasi-Lagrangian Perspective on the Potential Vorticity Dynamics of Blocked Weather Regime Life Cycles in the North Atlantic-European Region. Ph.D. thesis, Karlsruher Institut für Technologie (KIT), URL: `https://publikationen.bibliothek.kit.edu/1000162808`.

Hauser, S., S. Mueller, X. Chen, T.-C. Chen, J. G. Pinto, and C. M. Grams, 2023a: The Linkage of Serial Cyclone Clustering in Western Europe and Weather Regimes in the North Atlantic-European Region in Boreal Winter. *Geophys. Res. Lett.*, **50 (2)**, e2022GL101 900, DOI: 10.1029/2022GL101900.

Hauser, S., F. Teubler, M. Riemer, P. Knippertz, and C. M. Grams, 2023b: Towards a holistic understanding of blocked regime dynamics through a combination of complementary diagnostic perspectives. *Wea. Clim. Dyn.*, **4 (2)**, 399–425, DOI: 10.5194/wcd-4-399-2023.

Hersbach, H., B. Bell, P. Berrisford, S. Hirahara, A. Horányi, J. Muñoz-Sabater, J. Nicolas, C. Peubey, R. Radu, D. Schepers, A. Simmons, C. Soci, S. Abdalla, X. Abellan, G. Balsamo, P. Bechtold, G. Biavati, J. Bidlot, M. Bonavita, G. De Chiara, P. Dahlgren, D. Dee, M. Diamantakis, R. Dragani, J. Flemming, R. Forbes, M. Fuentes, A. Geer, L. Haimberger, S. Healy, R. J. Hogan, E. Hólm, M. Janisková, S. Keeley, P. Laloyaux, P. Lopez, C. Lupu, G. Radnoti, P. de Rosnay, I. Rozum, F. Vamborg, S. Villaume, and J.-N. Thépaut, 2020: The ERA5 global reanalysis. *Q. J. R. Meteorol. Soc.*, **146 (730)**, 1999–2049, DOI: 10.1002/qj.3803.

Heyer, E., 1988: *Witterung und Klima*, Vol. 8. Teubner Verlagsgesellschaft, Leipzig, Germany.

Heymsfield, A. and R. Wright, 2014: Graupel and hail terminal velocities: Does a "supercritical" reynolds number apply? *J. Atmos. Sci.*, **71 (9)**, 3392–3403, DOI: 10.1175/JAS-D-14-0034.1.

Hillier, J. K., H. C. Bloomfield, C. Manning, F. Garry, L. Shaffrey, P. Bates, and D. Kumar, 2025: Increasingly Seasonal Jet Stream Raises Risk of Co-Occurring Flooding and Extreme Wind in Great Britain. *Int. J. Climatol.*, **71 (e8763)**, 3392–3403, DOI: 10.1002/joc.8763.

Hillier, J. K. and R. S. Dixon, 2020: Seasonal impact-based mapping of compound hazards. *Environ. Res. Lett.*, **15 (11)**, 114 013, DOI: 10.1088/1748-9326/abbc3d.

Hillier, J. K., N. Macdonald, G. C. Leckebusch, and A. Stavrinides, 2015: Interactions between apparently 'primary' weather-driven hazards and their cost. *Environ. Res. Lett.*, **10**, 104 003, DOI: 10.1088/1748-9326/10/10/104003.

Hofherr, T. and M. Kunz, 2010: Extreme wind climatology of winter storms in Germany. *Clim. Res.*, **41 (2)**, 105–123, DOI: 10.3354/cr00844.

Hohl, R., H.-H. Schiesser, and D. Aller, 2002: Hailfall: the relationship between radar-derived hail kinetic energy and hail damage to buildings. *Atmos. Res.*, **63 (3)**, 177–207, DOI: 10.1016/S0169-8095(02)00059-5.

Houze, R. A., 1993: *Cloud Dynamics*, International Geophysics Series, Vol. 53. Academic Press.

Houze, R. A., 2014: *Cloud Dynamics*, International Geophysics Series, Vol. 104. Academic Press.

Huizinga, J., D. M. Hans, and W. Szewczyk, 2017: Global flood depth-damage functions: Methodology and the database with guidelines. EUR 28552 EN., DOI: 10.2760/16510.

Hurk, B. J. J. M. v. d., C. J. White, A. M. Ramos, P. J. Ward, O. Martius, I. Olbert, K. Roscoe, H. M. D. Goulart, and J. Zscheischler, 2023: Consideration of compound drivers and impacts in the disaster risk reduction cycle. *iScience*, **26 (3)**, DOI: 10.1016/j.isci.2023.106030.

Hurrell, J. W., 1995: Decadal Trends in the North Atlantic Oscillation: Regional Temperatures and Precipitation. *Science*, **269 (5224)**, 676–679, DOI: 10.1126/science.269.5224.676.

Insurance Europe, 2018: Insight briefing: Managing europe's flood risk. Tech. rep., Insurance Europe, URL: `http://insuranceeurope.eu/publications/691/insight-briefing-managing-the-eu-s-flood-risks/`.

Jäger, W. S., M. C. de Ruiter, T. Tiggeloven, and P. J. Ward, 2024: What can we learn from global disaster records about multi-hazards and their risk dynamics? *Nat. Hazards Earth Syst. Sci. Discussions*, **2024**, 1–31, DOI: 10.5194/nhess-2024-134.

Junghänel, T., P. Bissolli, J. Daßler, R. Fleckenstein, F. Imbery, W. Janssen, F. Kaspar, K. Lengfeld, T. Leppelt, M. Rauthe, A. Rauthe-Schöch, M. Rocek, E. Walawender, and E. Weigl, 2021: Hydroklimatologische Einordnung der Stark-und Dauerniederschläge in Teilen Deutschlands im Zusammenhang mit dem Tiefdruckgebiet „Bernd "vom 12. bis 19. Juli 2021. Deutscher Wetterdienst, Geschäftsbereich Klima und Umwelt, URL: `https://www.dwd.de/DE/leistungen/besondereereignisse/niederschlag/20210721_bericht_starkniederschlaege_tief_bernd.html`, accessed: 2025-04-20.

Kaiser, H. F., 1958: The varimax criterion for analytic rotation in factor analysis. *Psychometrika*, **23 (3)**, 187–200, DOI: 10.1007/BF02289233.

Kantonale Gebäudeversicherungen, 2012: Ereignisanalyse Hagel 2009. Tech. rep., Kantonale Gebäudeversicherungen and Université de Lausanne, Institut des sciences de la Terre, URL: `https://www.vkg.ch/de/publikationen/statistiken/hagel-2009`, accessed: 2024-11-15.

Kantonale Gebäudeversicherungen, 2015: Ereignisanalyse Hagel 2011. Tech. rep., Kantonale Gebäudeversicherungen and Université de Lausanne, Institut des sciences de la Terre, URL: `https://www.vkg.ch/de/publikationen/statistiken/hagel-2011`, accessed: 2024-11-15.

Kappes, M. S., M. Keiler, K. von Elverfeldt, and T. Glade, 2012: Challenges of analyzing multi-hazard risk: a review. *Nat. Hazards*, **64**, 1925–1958, DOI: 10.1007/s11069-012-0294-2.

Karremann, M. K., J. G. Pinto, P. J. von Bomhard, and M. Klawa, 2014: On the clustering of winter storm loss events over Germany. *Nat. Hazards Earth Syst. Sci.*, **14**, 2041–2052, DOI: 10.5194/nhess-14-2041-2014.

Kautz, L.-A., O. Martius, S. Pfahl, J. G. Pinto, A. M. Ramos, P. M. Sousa, and T. Woollings, 2022: Atmospheric blocking and weather extremes over the Euro-Atlantic sector - a review. *Wea. Clim. Dyn.*, **3 (1)**, 305–336, DOI: 10.5194/wcd-3-305-2022.

Khanduri, A. C. and G. C. Morrow, 2003: Vulnerability of buildings to windstorms and insurance loss estimation. *J. Wind Eng. Ind. Aerodyn.*, **91 (4)**, 455–467, DOI: 10.1016/S0167-6105(02)00408-7.

Klawa, M. and U. Ulbrich, 2003: A model for the estimation of storm losses and the identification of severe winter storms in Germany. *Nat. Hazards Earth Syst. Sci.*, **3 (6)**, 725–732, DOI: 10.5194/nhess-3-725-2003.

Klijn, F., K. de Bruijn, A. Ölfert, E. Penning-Rowsell, J. Simm, and M. Wallis, 2009: Flood risk assessment and flood risk management; an introduction and guidance based on experiences and findings of FLOODsite (an EU-funded integrated project). Tech. Rep. T29-09-01, Deltares | Delft Hydraulics, Delft, the Netherlands, URL: `http://www.floodsite.net/html/partner_area/project_docs/T29_09_01_Guidance_Screen_Version_D29_1_v2_0_P02.pdf`, accessed: 2025-02-10.

Koks, E. E. and T. Haer, 2020: A high-resolution wind damage model for Europe. *Scientific Reports*, **10 (1)**, 6866, DOI: 10.1038/s41598-020-63580-w.

Kopp, J., P. Rivoire, S. M. Ali, Y. Barton, and O. Martius, 2021: A novel method to identify sub-seasonal clustering episodes of extreme precipitation events and their contributions to large accumulation periods. *Hydrol. Earth Syst. Sci.*, **25 (9)**, 5153–5174, DOI: 10.5194/hess-25-5153-2021.

Kraus, H., 2004: *Die Atmosphäre der Erde: Eine Einführung in die Meteorologie*, Vol. 3. Springer-Verlag.

Kreibich, H., P. Bubeck, M. Kunz, H. Mahlke, S. Parolai, B. Khazai, J. Daniell, T. Lakes, and K. Schröter, 2014: A review of multiple natural hazards and risks in Germany. *Nat. Hazards*, **74**, DOI: 10.1007/s11069-014-1265-6.

Kron, W., P. Löw, and Z. W. Kundzewicz, 2019: Changes in risk of extreme weather events in Europe. *Environmental Science & Policy*, **100**, 74–83, DOI: 10.1016/j.envsci.2019.06.007.

Kunz, M., 2003: Simulation von Starkniederschlägen mit langer Andauer über Mittelgebirgen. Ph.D. thesis, Institut für Meteorologie und Klimaforschung (IMK), Universität Karlsruhe (TH), URL: `https://publikationen.bibliothek.kit.edu/1012003`.

Kunz, M., 2007: The skill of convective parameters and indices to predict isolated and severe thunderstorms. *Nat. Hazards Earth Syst. Sci.*, **7 (2)**, 327–342, DOI: 10.5194/nhess-7-327-2007.

Kunz, M., 2011: Characteristics of large-scale orographic precipitation in a linear perspective. *J. Hydrometeorol.*, **12 (1)**, 27–44, DOI: 10.1175/2010JHM1231.1.

Kunz, M., 2024: Schäden durch Hagel. *Klimanavigator*, URL: `https://klimanavigator.eu/dossier/artikel/030168/index.php`, accessed: 2024-12-09.

Kunz, M., U. Blahak, J. Handwerker, M. Schmidberger, H. J. Punge, S. Mohr, E. Fluck, and K. M. Bedka, 2018: The severe hailstorm in southwest Germany on 28 July 2013: characteristics, impacts and meteorological conditions. *Q. J. R. Meteorol. Soc.*, **144 (710)**, 231–250, DOI: 10.1002/qj.3197.

Kunz, M., M. K. Karremann, and S. Mohr, 2023: Auswirkungen des Klimawandels auf Starkniederschläge, Gewitter und Schneefall. *Klimawandel in Deutschland*, Brasseur, Guy P. and Jacob, Daniela and Schuck-Zöller, Susanne (Eds.), Ed., Springer, Berlin, Heidelberg, 73–84.

Kunz, M. and M. Puskeiler, 2010: High-resolution assessment of the hail hazard over complex terrain from radar and insurance data. *Meteorol. Z.*, **19 (5)**, 427, DOI: 10.1127/0941-2948/2010/0452.

Kunz, M., J. Wandel, E. Fluck, S. Baumstark, S. Mohr, and S. Schemm, 2020: Ambient conditions prevailing during hail events in central europe. *Nat. Hazards Earth Syst. Sci.*, **20 (6)**, 1867–1887, DOI: 10.5194/nhess-20-1867-2020.

Küpfer, K., A. Tuel, and M. Kunz, 2024: Impact-based temporal clustering of multiple meteorological hazard types in southwestern Germany. *EGUsphere [preprint]*, **2024**, DOI: 10.5194/egusphere-2024-2803.

Lee, R., C. J. White, M. S. G. Adnan, J. Douglas, M. D. Mahecha, F. E. O'Loughlin, E. Patelli, A. M. Ramos, M. J. Roberts, O. Martius, E. Tubaldi, B. van den Hurk, P. J. Ward, and J. Zscheischler, 2024: Reclassifying historical disasters: From single to multi-hazards. *Sci. Total. Environ.*, **912**, 169 120, DOI: 10.1016/j.scitotenv.2023.169120.

Lemon, L. R. and C. A. Doswell, 1979: Severe Thunderstorm Evolution and Mesocyclone Structure as Related to Tornadogenesis. *Mon. Weather Rev.*, **107 (9)**, 1184 – 1197, DOI: 10.1175/1520-0493(1979)107<1184:STEAMS>2.0.CO;2.

Lenggenhager, S. and O. Martius, 2019: Atmospheric blocks modulate the odds of heavy precipitation events in Europe. *Climate Dynamics*, **53 (7)**, 4155–4171, DOI: 10.1007/s00382-019-04779-0.

Li, Y., K. Porter, and K. Goda, 2024: Hail hazard modeling with uncertainty analysis and roof damage estimation of residential buildings in North America. *Int. J. Disaster Risk Reduct.*, **113**, 104 853, DOI: 10.1016/j.ijdrr.2024.104853.

Little, A. S., M. D. K. Priestley, and J. L. Catto, 2023: Future increased risk from extratropical windstorms in northern Europe. *Nat. Commun.*, **14 (1)**, 4434, DOI: 10.1038/s41467-023-40102-6.

Lowe, J. and J. Gregory, 2005: The effects of climate change on storm surges around the United Kingdom. *Philosophical Transactions of the Royal Society A: Mathematical, Physical and Engineering Sciences*, **363 (1831)**, 1313–1328, DOI: 10.1098/rsta.2005.1570.

Maddox, R. A., 1980: Mesoscale Convective Complexes. *Bull. Am. Meteorol. Soc.*, 1374–1387, https://www.jstor.org/stable/26221473.

Mailier, P., 2007: Serial Clustering of Extratropical Cyclones. PhD Thesis, University of Reading, Department of Meteorology, a thesis submitted for the degree of Doctor of Philosophy, URL: https://www.academia.edu/28116556/Serial_Clustering_of_Extratropical_Cyclones.

Mailier, P. J., D. B. Stephenson, C. A. Ferro, and K. I. Hodges, 2006: Serial clustering of extratropical cyclones. *Mon. Weather Rev.*, **134 (8)**, 2224–2240, DOI: 10.1175/MWR3160.1.

Manzato, A., S. Serafin, M. M. Miglietta, D. Kirshbaum, and W. Schulz, 2022: A pan-Alpine climatology of lightning and convective initiation. *Mon. Weather Rev.*, **150 (9)**, 2213–2230, DOI: 10.1175/MWR-D-21-0149.1.

Markowski, P. and Y. Richardson, 2010: *Mesoscale Meteorology in Midlatitudes*. John Wiley & Sons, Chichester, UK.

Martius, O., S. Pfahl, and C. Chevalier, 2016: A global quantification of compound precipitation and wind extremes. *Geophys. Res. Lett.*, **43 (14)**, 7709–7717, DOI: 10.1002/2016GL070017.

Masson-Delmotte, V., P. Zhai, A. Pirani, S. L. Connors, C. Péan, S. Berger, N. Caud, Y. Chen, L. Goldfarb, M. Gomis, M. Huang, K. Leitzell, E. Lonnoy, J. B. R. Matthews, T. K. Maycock, T. Waterfield, O. Yelekçi, R. Yu, and B. Zhou, (Eds.) , 2021: *Climate Change 2021 – The Physical Science Basis: Working Group I Contribution to the Sixth Assessment Report of the Intergovernmental Panel on Climate Change*. Cambridge University Press, available at: https://www.ipcc.ch/report/ar6/wg1/.

McDonald, J. R. and K. C. Mehta, 2006: *A recommendation for an Enhanced Fujita scale (EF-Scale)*. Wind Science and Engineering Center, Texas Tech University.

Merz, B., H. Kreibich, R. Schwarze, and A. Thieken, 2010: Review article "assessment of economic flood damage". *Nat. Hazards Earth Syst. Sci.*, **10 (8)**, 1697–1724, DOI: 10.5194/nhess-10-1697-2010.

Merz, B., H. Kreibich, A. Thieken, and R. Schmidtke, 2004: Estimation uncertainty of direct monetary flood damage to buildings. *Nat. Hazards Earth Syst. Sci.*, **4 (1)**, 153–163, DOI: 10.5194/nhess-4-153-2004.

Michel, C. and G. Rivière, 2011: The Link between Rossby Wave Breakings and Weather Regime Transitions. *J. Atmos. Sci.*, **68 (8)**, 1730 – 1748, DOI: 10.1175/2011JAS3635.1.

Michelangeli, P.-A., R. Vautard, and B. Legras, 1995: Weather Regimes: Recurrence and Quasi Stationarity. *J. Atmos. Sci.*, **52 (8)**, 1237 – 1256, DOI: 10.1175/1520-0469(1995)052<1237:WRRAQS>2.0.CO;2.

Mitchell-Wallace, K., M. Jones, J. Hillier, and M. Foote, 2017: *Natural catastrophe risk management and modelling: A practitioner's guide*. John Wiley & Sons.

Moemken, J., I. Alifdini, A. M. Ramos, A. Georgiadis, A. Brocklehurst, L. Braun, and J. G. Pinto, 2024: Insurance loss model vs. meteorological loss index – how comparable are their loss estimates for european windstorms? *Nat. Hazards Earth Syst. Sci.*, **24 (10)**, 3445–3460, DOI: 10.5194/nhess-24-3445-2024.

Mohamed, I., M. R. Najafi, P. Joe, and J. Brimelow, 2024: Multivariate analysis of compound hail, wind and rainfall extremes in Alberta's hail alley. *Wea. Clim. Extrem.*, **46**, 100 718, DOI: 10.1016/j.wace.2024.100718.

Mohr, S., U. Ehret, M. Kunz, P. Ludwig, A. Caldas-Alvarez, J. E. Daniell, F. Ehmele, H. Feldmann, M. J. Franca, C. Gattke, M. Hundhausen, P. Knippertz, K. Küpfer, B. Mühr, J. G. Pinto, J. Quinting, A. M. Schäfer, M. Scheibel, F. Seidel, and C. Wisotzky, 2023: A multi-disciplinary analysis of the exceptional flood event of July 2021 in central Europe – Part 1: Event description and analysis. *Nat. Hazards Earth Syst. Sci.*, **23 (2)**, 525–551, DOI: 10.5194/nhess-23-525-2023.

Mohr, S., M. Kunz, and B. Geyer, 2015a: Hail potential in Europe based on a regional climate model hindcast. *Geophys. Res. Lett.*, **42 (24)**, 10,904–10,912, DOI: 10.1002/2015GL067118.

Mohr, S., M. Kunz, and K. Keuler, 2015b: Development and application of a logistic model to estimate the past and future hail potential in Germany. *J. Geophys. Res.: Atmospheres*, **120 (9)**, 3939–3956, DOI: 10.1002/2014JD022959.

Mohr, S., M. Kunz, A. Richter, and B. Ruck, 2017: Statistical characteristics of convective wind gusts in germany. *Nat. Hazards Earth Syst. Sci.*, **17 (6)**, 957–969, DOI: 10.5194/nhess-17-957-2017.

Mohr, S., J. Wandel, S. Lenggenhager, and O. Martius, 2019: Relationship between atmospheric blocking and warm season thunderstorms over western and central Europe. *Q. J. R. Meteorol. Soc.*, **145**, 3040–3056, DOI: 10.1002/qj.3603.

Mohr, S., J. Wilhelm, J. Wandel, M. Kunz, R. Portmann, H. J. Punge, J. F. Schmidberger, M. Quinting, and C. M. Grams, 2020: The role of large-scale dynamics in an exceptional sequence of severe thunderstorms in Europe May–June 2018. *Wea. Clim. Dyn.*, **1**, 325–348, DOI: 10.5194/wcd-1-325-2020.

Mühr, B., L. Eisenstein, J. G. Pinto, P. Knippertz, S. Mohr, and M. Kunz, 2022: CEDIM Forensic Disaster Analysis Group (FDA): Winter storm series: Ylenia, Zeynep, Antonia (int: Dudley, Eunice, Franklin)-February 2022 (NW & Central Europe). Tech. rep., Center for Disaster Management and Risk Reduction Technology (CEDIM), available at: `https://www.cedim.kit.edu/download/FDA_Storms_Feb2022_report1_all.pdf`.

Möller, A., 2023: Ein Jahr danach: Tornados verwüsten Lippstadt, Paderborn und Höxter. https://www1.wdr.de/nachrichten/westfalen-lippe/bilanz-tornado-lippstadt-paderborn-118.html, accessed: 2025-02-19.

NOAA, 2025: Flood and flash flood definitions. National Oceanic and Atmospheric Administration (NOAA), US Department of Commerce, URL: https://www.weather.gov/mrx/flood_and_flash, accessed: 2025-01-19.

NOAA Climate Prediction Center, 2005: Teleconnection Pattern Maps: North Atlantic Oscillation (NAO), East Atlantic (EA), and Scandinavia (SCAND). URL: https://www.cpc.ncep.noaa.gov/data/teledoc/, URL: https://www.cpc.ncep.noaa.gov/data/teledoc/, accessed: 2025-05-02. Includes NAO map: https://www.cpc.ncep.noaa.gov/data/teledoc/nao_map.shtml, EA map: https://www.cpc.ncep.noaa.gov/data/teledoc/ea_map.shtml, and SCAND map: https://www.cpc.ncep.noaa.gov/data/teledoc/scand_map.shtml.

Nordhaus, W. D., 2010: The economics of hurricanes and implications of global warming. *Climate Change Economics*, **01 (01)**, 1–20, DOI: 10.1142/S2010007810000054.

NWS, 2025: Flash Flooding Definition. US Department of Commerce, NOAA's National Weather Service (NWS), URL: https://www.weather.gov/phi/FlashFloodingDefinition, accessed: 2025-02-26.

Osborn, T. J., 2011: Winter 2009/2010 temperatures and a record-breaking North Atlantic Oscillation index. *Weather*, **66 (1)**, 19–21, DOI: 10.1002/wea.660.

Paprotny, D., B. Rhein, M. I. Vousdoukas, P. Terefenko, F. Dottori, S. Treu, J. Śledziowski, L. Feyen, and H. Kreibich, 2024: Merging modelled and reported flood impacts in Europe in a combined flood event catalogue for 1950–2020. *Hydrol. Earth Syst. Sci.*, **28 (17)**, 3983–4010, DOI: 10.5194/hess-28-3983-2024.

Paprotny, D., A. Sebastian, O. Morales-Nápoles, and S. N. Jonkman, 2018: Trends in flood losses in Europe over the past 150 years. *Nature Communications*, **9 (1)**, 1985, DOI: 10.1038/s41467-018-04253-1.

Pinto, J. G., N. Bellenbaum, M. K. Karremann, and P. M. Della-Marta, 2013: Serial clustering of extratropical cyclones over the North Atlantic and Europe under recent and future climate conditions. *J. Geophys. Res.*, **118 (22)**, 12,476–12,485, DOI: 10.1002/2013JD020564.

Pinto, J. G., E. L. Fröhlich, G. C. Leckebusch, and U. Ulbrich, 2007: Changing European storm loss potentials under modified climate conditions according to ensemble simulations of the ECHAM5/MPI-OM1 GCM. *Nat. Hazards Earth Syst. Sci.*, **7 (1)**, 165–175, DOI: 10.5194/nhess-7-165-2007.

Pinto, J. G., I. Gómara, G. Masato, H. F. Dacre, T. Woollings, and R. Caballero, 2014: Large-scale dynamics associated with clustering of extratropical cyclones affecting Western Europe. *J. Geophys. Res.*, **119 (24)**, 13,704–13,719, DOI: 10.1002/2014JD022305.

Pinto, J. G., S. Ulbrich, T. Economou, D. B. Stephenson, M. K. Karremann, and L. C. Shaffrey, 2016: Robustness of serial clustering of extratropical cyclones to the choice of tracking method. *Tellus A: Dynamic Meteorology and Oceanography*, **68 (1)**, 32 204, DOI: 10.3402/tellusa.v68.32204.

Piper, D. and M. Kunz, 2017: Spatiotemporal variability of lightning activity in Europe and the relation to the North Atlantic Oscillation teleconnection pattern. *Nat. Hazards Earth Syst. Sci.*, **17**, 1319–1336, DOI: 10.5194/nhess-17-1319-2017.

Piper, D., M. Kunz, J. Allen, and S. Mohr, 2019: Investigation of the temporal variability of thunderstorms in Central and Western Europe and the relation to large-scale flow and teleconnection patterns. *Q. J. R. Meteorol. Soc.*, **145**, 3644–3666, DOI: 10.1002/qj.3647.

Piper, D., M. Kunz, F. Ehmele, S. Mohr, B. Mühr, A. Kron, and J. Daniell, 2016: Exceptional sequence of severe thunderstorms and related flash floods in May and June 2016 in Germany–Part 1: Meteorological background. *Nat. Hazards Earth Syst. Sci.*, **16 (12)**, 2835–2850, DOI: 10.5194/nhess-16-2835-2016.

Plavcova, E. and A. Urban, 2020: Intensified impacts on mortality due to compound winter extremes in the Czech Republic. *Sci. Total. Environ.*, **746**, 141 033, DOI: 10.1016/j.scitotenv.2020.141033.

Poelman, D. R. and W. Schulz, 2020: Comparing lightning observations of the ground-based European lightning location system EUCLID and the space-based Lightning Imaging Sensor (LIS) on the International Space Station (ISS). *Atmos. Meas. Tech.*, **13 (6)**, 2965–2977, DOI: 10.5194/amt-13-2965-2020.

Polt, K. D., P. J. Ward, M. d. Ruiter, E. Bogdanovich, M. Reichstein, D. Frank, and R. Orth, 2023: Quantifying impact-relevant heatwave durations. *Environ. Res. Lett.*, **18 (10)**, 104 005, DOI: 10.1088/1748-9326/acf05e.

Potter, S., 2007: Fine-Tuning Fujita: After 35 years, a new scale for rating tornadoes takes effect. *Weatherwise*, **60 (2)**, 64–71, DOI: 10.3200/WEWI.60.2.64-71.

Prahl, B. F., D. Rybski, O. Burghoff, and J. P. Kropp, 2015: Comparison of storm damage functions and their performance. *Nat. Hazards Earth Syst. Sci.*, **15 (4)**, 769–788, DOI: 10.5194/nhess-15-769-2015.

Priestley, M. D., H. F. Dacre, L. C. Shaffrey, K. I. Hodges, and J. G. Pinto, 2018: The role of serial European windstorm clustering for extreme seasonal losses as determined from multi-centennial simulations of high-resolution global climate model data. *Nat. Hazards Earth Syst. Sci.*, **18 (11)**, 2991–3006, DOI: 10.5194/nhess-18-2991-2018.

Priestley, M. D. K., J. G. Pinto, H. F. Dacre, and L. C. Shaffrey, 2017: Rossby wave breaking, the upper level jet, and serial clustering of extratropical cyclones in western Europe. *Geophys. Res. Lett.*, **44 (1)**, 514–521, DOI: 10.1002/2016GL071277.

Priestley, M. D. K., D. B. Stephenson, A. A. Scaife, D. Bannister, C. J. T. Allen, and D. Wilkie, 2023: Return levels of extreme European windstorms, their dependency on the North Atlantic Oscillation, and potential future risks. *Nat. Hazards Earth Syst. Sci.*, **23 (12)**, 3845–3861, DOI: 10.5194/nhess-23-3845-2023.

Pruppacher, H. R., J. D. Klett, and P. K. Wang, 1998: Microphysics of Clouds and Precipitation. *Aerosol Sci. Technol.*, **28 (4)**, 381 – 382, DOI: 10.1080/02786829808965531.

Punge, H. and M. Kunz, 2016: Hail observations and hailstorm characteristics in Europe: A review. *Atmos. Res.*, **176-177**, 159–184, DOI: 10.1016/j.atmosres.2016.02.012.

Puskeiler, M., M. Kunz, and M. Schmidberger, 2016: Hail statistics for Germany derived from single-polarization radar data. *Atmos. Res.*, **178-179**, 459–470, DOI: 10.1016/j.atmosres.2016.04.014.

Púčik, T., C. Castellano, P. Groenemeijer, T. Kühne, A. T. Rädler, B. Antonescu, and E. Faust, 2019: Large Hail Incidence and Its Economic and Societal Impacts across Europe. *Mon. Weather Rev.*, **147 (11)**, 3901–3916, DOI: 10.1175/MWR-D-19-0204.1.

Rädler, A. T., P. H. Groenemeijer, E. Faust, R. Sausen, and T. Púčik, 2019: Frequency of severe thunderstorms across Europe expected to increase in the 21st century due to rising instability. *npj Climate and Atmospheric Science*, **2 (1)**, 1–5, DOI: 10.1038/s41612-019-0083-7.

Raupach, T. H., O. Martius, J. T. Allen, M. Kunz, S. Lasher-Trapp, S. Mohr, K. L. Rasmussen, R. J. Trapp, and Q. Zhang, 2021: The effects of climate change on hailstorms. *Nat. Rev. Earth Environ.*, **2 (3)**, 213–226, DOI: 10.1038/s43017-020-00133-9.

Rauthe, M., H. Steiner, U. Riediger, A. Mazurkiewicz, and A. Gratzki, 2013: A Central European precipitation climatology – Part I: Generation and validation of a high-resolution gridded daily data set (HYRAS). *Meteorol. Z.*, 235–256, DOI: 10.1127/0941-2948/2013/0436.

Raymond, C., R. M. Horton, J. Zscheischler, O. Martius, A. AghaKouchak, J. Balch, S. G. Bowen, S. J. Camargo, J. Hess, K. Kornhuber, M. Oppenheimer, A. C. Ruane, T. Wahl, and K. White, 2020: Understanding and managing connected extreme events. *Nat. Clim. Change*, **10 (7)**, 611–621, DOI: 10.1038/s41558-020-0790-4.

Ripley, B. D., 1976: The Second-Order Analysis of Stationary Point Processes. *Journal of Applied Probability*, **13 (2)**, 255–266, DOI: 10.2307/3212829.

Ripley, B. D., 1981: *Spatial statistics*. Wiley Series in Probability and Statistics, John Wiley & Sons, Hoboken, NJ, USA.

Roberts, J. F., A. J. Champion, L. C. Dawkins, K. I. Hodges, L. C. Shaffrey, D. B. Stephenson, M. A. Stringer, H. E. Thornton, and B. D. Youngman, 2014: The XWS open access catalogue of extreme European windstorms from 1979 to 2012. *Nat. Hazards Earth Syst. Sci.*, **14 (9)**, 2487–2501, DOI: 10.5194/nhess-14-2487-2014.

Ruiter, M. C. d., A. Couasnon, M. J. C. v. d. Homberg, J. E. Daniell, J. C. Gill, and P. J. Ward, 2020: Why we can no longer ignore consecutive disasters. *Earth's Future*, **8 (3)**, e2019EF001 425, DOI: 10.1029/2019EF001425.

Ruiter, M. C. d. and A. F. v. Loon, 2022: The challenges of dynamic vulnerability and how to assess it. *iScience*, **25 (8)**, DOI: 10.1016/j.isci.2022.104720.

Rädler, A. T., P. Groenemeijer, E. Faust, and R. Sausen, 2018: Detecting Severe Weather Trends Using an Additive Regressive Convective Hazard Model (AR-CHaMo). *J. Appl. Meteorl. Climatol.*, **57 (3)**, 569 – 587, DOI: 10.1175/JAMC-D-17-0132.1.

Schmid, T., R. Portmann, L. Villiger, K. Schröer, and D. N. Bresch, 2024: An open-source radar-based hail damage model for buildings and cars. *Nat. Hazards Earth Syst. Sci.*, **24 (3)**, 847–872, DOI: 10.5194/nhess-24-847-2024.

Schmidberger, M., 2018: Hagelgefährdung und Hagelrisiko in Deutschland basierend auf einer Kombination von Radardaten und Versicherungsdaten. Ph.D. thesis, Karlsruher Institut für Technologie (KIT), Karlsruhe, URL: `https://publikationen.bibliothek.kit.edu/1000086012`.

Schmidt, S. M., 2024: Fassade – Bauphysik: Aerophysik und Windlasten. URL: `https://www.baunetzwissen.de/fassade/fachwissen/bauphysik/windlasten-1637959`, accessed: 2025-02-25.

Schröder, C., C. Bartels, M. M. Grabka, J. König, M. Kroh, and R. Siegers, 2020: A Novel Sampling Strategy for Surveying High Net-Worth Individuals – A Pretest Application Using the Socio-Economic Panel. *Review of Income and Wealth*, **66 (4)**, 825–849, DOI: 10.1111/roiw.12452.

Schröter, K., M. Kunz, F. Elmer, B. Mühr, and B. Merz, 2015: What made the June 2013 flood in Germany an exceptional event? A hydro-meteorological evaluation. *Hydrol. Earth Syst. Sci.*, **19 (1)**, 309–327, DOI: 10.5194/hess-19-309-2015.

Schulz, W. and G. Diendorfer, 2002: EUCLID network performance and data analysis. *Proceedings of the 17th International Lightning Detection Conference (ILDC), Tucson, AZ*, URL: `https://www.aldis.at/fileadmin/userdaten/aldis/publication/2002/7_ILDC2002_Schulz.pdf`.

Schumacher, R. S. and K. L. Rasmussen, 2020: The formation, character and changing nature of mesoscale convective systems. *Nat. Rev. Earth Environ.*, **1 (6)**, 300–314, DOI: 10.1038/s43017-020-0057-7.

Schuster, S. S., R. J. Blong, and K. J. McAneney, 2006: Relationship between radar-derived hail kinetic energy and damage to insured buildings for severe hailstorms in Eastern Australia. *Atmos. Res.*, **81 (3)**, 215–235, DOI: 10.1016/j.atmosres.2005.12.003.

Schwierz, C., P. Köllner-Heck, E. Zenklusen Mutter, D. N. Bresch, P.-L. Vidale, M. Wild, and C. Schär, 2010: Modeling European Winter Wind Storm Losses in current and future climate. *Clim. Change*, **101 (3)**, 485–514, DOI: 10.1007/s10584-009-9712-1.

Simpson, N. P., K. J. Mach, A. Constable, J. Hess, R. Hogarth, M. Howden, J. Lawrence, R. J. Lempert, V. Muccione, B. Mackey, M. G. New, B. O'Neill, F. Otto, H.-O. Pörtner, A. Reisinger, D. Roberts, D. N. Schmidt, S. Seneviratne, S. Strongin, M. van Aalst, E. Totin, and C. H. Trisos, 2021: A framework for complex climate change risk assessment. *One Earth*, **4 (4)**, 489–501, DOI: 10.1016/j.oneear.2021.03.005.

Statistisches Landesamt Baden-Württemberg, 2022: Pressemitteilung 28/2022. URL: `https://www.statistik-bw.de/Presse/Pressemitteilungen/2022028`, accessed: 17 December 2024.

Steptoe, H., S. E. O. Jones, and H. Fox, 2018: Correlations Between Extreme Atmospheric Hazards and Global Teleconnections: Implications for Multihazard Resilience. *Reviews of Geophysics*, **56 (1)**, 50–78, DOI: 10.1002/2017RG000567.

Storelvmo, T. and I. Tan, 2015: The Wegener-Bergeron-Findeisen process – Its discovery and vital importance for weather and climate. *Meteorologische Zeitschrift*, **24 (4)**, 455–461, DOI: 10.1127/metz/2015/0626.

Stucki, M. and T. Egli, 2007: Synthesebericht Elementarschutzregister Hagel: Untersuchungen zur Hagelgefahr und zum Widerstand der Gebäudehülle. Tech. rep., Präventionsstiftung der kantonalen Gebäudeversicherungen, Bern, URL: `https://cms.vkg.ch/media/g4yhbbas/hagel_d.pdf`.

Stull, R., 2017: *Practical Meteorology – An Algebra-based Survey of Atmospheric Science*. Department of Earth, Ocean & Atmospheric Sciences, University of British Columbia, Vancouver, BC.

Swiss Re, 2014: sigma 01/2014: Natural catastrophes and man-made disasters in 2013: large losses from floods and hail; Haiyan hits the Philippines. Tech. rep., Swiss Re Management Ltd, Swiss Re Institute, Authors: Bevere, L., Mueller, L., Ronke, P., and Kurt, K., URL: `https://www.swissre.com/institute/research/sigma-research/sigma-2024-01.html`, accessed: 2023-05-20.

Swiss Re, 2019: Weihnachten vor 20 Jahren: Die Stürme Lothar und Martin richten verheerende Schäden in ganz Europa an. URL: `https://www.swissre.com/risk-knowledge/mitigating-climate-`

risk/winter-storms-in-europe/weihnachten-vor-20-jahren-die-sturme-lothar-martin.html, accessed: 2024-06-28.

Swiss Re, 2021: sigma 1/2021 - Natural catastrophes in 2020. Tech. rep., Swiss Re Management Ltd, Swiss Re Institute, Authors: Bevere, L., Weigel, A., Bhattacharya, A., Lindgren, E., Sharan, R., Velichkova, Y., Winkler, J. and Ronke, P., URL: https://www.swissre.com/institute/research/sigma-research/sigma-2021-01.html, accessed: 2024-10-20.

Swiss Re, 2024: sigma 01/2024 - natural catastrophes in 2023. Tech. rep., Swiss Re Management Ltd, Swiss Re Institute, Authors: Banerjee, C., Bevere, L., Gabers, H., Grollimund, B., Lechner, R., and Weigel, A., URL: https://www.swissre.com/institute/research/sigma-research/sigma-2024-01.html, accessed: 2024-02-10.

Sävert, T., 2024: Pforzheim 1968 - Verheerender Tornado in Pforzheim am 10.07.1968. URL: https://tornadoliste.de/pforzheim1968.htm, accessed: 2025-03-24.

Tamura, Y., 2009: Wind-induced damage to buildings and disaster risk reduction. *Proceedings of the APCWE-VII, Taipei, Taiwan*, URL: https://engineeringshelter.wordpress.com/wp-content/uploads/2016/01/ks1.pdf.

Taszarek, M., J. T. Allen, P. Groenemeijer, R. Edwards, H. E. Brooks, V. Chmielewski, and S.-E. Enno, 2020: Severe Convective Storms across Europe and the United States. Part I: Climatology of Lightning, Large Hail, Severe Wind, and Tornadoes. *J. Climate*, **33 (23)**, 10 239 – 10 261, DOI: 10.1175/JCLI-D-20-0345.1.

Thieken, A. and J. v. Keyserlingk, 2025: Extreme Ereignisse in Deutschland: Überblick und Schadenstatistik. *Klimanavigator*, URL: https://klimanavigator.eu/dossier/artikel/116418/index.php, accessed: 2025-01-09.

Thieken, A. H., T. Bessel, S. Kienzler, H. Kreibich, M. Müller, S. Pisi, and K. Schröter, 2016: The flood of June 2013 in Germany: how much do we know about its impacts? *Nat. Hazards Earth Syst. Sci.*, **16 (6)**, 1519–1540, DOI: 10.5194/nhess-16-1519-2016.

Tilloy, A., B. D. Malamud, H. Winter, and A. Joly-Laugel, 2019: A review of quantification methodologies for multi-hazard interrelationships. *Earth-Science Reviews*, **196**, 102 881, DOI: 10.1016/j.earscirev.2019.102881.

Trenczek, J., O. Lühr, L. Eiserbeck, M. Sandhövel, and V. Leuschner, 2022: Übersicht vergangener Extremwetterschäden in Deutschland. Tech. rep., Prognos AG, Institut für ökologische Wirtschaftsforschung (IÖW), Gesellschaft für Wirtschaftliche Strukturforschung mbH (GWS), URL: https://www.prognos.com/sites/default/files/2022-07/Prognos_KlimawandelfolgenDeut

schland_%C3%9Cbersicht%20vergangener%20Extremwettersch%C3%A4den_AP2_1.pdf, accessed: 2025-02-20.

Trigo, I. F., T. D. Davies, and G. R. Bigg, 1999: Objective Climatology of Cyclones in the Mediterranean Region. *J. Climate*, **12 (6)**, 1685–1696, DOI: 10.1175/1520-0442(1999)012<1685:OCOCIT>2.0.CO;2.

Tuel, A. and O. Martius, 2021a: A climatology of sub-seasonal temporal clustering of extreme precipitation in Switzerland and its impacts. *Nat. Hazards Earth Syst. Sci.*, 1–28, DOI: 10.5194/nhess-2021-93.

Tuel, A. and O. Martius, 2021b: A global perspective on the sub-seasonal clustering of precipitation extremes. *Wea. Clim. Extrem.*, **33**, 100 348, DOI: 10.1016/j.wace.2021.100348.

Tuel, A. and O. Martius, 2022: Subseasonal Temporal Clustering of Extreme Precipitation in the Northern Hemisphere: Regionalization and Physical Drivers. *J. Climate*, **35 (11)**, 3537–3555, DOI: 10.1175/JCLI-D-21-0562.1.

Uhlemann, S., A. H. Thieken, and B. Merz, 2010: A consistent set of trans-basin floods in Germany between 1952 and 2002. *Hydrol. Earth Syst. Sci.*, **14 (7)**, 1277–1295, DOI: 10.5194/hess-14-1277-2010.

UNDRR, 2007: Definition: Hazard. URL: https://www.undrr.org/terminology/hazard.

UNDRR, 2016: Report of the Open-ended Intergovernmental Expert Working Group on Indicators and Terminology relating to Disaster Risk Reduction. Tech. rep., United Nations Office for Disaster Risk Reduction (UNDRR), United Nations General Assembly, URL: https://digitallibrary.un.org/record/852089, accessed: 2024-07-22.

Villarini, G., J. A. Smith, A. A. Ntelekos, and U. Schwarz, 2011: Annual maximum and peaks-over-threshold analyses of daily rainfall accumulations for Austria. *J. Geophys. Res.: Atmospheres*, **116 (D5)**, DOI: 10.1029/2010JD015038.

Vitolo, R., D. B. Stephenson, I. M. Cook, and K. Mitchell-Wallace, 2009: Serial clustering of intense European storms. *Meteorol. Z.*, **18**, 411–424, DOI: 10.1127/0941-2948/2009/0393.

Walz, M. A., D. J. Befort, N. O. Kirchner-Bossi, U. Ulbrich, and G. C. Leckebusch, 2018: Modelling serial clustering and inter-annual variability of European winter windstorms based on large-scale drivers. *Int. J. Climatol.*, **38 (7)**, 3044–3057, DOI: 10.1002/joc.5481.

Wang, Y., L. Tang, P.-L. Chang, and Y.-S. Tang, 2021: Separation of convective and stratiform precipitation using polarimetric radar data with a support vector machine method. *Atmos. Meas. Tech.*, **14**, 185–197, DOI: 10.5194/amt-14-185-2021.

Ward, P. J., J. Daniell, M. Duncan, A. Dunne, C. Hananel, S. Hochrainer-Stigler, A. Tijssen, S. Torresan, R. Ciurean, J. C. Gill, et al., 2022: Invited perspectives: A research agenda towards disaster risk management pathways in multi-(hazard-) risk assessment. *Nat. Hazards Earth Syst. Sci.*, **22 (4)**, 1487–1497.

Watson, A. I., J. Meitín, and J. B. Cunning, 1988: Evolution of the Kinematic Structure and Precipitation Characteristics of a Mesoscale Convective System on 20 May 1979. *Mon. Weather Rev.*, **116 (8)**, 1555 – 1567, DOI: 10.1175/1520-0493(1988)116<1555:EOTKSA>2.0.CO;2.

Welker, C., O. Martius, P. Stucki, D. Bresch, S. Dierer, and S. Brönnimann, 2016: Modelling economic losses of historic and present-day high-impact winter windstorms in Switzerland. *Tellus A: Dynamic Meteorology and Oceanography*, **68 (1)**, 29 546, DOI: 10.3402/tellusa.v68.29546.

Wettergefahren-Frühwarnung, 2005: Archiv: Extreme Wetterereignisse 2005. URL: `https://www.wettergefahren-fruehwarnung.de/Ereignis/archiv_2005.html`, accessed: 18 May 2025.

White, G. F., 1942: Human adjustment to floods: a geographical approach to the flood problem in the United States. Ph.D. thesis, The University of Chicago, URL: `https://biotech.law.lsu.edu/climate/docs/Human_Adj_Floods_White.pdf`.

Wilhelm, J., S. Mohr, H. J. Punge, B. Mühr, M. Schmidberger, J. E. Daniell, K. M. Bedka, and M. Kunz, 2021: Severe thunderstorms with large hail across Germany in June 2019. *Weather*, **76 (7)**, 228–237, DOI: 10.1002/wea.3886.

Wilks, D. S., 2006: *Statistical Methods in the Atmospheric Sciences*. Academic Press.

Wilson, J. and R. Wakimoto, 2001: The Discovery of the Downburst: T. T. Fujita's Contribution. *Bull. Am. Meteorol. Soc.*, **82**, DOI: 10.1175/1520-0477(2001)082<0049:TDOTDT>2.3.CO;2.

WMO, 2010: Assessment of the Observed Extreme Conditions During the 2009/2010 Boreal Winter. Tech. Rep. WMO/TD-No. 1550, World Meteorological Organization, Authors: Bissolli, P, Cassou, C., Chen, L, Kiktev, D., Kryjov, V., Pattanaik, D.R., Schneider, M., and Vinit, F., URL: `https://www.dwd.de/DE/leistungen/besondereereignisse/verschiedenes/20100921_winter2009-2010_td1550_en_web.pdf?__blob=publicationFile&v=3`, accessed: 2025-01-05.

WMO, 2017: WMO International Cloud Atlas. URL: `https://cloudatlas.wmo.int/home.html`, accessed: 2025-02-12.

WMO, 2021: Technical Regulations - Basic Documents No. 2. URL: `https://library.wmo.int/viewer/35631/download?file=49_III_en.pdf&type=pdf&navigator=1`, accessed: 2024-11-25.

Xoplaki, E., F. Ellsäßer, J. Grieger, K. M. Nissen, J. G. Pinto, M. Augenstein, T.-C. Chen, H. Feldmann, P. Friederichs, D. Gliksman, L. Goulier, K. Haustein, J. Heinke, L. Jach, F. Knutzen, S. Kollet, J. Luterbacher, N. Luther, S. Mohr, C. Mudersbach, C. Müller, E. Rousi, F. Simon, L. Suarez-Gutierrez, S. Szemkus, S. M. Vallejo-Bernal, O. Vlachopoulos, and F. Wolf, 2025: Compound events in Germany in 2018: Drivers and Case studies. *Nat. Hazards Earth Syst. Sci.*, **25 (2)**, 541–564, DOI: 10.5194/nhess-25-541-2025.

Zanardo, S., L. Nicotina, A. G. Hilberts, and S. P. Jewson, 2019: Modulation of economic losses from European floods by the North Atlantic Oscillation. *Geophys. Res. Lett.*, **46 (5)**, 2563–2572, DOI: 10.1029/2019GL081956.

Zscheischler, J., O. Martius, S. Westra, E. Bevacqua, C. Raymond, R. M. Horton, B. van den Hurk, A. AghaKouchak, A. Jézéquel, M. D. Mahecha, D. Maraun, A. M. Ramos, N. N. Ridder, W. Thiery, and E. Vignotto, 2020: A typology of compound weather and climate events. *Nat. Rev. Earth Environ.*, **1 (7)**, 333–347, DOI: 10.1038/s43017-020-0060-z.

Zscheischler, J., C. Raymond, Y. Chen, N. Le Grix, R. Libonati, C. D. W. Rogers, C. J. White, and P. Wolski, 2025: Compound weather and climate events in 2024. *Nat. Rev. Earth Environ.*, **6 (4)**, 240–242, DOI: 10.1038/s43017-025-00657-y.

Zscheischler, J., S. Westra, B. J. J. M. van den Hurk, S. I. Seneviratne, P. J. Ward, A. Pitman, A. AghaKouchak, D. N. Bresch, M. Leonard, T. Wahl, and X. Zhang, 2018: Future climate risk from compound events. *Nat. Clim. Change*, **8 (6)**, 469–477, DOI: 10.1038/s41558-018-0156-3.

A. Appendix for Chapter 5

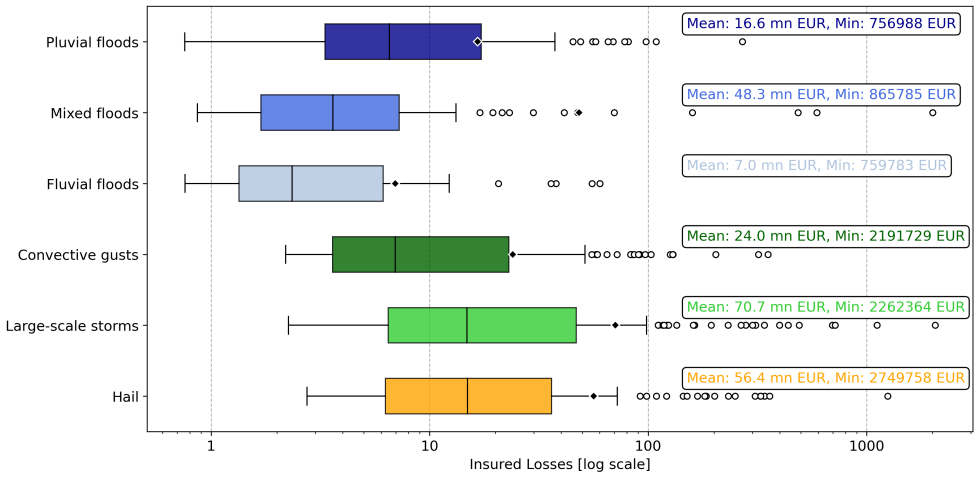

Figure A1.: Scope GER: Distribution of loss values by hazard type (logarithmic scale), including mean values and the minimum loss event by hazard in the p90 dataset.

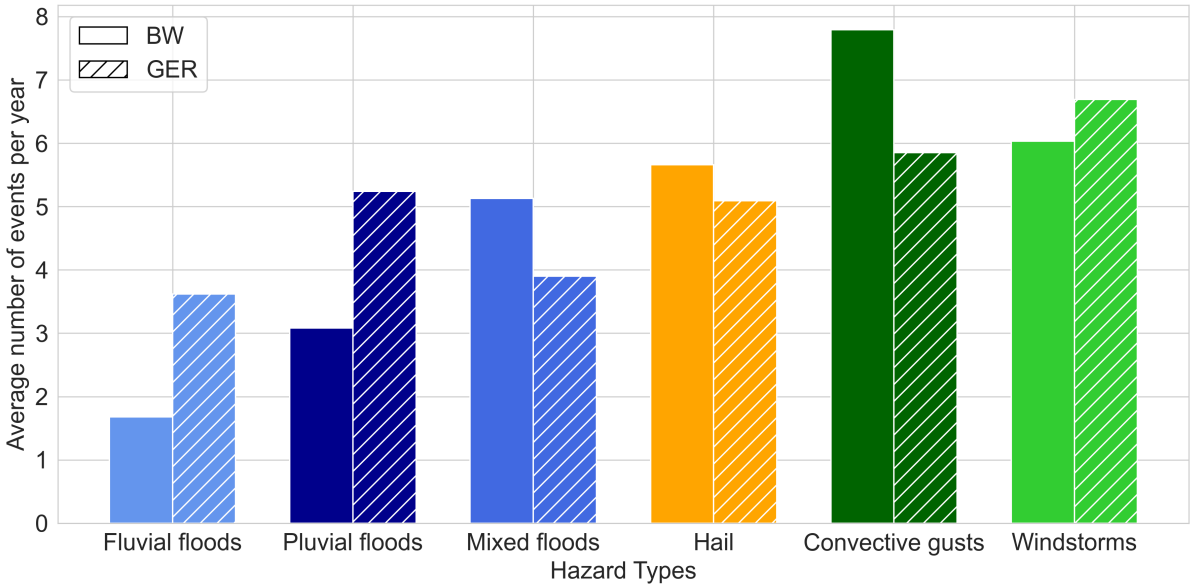

Figure A2.: Average annual number of events by hazard type in BW (1997/2002–2022) and GER (1986–2023, hatched) as a result of the p90 filter of losses and claims.

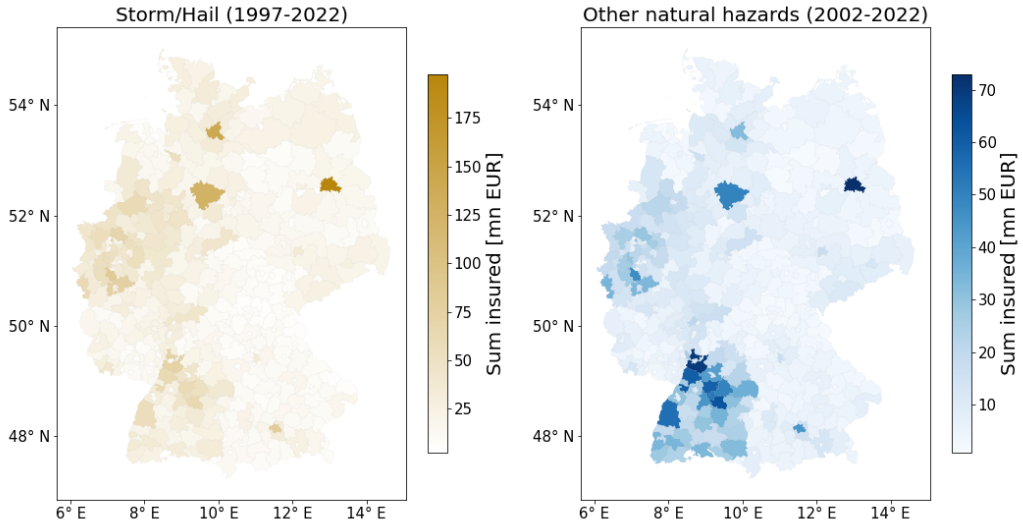

Figure A3.: Sum insured in million EUR by administrative district for (a) storm and hail insurance (b) other natural hazards insurance.

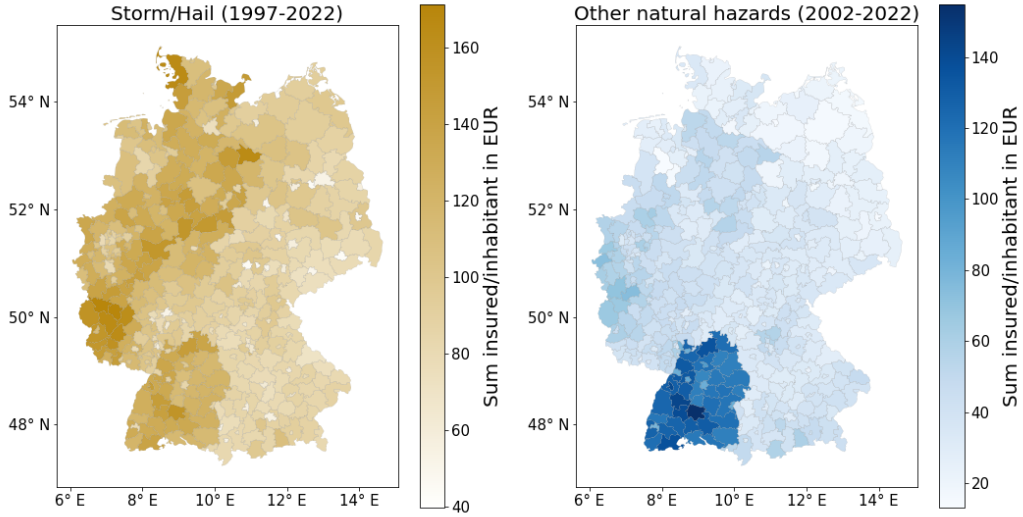

Figure A4.: Total premium (i. e., sum insured) per inhabitant for (a) storm and hail insurance and (b) other natural hazards insurance.

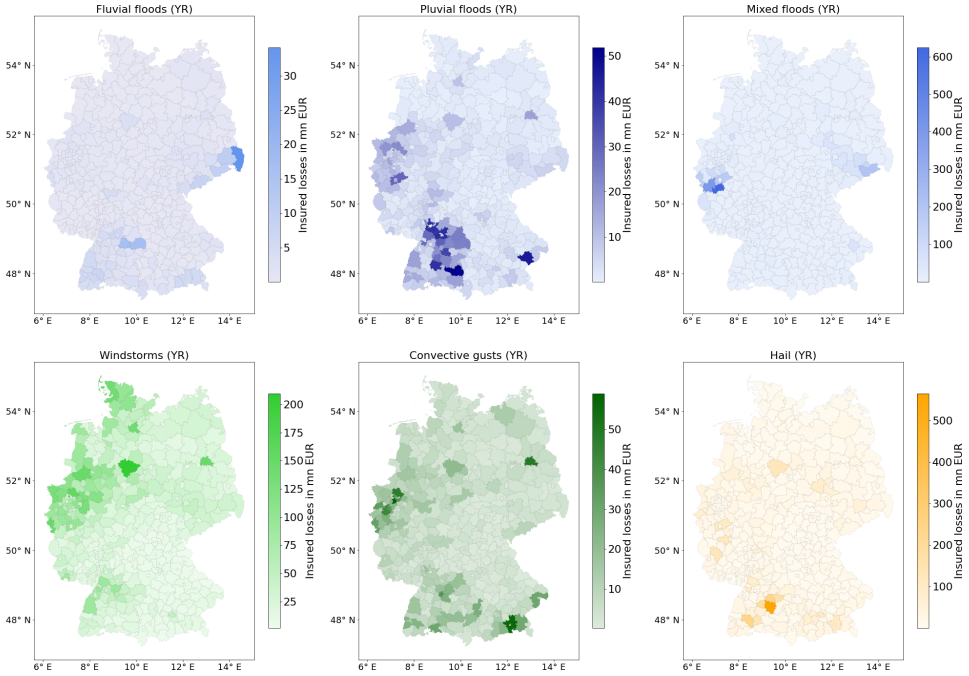

Figure A5.: Total insured losses cumulated over 1997-2022 per administrative district in Germany and hazard type, with respect to (a) fluvial floods, (b) pluvial floods, (c) mixed floods, (d) windstorms, (e) convective gusts, and (f) hailstorms. Note that scales differ depending on the hazard type for visibility reasons.

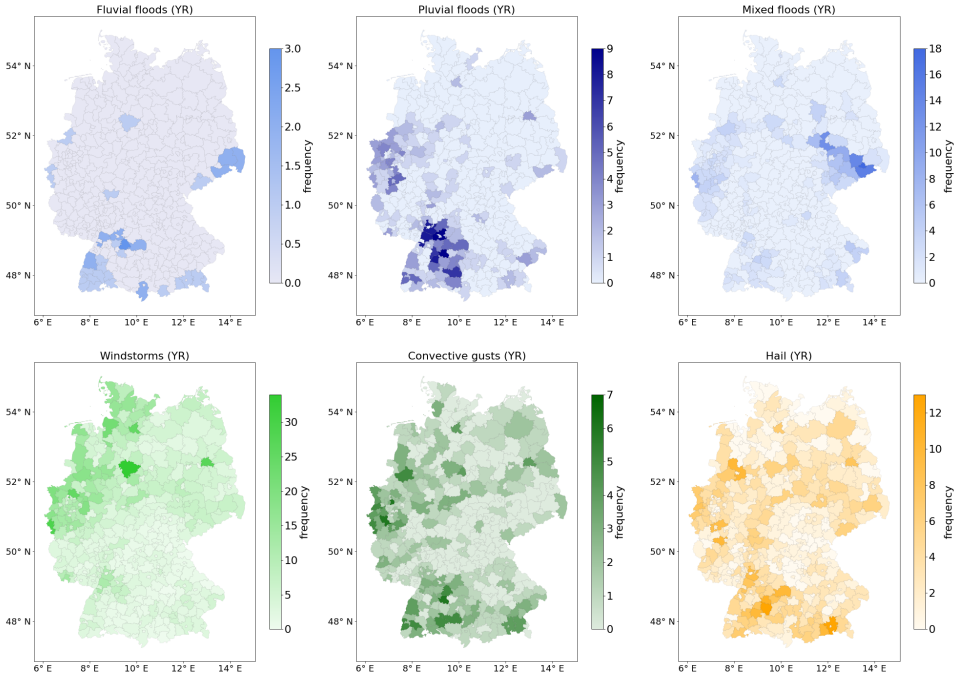

Figure A6.: Occurrence (number of distinct events) of losses larger than €1 million by administrative district in Germanyand hazard type, with respect to (a) fluvial floods, (b) pluvial floods, (c) mixed floods, (d) windstorms, (e) convective gusts, and (f) hailstorms.

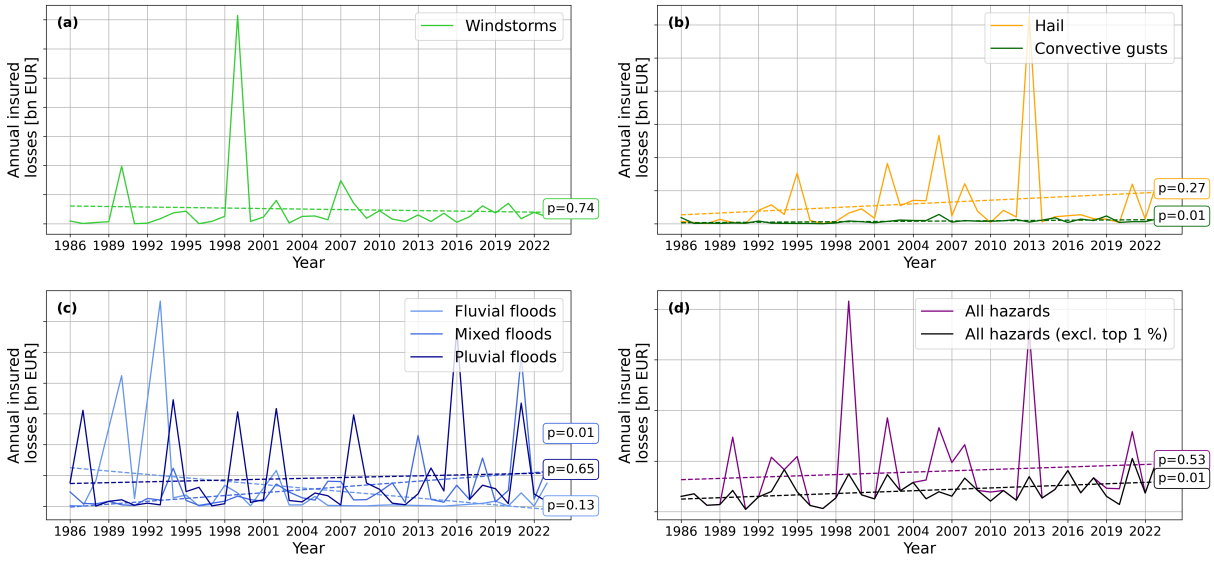

Figure A7.: Total losses across BW by hazard type and year (1986–2023), for (a) windstorms, (b) convective gust events and hail, (c) flood events and (d) all hazards with and without the top 1 % of losses and claims

B. Appendix for Chapter 6

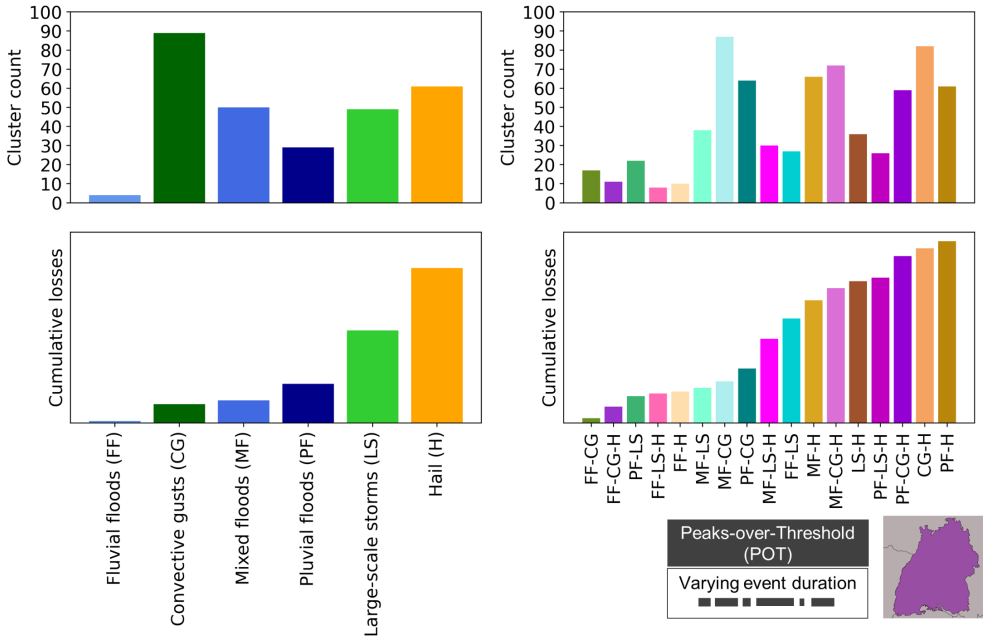

Figure B1.: Scope BW, event identification method POT and clustering window of 21 days: Frequency (upper panel) of events in clusters by hazard type for single types (left) and multiple types (right). Cumulative losses (lower panel) depending on the type of the cluster.

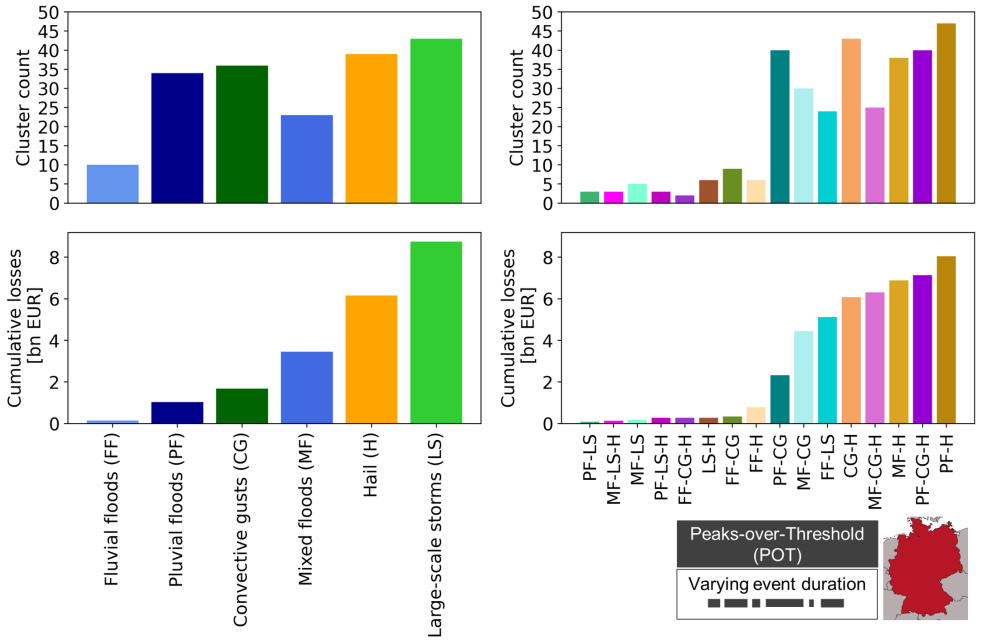

Figure B2.: Scope GER, event identification method POT and clustering window of 21 days: Frequency (upper panel) of events in clusters by hazard type for single types (left) and multiple types (right). Cumulative losses (lower panel) depending on the type of the cluster.

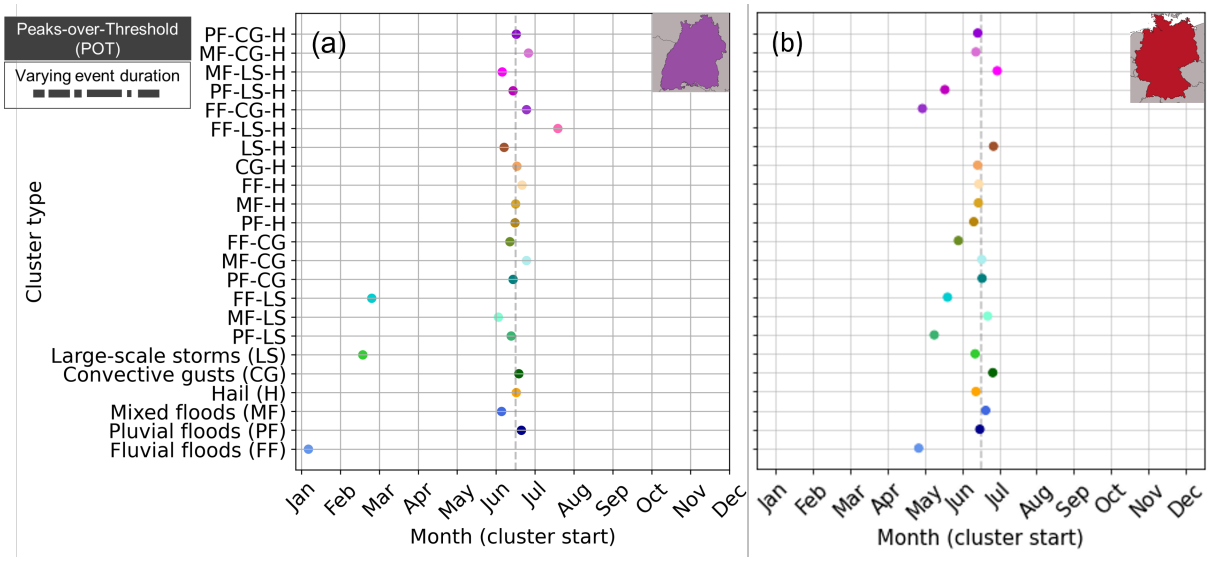

Figure B3.: Mean start day of the year by cluster type, for (a) BW and (b) GER. The dashed vertical line shows July 1st, around which most average start dates (mainly related to convective events) are grouped.

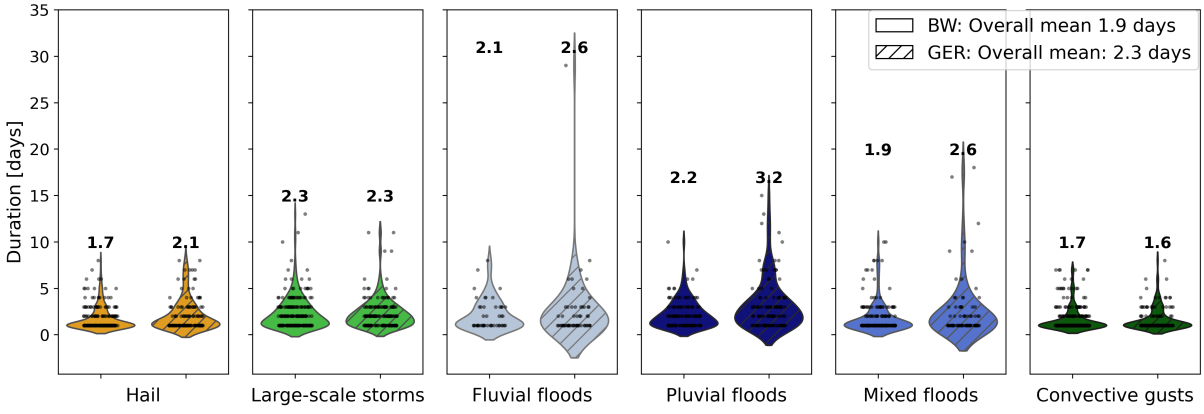

Figure B4.: Duration of events as identified with POT by hazard type (colors) and scope (hatching). Added text refers to the mean.

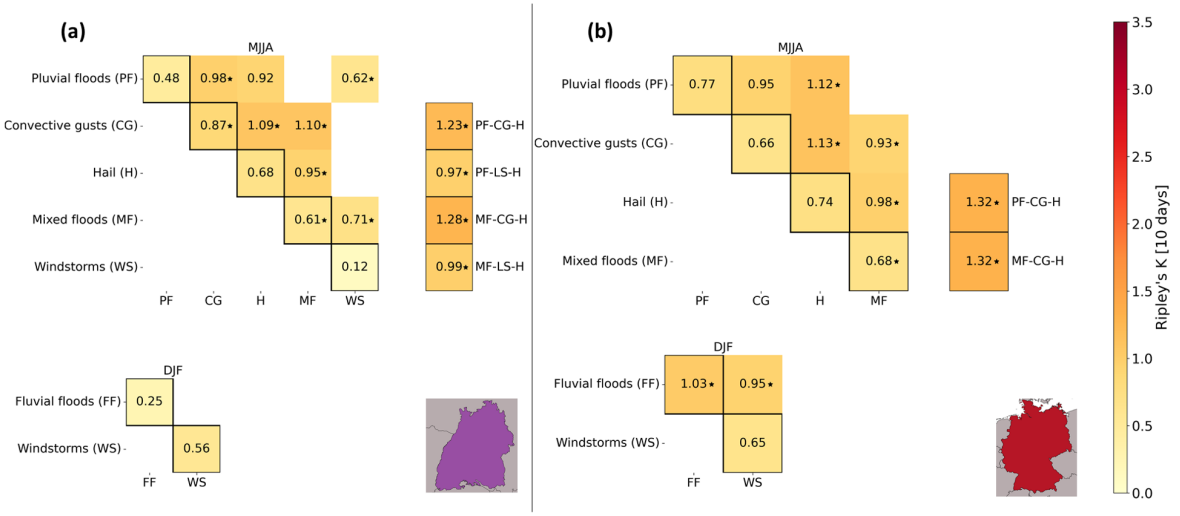

Figure B5.: Same as Fig. 6.12, but for a time window of 10 days.

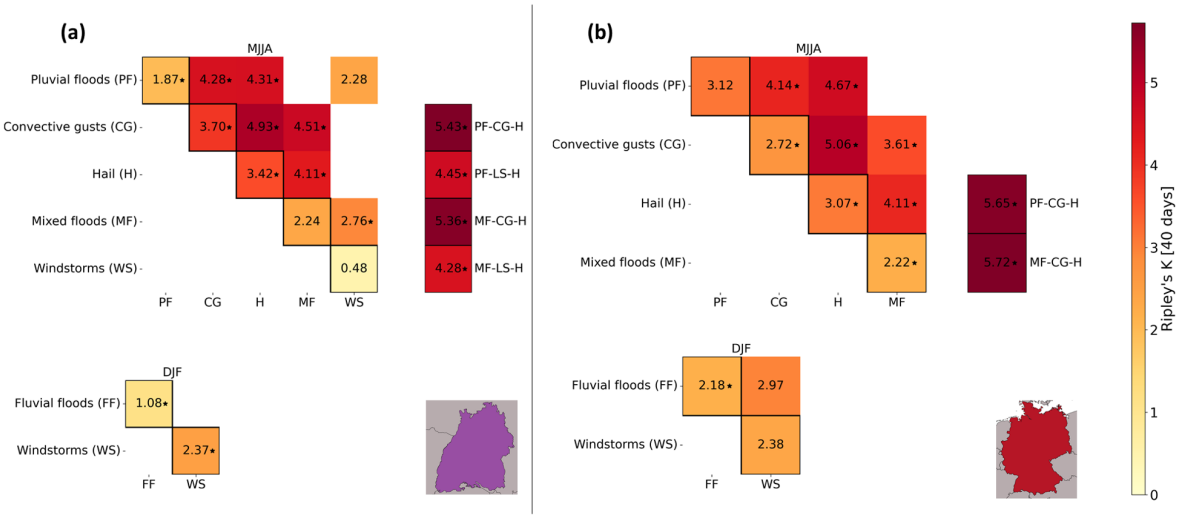

Figure B6.: Same as Fig. 6.12, but for a time window of 40 days.

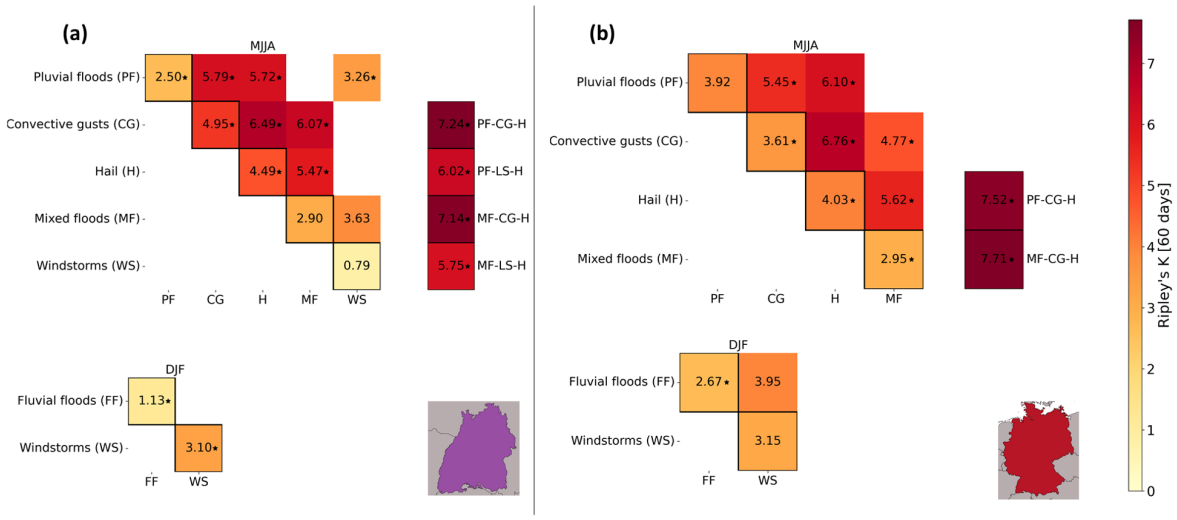

Figure B7.: Same as Fig. 6.12, but for a time window of 60 days.

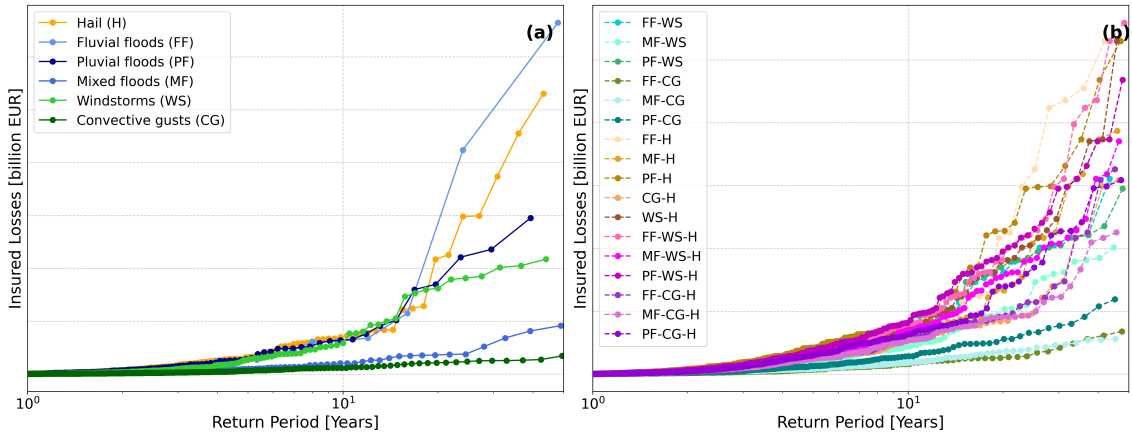

Figure B8.: Scope BW: Return period of events (logarithmic scale) vs. insured losses caused by (a) single-hazard and (b) multi-hazard clusters.

C. Appendix for Chapter 7

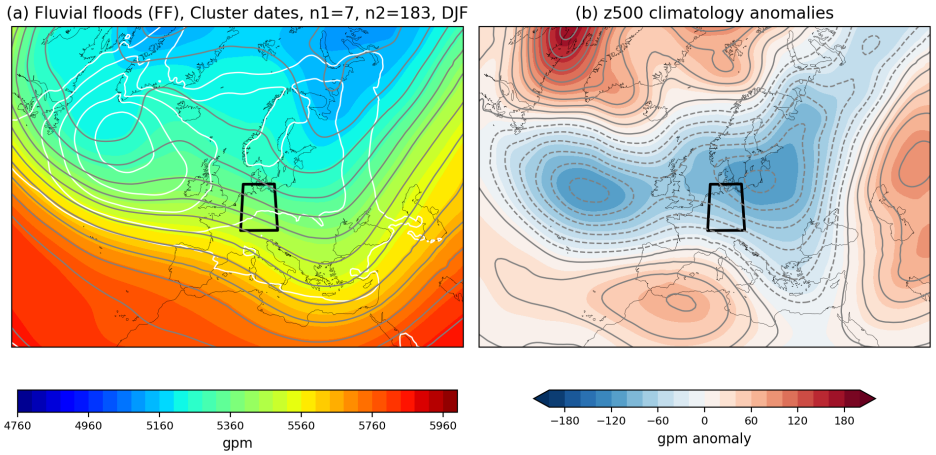

Figure C1.: Same as Fig. 7.1, but for clustered fluvial floods in BW.

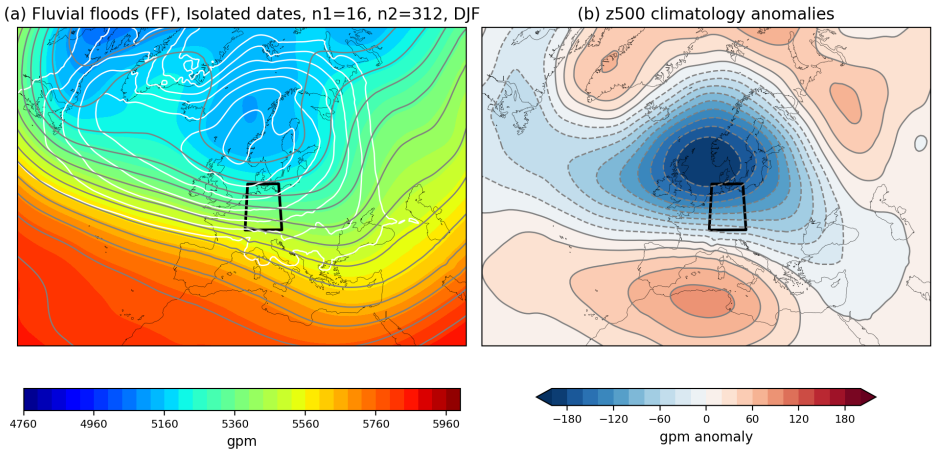

Figure C2.: Same as Fig. 7.1, but for isolated fluvial floods in BW.

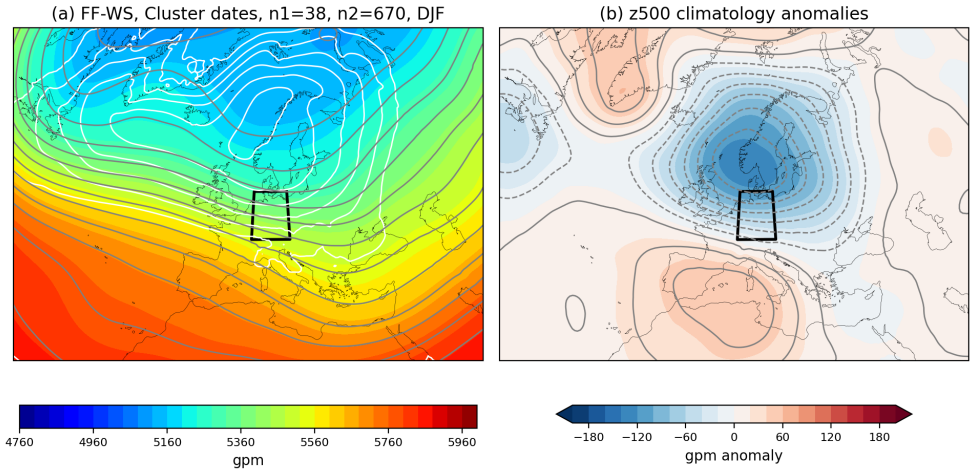

Figure C3.: Same as Fig. 7.1, but for clustered windstorms and fluvial floods.

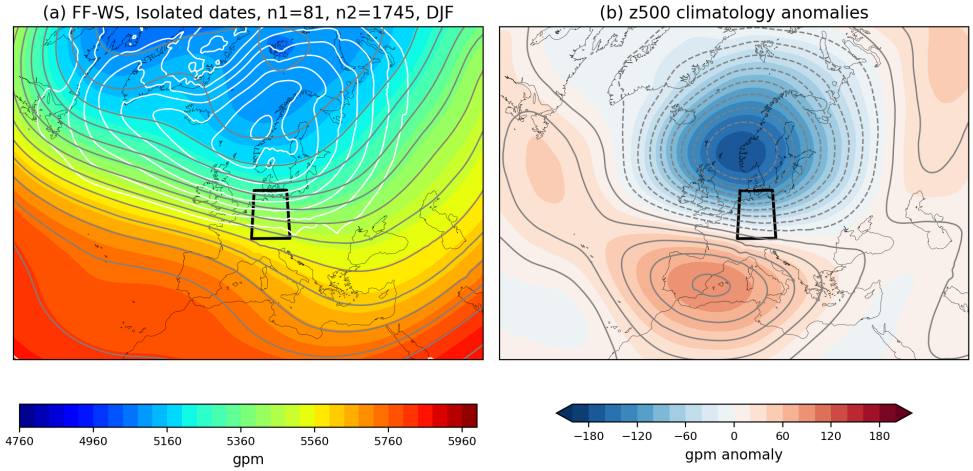

Figure C4.: Same as Fig. 7.1, but for isolated windstorms or fluvial floods.

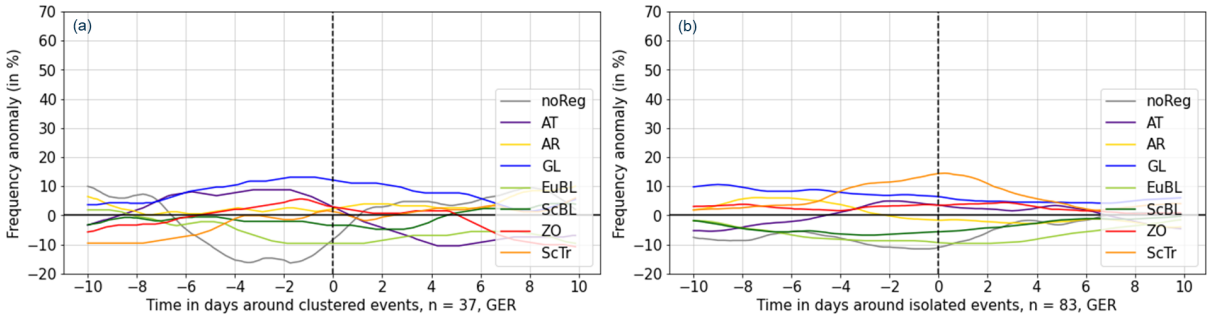

Figure C5.: As Fig. 7.4, but for combined windstorm and flood events in GER.

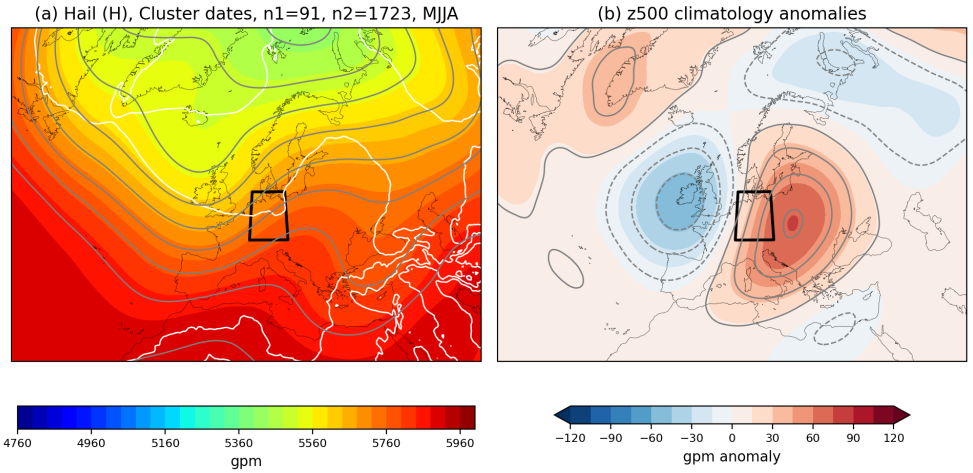

Figure C6.: Same as Fig. 7.1, but for clustered convective gusts during MJJA. Note that the color is adjusted to a smaller range compared to DJF.

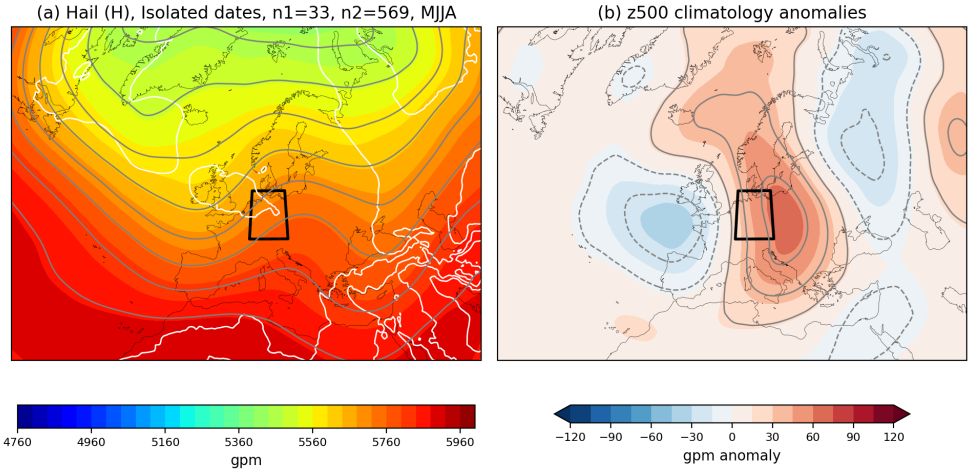

Figure C7.: Same as Fig. 7.1, but for isolated hail during MJJA. Note that the color is adjusted to a smaller range compared to DJF.

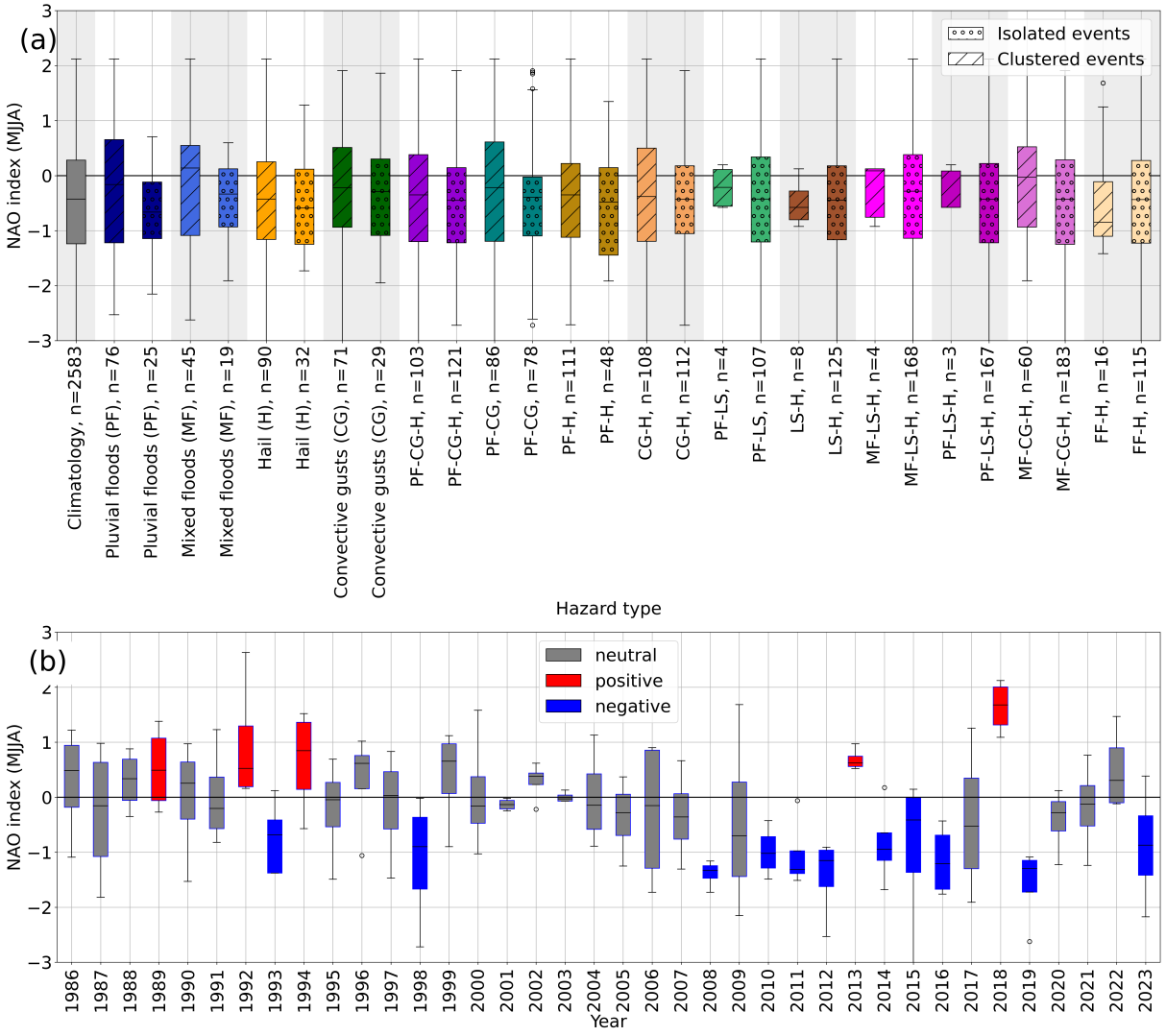

Figure C8.: May–August: (a) Distribution of monthly NAO values during 1986–2023, depending on the event type (colors), isolated occurrence or occurrence in clusters (hatches), (b) monthly mean NAO values from 1986–2023. Positive NAO values are detected when with mean values > 0.5 and max values > 0.75. Negative values relate to mean values < -0.5 and max values < -0.75. Neutral years are all years neither classified as positive nor as negative.

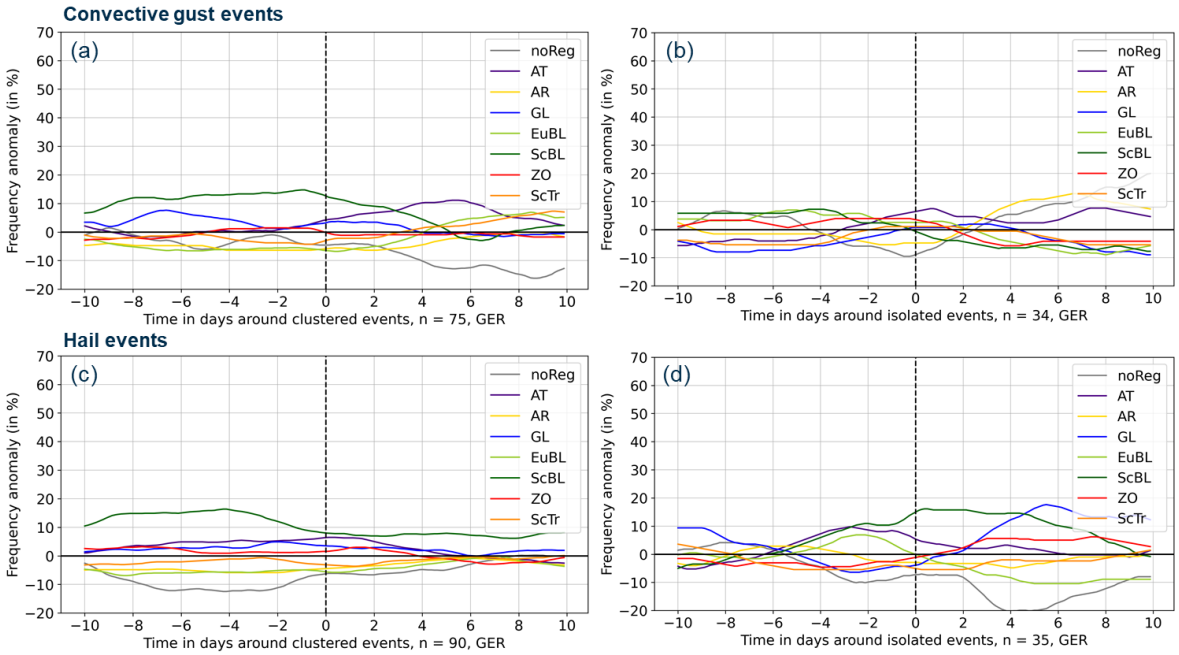

Figure C9.: Same as Fig. 7.10, but for convective gust events and hail.

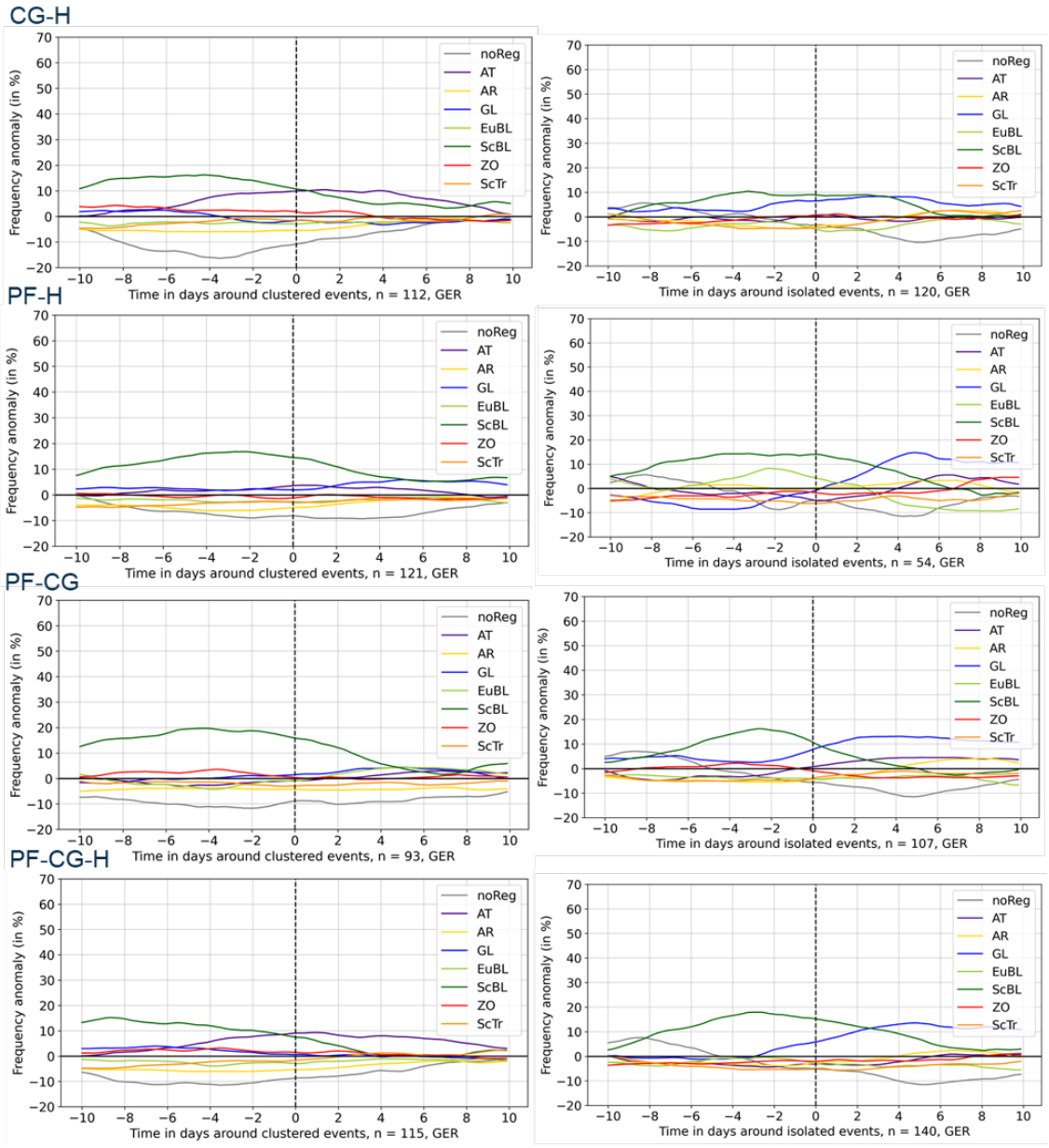

Figure C10.: As Fig. 7.4, but for combinations of single convective hazards.

Acknowledgements

Writing this thesis would not have been possible without the support of many. First and foremost, I would like to thank my supervisor at IMKTRO, Prof. Dr. Michael Kunz. Thank you for taking the risk (;)) to welcoming a PhD student with such a different background than usual to your group. Thank you for your immense support, especially in critical situations, and for trusting in my research, sometimes even more than I did. Thank you for giving me freedom in the choice of my methods and the general research direction. I would also like to thank you for your thorough proofreading, even on weekends and in airplanes. I am also very grateful for the support you gave me to visit campaigns, conferences, workshops, a summer and winter school and many other activities. Lastly, thank you for showing your enthusiasm for meteorology. This made me learn a lot from you.

To my supervisor at the BGU, Prof. Dr.-Ing. Stefan Hinz, I would first like to thank you for supervising me as an external candidate, which is certainly not a given. I would like to thank you for your always helpful input in our regular meetings, and for your interest in topics far from your day-to-day work. I would also like to thank you for including me in the doctoral retreat of the IPF, for your support with the PhD registration and submission, and for taking a stance for PhD students in general. I could tell from the beginning that *Hinz und Kunz* make a great team, thank you both for the positive atmosphere at our meetings. I would also like to express my gratitude to Prof. Dr. Jan Cermak and Prof. Dr. Jochen Schanze for being part of my PhD committee.

I would like to thank the *Stiftung Umwelt und Schadenvorsorge* for funding my research, and for fostering academic and practitioner exchange. I would also like to thank the *SV SparkassenVersicherung AG* and Achim Gegler in particular for the provision of data. Many thanks also go to the German Insurance Association for providing additional data. In addition, I thank the GRACE Graduate School for supporting several travel activities, and the EU COST Action DAMOCLES for financial support.

I would also like to thank several other people who contributed to my PhD. Thank you Alexandre Tuel for making my short research stay extremely productive. Your input on the clustering metrics was invaluable. Thank you also for your thorough reading of my paper. James Daniell, thank you for your interest in my project and for connecting me with the right people: Marleen de Ruiter, thank you for the interesting and encouraging exchange, and for the nice discussions during my research stay in Amsterdam. Thank you also especially to Prof. Philip Ward, and the Early Career Researchers of the MYRIAD team in Amsterdam for their motivation and exchange. I am also thankful for being part of the compoundNET

community, starting with a summer school in Budapest, over a conference in Lisbon, to workshops in Glasgow and Karlsruhe. I thoroughly enjoyed to learn from such brilliant minds.

In addition, I would also like to thank the Atmospheric Risks group. Thank you all for your input during group meetings and for the positive vibe in the past years. First of all, Markus, you helped me a lot in this past year and months especially, thank you for all of your help, both subject-related and mentally. Thank you for your constant motivation boosts and encouragement, for proofreading a large part of my thesis, and for patiently answering all of my questions. Sanna, thank you for your support, feedback and encouragement especially during the first years of my PhD, and for encouraging me to contribute to my first CEDIM FDA report. Jannick, thank you for your help in many subject-related questions, and for being empathic. Mathis, thank you for your help with IT emergencies and non-emergencies, and for bringing an enjoyable atmosphere in the group. Markus, Jannick, Mathis, Christian, and Elias, thank you all for proofreading parts of my thesis.

I would also like to thank several other IMKTRO members: First, I thank the former AG Grams, particularly Christian Grams and Seraphine Hauser for the provision of the weather regimes data. Sera, your help with the regimes was indispensable for my thesis, I cannot thank you enough for that. Thank you also for being a kind and caring friend. Starting a PhD during COVID was definitely a challenge. The Swabian MOSES campaign at the beginning helped me to dive into meteorology and to get to know the institute. Thank you especially Martin, Jannik, and Sanna for the nice time we spent together on site, for your patience and support. Many others contributed to making my time at Campus Nord (or the bike rides to it) enjoyable. Marie, thank you for the walks and bike rides, and your friendship also beyond that. Thank you Hannah for starting the PhD seminar together and all the rants. I am glad we got through this together. Thank you Lutz for the roof terrace breaks and for being the best (maybe second best) pancake master. Gabriella, thank you for your energy and motivation to change things for the better. Starting the PhD council (and the diversity network!) with you was one of the best things of my PhD. Athul, thank you for taking time to proofread as well. Thanks to all of you for your support, I am glad to have met you all and happy that our connections extend beyond work.

I am really looking forward to spending more time with my friends. Miri, thank you for your support especially in this last phase, with food and proofreading. Thank you Adrián for proofreading and for always believing in me. Möm, I am looking forward to our bike tour, thank you for being there always. A big thank you also to Johannes, without whom I would probably still not be using for-loops, and to Simon for all the brunches and your support particularly in the first years of the PhD. Many more could be mentioned here - thank you for all of your support, you know who you are.

To Mama and Papa, thank you for providing me with the possibility to do this PhD. I would not be the person I am now without your heartfelt upbringing. Thank you for your support, always. Lastly, Sebastian, I have no words to express how thankful I am for all of your support. I am so glad to have you in my life.

While this PhD journey was inherently challenging and came with a lot of ups and downs, it was also an enriching time where I pushed far off my limits. I am thankful for having had such a privilege.